NUREG/CR-3334
Volume 1
ORNL/TM-8787/V1

ornl

OAK
RIDGE
NATIONAL
LABORATORY

UNION
CARBIDE

Heavy-Section Steel Technology Program Quarterly Progress Report for January–March 1983

C. E. Pugh

Prepared for the U.S. Nuclear Regulatory Commission
Office of Nuclear Regulatory Research
Under Interagency Agreements DOE 40-551-75 and 40-552-75

OPERATED BY
UNION CARBIDE CORPORATION
FOR THE UNITED STATES
DEPARTMENT OF ENERGY

DISCLAIMER

The following pages are an exact representation of what is in the original document folder.

Printed in the United States of America. Available from
National Technical Information Service
U.S. Department of Commerce
5285 Port Royal Road, Springfield, Virginia 22161

Available from

GPO Sales Program
Division of Technical Information and Document Control
U.S. Nuclear Regulatory Commission
Washington, D.C. 20555

NUREG/CR--3334-Vol.1

DE83 016994

NUREG/CR-3334
Volume 1
ORNL/TM-8787/V1
Dist. Category RF

Engineering Technology Division

HEAVY-SECTION STEEL TECHNOLOGY PROGRAM QUARTERLY PROGRESS REPORT FOR JANUARY–MARCH 1983

C. E. Pugh

Manuscript Completed – July 28, 1983
Date Published – September 1983

Prepared for the
U.S. Nuclear Regulatory Commission
Office of Nuclear Regulatory Research
Under Interagency Agreements DOE 40-551-75 and 40-552-75

NRC FIN No. B0119

Prepared by the
OAK RIDGE NATIONAL LABORATORY
Oak Ridge, Tennessee 37830
operated by
UNION CARBIDE CORPORATION
for the
U.S. DEPARTMENT OF ENERGY
under Contract No. W-7405-eng-26

DISCLAIMER

CONTENTS

Page

LIST OF FIGURES

LIST OF TABLES

PREFACE

The Heavy-Section Steel Technology (HSST) Program, which is sponsored by the Nuclear Regulatory Commission, is an engineering research activity devoted to extending and developing the technology for assessing the margin of safety against fracture of the thick-walled steel pressure vessels used in light-water-cooled nuclear power reactors. The program is being carried out in close cooperation with the nuclear power industry. This report covers HSST work performed in January–March 1983. The work performed by Oak Ridge National Laboratory (ORNL) and by subcontractors is managed by the Engineering Technology Division. Major tasks at ORNL are carried out by the Engineering Technology Division and the Metals and Ceramics Division. Prior progress reports on this program are ORNL-4176, ORNL-4315, ORNL-4377, ORNL-4463, ORNL-4512, ORNL-4590, ORNL-4653, ORNL-4681, ORNL-4764, ORNL-4816, ORNL-4855, ORNL-4918, ORNL-4971, ORNL/TM-4655 (Vol. II), ORNL/TM-4729 (Vol. II), ORNL/TM-4805 (Vol. II), ORNL/TM-4914 (Vol. II), ORNL/TM-5021 (Vol. II), ORNL/TM-5170, ORNL/NUREG/TM-3, ORNL/NUREG/TM-28, ORNL/NUREG/TM-49, ORNL/NUREG/TM-64, ORNL/NUREG/TM-94, ORNL/NUREG/TM-120, ORNL/NUREG/TM-147, ORNL/NUREG/TM-166, ORNL/NUREG/TM-194, ORNL/NUREG/TM-209, ORNL/NUREG/TM-239, NUREG/CR-0476 (ORNL/NUREG/TM-275), NUREG/CR-0656 (ORNL/NUREG/TM-298), NUREG/CR-0818 (ORNL/NUREG/TM-324), NUREG/CR-0980 (ORNL/NUREG/TM-347), NUREG/CR-1197 (ORNL/NUREG/TM-370), NUREG/CR-1305 (ORNL/NUREG/TM-380), NUREG/CR-1477 (ORNL/NUREG/TM-393), NUREG/CR-1627 (ORNL/NUREG/TM-401), NUREG/CR-1806 (ORNL/NUREG/TM-419), NUREG/CR-1941 (ORNL/NUREG/TM-437), NUREG/CR-2141/Vol. 1 (ORNL/TM-7822), NUREG/CR-2141, Vol. 2 (ORNL/TM-7955), NUREG/CR-2141, Vol. 3 (ORNL/TM-8145), NUREG/CR-2141, Vol. 4 (ORNL/TM-8252), NUREG/CR-2751, Vol. 1 (ORNL/TM-8369/V1), NUREG/CR-2751, Vol. 2 (ORNL/TM-8369/V2), NUREG/CR-2751, Vol. 3 (ORNL/TM-8369/V3), and NUREG/CR-2751, Vol. 4 (ORNL/TM-8369/V4).

SUMMARY

1. PROGRAM ADMINISTRATION AND PROCUREMENT

The Heavy-Section Steel Technology (HSST) Program is an engineering research activity conducted by the Oak Ridge National Laboratory (ORNL) for the Nuclear Regulatory Commission in coordination with other research sponsored by the federal government and private organizations. The program comprises studies related to all areas of the technology of materials fabricated into thick-section primary-coolant containment systems of light-water-cooled nuclear power reactors. The principal area of investigation is the behavior and structural integrity of steel pressure vessels containing cracklike flaws. Current work is organized into the following tasks: (1) program administration and procurement, (2) fracture-mechanics analyses and investigations, (3) investigations of irradiated materials, (4) thermal-shock investigations, (5) pressure vessel investigations, (6) stainless steel cladding investigations, and (7) environmentally assisted crack-growth studies.

The work performed at ORNL and under existing research and development subcontracts is included in this report. During the quarter, eight program briefings, reviews, or presentations were made, and two technical reports were published.

2. FRACTURE-MECHANICS ANALYSES AND INVESTIGATIONS

A modified deformation-plasticity formulation has been incorporated into the ADINA-ORVIRT fracture-mechanics analysis system for application to pressurized-thermal-shock (PTS) conditions. The formulation incorporates a thermal-strain modification and has been applied to a previously analyzed center-cracked plate.

In its HSST support program, Battelle Columbus Laboratories (BCL) carried out work in support of PTS technology, crack-initiation tests, and crack-arrest studies. In connection with their PTS studies, the literature was reviewed to identify wide-plate crack-arrest tests with sufficient information available to allow dynamic finite-element analyses to be performed. Two types of finite-element analyses were performed for double-tension tests conducted in Japan, and the results were compared with published data and analyses. The crack-initiation work included a new series of thermal-shock experiments (TSEs) on TSE-5A steel that addresses reinitiation toughness values measured with compact specimens. Crack-arrest tests were carried out for TSE material with three different heat treatments, and K_{Ia} values were obtained at temperatures associated with the upper-shelf of Charpy V-notch impact tests. Plans were developed for crack-arrest tests at lower temperatures for the low-upper-shelf weld metal from intermediate test vessel (ITV)-8A.

The study continued at the University of Maryland on the transition from ductile fracture at high temperatures to brittle cleavage at lower temperatures. Charpy testing of A508 material was performed, topological

and microstructural examinations of an A533B material were made, improvements were made to the finite-element code SAMCR, and analysis work was performed to support ESSO-type test planning.

3. INVESTIGATION OF IRRADIATED MATERIALS

Charpy V-notch tests on unirradiated (control) specimens from the Fourth HSST Irradiation series (state-of-the-art weld metal) have been essentially completed by Materials Engineering Associates (MEA) and ORNL, and statistical analyses of the data have been performed. Scoping tests on irradiated specimens have been completed and test temperatures assigned for the main matrix. A contract was placed with MEA for capsule construction and irradiation (at the Nuclear Science and Technology Facility at the State University of New York in Buffalo) of one-wire stainless-steel-clad specimens. Charpy tests were performed on unirradiated clad specimens, and the data showed variations that are attributed to the metallurgical structure of this multilayer cladding.

4. THERMAL-SHOCK INVESTIGATIONS

The computer code OCA-II was modified to include finite-length flaws, and a parametric study was conducted to determine the advantage in replacing two-dimensional flaws in its modeling with specific finite-length flaws. Collection of material properties continued in support of the planned TSE-7, and a preliminary thermal shock was applied to the unflawed TSE-7 cylinder to ensure that an appropriate shock can be achieved.

5. PRESSURE VESSEL INVESTIGATIONS

Posttest evaluation of intermediate test vessel V-8A continued with measurement of properties of the low-upper-shelf weld seam and determination of flaw geometry. Preparations are being made for the first PTS test (PTSE-1). Two test vessels are being fabricated – one to be used for testing of the PTS experimental facility and the other for the first experiment, PTSE-1. Fracture-mechanics analyses that correspond to candidate transients for the PTSE-1 were made with upper-shelf behavior being considered explicitly for the first time. Further developmental tests of seals, thermocouples, and other apparatus were conducted, and test facility construction was nearly completed. Material property studies were continued for the purpose of defining the desired heat treatment of the vessel for PTSE-1.

6. STAINLESS STEEL CLADDING INVESTIGATIONS

Further testing of one-wire-clad plate specimens has been deferred until data on the effects of irradiation have been obtained. Purchase specifications were prepared for procurement of three-wire series-arc-clad plates for future study. Metallographic examinations were made of the multilayer one-wire cladding, and a higher than anticipated degree of dilution was observed. The inclusion of such material in the clad plate and irradiation investigations should provide data relevant to the behavior of similar cladding that is actually in use.

7. ENVIRONMENTALLY ASSISTED CRACK-GROWTH STUDIES

Westinghouse Electric Corporation's Power Systems, Nuclear Technology Division continued their studies to characterize the effects of chemistry on the environmentally assisted acceleration of fatigue crack growth. Further tests were completed on A533B material with an intermediate sulfur content, and the data revealed a relatively high susceptability to environmental enhancement. Further comparisons were made of the fracture surfaces of statically loaded and cyclically loaded specimens. Preparations are being made to study the effects of the rate of water flow over specimens by the use of an electrochemical potential system.

HEAVY-SECTION STEEL TECHNOLOGY PROGRAM QUARTERLY PROGRESS REPORT FOR JANUARY–MARCH 1983*

C. E. Pugh

ABSTRACT

The Heavy-Section Steel Technology (HSST) Program is an engineering research activity conducted by the Oak Ridge National Laboratory for the Nuclear Regulatory Commission. The program comprises studies related to all areas of the technology of materials fabricated into thick-section primary-coolant containment systems of light-water-cooled nuclear power reactors. The investigation focuses on the behavior and structural integrity of steel pressure vessels containing cracklike flaws. Current work is organized into seven tasks: (1) program administration and procurement, (2) fracture-mechanics analyses and investigations, (3) investigations of irradiated materials, (4) thermal-shock investigations, (5) pressure vessel investigations, (6) stainless steel cladding investigations, and (7) environmentally assisted crack-growth studies.

A thermal-strain modification was made to the deformation-plasticity model in the ADINA-ORVIRT fracture-mechanics analysis system in order to be more applicable to combined pressure and thermal loadings. Subcontractors continued studies on crack arrest, cleavage fracture transition, and environmentally assisted crack growth. Charpy testing of state-of-the-art weld specimens in the Fourth HSST Irradiation Series was performed on unirradiated specimens and on a few irradiated specimens for scoping purposes. A contract was placed for the irradiation of one-wire cladding specimens. Finite-flaw capabilities were incorporated into the OCA-II computer code, and parametric studies were carried out to compare fracture predictions with two-dimensional and specific finite flaws. Preparations continued for thermal-shock experiment TSE-7 to be conducted in May. Preparations for the first pressurized-thermal-shock experiment continued: the contractor is nearing completion of facility construction; analyses that explicitly consider upper-shelf behavior have been performed; and developmental tests on seals, thermocouples, and other facility apparatus have been carried out.

---

*Conversions from SI to English units for all SI quantities are listed on a foldout page at the end of this report.

1. PROGRAM ADMINISTRATION AND PROCUREMENT

C. E. Pugh

The Heavy-Section Steel Technology (HSST) Program, a major safety program sponsored by the Nuclear Regulatory Commission (NRC) at the Oak Ridge National Laboratory, is concerned with the structural integrity of the primary systems [particularly the reactor pressure vessels (RPVs)] of light-water-cooled nuclear power reactors. The structural integrity of these vessels is ensured by (1) designing and fabricating RPVs according to standards set by the code for nuclear pressure vessels, (2) detecting flaws of significant size that occur during fabrication and in service, and (3) developing methods of producing quantitative estimates of conditions under which fracture could occur. The program is concerned mainly with developing pertinent fracture technology, including knowledge of (1) the material used in these thick-walled vessels, (2) the flaw-growth rate, and (3) the combination of flaw size and load that would cause fracture and thus limit the life and/or the operating conditions of this type of reactor plant.

The program is coordinated with other government agencies and with the manufacturing and utility sectors of the nuclear power industry in the United States and abroad. The overall objective is a quantification of safety assessments for regulatory agencies, for professional code-writing bodies, and for the nuclear power industry. Several activities are conducted under subcontract by research facilities in the United States and through informal cooperative effort on an international basis. Three research and development subcontracts are currently in force.

Administratively, the program is organized into seven tasks, as reflected in this report: (1) program administration and procurement, (2) fracture-mechanics analyses and investigations, (3) investigations of irradiated material, (4) thermal-shock investigations, (5) pressure vessel investigations, (6) stainless steel cladding investigations, and (7) environmentally assisted crack-growth studies.

During this quarter, eight program briefings, reviews, or presentations were made by the HSST staff at technical meetings and at program reviews for the NRC staff or visitors. Two technical reports were published.[1,2]

References

1. R. D. Cheverton, S. K. Iskander, and D. G. Ball, *PWR Pressure Vessel Integrity During Overcooling Accidents: A Parametric Analysis*, NUREG/CR-2895 (ORNL/TM-7931), Union Carbide Corp. Nuclear Div., Oak Ridge Natl. Lab., February 1983.

2. B. R. Bass and J. W. Bryson, *Applications of Energy Release Rate Techniques to Part-Through Cracks in Plates and Cylinders, Volume 2. ORVIRT: A Finite Element Program for Energy Release Rate Calculations for 2-Dimensional and 3-Dimensional Crack Models*, NUREG/CR-2997, Vol. 2 (ORNL/TM-8527/V2), Union Carbide Corp. Nuclear Div., Oak Ridge Natl. Lab., February 1983.

2. FRACTURE-MECHANICS ANALYSIS AND INVESTIGATIONS

2.1 Deformation Theory of Plasticity with Initial Thermal Strains

B. R. Bass* R. H. Bryan
J. W. Bryson J. G. Merkle

2.1.1 Introduction

A previous report[1] described implementation of a deformation-plasticity material model in the ADINA-ORVIRT fracture-mechanics (FM) analysis system.[2,3] The two- (2-D) and three-dimensional (3-D) finite-element formulations of this model are essentially those of deLorenzi and Shih[4] but are modified to incorporate a multilinear stress-strain curve. The deformation-plasticity approach has distinct advantages over the more common incremental flow theory, namely computational economy and numerical stability.

Certain studies of fracture phenomena, such as those associated with pressurized-thermal shock (PTS) (see Sect. 5 of this report), require that cracked structures be analyzed for combined thermal and mechanical loads. A method is proposed here that modifies the isothermal deformation-plasticity formulation of Ref. 4 to account for the presence of thermal strains. The modification is strictly valid for hyperelastic materials, but an approximation to incremental thermo-elastic-plastic theory can be achieved if there is no unloading and the departure from a radial stress path is not severe.

The following section presents a summary of the deformation-plasticity formulation that incorporates the proposed thermal-strain modifications. For brevity, only the essential alterations to the development of Ref. 4 are presented here. This is followed by an application of the modified technique to a center-cracked panel previously analyzed by Ainsworth et al.[5] A second application to a thermally shocked intermediate test vessel (ITV) is presented in Sect. 5 of this report.

2.1.2 Thermal-strain modifications

In the general 3-D formulation, the components of the total strain tensor are expressed as the sum of the elastic strains, the plastic strains, and the free thermal expansion strains:

$$\varepsilon_{ij} = \varepsilon^{e}_{ij} + \varepsilon^{p}_{ij} + \varepsilon^{T}_{ij} \ . \qquad (2.1)$$

---

*Computer Sciences Division, Union Carbide Corporation-Nuclear Division (UCC-ND).

When substitution is made for the conventional relations between strains, stresses, and temperature, Eq. (2.1) becomes

$$\varepsilon_{ij} = \frac{1 + \nu}{E} S_{ij} + \frac{1 - 2\nu}{3E} \sigma_{kk}\delta_{ij} + \frac{3}{2} \frac{S_{ij}}{\sigma_e} \varepsilon_p + \alpha T \delta_{ij} \ . \tag{2.2}$$

Here, σ_{ij} are the components of the stress tensor, $S_{ij} = \sigma_{ij} - 1/3\ \sigma_{kk}\delta_{ij}$ are the deviatoric stress components, $\sigma_e = (3/2\ S_{ij} S_{ij})^{1/2}$ is the effective stress, ε_p is the effective plastic strain, T is the temperature, α is the coefficient of thermal expansion, E is Young's modulus, and ν is Poisson's ratio. Setting i = j in Eq. (2.2) and using $S_{jj} = 0$, it follows that

$$\sigma_{kk} = \frac{E}{1 - 2\nu} (\varepsilon_{kk} - 3\alpha T) \ . \tag{2.3}$$

Equation (2.2) can be inverted to yield an expression for the components of the stress tensor,

$$\sigma_{ij} = \frac{E}{1 + \nu} (\varepsilon_{ij} - \alpha T \delta_{ij}) + \frac{\nu E}{(1 + \nu)(1 - 2\nu)} (\varepsilon_{kk} - 3\alpha T)\delta_{ij}$$

$$- \frac{3}{2} \frac{E}{1 + \nu} \frac{\varepsilon_p}{\sigma_e} S_{ij} \ . \tag{2.4}$$

By substituting Eq. (2.2) into the definition of the deviatoric strain

$$e_{ij} = \varepsilon_{ij} - \frac{1}{3} \varepsilon_{kk}\delta_{ij} \ , \tag{2.5}$$

it can be shown that

$$e_{ij} = \frac{1 + \nu}{E} S_{ij} + \frac{3}{2} \frac{\varepsilon_p}{\sigma_e} S_{ij} \ . \tag{2.6}$$

When Eq. (2.6) is used in the definition of the effective strain,

$$e_e = \left(\frac{2}{3} e_{ij} e_{ij} \right)^{1/2} \ , \tag{2.7}$$

it follows that

$$e_e = \frac{2}{3}\frac{(1+\nu)}{E}\sigma_e + \varepsilon_p \ . \tag{2.8}$$

From Eqs. (2.6) and (2.8),

$$\frac{2}{3}\frac{e_{ij}}{e_e} = \frac{S_{ij}}{\sigma_e} \ . \tag{2.9}$$

Equation (2.8) and the equation resulting from substitution of Eq. (2.5) into Eq. (2.9) can be used to eliminate S_{ij} and ε_p from Eq. (2.4),

$$\sigma_{ij} = \frac{E}{3(1-2\nu)}(\varepsilon_{kk} - 3\alpha T)\delta_{ij} + \frac{2}{3}\frac{\sigma_e}{e_e}\left(\varepsilon_{ij} - \frac{1}{3}\varepsilon_{kk}\delta_{ij}\right) \ . \tag{2.10}$$

Introducing the relation

$$\varepsilon'_{ij} = \varepsilon_{ij} - \alpha T\delta_{ij} \tag{2.11}$$

into Eq. (2.10) gives

$$\sigma_{ij} = \frac{E}{3(1-2\nu)}\varepsilon'_{kk}\delta_{ij} + \frac{2}{3}\frac{\sigma_e}{e_e}\left(\varepsilon'_{ij} - \frac{1}{3}\varepsilon'_{kk}\delta_{ij}\right) \ . \tag{2.12}$$

For finite-element applications, a convenient matrix relation for evaluating the stress tensor is given by

$$\begin{Bmatrix} \sigma_{11} \\ \sigma_{22} \\ \sigma_{33} \\ \sigma_{12} \\ \sigma_{23} \\ \sigma_{31} \end{Bmatrix} = [D] \begin{Bmatrix} \varepsilon'_{11} \\ \varepsilon'_{22} \\ \varepsilon'_{33} \\ 2\varepsilon'_{12} \\ 2\varepsilon'_{23} \\ 2\varepsilon'_{31} \end{Bmatrix} , \tag{2.13}$$

where

$$\left[D\right] = C_1 \begin{bmatrix} 1 & 1 & 1 & 0 & 0 & 0 \\ & 1 & 1 & 0 & 0 & 0 \\ & & 1 & 0 & 0 & 0 \\ & & & 0 & 0 & 0 \\ & & & & 0 & 0 \\ \text{symmetric} & & & & & 0 \end{bmatrix} + C_2 \begin{bmatrix} 2 & -1 & -1 & 0 & 0 & 0 \\ & 2 & -1 & 0 & 0 & 0 \\ & & 2 & 0 & 0 & 0 \\ & & & 1.5 & 0 & 0 \\ & & & & 1.5 & 0 \\ \text{symmetric} & & & & & 1.5 \end{bmatrix}$$

and

$$C_1 = \frac{E}{3(1 \quad 2\nu)} , \qquad C_2 = \frac{2}{9} \frac{\sigma_e}{\dot{e}_e} .$$

In the absence of thermal strains, Eq. (2.13) for the stress tensor reduces to Eq. (2.12) of Ref. 4. The effective stress σ_e in Eq. (2.13) is evaluated from Eq. (2.8), and an appropriate effective stress-effective plastic strain curve is usually taken from a uniaxial tensile test.

Formulations for 2-D plane stress, plane strain, and axisymmetry cases can be obtained from Eq. (2.13) by introducing the necessary modifications previously outlined in Ref. 4 for the isothermal case. For plane stress conditions, $\sigma_{33} = \sigma_{13} = \sigma_{23} = 0$.

From Eq. (2.13),

$$\sigma_{33} = \frac{E}{3(1 - 2\nu)} (\varepsilon'_{11} + \varepsilon'_{22} + \varepsilon'_{33}) + \frac{2}{9} \frac{\sigma_e}{e_e} (-\varepsilon'_{11} - \varepsilon'_{22} + 2\varepsilon'_{33}) . \qquad (2.14)$$

Thus, $\sigma_{33} = 0$ implies

$$\varepsilon'_{33} = - \frac{1 - \beta}{1 + 2\beta} (\varepsilon'_{11} + \varepsilon'_{22}) , \qquad (2.15)$$

where

$$\beta = \frac{2}{3} \frac{(1 - 2\nu)}{E} \frac{\sigma_e}{e_e} . \qquad (2.16)$$

When Eq. (2.15) is substituted into Eq. (2.13), the plane-stress constitutive relation has the matrix form given by

$$\begin{Bmatrix} \sigma_{11} \\ \sigma_{22} \\ \sigma_{12} \end{Bmatrix} = \frac{\beta E}{(1 - 2\nu)(1 + 2\beta)} \begin{bmatrix} 2 + \beta & 1 - \beta & 0 \\ & 2 + \beta & 0 \\ \text{symmetric} & & 0.5 + \beta \end{bmatrix} \begin{Bmatrix} \varepsilon'_{11} \\ \varepsilon'_{22} \\ 2\varepsilon'_{12} \end{Bmatrix} . \tag{2.17}$$

In the plane-stress case, the effective strain e_e is obtained from Eq. (2.5) (written in the form $\varepsilon_{ij} = \varepsilon'_{ij} - 1/3\, \varepsilon'_{kk}\delta_{ij}$) and from Eqs. (2.7) and (2.15) as

$$e_o^2 = \frac{4}{3} \frac{1 + \beta + \beta^2}{(1 + 2\beta)^2} (\varepsilon'_{11} + \varepsilon'_{22})^2 - \frac{4}{3} \varepsilon'_{11}\varepsilon'_{22} + \frac{1}{3} (2\varepsilon'_{12})^2 . \tag{2.18}$$

The effective stress σ_e is again found from Eq. (2.8).

For plane-strain conditions given by $\varepsilon_{33} = \varepsilon_{13} = \varepsilon_{23} = 0$, Eq. (2.13) reduces to

$$\begin{Bmatrix} \sigma_{11} \\ \sigma_{22} \\ \sigma_{33} \\ \sigma_{12} \end{Bmatrix} = \left[C_1 \begin{bmatrix} 1 & 1 & 1 & 0 \\ & 1 & 1 & 0 \\ & & 1 & 0 \\ \text{symmetric} & & & 0 \end{bmatrix} + C_2 \begin{bmatrix} 2 & -1 & -1 & 0 \\ & 2 & -1 & 0 \\ & & 2 & 0 \\ \text{symmetric} & & & 1.5 \end{bmatrix} \right] \begin{Bmatrix} \varepsilon_{11} - \alpha T \\ \varepsilon_{22} - \alpha T \\ -\alpha T \\ 2\varepsilon_{12} \end{Bmatrix} . \tag{2.19}$$

Thus, the σ_{33} stress component is given by the relation

$$\sigma_{33} = (C_1 - C_2)(\varepsilon_{11} + \varepsilon_{22}) - C_1\, 3\alpha T . \tag{2.20}$$

The remaining stress components are conveniently determined from the expression

$$\begin{Bmatrix} \sigma_{11} \\ \sigma_{22} \\ \sigma_{12} \end{Bmatrix} = \left[C_1 \begin{bmatrix} 1 & 1 & 0 \\ & 1 & 0 \\ \text{symmetric} & & 0 \end{bmatrix} + C_2 \begin{bmatrix} 2 & -1 & 0 \\ & 2 & 0 \\ \text{symmetric} & & 1.5 \end{bmatrix} \right] \begin{Bmatrix} \varepsilon_{11} - k\alpha T \\ \varepsilon_{22} - k\alpha T \\ 2\varepsilon_{12} \end{Bmatrix} , \tag{2.21}$$

where

$$k = \frac{3C_1}{2C_1 + C_2} . \tag{2.22}$$

For the linearly elastic case, it can be shown that

$$C_2 = \frac{E}{3(1 + \nu)} ,$$

and

$$k = (1 + \nu) .$$

Finally, for the axisymmetric case, the constitutive relation becomes

$$\begin{Bmatrix} \sigma_{11} \\ \sigma_{22} \\ \sigma_{12} \\ \sigma_{33} \end{Bmatrix} = \left[C_1 \begin{bmatrix} 1 & 1 & 0 & 1 \\ & 1 & 0 & 1 \\ & & 0 & 0 \\ \text{symmetric} & & & 1 \end{bmatrix} + C_2 \begin{bmatrix} 2 & -1 & 0 & -1 \\ & 2 & 0 & -1 \\ & & 1.5 & 0 \\ \text{symmetric} & & & 2 \end{bmatrix} \right] \begin{Bmatrix} \varepsilon'_{11} \\ \varepsilon'_{22} \\ 2\varepsilon'_{12} \\ \varepsilon'_{33} \end{Bmatrix} . \quad (2.23)$$

2.1.3 Numerical applications

The modified deformation-plasticity formulation of the previous section has been implemented in the ADINA-ORVIRT system[2,3] and is applied here to a center-cracked plate previously analyzed in Ref. 5. The plate configuration shown in Fig. 2.1 is subjected to a uniform tensile stress σ and a parabolic temperature distribution given by

$$T(y) = \Delta T \left(\frac{y}{w}\right)^2 , \quad (2.24)$$

and

$$\Delta T = \frac{1.8\ \sigma_y}{E\alpha} . \quad (2.25)$$

Here, σ_y is the yield stress in uniaxial tension, and y is measured from the center of the crack. An elastic-perfectly-plastic material model is assumed.

Figure 2.2 shows the finite-element discretization used to model one-quarter of the plate for the 2-D plane-stress analysis. The model consists of 713 nodes and 216 isoparametric elements. The details of the model near the crack tip (Fig. 2.2) illustrate the collapsed wedge elements with midside nodes that allow for a 1/r singularity at the crack tip.[6] In the collapsed elements, the nodes that initially share the same locations at the tip will separate with increasing load to allow for blunting of the crack.

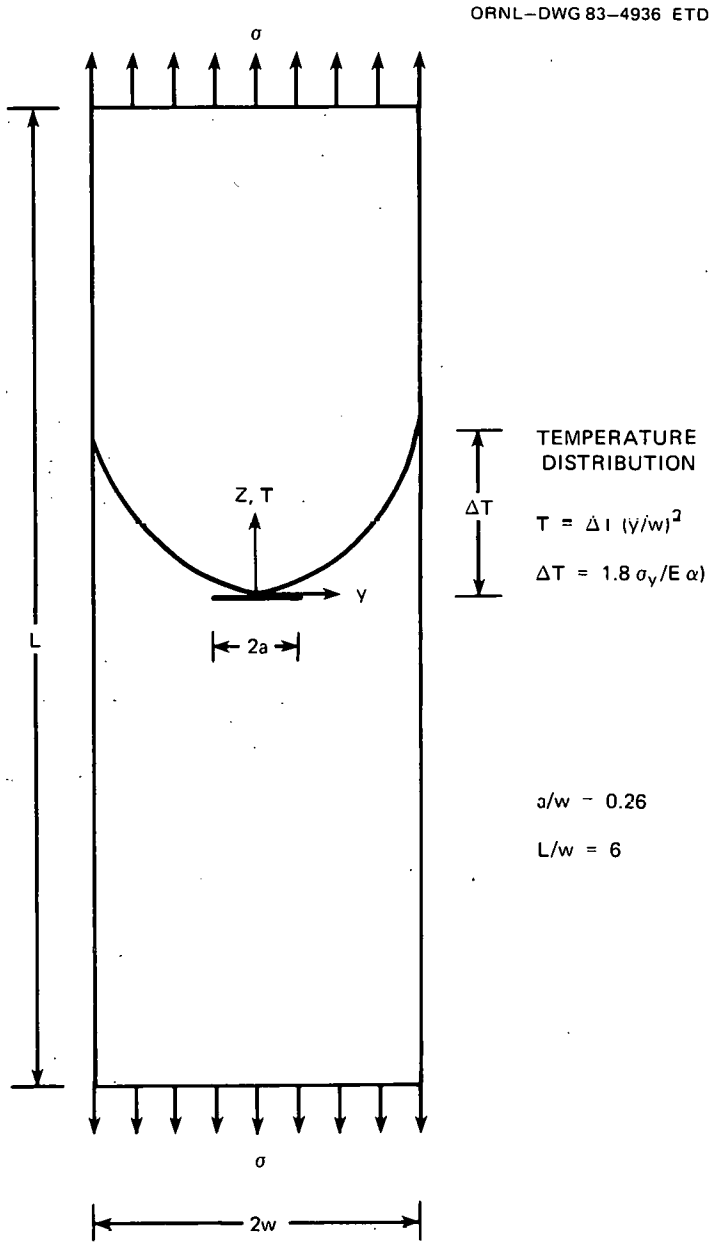

Fig. 2.1. Center-cracked plate subjected to a parabolic temperature distribution and uniform tensile loading.

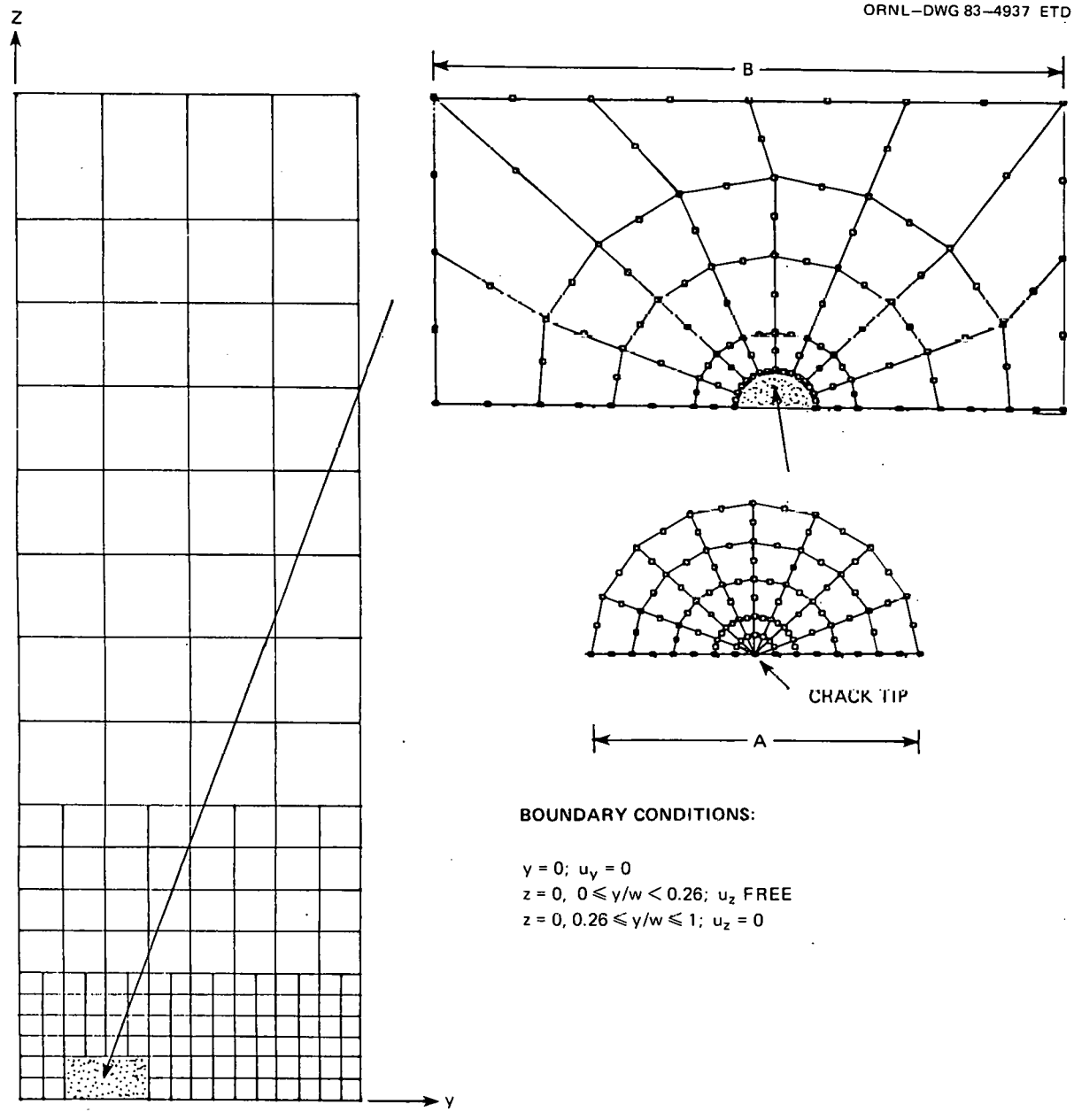

Fig. 2.2. Finite-element discretization of center-cracked plate.

The thermal load represented by Eqs. (2.24) and (2.25) was applied to the model first, followed by application of the uniform mechanical load σ. The extent of the plastic zone around the crack tip at selected values of the applied load is shown in Fig. 2.3. Energy release rate values G_θ, normalized by the thermoelastic value G_e, are depicted in Fig. 2.4 as a function of applied load. For comparison, results obtained for the G_θ parameter in the analysis of Ref. 5 are also included in this figure.

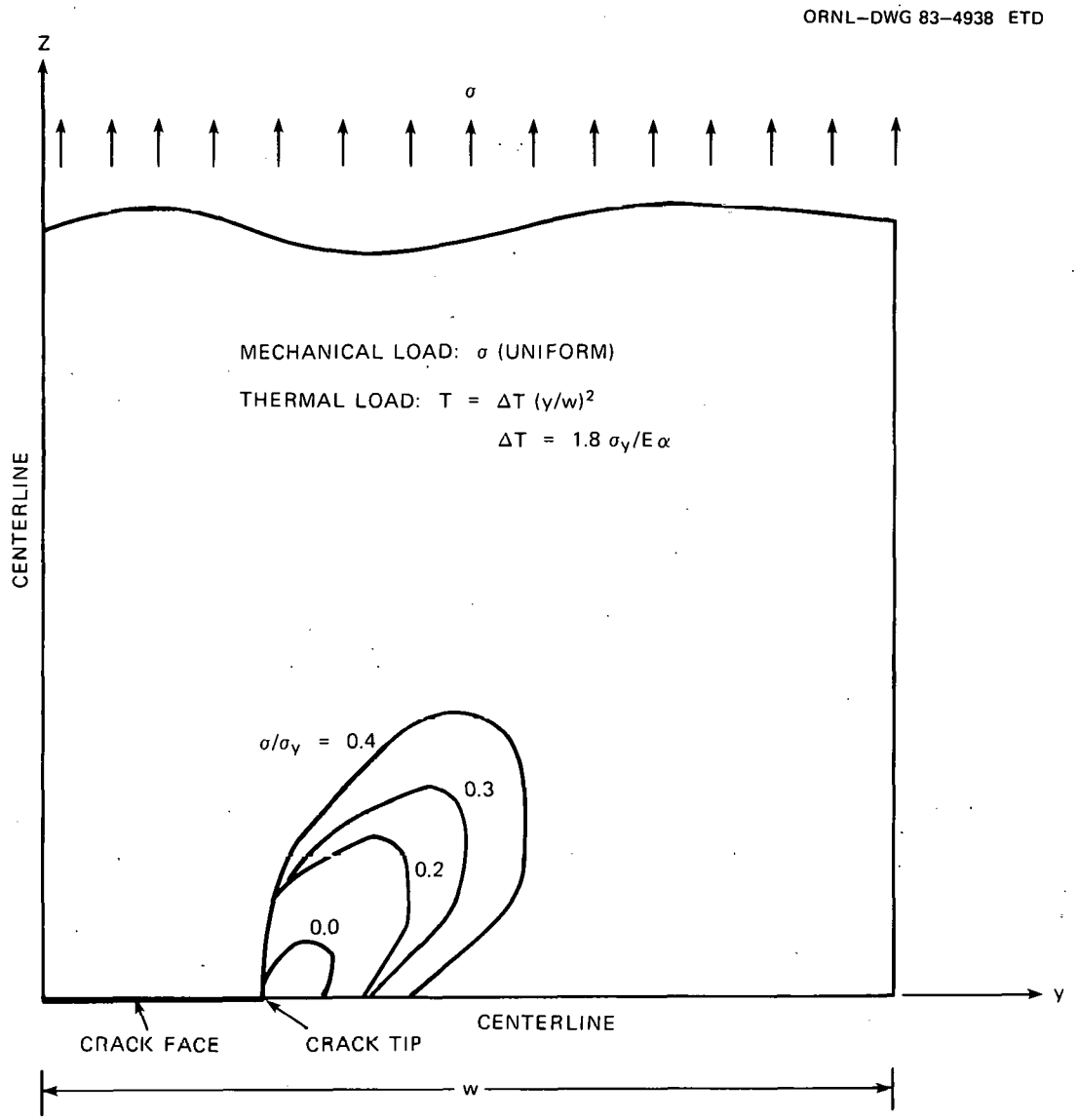

Fig. 2.3. Extent of plastic zones around crack tip at selected values of applied stress.

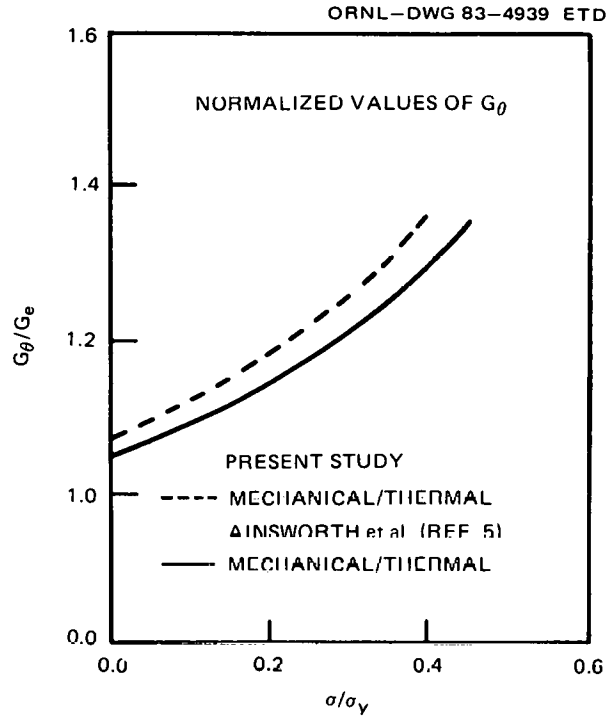

Fig. 2.4. Normalized energy release rate values as functions of applied stress σ (normalized by room temperature yield stress σ_y) for center-cracked plate.

2.2 BCL HSST Support Program*

A. R. Rosenfield† C. W. Marschall†
T. A. Bishop† J. K. McCoy†
A. J. Markworth† P. N. Mincer†
D. K. Shetty†

2.2.1 Task 1: Administration — Introduction and summary

The objective of the Battelle-Columbus Laboratory (BCL) Heavy-Section Steel Technology (HSST) Support Program is to provide research on material properties associated with thermal-stress fracture of reactor-pressure-vessel (RPV) steels. Its emphasis is on the toughness associated with crack arrest. The program consists of four research tasks.

Task 2 research during the report period has been confined to planning future BCL crack-arrest experiments. The next series of tests will be on low-upper-shelf weld metal from ITV V-8A.

---

*Work sponsored by HSST Program under UCC-ND Subcontract 85X-17624C between UCC-ND and BCL.

†Battelle-Columbus Laboratories, Columbus, Ohio.

In Task 3 (crack initiation), a new series of experiments using TSE-5A steel confirmed that the reinitiation toughness measured with compact specimens provides values representative of full-scale results. More importantly, the toughness associated with reinitiation of an arrested cleavage crack is lower than that associated with reinitiation after crack blunting or ductile tearing. On the other hand, the scatter in reinitiation toughness is on the order of that associated with fatigue precracks, even when only reinitiation after cleavage is considered. To illustrate the extent of the scatter, the compact-specimen reinitiation data shown at 0 and 16°C bracket those of the four jumps in TSE-5A (temperature range from −11 to +21°C). Additional fractographic data on rapidly loaded fatigue-precracked specimens of TSE-6 material are reported. The micromechanism of cleavage triggering was found to be complex, with both sulfide and carbide cleavage origins identified. In some cases, apparent multiple origins were found.

The Task 4 research emphasized experiments carried out on TSE steel with three different heat treatments with the goal of obtaining crack-arrest (K_a) data on the upper shelf. For all three heat treatments, K_a values were obtained at temperatures associated with the upper shelf of Charpy V-notch impact tests. Even so, no evidence of upper-shelf behavior was obtained for the crack-arrest specimens. Two data points were obtained at RT_{NDT} + 100°C, matching the highest test temperature previously obtained at BCL and exceeding the literature maximum by about 15°C. The data obtained at the highest temperature corresponded to the upper shelf of the K_{IR} curve and exceeded the plateau value of 220 MPa·$\sqrt{m}$. (However, the K_a value obtained for a BCL specimen tested previously at that temperature was slightly below the K_{IR} shelf.) The high-temperature data were obtained using a combination of procedure changes: use of duplex specimens, reduction of friction during crack propagation, and modification of the side-groove geometry.

In Task 5 (data base), computer programs for analyzing raw crack-arrest data, storing literature data, and performing statistical analysis have been completed. The statistical program provides percentiles of the K_a and temperature curves and their associated confidence intervals. It has the virtue of allowing the scatter around the mean to depend on temperature, which provides a more realistic description of the distribution than does the temperature-independent variance usually assumed. Plans to link this program with the data-generation and storage programs are discussed, and examples of the statistical analysis are given.

2.2.2 Task 3: Crack initiation

The principal objective of Task 3 is to refine and validate the single-specimen K_{Ic}/K_{Ia} test procedure. During the current quarter, the effect of precrack temperature on K_{Ic} at reinitiation was investigated. In addition, the fractographic studies of TSE-6 were completed.

2.2.2.1 Reinitiation tests. There is a two-step procedure for reinitiation of an arrested cleavage crack.[7] A compact-crack-arrest specimen is used to provide the cleavage precrack by transverse-wedge loading as in a regular K_a experiment.[8] The crack then is reinitiated using the

same wedge. A second clip gage is placed ahead of the load line, and the K_Q value associated with reinitiation is calculated using the procedure of ASTM E561 (R-curve determination). In previous reports,[8,9] it was shown that this procedure can provide data comparable to large-cylinder K_{Ic} and K_{Ia} data for TSE-5A and -6.

The new results were obtained with 101.6 x 98.8 x 25.4 mm weld-embrittled specimens from TSE-5A. Face dimensions on the earlier specimens were both 150 mm. Inverted split pins were used successfully to produce unstable cleavage cracks at higher temperatures than before in six out of ten specimens. Those data are described in the crack-arrest section (Sect. 2.2.3.2) of this report. Reinitiation also was carried out using the inverted-split-pin arrangement.

Both earlier and new reinitiation results are given in Table 2.1. Some of the tendencies that were suggested by the limited earlier data[7] were not confirmed. Specifically, the added data do not result in either a consistent trend of decreasing ratio of effective-to-physical crack length with increasing K_a (precrack) or with a greater probability of cleavage reinitiation with increasing K_a (precrack). All but one of the new samples resulted in unstable cleavage reinitiation. It is not clear whether this improved success is due to the higher precrack temperature or the use of inverted split pins.

Because of the mixed success in initiating unstable fracture during the precrack operation, some of the reinitiation experiments involved precracks that resulted in blunting or small amounts of stable crack growth. All of these points resulted in high values of cleavage-reinitiation K_Q and may be a manifestation of the warm-prestress effect.[10]

Figure 2.5 illustrates all of the results. The data for both reinitiation temperatures are plotted on the same graph. The new K_Q values (precrack temperatures >60°C) tend to be lower than the earlier, low-temperature, precrack data. Thus, a general trend towards higher K_Q values with decreasing precrack temperature is indicated on the graph. The reason for this behavior is not clear.

TSE-5A reinitiation data are compared with the ORNL cylindor results in Fig. 2.6. Only those data are included for which reinitiation from an arrested cleavage crack was obtained. The compact-specimen values bracket the cylinder values, suggesting that the compact specimen can be used to obtain reliable estimates of large-specimen data. The 16°C data appear to be lower than the 0°C data, but this is due to one very low point at 16°C and one very high point at 0°C. It is believed that these points are manifestations of the data scatter. To examine this suggestion, the data at both temperatures were combined and plotted as a Weibull distribution in Fig. 2.7. The data fit the distribution well, thus indicating that the temperature variation of K_{Ic} between 0 and 16°C is much less important than the specimen-to-specimen variation at a given temperature. The Weibull modulus for these data is 4, a value characteristic of large scatter. The K_{Ic} values for the cylinder are shown for reference and to indicate that the compact-specimen reinitiation data do indeed bracket the TSE data.

2.2.2.2 Fractographic examination. The results of the fractographic examination of fatigue-precracked 1TCT TSE-6 samples tested at high rate

Table 2.1. Reinitiation of arrested cleavage cracks: TSE-5A prolong, second piece

Specimen No.	Pretest		Reinitiation					
	Temperature (°C)	K_a (MPa·$\sqrt{m}$)	Temperature (°C)	Displacement (mm)		Crack length (mm)		K_Q[a] (MPa·$\sqrt{m}$)
				−0.25w location	0.303w location	a_p/w	a_{eff}/w	
150-mm face dimension								
5A-107	27	65	0	[b]	[b]	[b]	[b]	[b]
-108	42	81	0	2.24	1.02	0.765	0.744	212
-109	51	88	0	0.86	0.37	0.733	0.693	92
-110	53	87	0	1.12	0.40	0.766	0.570	156
-111	53	94	16	1.85	0.88	0.723	0.788	154
-112	54	95	16	1.56	0.81	0.697	0.895	86
-113	22	63	0	1.80	0.86	0.738	0.795	146
-114	40	81	0	0.82	0.38	0.804	0.760	74
-115	42	70	16	[b]	[b]	[b]	[b]	[b]
-116	53	95	16	[b]	[b]	[b]	[b]	[b]
101.6-mm face dimension								
5A-120	66	100	0	[b]	[b]	[b]	[b]	[b]
-121	66	94	0	0.76	0.37	0.795	0.813	59
-122	70	[b]	16	1.36	0.34	0.435	0.433	244
-123	66	[b]	16	2.11	0.83	0.871	0.741	203
-124	66	87	16	0.89	0.48	0.913	0.951	33
-125	66	87	0	0.79	0.36	0.932	0.744	75
-126	66	101	16	0.83	0.38	0.835	0.748	78
-127	79	[b]	16	1.60	0.47	0.433	0.484	263
-128	79	[b]	0	1.12	0.36	0.421	0.519	173
-129	70	152	0	1.09	0.46	0.571	0.677	122

[a] Calculated from $a_{eff/w}$.

[b] Stable tearing.

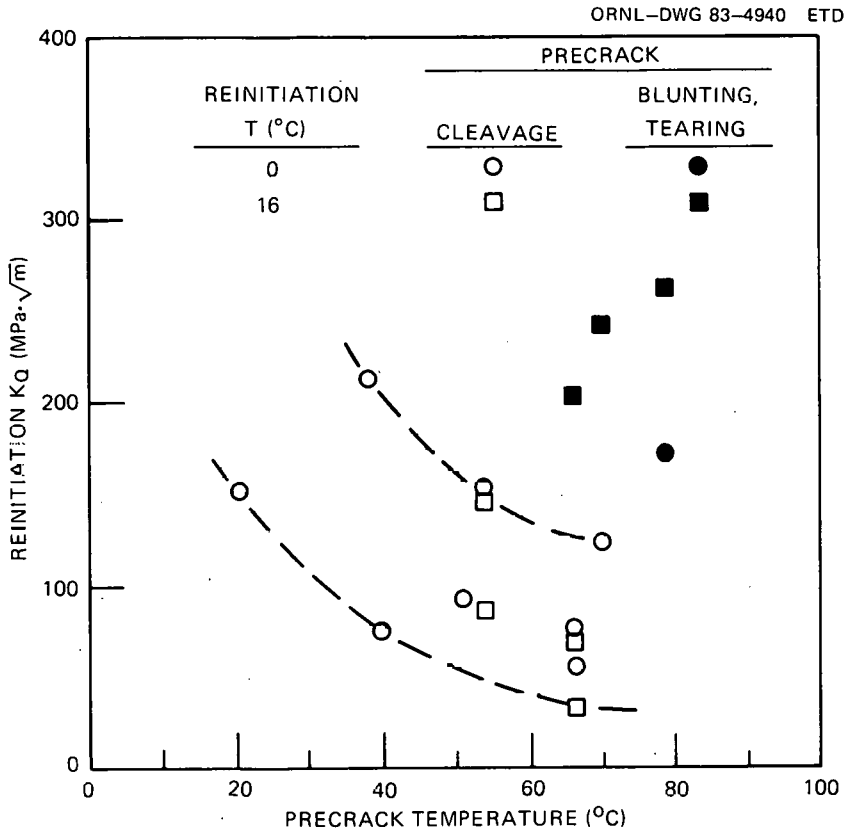

Fig. 2.5. Effect of precracking temperature on reinitiation toughness of TSE-5A steel.

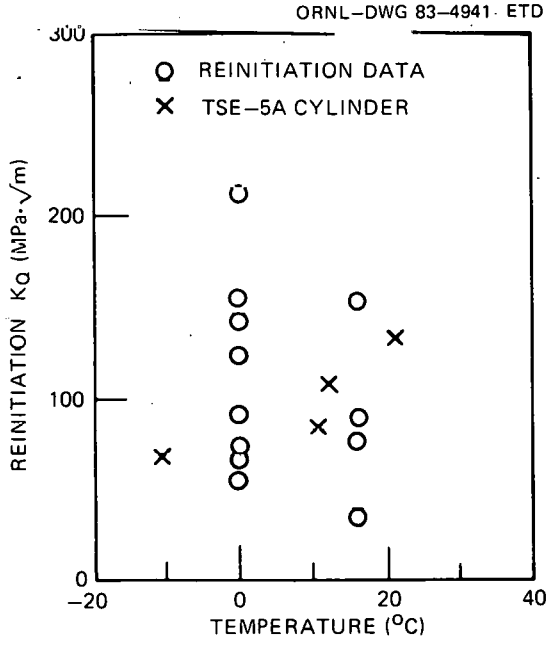

Fig. 2.6. Comparison of reinitiation-toughness and full-scale data.

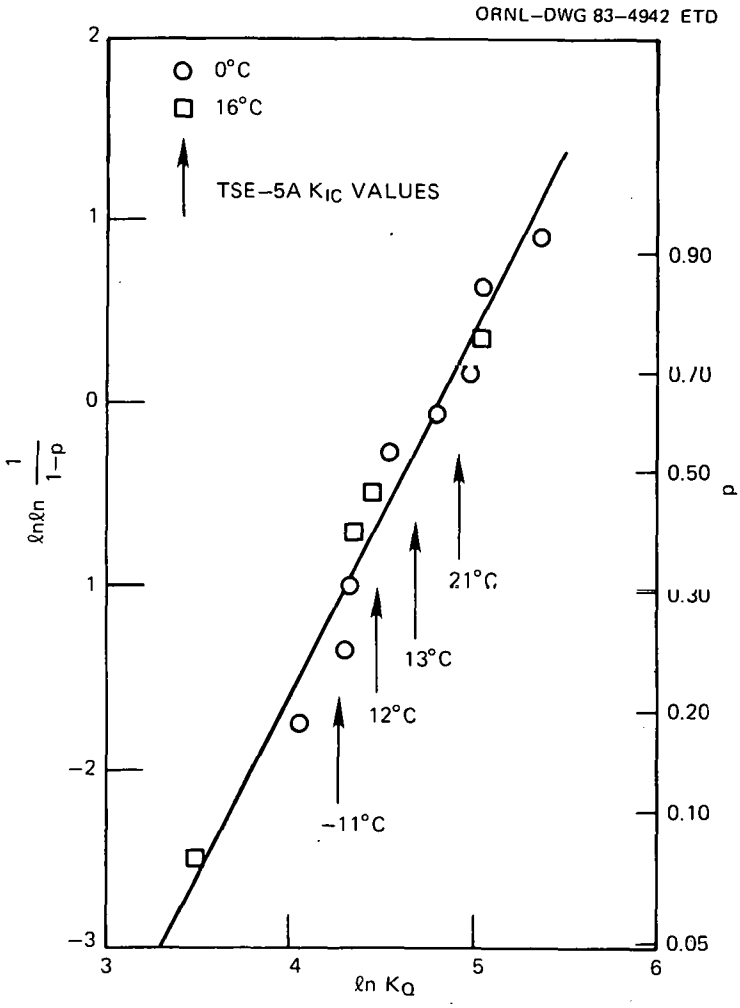

Fig. 2.7. Reinitiation-toughness values plotted according to Weibull distribution.

and at a temperature of 22°C were included in the previous report. Data obtained for samples tested at 82°C have now been examined, and the combined results are given in Table 2.2. Included in the table are fracture toughness K_{QJ} (calculated from the total area under the load-displacement curve), stable crack growth by dimple rupture (Δa, measured in the vicinity of the cleavage origins), the number of cleavage origins in each specimen, the location of the cleavage origin ahead of the stable crack front (x), and the cleavage-triggering inclusion whenever it was identified. The majority of the specimens exhibited single, well-defined cleavage origins; three specimens contained multiple origins. There was no apparent correlation between fracture toughness and the number of cleavage origins. As might be expected, fracture toughness did increase with increasing amounts of stable crack growth. A more interesting observation was that in specimens with no stable crack growth (Δa = 0),

Table 2.2. Summary of fractographic measurements on rapidly loaded precracked 1T compact specimens of TSE-6 steel (A503 steel)

Specimen No.	Test temperature (°C)	K_{QJ} (MPa·√m)	Stable crack growth (Δa) (mm)	Number of cleavage origins	Cleavage-origin location (x) (mm)	Cleavage-triggering inclusion
90-2	22	180	0.05	1	1.74	g.b.c.[a]
86-1	22	86	0	1	0	u[b]
101	22	133	0	3	0.1, 0.1, 0.15	u, u, g.b.c.
102	22	103	0	1	0	u
103	22	116	0	3	0.07, 0.08, 0	u, u, MnS
104	22	84	0	*c*	*c*	*c*
90-1	83	276	0.6-0.7	2	2.0, 0.7	MnS, MnS
105	82	293	0.7	1	1.1	MnS
106	82	293	0.8	1	1.25	u
107	82	235	0.3	1	0.3	MnS
108	82	131	0	1	~0	u
109	82	217	0.08	1	0.175	MnS

[a] g.b.c. = grain-boundary carbide.

[b] u = cleavage-triggering inclusion could not be identified, but most of these origins were located at grain boundaries.

[c] Cleavage origin could not be identified.

fracture toughness appeared to correlate with the location of the cleavage origin relative to the fatigue-crack; that is, K_{QJ} increased with increasing x. This observation is, of course, consistent with the concept of a critical value of tensile stress required to initiate cleavage in the stress field of a crack, as included in the Ritchie-Knott-Rice model.[11] But the location of the cleavage origin (x) did not lend itself to any simple microstructural interpretation. The characteristic distance x varied anywhere from 0 to 2 mm. For comparison, the largest microstructural features in this class of steel are local variations in hardness and grain size caused by carbon segregation. These variations reveal themselves as bands that are almost 1 mm wide.[12]

Two unexpected observations were made in this study. A significant fraction of the cleavage fractures initiated at MnS inclusions of small size (~1 μm) instead of at the carbides usually considered to be initiation sites. The authors are not aware of any similar observations in any steels. However, Melander and Steninger[13] found that sulfides crack at considerably lower strains than does pearlite. If sulfides also crack more readily than grain-boundary carbides in this A508 steel, they could serve as cleavage nuclei. However, this does not explain the observation that the microstructural features of the origins were not particularly unusual for the steel, even though some cleavage origins were located as far as 2 mm from the stable crack fronts, and in some cases cleavage occurred only after significant amounts of stable crack growth. It is now generally recognized, for example by Curry and Knott,[14] that the characteristic distance x must be viewed in statistical terms to account for the distribution of the critical microstructural dimensions, namely, the thickness of the grain-boundary carbides. The present observations suggest that, at least in this quenched-and-tempered steel, a secondary microstructural feature is more important in locating the cleavage origin, or the so-called "weak spot." One tentative suggestion based on the fractographic examinations is that the secondary feature might be a collection of ferrite grains, possibly within the same prior-austenite grain, all of which have the same favorably oriented cleavage planes. A similar observation has been made by Ogawa et al.[12] Alternatively, the weak spots may be associated with the segregation bands. A more positive identification of the nature of the weak spots would be required, however, to fully understand the cleavage-triggering phenomenon and the associated scatter of fracture toughness of RPV steels in the ductile-brittle transition region.

2.2.3 Task 4: Crack arrest

The objective of Task 4 is to develop techniques to measure the crack-arrest toughness on the upper shelf of the ductile-brittle transition curve. During the current quarter, crack-arrest data were obtained at temperatures that correspond with the upper shelf of the Charpy V-notch curve. Two successful experiments were carried out at temperatures above those for which ESSO test data are available from Japanese experiments.

2.2.3.1 Review of previous work. The last progress report[15] discussed the capacity of the current-design wedge-loaded compact

specimen to provide large K_a values. Several problems were noted:

1. the friction between the transverse-wedge-loaded specimen and the support plate may inhibit rapid crack propagation,
2. the maximum value of initiation toughness K_o is limited by notch-tip plasticity,
3. the static stress intensity at a given displacement decreases with crack length, and
4. current specimen sizes may be too small.

It was suggested that use of the duplex compact specimen[16] will provide for higher K_o values. In addition, use of an inverted split pin[17] eliminates the clamping action inherent in conventional transverse wedge loading. Finally, the negative stress-intensity gradient can be eliminated if the side grooves are contoured. These three modifications have been made during the present quarter. Size increases have not yet been investigated.

2.2.3.2 Inverted-split-pin loading results. The new series of reinitiation specimens (101.6 x 98.8 x 25.4 mm) made from TSE-5A steel provided an opportunity to assess the inverted-split-pin loading using weld-embrittled specimens. Existing BCL crack-arrest data obtained on weld-embrittled specimens are limited to temperatures up to RT_{NDT} + 45°C.[9] This limitation may be partly caused by the clamping action associated with the usual pin design. In some respects, this clamping action is beneficial because it allows the experiment to be run at conditions close to fixed-grip loading. In contrast, use of the inverted split pin at temperatures below RT_{NDT} resulted in large postinitiation arm displacement.[8] It was concluded that this extra specimen freedom might be harnessed to produce unstable cracks under conditions for which they normally are not obtained.

For this reason, the weld-embrittled reinitiation specimens were cleavage precracked using Irwin's inverted-split-pin arrangement.[17] The precracking temperatures were all higher than had been used previously at BCL on weld-embrittled specimens. As is shown in Table 2.3, five of six specimens tested at 66°C (RT_{NDT} + 56°C) produced unstable crack growth. Success was also achieved in one of two specimens tested at 70°C (RT_{NDT} + 60°C). However, both specimens tested at 79°C (RT_{NDT} + 69°C) displayed stable crack growth. This result is encouraging because use of the inverted split pin appears to have resulted in an ~15°C increase in the temperature capability of the weld-embrittled specimen. It should be noted, however, that Crosley and Ripling[18] have reported weld-embrittled-specimen data at a comparable temperature for one plate of A533B steel using the conventional loading arrangement.

Table 2.3 also shows that the arrest displacements exceeded the initiation displacements by no more than 7%. This result is in sharp contrast to those of the inverted-split-pin experiments at 0°C,[8] where the postinitiation displacements were so large that the clip gage flew out of its seating blocks. The difference is possibly caused by the higher crack-growth resistance (K_D) at the higher temperatures. The physical mechanism controlling the level of K_D is believed to be ligament formation and tearing.[16] At higher temperatures, the ligaments are more prevalent; acting as pinching forces, they serve to hold the crack faces

Table 2.3. Crack-arrest data for TSE-5A steel (inverted-split-pin loading)[a]

Specimen No.	Test temperature (°C)	Displacement (mm)		Crack length (mm)		Stress intensity (MPa·√m)	
		Initiation	Arrest	Initiation	Arrest	K_o	K_a
5A-120	66	1.14	1.22	32.8	67.2	219	100
-121	66	1.09	1.14	32.8	67.2	211	94
-122	70	*b*	*b*	*b*	*b*	*b*	*b*
-123	66	*b*	*b*	*b*	*b*	*b*	*b*
-124	66	0.93	0.99	33.5	65.5	177	87
-125	66	0.91	0.92	33.5	63.1	174	87
-126	66	0.98	1.01	33.5	61.3	187	101
-127	79	*b*	*b*	*b*	*b*	*b*	*b*
-128	79	*b*	*b*	*b*	*b*	*b*	*b*
-129	70	1.06	1.09	32.3	48.3	207	152[c]

[a] Specimen size = 101.6 x 98.8 x 25.4 mm.

[b] Stable crack growth.

[c] Irregular crack front.

together and limit postinitiation displacements. For this reason, the observed clip-gage response is consistent with current ideas of dynamic fracture toughness.

As is shown in Table 2.3 and Fig. 2.8, the values of K_a at 66°C are close to those obtained at 51–54°C using the conventional split-pin arrangement. While lowered friction has previously been shown[9] to lower K_a, those low K_a values were associated with larger ratios of arrest-to-initiation displacement than were observed in the present tests. The compact-specimen values at 66°C are also much lower than the K_{Ia} value for Jump 4 of TSE-5A; in fact, two points lie below the K_{IR} curve. In contrast, the one datum point at 70°C (RT_{NDT} + 60°C) lies above the TSE-5A result. However, there is considerable uncertainty in the absolute value of this point. The specimen was highly ligamented and displayed a very irregular crack front, making a precise determination of K_a difficult. Nevertheless, the surface appearance suggested a high value of K_a.

In summary, there is some question about the meaning of K_a values obtained with the inverted split pin. However, this loading arrangement appears to provide a useful tool for raising the temperature capability of the compact crack-arrest specimen.

2.2.3.3 Duplex specimens with contoured side grooves. A new shipment of steel from TSE-6 was used for the balance of the experiments. As a result of the heat treatment used, the as-received material had a very high value of RT_{NDT} (66°C), and the Charpy upper shelf was reached at about 100°C. This behavior necessitated the use of quite high test temperatures.

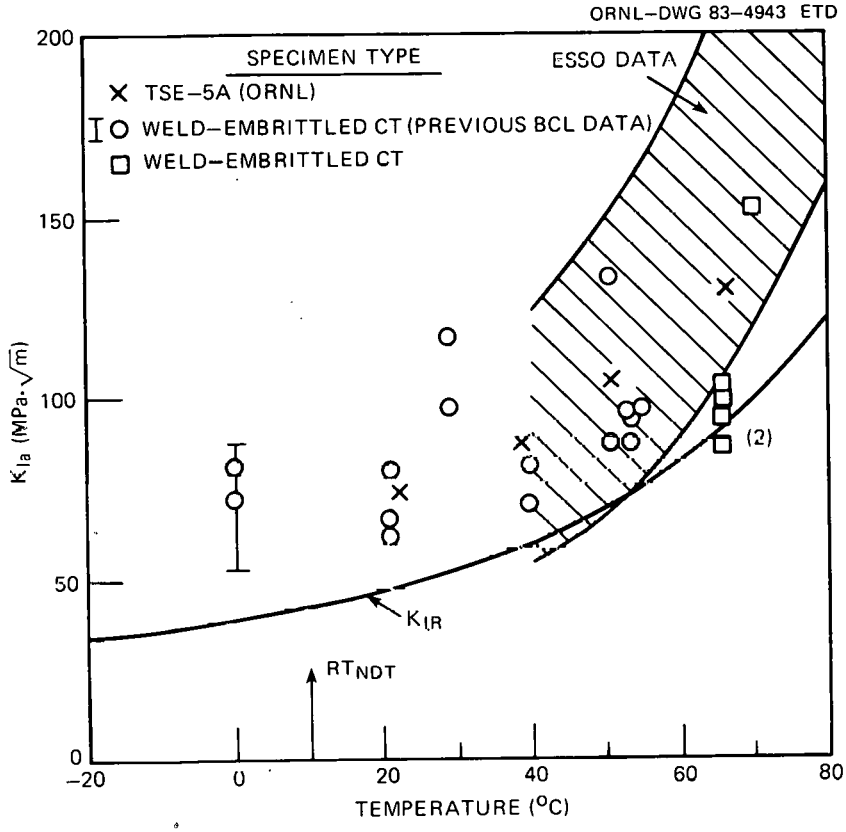

Fig. 2.8. Master plot of crack-arrest data for TSE-5A steel.

Duplex compact-crack-arrest specimens were fabricated from this steel. The specimens consisted of a block of SAE 4340 steel electron-beam (EB) welded to a block of the TSE-6 steel. These specimens also employed a modification of the side-groove design, as is illustrated in Fig. 2.9. Previous experience using duplex specimens resulted in data up to RT_{NDT} + 60°C and one point at RT_{NDT} + 100°C. Several other attempts to obtain data in this temperature range resulted in the crack arresting at the weld line or within the heat-affected zone (HAZ). The side groove design shown in Fig. 2.9 is intended to mitigate this problem. Specifically, the depth of the side grooves is 60% within most of the test section, but only 10% within most of the starter section. These two segments are connected by a smooth radius that spans the weld zone. Within the transition region, the static stress intensity at a given displacement increases with increasing crack length. As a result, relatively large ratios of K_a/K_o are possible for a crack that arrests within the test section.

Table 2.4 reports the data. In all but one specimen, the crack arrested at the weld line. When weld-line arrest was observed, the temperature was lowered, and the specimen was retested. In this way, four additional data points were obtained. These are plotted in Fig. 2.10, along with the balance of the TSE-6 crack-arrest data both from BCL and Oak

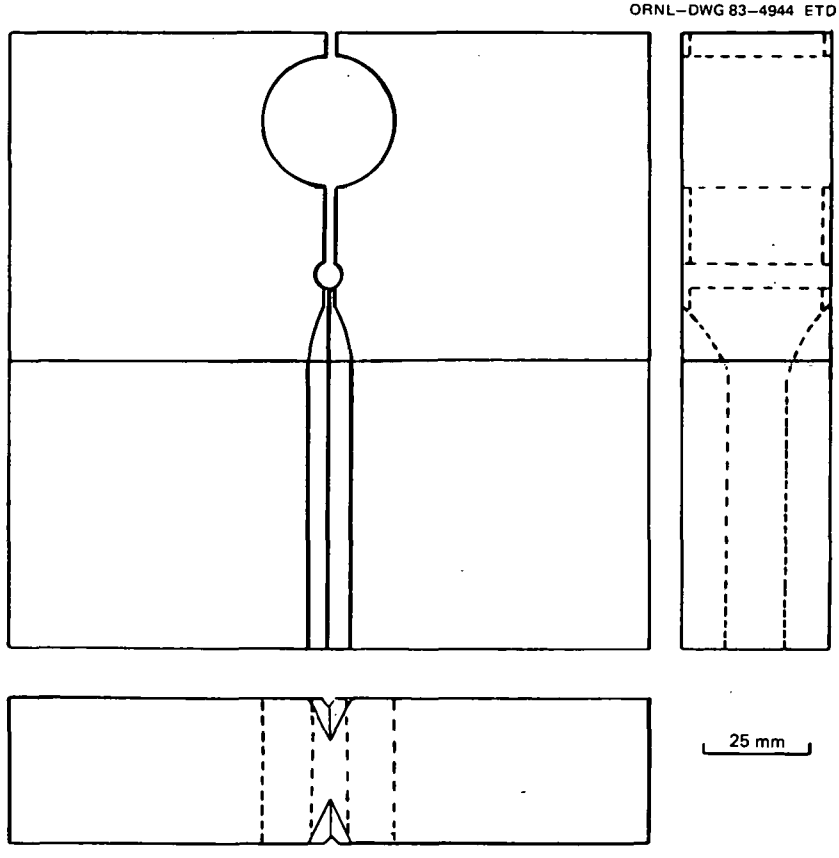

Fig. 2.9. Schematic drawing of duplex crack-arrest specimen with contoured side grooves.

Table 2.4. Crack-arrest data for TSE-6 steel (duplex specimens, contoured side groove, split-pin loading)

Specimen No.	Test temperature (°C)	Displacement (mm)		Crack length (mm)		Stress intensity (MPa·√m)	
		Initiation	Arrest	Initiation	Arrest	Initiation	Arrest
6-92[b]	143	1.24	1.36	40.64	60.96[a]	215	a
-92[b]	93	0.75	0.81	60.96	104.60	137	67
-93[b]	135	1.14	1.25	40.64	60.53[a]	198	a
-93[b]	124	0.97	1.03	60.53	103.20	166	89
-94[b]	121	1.06	1.15	40.64	60.96	183	a
-94[b]	94	0.93	1.00	60.96	103.78	170	85
-95[b]	121	1.52	1.62	40.64	60.8[a]	265	a
-95[b]	66	1.30	1.40	60.80	108.2	174	77
-98	121	1.17	1.34	40.64	88.9	204	157

[a]Arrested in weld zone.

[b]Reinitiation of arrested crack.

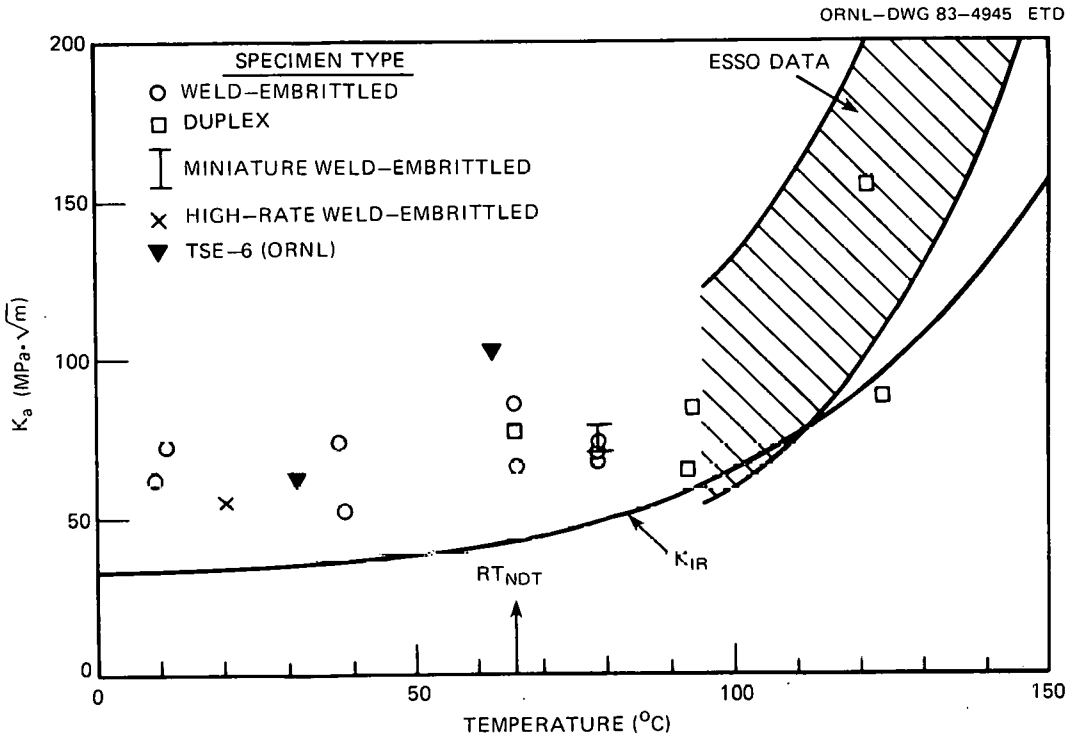

Fig. 2.10. Master plot of crack-arrest data for TSE-6 steel.

Ridge National Laboratory (ORNL). The new data have some similarities to those for TSE-5A in that they tend to fall within the ESSO-test scatter band with the exception of one specimen that has a K_{Ia} value that is not only lower than the comparable ESSO data, but also falls below K_{IR}. A final point with regard to these data is that in all cases but one, the arrest displacement was no more than 10% greater than the initiation displacement, which is comparable to BCL experience for the usual split-pin arrangement at lower test temperatures and for TSE-5A at higher test temperatures.

One possible explanation for the arrest in the weld zone is that the weld and/or HAZ pass through a ductile-brittle transition. It should be recalled that the duplex specimens used on the Cooperative Test Program had side grooves that were deepened in the weld region because this effect was suspected. A pseudo-Charpy impact specimen was designed to investigate the weld-zone toughness. Figure 2.11 shows the specimen. It was cut from half of a broken duplex crack-arrest specimen so that the crack path ran across the weld and HAZs in the same direction as in the duplex crack-arrest specimen. The specimens were then tested in a Charpy machine in the same way as impact specimens of conventional design. The absorbed energies are plotted in Fig. 2.12. There was a slight increase of energy absorption with increasing temperature, but no indication that the weld zone passed through a ductile-brittle transition.

On reviewing the results from TSE-6, it was decided that progress would be facilitated if the experiments could be run at lower absolute

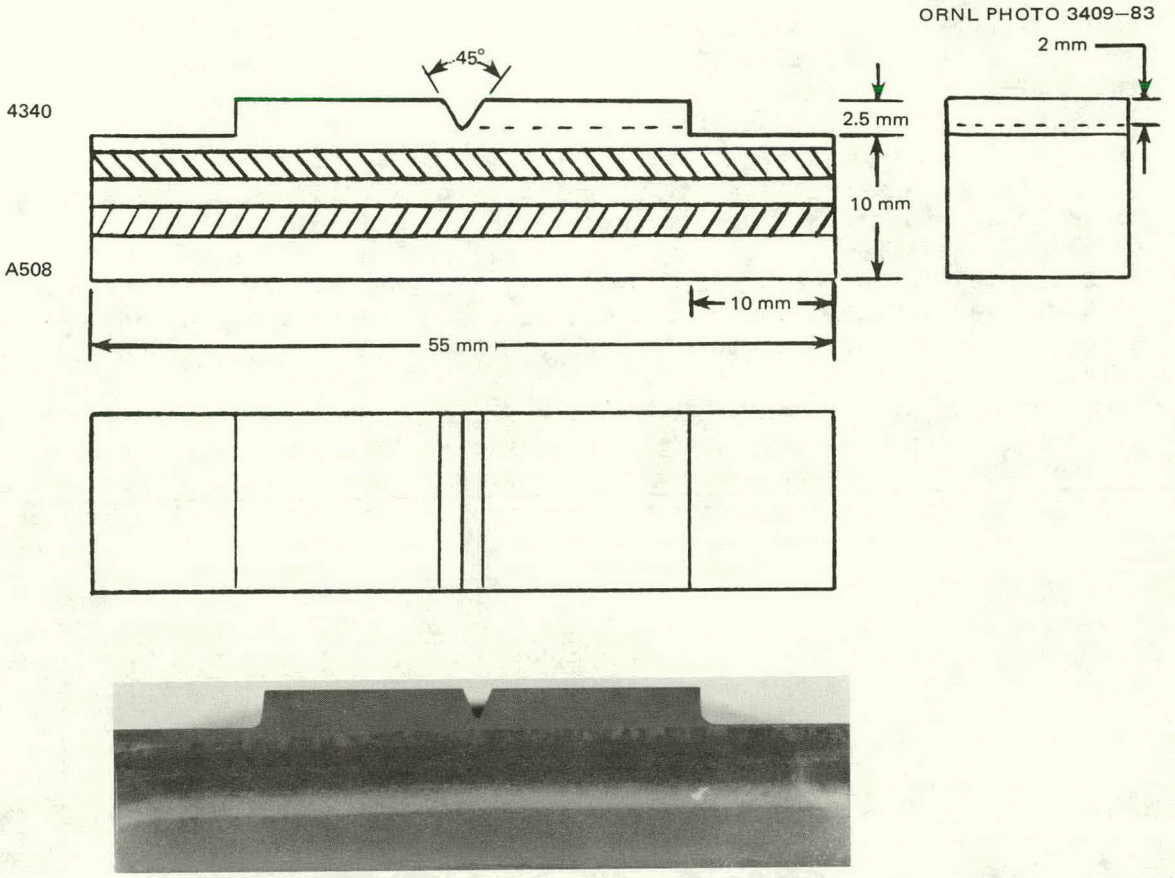

Fig. 2.11. Modified Charpy V-notch specimen made from weld region of duplex crack-arrest specimen.

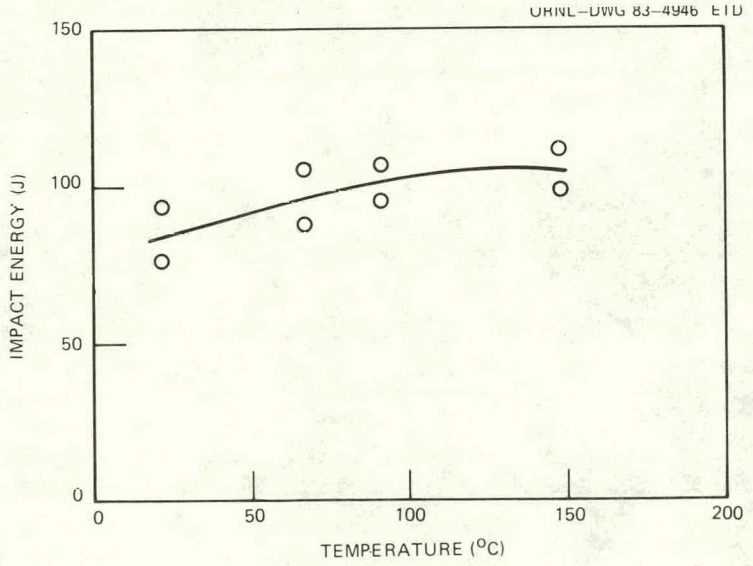

Fig. 2.12. Absorbed-energy/temperature data for weld-HAZs of duplex specimens of TSE-6. Modified Charpy V-notch specimen.

test temperatures. For this reason, a piece of the TSE-6 steel was tempered at high temperature (705°C) for 4 h and furnace cooled. Tensile and Charpy-impact properties for steel subjected to this heat treatment are given in Table 2.5 and Fig. 2.13. Based on the 41-J Charpy temperature, the provisional RT_{NDT} was −29°C. Duplex crack-arrest specimens were fabricated from this piece of steel, and a series of crack-arrest tests was performed. The design and procedures were identical to those of the previous series except for specimen 60RR-5. In that case, the side grooves in the weld region and test section were V-shaped to a depth of 4 mm, and a 0.6-mm-thick slot was extended from the tip of the vee for a distance of 6 mm. The total goove depth was 60%, as it was for the remaining specimens.

The data are presented in Table 2.6 and plotted in Fig. 2.14. There are several notable points. Most importantly, crack-arrest data have been obtained at ~100°C above the estimated level of RT_{NDT}. The largest K_{Ia} values were quite high (for CT specimens), in excess of 200 MPa·√m.

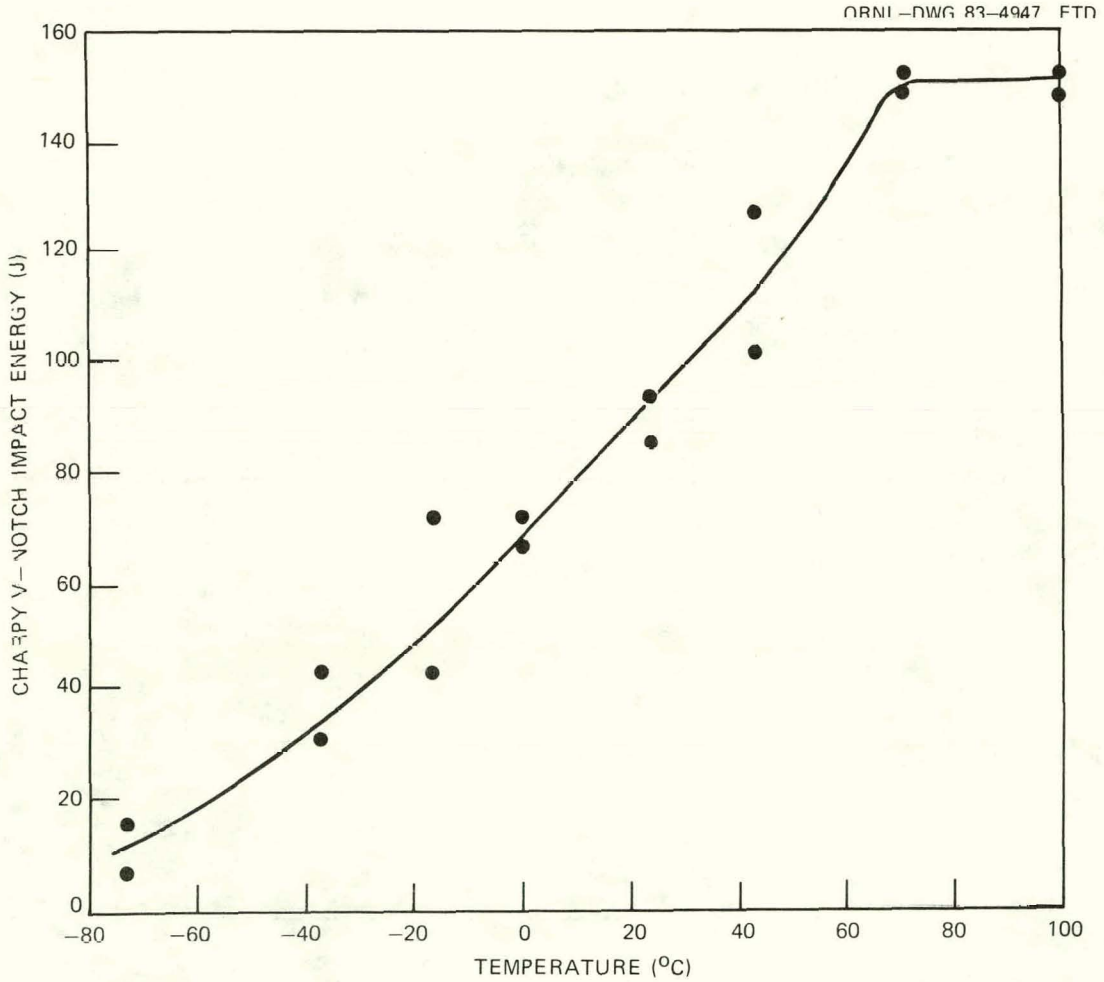

Fig. 2.13. Energy absorption as function of test temperature for reheat-treated TSE-6 steel (Code TSE-6R). Charpy V-notch specimens.

Table 2.5. Mechanical properties of reheat-treated steel from TSE-6 steel, TSE-6R[a]

Temperature (°C)	Tensile data			Charpy V-notch impact data
	0.2% Offset yield strength (MPa)	Ultimate tensile strength (MPa)	Reduction in area (%)	Energy (J)
26	558	692	66	
100	534	661	66	
−29				41
−1				68[b]
6				75[c]
71				149

[a]Retempered at 705°C for 4 h and furnace cooled.

[b]Half-shelf energy.

[c]Shelf energy.

Table 2.6. Crack-arrest data for reheat-treated TSE-6 steel, TSE-6R (duplex specimens, contoured side grooves, split-pin loading)

Specimen No.	Test temperature (°C)	Displacement (mm)		Crack length (mm)		Stress intensity (MPa·√m)	
		Initiation	Arrest	Initiation	Arrest	K_o	K_a
60RR-4[b]	23	1.45	1.57	40.64	81.9[a]	230	205[a]
-4[b]	0	2.56	2.58	81.90[a]	108.4[a]	334[a]	189[a]
-5	71	1.61	1.71	41.15	72.6	254	260
-5[b]	40	c	c	c	c	c	c
-8	53	1.38	1.55	40.64	80.6	219	207
-8[b]	0	1.11	1.16	80.60	110.9	148	78
-9	71	d	d	44.45	61.1	d	e
-9[b]	24	1.01	1.13	61.1	106.2	183	89
-10	71	1.69	1.86	44.2	84.84	259	233
-14	93	1.93	2.10	40.64	59.44[e]	307	e

[a]Values questionable due to very irregular crack.

[b]Reinitiation of arrested crack.

[c]Stable crack growth.

[d]Two apparent initiation/arrest events before crack finally arrested in weld zone. It was not possible to assign an unambiguous K_o to this specimen.

[e]Arrested in weld zone.

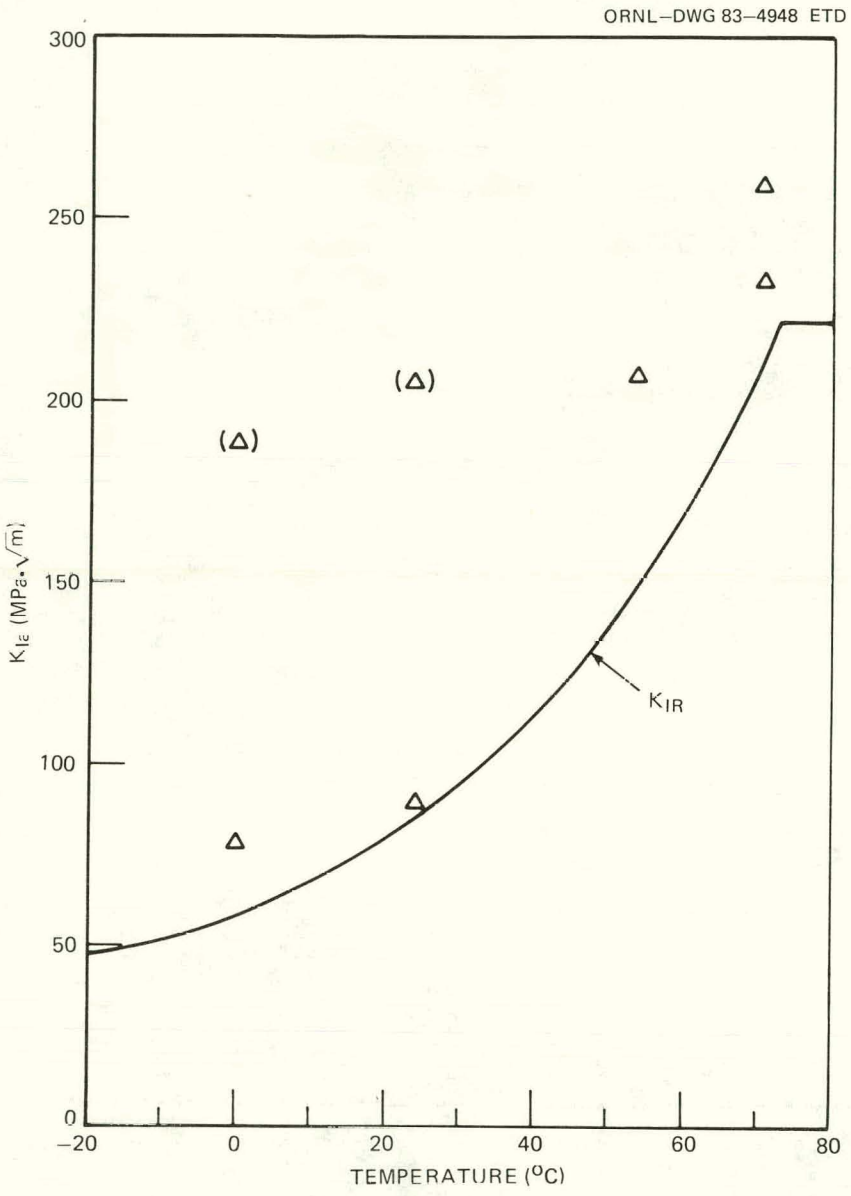

Fig. 2.14. Effect of test temperature on crack-arrest toughness of reheat-treated TSE-6 steel (Code TSE-6R).

However, one of the four specimens (60RR-4) with K_{Ia} at >200 MPa·√m had a very ragged crack, and its K_a values are suspect, both after the original arrest and after arrest following reinitiation. Data points for that specimen are enclosed in parentheses in Fig. 2.14. The second point is that the contoured side grooves performed their function by extending the K_{Ia}/K_o ratio to levels close to unity. Several very high values of K_o were noted; this is believed to be caused by better notch preparation. Finally, no evidence of ductile fracture was observed on any crack surface examined at low-power magnification. (A typical broken specimen is shown in Fig. 2.15.) Scanning-electron-microscope (SEM) fractographic

ORNL–PHOTO 3410–83

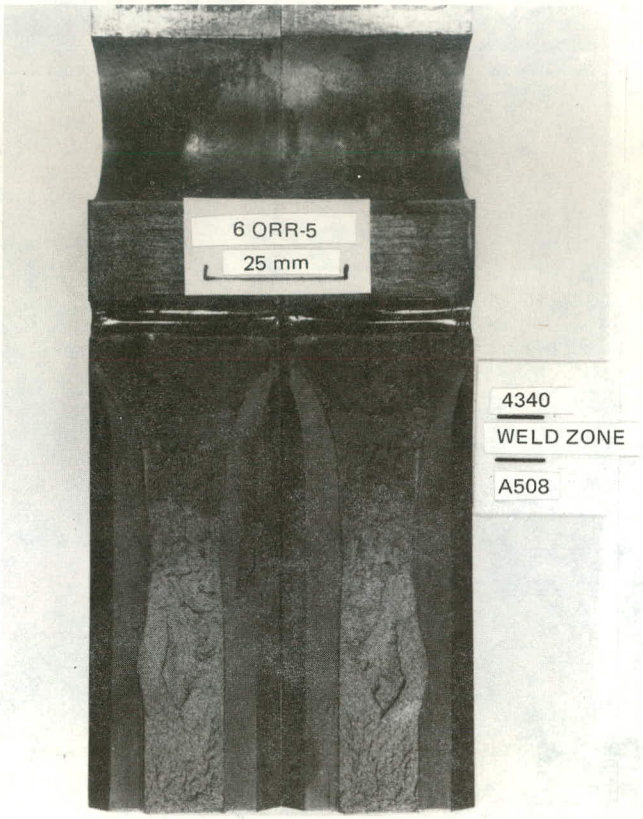

Fig. 2.15. Photo of typical broken crack-arrest specimen of reheat-treated TSE-6 steel.

examinations will be performed next quarter to determine whether a significant amount of dimpled rupture was present in any of the specimens.

Finally, note that the specimen with the slots that extended from the roots of the V-notches (60RR-5) had a K_{Ia} value 12% higher than that of the companion specimen with regular V-notches only. This result suggests that the slot may have only a minor effect on the K_I level, although this point requires more thorough investigation.

Discussion. As shown in Table 2.7, crack-arrest data have been obtained at Charpy upper-shelf temperatures for TSE steel with all three heat treatments. In addition, test temperatures as high as 121°C have been used. The two highest data points for TSE-6R are 100°C above the estimated RT_{NDT}, a relative temperature reached once previously with a duplex double-cantilever-beam (DCB) specimen.[16] Slightly higher absolute temperatures were reached on the steel from TSE-4, also with a duplex DCB specimen.[19]

Because of these results, supplemented by work at other laboratories at lower temperatures, there is some basis for comparison of the new BCL results with literature values. Figure 2.16 collects RPV-steel base-plate K_{Ia} values for pin-loaded specimens (CT and DCB) for temperatures

Table 2.7. Comparison of crack-arrest test data and Charpy upper-shelf data

Thermal shock test material	Charpy shelf		K_{Ia} tests	
	Energy (J)	Approximate temperature (°C)	Highest temperature (°C)	Highest K_{Ia} (MPa·$\sqrt{m}$)
TSE-5A	160	70	70	152
-6	106	100	121	157
-6R	150	70	71	260

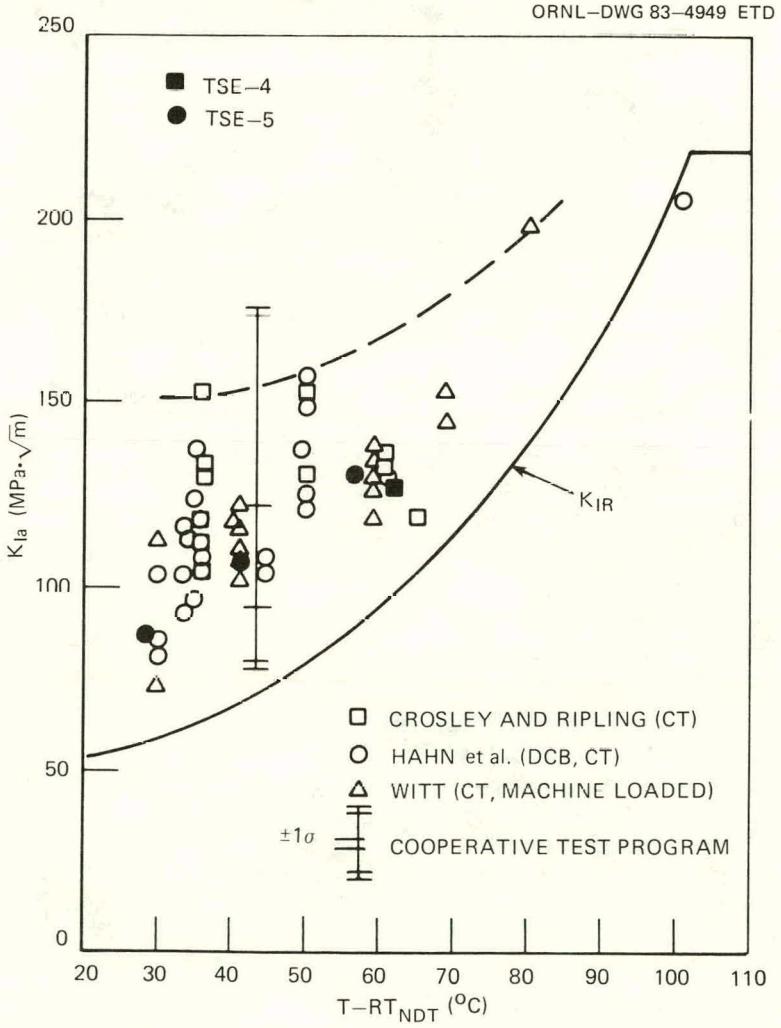

Fig. 2.16. Compilation of compact-specimen crack-arrest data.

$\gtrsim RT_{NDT}$ + 30°C.[16,18,20,21] The appropriate ORNL thermal-shock data are also included. There is surprisingly good agreement among laboratories, considering the variety of steels, specimen designs, and test procedures. The insensitivity of K_{Ia} to specimen design for wedge-loaded samples has been reported previously.[22] Surprisingly, the machine-loaded 1/2T and 1TCT-specimen data of Witt[20] are consistent with the other results. Witt measured load and crack length after arrest, calculating K_{Ia} from an equivalent-energy estimate. He also reported "tearing" for many of the specimens plotted in Fig. 2.16, where other authors observed cleavage. The reason for the agreement between the results of Witt[20] and those of other authors is not at all clear.

The largest K_{Ia} values in Fig. 2.16 are on the order of 200 MPa·$\sqrt{m}$. This is much smaller than the largest reported ESSO-test result from our literature survey,[23] where K_{Ia} was close to 400 MPa·$\sqrt{m}$. As shown in Fig. 2.17, the ESSO data and CT or DCB data are not very different between 30 and 50°C above RT_{NDT}. However, the ESSO results show a much larger temperature dependence, and the region of overlap of the scatter bands apparently stops at ~RT_{NDT} + 75°C. However, the scarcity of pin-loaded-specimen data at the highest temperature makes the scatter band very approximate at higher temperatures.

The data obtained in the present program are compared with the pin-loaded scatter band in Fig. 2.18. The new points are well represented by the scatter band except for the RT_{NDT} + 100°C data, which require extrapolation, and the data point for specimen 60RR-4, which had the very uneven crack front. The data extend to the upper shelf of the K_{IR} curve (K_{IR} = 220 MPa·$\sqrt{m}$), and there is no good indication that the slope decreases as the test temperature is raised. Therefore, upper-shelf behavior apparently has not been obtained yet.

2.2.4 Task 5: Data base

The objective of this task is to collect, organize, and analyze all available crack-arrest data relative to RPV steels, weldments, and weld HAZs. Data for both unirradiated and irradiated specimens are to be included. Realistic lower-bound estimates for K_{Ia} will be obtained by means of statistical analyses of the data. Efforts during the current quarter involved data collection, development of computer programs to facilitate data storage and analysis, and the development and application of statistical-analysis procedures.

This task consists of the following elements: (1) collection of K_{Ia} data from BCL and other sources, (2) development of procedures for data storage and retrieval, and (3) statistical analysis of data. In the following sections, current efforts in each of these tasks are described.

2.2.4.1 Data collection. Collection of K_{Ia} data from various sources has continued during this report period. Formal organization and tabulation of these data will be carried out as part of the following subtask. The data collection effort will be continued, with new data being added as they are acquired.

2.2.4.2 Data tabulation. Two programs have been written to maintain the data set. The first of these enables the user to enter, modify,

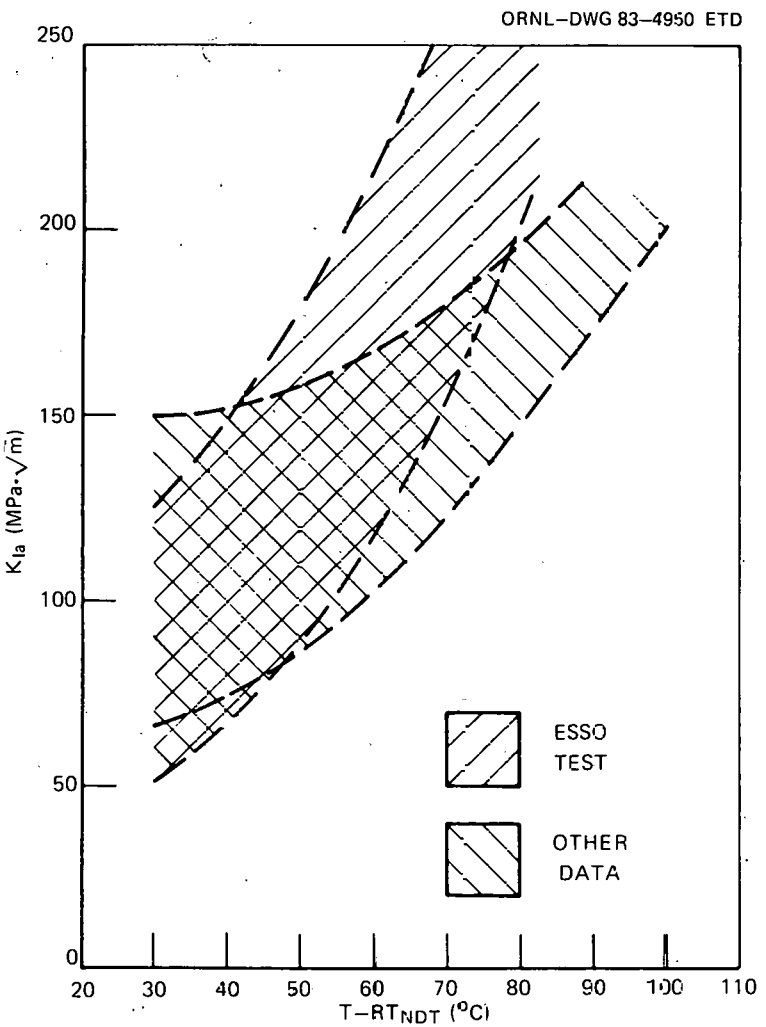

Fig. 2.17. Comparison between compact-specimen and ESSO-test crack-arrest-toughness data scatter bands.

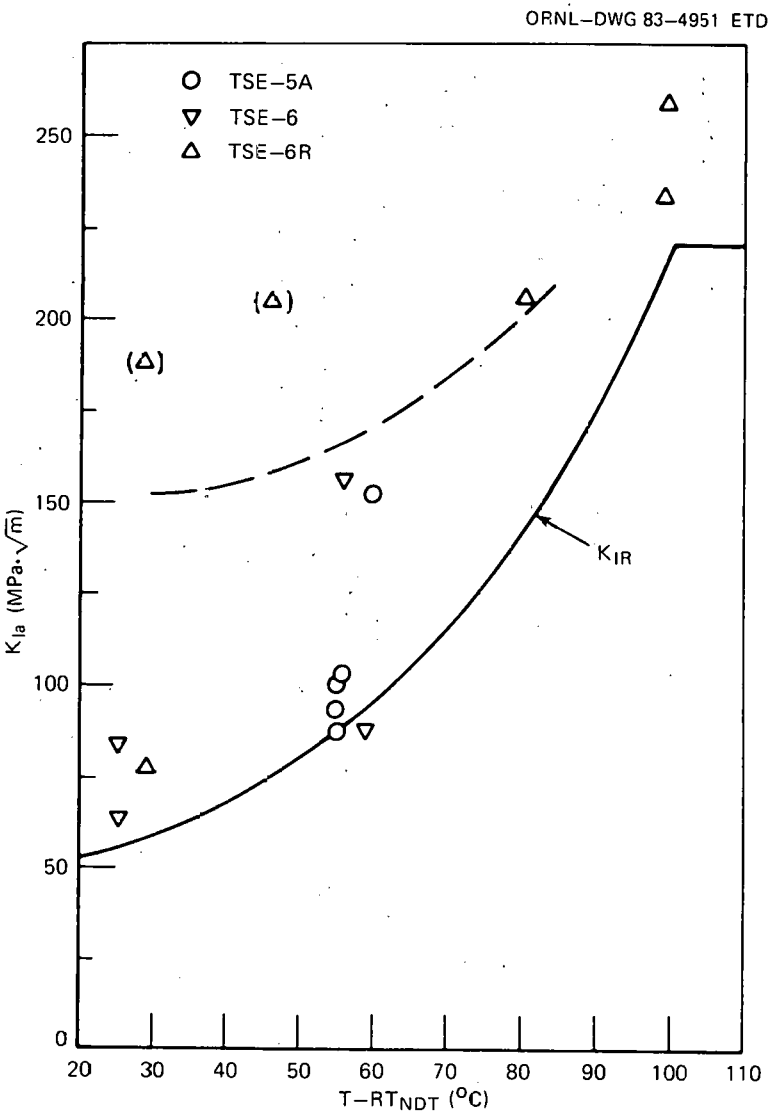

Fig. 2.18. Crack-arrest-toughness data obtained in present program compared with scatter band for pin-loaded specimens.

and delete data, while the second provides a convenient method for printing selected portions of the data. Both programs have been tested at some length, and all known problems have been solved. Certain enhancements to both programs may be necessary to provide slightly more convenient entry of data, additional capabilities for handling unknown or inapplicable data, and a more pleasing appearance for the printed report.

The programs can generate two types of printed reports. The long form, shown in Table 2.8, gives complete information on the dimensions of the sample. This form can be used for data generated in house. Because the literature rarely includes such detail, a short form is also available, as shown in Table 2.9. In-house data may also be printed in the short form to avoid visual clutter.

In their current state, the programs do not interact with the statistical package. It is anticipated that this will not be a significant difficulty; the report-generating program has been written so that only minor modifications will be necessary to produce a file that may be used as input by the statistical routines.

2.2.4.3 Outline of the statistical analysis. A new procedure has been developed for the estimation of transition curves.[24-26] During this report period, the procedure was generalized to include confidence bounds for the estimated transition curves. In addition, a computer code ITLSANAL was written that allows for a straightforward application of the method on any given set of crack-arrest data. Finally, the procedure was applied to two sets of crack-arrest data to illustrate the procedure. The results of these efforts are described in more detail below.

The statistical analysis of crack-arrest data depends on the following model. Let E_T denote the observed value at temperature T (for example K_a data or Charpy-impact data). The probability that the observed measurement E_T will be less than or equal to x is given by

$$P[E_T \leq x] = \begin{cases} 1 - \exp\left\{-[x/\beta Z(T)]^{\alpha(T)}\right\} & \text{for } x \geq 0 \\ 0 \quad \text{for } x < 0 \end{cases} . \qquad (2.26)$$

The right side of Eq. (2.26) represents the cumulative distribution function for the Weibull distribution with scale parameter $\beta(T)$ and shape parameter $\alpha(T)$, which are allowed to depend on temperature.

The 100 pth percentile of the distribution defined by Eq. (2.26) is the parameter $C_p(T)$ such that $P[E_T \leq C_p(T)] = p$. It is the parameter of primary interest, and it is calculated by

$$C_p(T) = \beta(T)\left[-\ell n(1 - p)\right]^{1/\alpha(T)} . \qquad (2.27)$$

Based on the estimation procedure described in Ref. 24, estimates $\hat{\alpha}(T)$ and $\hat{\beta}(T)$ are obtained for $\alpha(T)$ and $\beta(T)$. These estimates are combined,

Table 2.8. Computer printout for long-form crack-arrest-data tabulation

Series B001 16-MAR-83

Material: low-Cu, high-upper-shelf A533B plate

Condition:
Q, T, SR at 620 C 40+20 hr.

CRACK ARREST DATA
Author: C. W. Marschall et al.
Laboratory: Battelle-Columbus Laboratories
Reference:
Pressure Vessel Design-PVP Vol. 57, G. Widera, ed., ASME, New York (1982)

MATERIAL DATA
Author: C. W. Marschall et al.
Laboratory: Battelle-Columbus Laboratories
Reference:
BCL Report to Westinghouse on EPRI RP1326-1, July 26, 1982.

RTNDT	-18.0°C
CV30	-39.0°C
NDT	-34.0°C
FATT	29.0°C

Restrictions on release: none

Young's modulus calculated from data for A508

Comments:
Specimens of several sizes tested by sequential loading.

Sample ID	GP-90	GP-91	GP-93	GP-94
Sample type	1	1	1	1
Temperature, °C	19.0	19.0	-19.0	-1.0
Ka, MPa$\sqrt{m}$	95.	97.	55.	74.
Young's modulus, MPa	209662.	209662.	211738.	210755.
Yield strength, MPa	503.0	503.0	531.0	517.0
Height, mm	152.40	152.40	101.60	101.60
Width, mm	127.30	127.20	84.50	84.30
Thickness, mm	38.10	38.10	25.40	25.40
Thickness at groove, mm	28.50	28.60	18.90	19.00
Slot height, mm	11.20	10.70	7.60	7.60
Notch radius, mm	1.40	1.37	0.64	0.66
Init. crack length, mm	46.50	50.20	32.90	32.00
Arr. crack length, mm	88.90	89.20	72.40	67.20
Init. displacement, mm	1.02	1.02	0.69	0.80
Arr. displacement, mm	1.09	1.12	0.81	0.89
Non-elastic disp., mm	0.01	0.05	0.08	0.02
Loading cycles	15	11	10	13
Validity checks (w-a)	1.707	1.627	1.753	1.315
(B)	2.117	2.039	4.599	2.442
(Δa/Δa min)	1.893	1.822	2.599	2.316
(b/w)	3.016	2.987	1.432	2.028
(2H)	1.966	2.168	2.233	1.545
(a/p)	3.608	3.660	5.729	3.531
Comments				

Table 2.9. Computer printout for short-form crack-arrest-data tabulation

Series B001 16-MAR-83

Material: low-Cu, high-upper-shelf A533B plate

Condition:
Q, T, SR at 620 C 40+20 hr.

CRACK ARREST DATA
Author: C. W. Marschall et al.
Laboratory: Battelle-Columbus Laboratories
Reference:
Pressure Vessel Design-PVP Vol. 57, G. Widera, ed., ASME, New York (1982)

MATERIAL DATA
Author: C. W. Marschall et al.
Laboratory: Battelle-Columbus Laboratories
Reference:
BCL Report to Westinghouse on EPRI RP1326-1, July 26, 1982.

RTNDT	-18.0°C
CV30	-39.0°C
NDT	-34.0°C
FATT	29.0°C

Restrictions on release: none

Young's modulus calculated from data for A508

Comments:
Specimens of several sizes tested by sequential loading.

Sample ID	GP-90	GP-91	GP-93	GP-94
Sample type	1	1	1	1
Temperature, °C	19.0	19.0	-19.0	-1.0
Ka, MPa$\sqrt{m}$	95.	97.	55.	74.
Yield strength, MPa	503.0	503.0	531.0	517.0
Comments				

Sample ID	GP-95	GP-97	GP-99A	GP-101
Sample type	1	1	1	1
Temperature, °C	0.0	-19.0	40.0	-1.0
Ka, MPa$\sqrt{m}$	66.	59.	132.	75.
Yield strength, MPa	517.0	531.0	489.0	517.0
Comments				

Sample ID	GP-104
Sample type	1
Temperature, °C	-39.0
Ka, MPa$\sqrt{m}$	66.
Yield strength, MPa	544.0
Comments	

via Eq. (2.27), to obtain an estimate for $C_p(T)$ given by

$$\hat{C}_p(T) = \hat{\beta}(T)\left[-\ell n(1 - p)\right]^{1/\hat{\alpha}(T)} . \tag{2.28}$$

The estimation procedure has been generalized to include confidence bounds for $C_p(T)$. Once the estimation procedure is complete, $\hat{C}_p(T)$ is given by Eq. (2.28), where $\hat{\beta}(T)$ and $\hat{\alpha}(T)$ are estimates of $\beta(T)$ and $\alpha(T)$ obtained from the crack-arrest data, and they are therefore random variables. Viewing $\hat{C}_p(T)$ as a function of the random variables $\hat{\beta}(T)$ and $\hat{\alpha}(T)$, the variance of $\hat{C}_p(T)$ may be obtained using standard error-propagation techniques.

The resulting form for the estimated variance for $\hat{C}_p(T)$ (see Ref. 26 for details) is given by

$$\hat{V}[\hat{C}_p(T)] = H^{1/\hat{\alpha}(T)} \left\{\hat{\sigma}_\beta^2 + [\hat{\beta}/\hat{\alpha}^2(T)]^2 \ \ell n^2(H) \ \hat{\sigma}_\alpha^2\right\} , \tag{2.29}$$

where $H = -\ell n(1 - p)$ and $\hat{\sigma}_\beta^2$ and $\hat{\sigma}_\alpha^2$ are the estimated variances for $\hat{\beta}(T)$ and $\hat{\alpha}(T)$, respectively, obtained from the regression analyses employed by the estimation procedure.

The approximation to the variance of $\hat{C}_p(T)$ given by Eq. (2.29) ignores any correlation between the estimates $\hat{\beta}(T)$ and $\hat{\alpha}(T)$. However, the effect of a nonzero correlation can be assessed, and a conservative estimate of the variance for $\hat{C}_p(T)$ can be obtained.[26]

Approximate 95% confidence bounds for $\hat{C}_p(T)$ are then calculated by

$$\hat{C}_p(T) \pm 2 \sqrt{\hat{V}[\hat{C}_p(T)]} . \tag{2.30}$$

A computer code ITLSANAL has been developed that performs the calculations required to obtain the estimates $\hat{\beta}(T)$, $\hat{\alpha}(T)$, $\hat{C}_p(T)$, and $\hat{V}[\hat{C}_p(T)]$. In addition, the program creates computer plots of (1) the crack-arrest data $\{E_T\}$ and $\hat{C}_p(T)$ vs temperature and (2) $\hat{C}_p(T)$ and the associated upper and lower 95% confidence bounds vs temperature.

The user is only required to input (1) the crack-arrest and temperature data, (2) the percentile to be estimated (e.g., fifth, tenth, etc.), (3) the order of the polynomial to be used in estimating the natural logarithm of $\beta(T)$, (4) the order of the polynomial to be used in estimating the natural logarithm of $\alpha(T)$, (5) the convergence criteria for the estimation procedure, and (6) the maximum number of iterations allowed for the estimation procedure.

During the next report period, the program ITLSANAL will be interfaced with the data storage and retrieval program.

2.2.4.4 Example analyses. Two sets of data have been chosen to illustrate the statistical analysis procedure and the ITLSANAL computer code. The first data set, presented in Table 2.10, includes crack-arrest data from ORNL experiments TSE-4 through -6.[19,27] The second data set, presented in Table 2.11, is the original BCL crack-arrest data for the experiments (TSE-4: Ref. 19; TSE-5: Ref. 28; TSE-5A: Ref. 22; and TSE-6: Ref. 24).

The estimation procedure was applied to both sets of data, and the fifth percentile curve was estimated for both sets of data. The numerical results for the data presented in Table 2.10 are presented in Table 2.12. The graphical results are presented in Figs. 2.19 and 2.20. The numerical results for the data presented in Table 2.11 are presented in Table 2.13, and the graphical results are presented in Figs. 2.21 and 2.22.

These results should be viewed only as examples of the statistical analysis technique. The irregular curve shapes are due to the large scatter and relatively small number of points. This problem is accentuated at either end of the curves. A better fit to the BCL data can be achieved by using a higher order polynomial approximation for $\beta(T)$ and/or $\alpha(T)$. Because these data were analyzed for illustrative purposes, these refinements were not made in the analyses.

2.3 Finite-Element Analyses of ESSO Tests*

M. F. Kanninen† J. Ahmad†
C. R. Barnes†

2.3.1 Introduction

This task focused on an assessment of the validity of wide-plate tests [ESSO, double tension (DT)] to provide reliable upper-shelf crack-arrest toughness data for use in the thermal-shock analyses. The effort in this task included a literature review to identify existing wide-plate test data containing enough information to enable a dynamic finite-element interpretation of the test results.

It was found that sufficient data are available only for DT tests conducted in Japan, and even for this case, exact initial conditions of the test are ill-defined. Specifically, the geometry of the crack starter section and the initial notch length are not given.

As a subtask, preliminary activities were initiated toward establishing optimum specimen instrumentation procedures for the test matrix in the proposed Japan-U.S. cooperative research effort for developing crack-arrest properties pertinent to the pressurized-thermal-shock problem. The procedures were specifically designed to supply the information needed for the dynamic finite-element analyses.

---

*Work sponsored by HSST Program under UCC-ND Subcontract 85X-17624C between UCC-ND and BCL.

†BCL, Columbus, Ohio.

Table 2.10. ORNL crack-arrest data

Experiment	K_a (MPa·$\sqrt{m}$)	$T-RT_{NDT}$ (°C)
TSE-4	127	63
-5-1	86	−30
-5-2	104	16
-5-3	92	23
-5A-1	76	12
-5A-2	86	28
-5A-3	107	41
-5A-4	130	57
-6-1	63	−32
-6-2	105	−2

Table 2.11. BCL crack-arrest data

Experiment	K_a (MPa·$\sqrt{m}$)	$T-RT_{NDT}$ (°C)
TSE-4-5	122	58
-4-6	125	58
-4-9	113	59
-4-7	106	10
-4-8	100	10
-5A-45	82	−10
-5A-46	118	18
-5A-48	97	18
-5A-53	80	12
-5A-54	134	41
-5A-55	73	−10
-5-37	61	−38
-5-39	89	16
-5-40	78	18
-5-41	71	−39
-5-42	109	15
-6-85	72	−55
-6-88	64	−57
-6-82	78	−27
-6-80	51	−27
-6-83	69	0
-6-86	86	0
-6-81	69	12
-6-89	71	13
-6-84	74	13

Table 2.12. Estimates associated with ORNL data

Temperature (°C)	Estimates (MPa·√m)			Beta (MPa·√m)	Alpha
	Lower confidence limit	Fifth percentile estimate	Upper confidence limit		
−32.00	−7.37	40.68	88.72	77.75	4.58
−30.00	−4.74	43.09	90.92	80.81	4.72
−2.00	30.62	66.66	102.70	100.83	7.18
12.00	44.65	71.06	97.47	99.41	8.85
16.00	47.29	71.97	96.66	99.74	9.39
23.00	49.92	73.73	97.54	98.03	10.43
28.00	50.67	75.41	100.14	98.22	11.24
41.00	53.92	83.51	113.09	103.82	13.64
57.00	71.81	109.85	147.90	130.39	17.33
63.00	75.72	129.33	182.95	151.28	18.95

Table 2.13. Estimates associated with BCL data

Temperature (°C)	Estimates (MPa·√m)			Beta (MPa·√m)	Alpha
	Lower confidence limit	Fifth percentile estimate	Upper confidence limit		
−57.00	31.28	53.47	75.66	76.21	8.38
−55.00	31.65	52.42	73.19	74.95	8.31
−39.00	32.62	47.95	63.28	70.35	7.75
−38.00	32.68	47.86	63.03	70.33	7.71
−27.00	34.08	47.95	61.83	71.82	7.35
−10.00	39.07	51.40	63.72	79.41	6.83
0.00	42.67	54.84	67.01	86.39	6.54
10.00	45.42	58.99	72.56	94.84	6.26
12.00	45.79	59.87	73.56	96.66	6.20
13.00	45.95	60.32	74.96	97.58	6.17
15.00	46.21	61.22	76.22	99.45	6.12
16.00	46.32	61.67	77.02	100.40	6.09
18.00	46.48	62.57	78.62	102.30	6.04
41.00	43.48	71.52	99.62	123.18	5.46
58.00	33.24	73.11	112.99	131.31	5.07
59.00	32.32	72.99	113.66	131.42	5.05

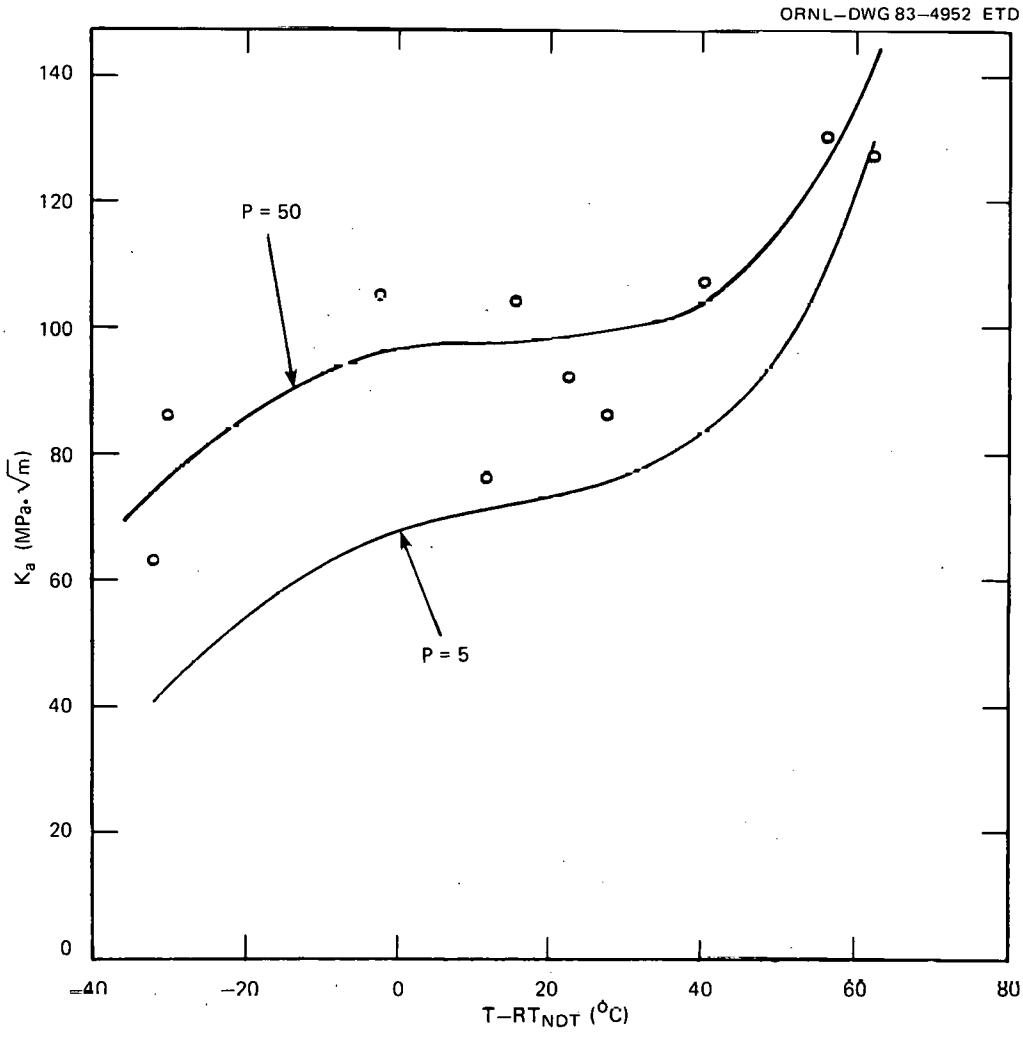

Fig. 2.19. Crack-arrest data and estimated percentiles vs temperature (ORNL data).

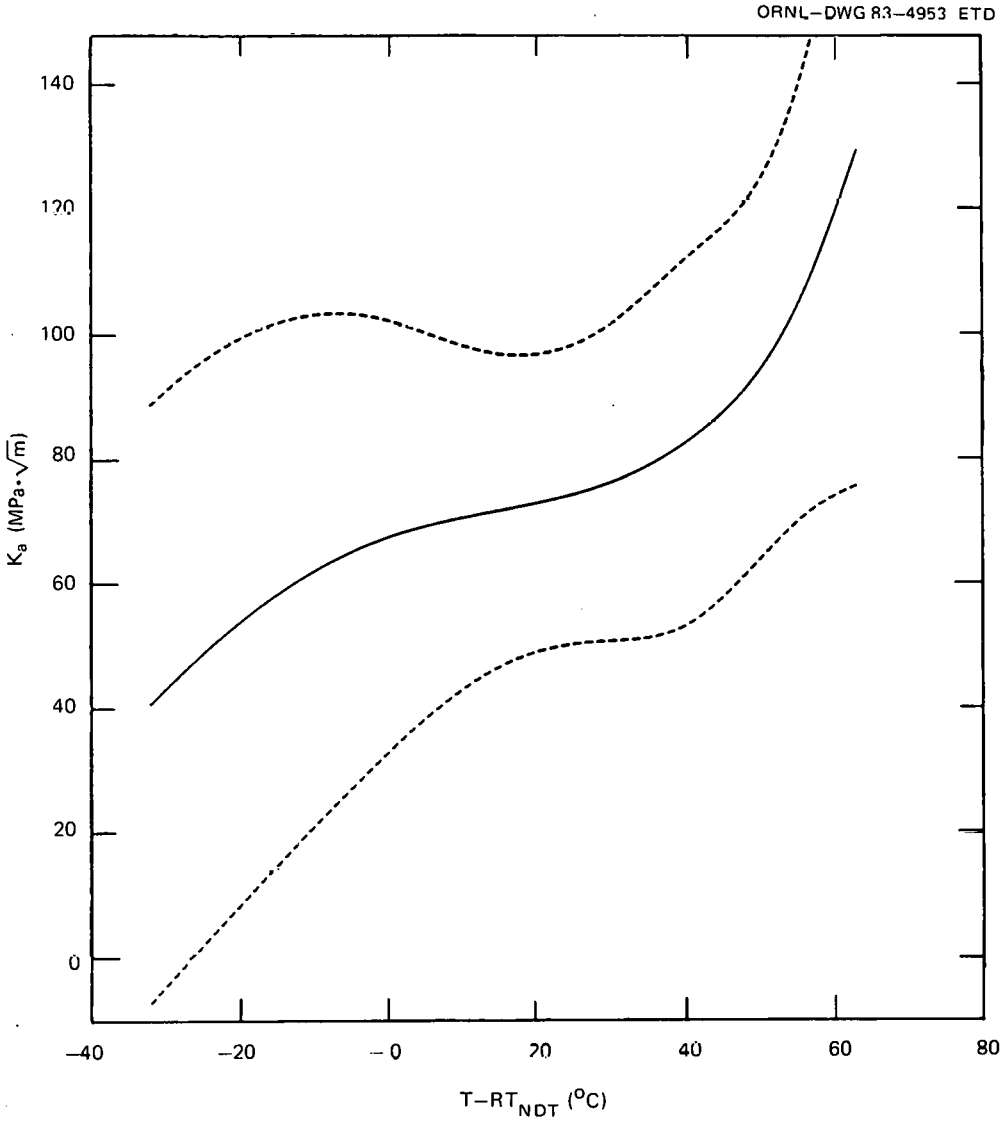

Fig. 2.20. Estimated fifth percentile and confidence bounds vs temperature (ORNL data).

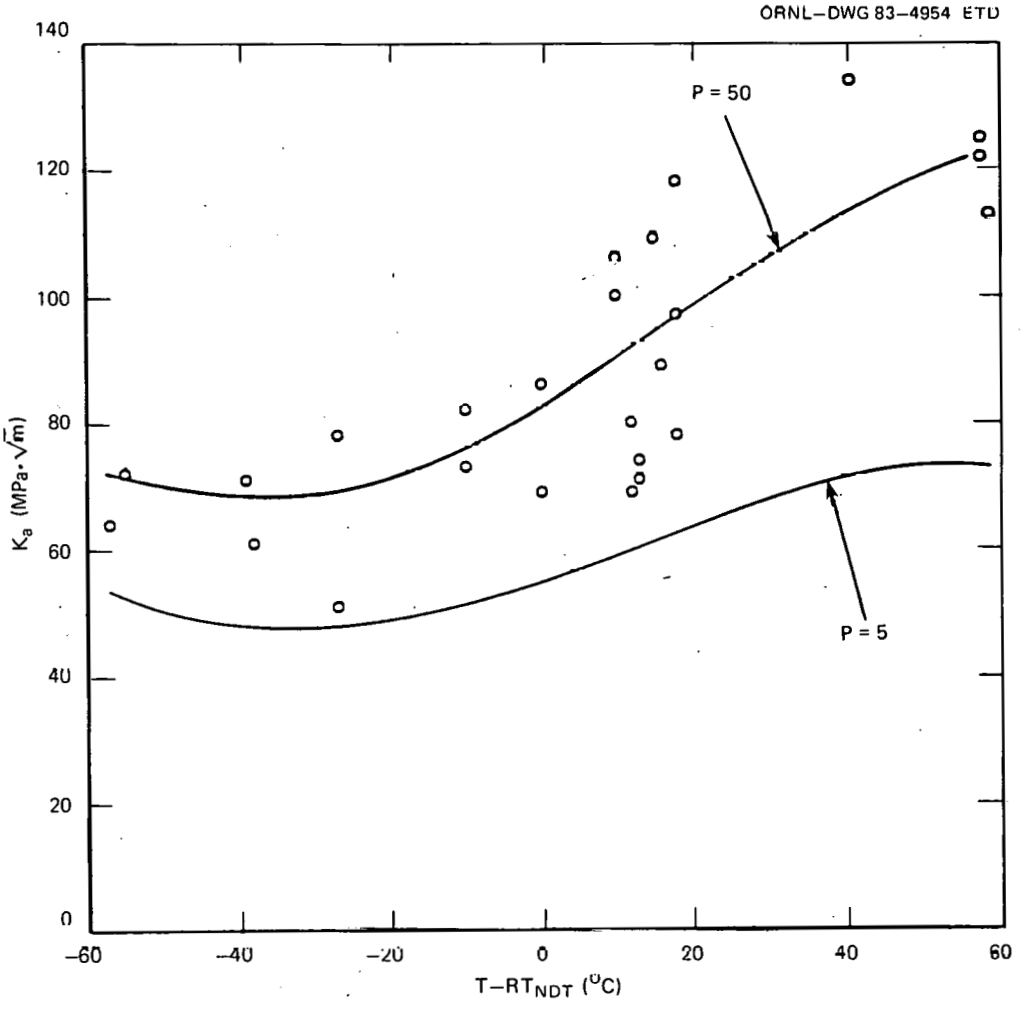

Fig. 2.21. Crack-arrest data and estimated percentiles vs temperature (BCL data).

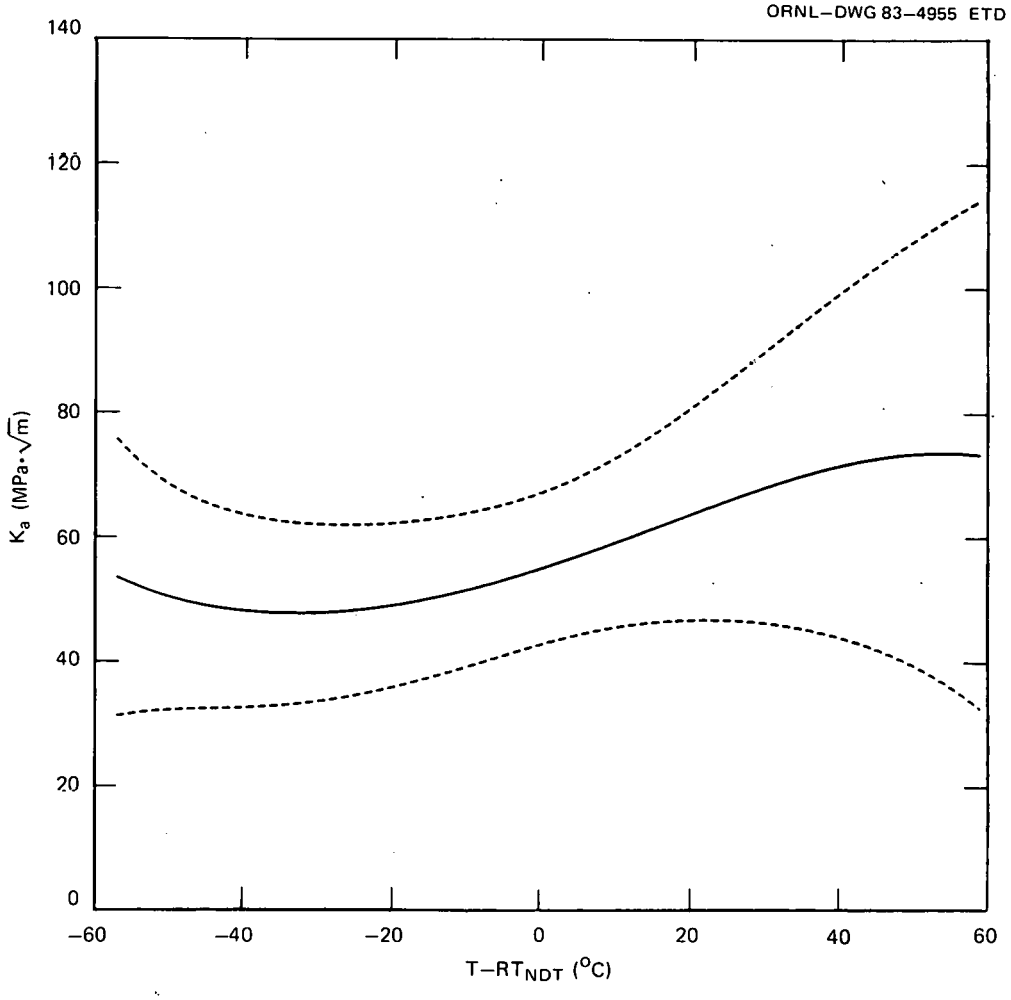

Fig. 2.22. Estimated fifth percentile and confidence bounds vs temperature (BCL data).

2.3.2 Elastodynamic finite-element analyses

The elastodynamic finite-element analyses conducted in this task consisted of two types of computations: generation phase and application phase.

2.3.2.1 Generation-phase analyses. In this type of computation, the experimental crack length vs time data are provided as part of the input to the finite-element method.* The result of this type of analysis gives the variation of K_D with crack velocity.

The specific case analyzed was a DT test of a ship-hull steel (code KAS) specimen conducted at −40°C. A schematic diagram of the specimen with loading fixtures is shown in Fig. 2.23. The results of this analysis, along with those of Kanazawa et al.,[29] are shown in Fig. 2.24. In both these analyses, the step changes in thicknesses of the test piece (15 mm), pulling plates (23 mm), and the loading fixture (30 mm) were ignored.

A second computation was performed in which the mass and stiffness of each component in the 2-D finite-element model were appropriately adjusted to account for the varying thickness. As expected, the results showed an elevation in K_D values at all crack velocities, thus widening even further the difference between the present results and those of Kanazawa et al.[29] Regardless of the source of discrepency between the present results and those from Ref. 29, the assumption of uniform thickness for the whole structure appears to be dubious.

2.3.2.2 Application-phase analyses. In this type of computation, a functional form of K_D (a, T) is provided as part of the input to the

*BCL's FRACTDYN computer code was used in all computations.

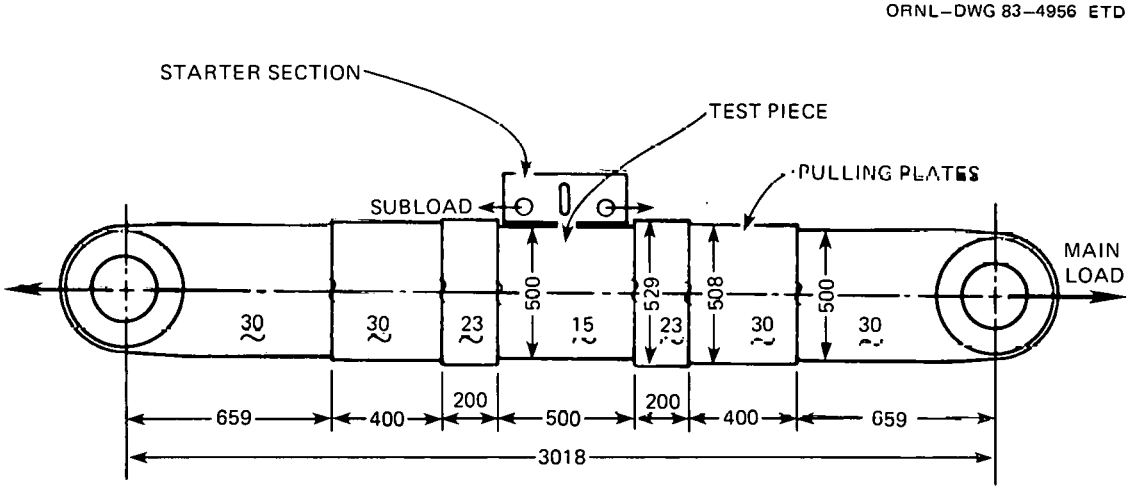

Fig. 2.23. Specimen geometry and loading arrangement for DT test.

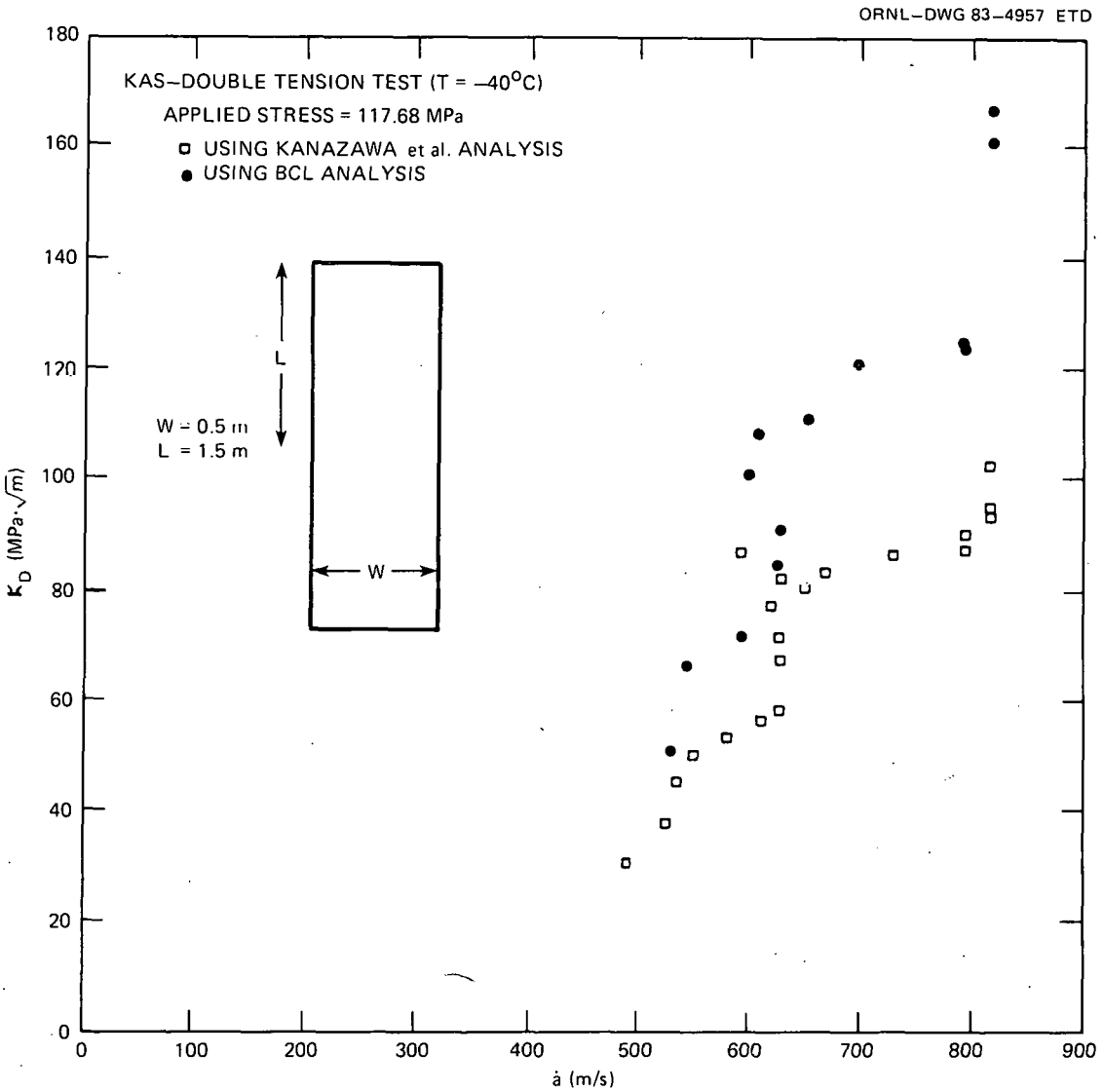

Fig. 2.24. Result of generation-phase computation.

finite-element model, and the results of the analysis give the variation of crack length with time including the crack length at arrest, if arrest occurs. The needed K_D (ȧ, T) function was obtained by using available data on KAS steel for $80 < T < 20°C$.

The specific case analyzed was a test with a bilinear temperature gradient imposed along the crack propagation direction (Fig. 2.25). Computations were performed using three different K_Q values. The prediction of crack-arrest length is shown in Fig. 2.25 along with the experimental results. It is important to note that uniform thickness had to be assumed in all application-phase analyses because the K_D data found in the literature were obtained using the same assumption. However, if proper account of the varying thickness was taken in both generation-phase and

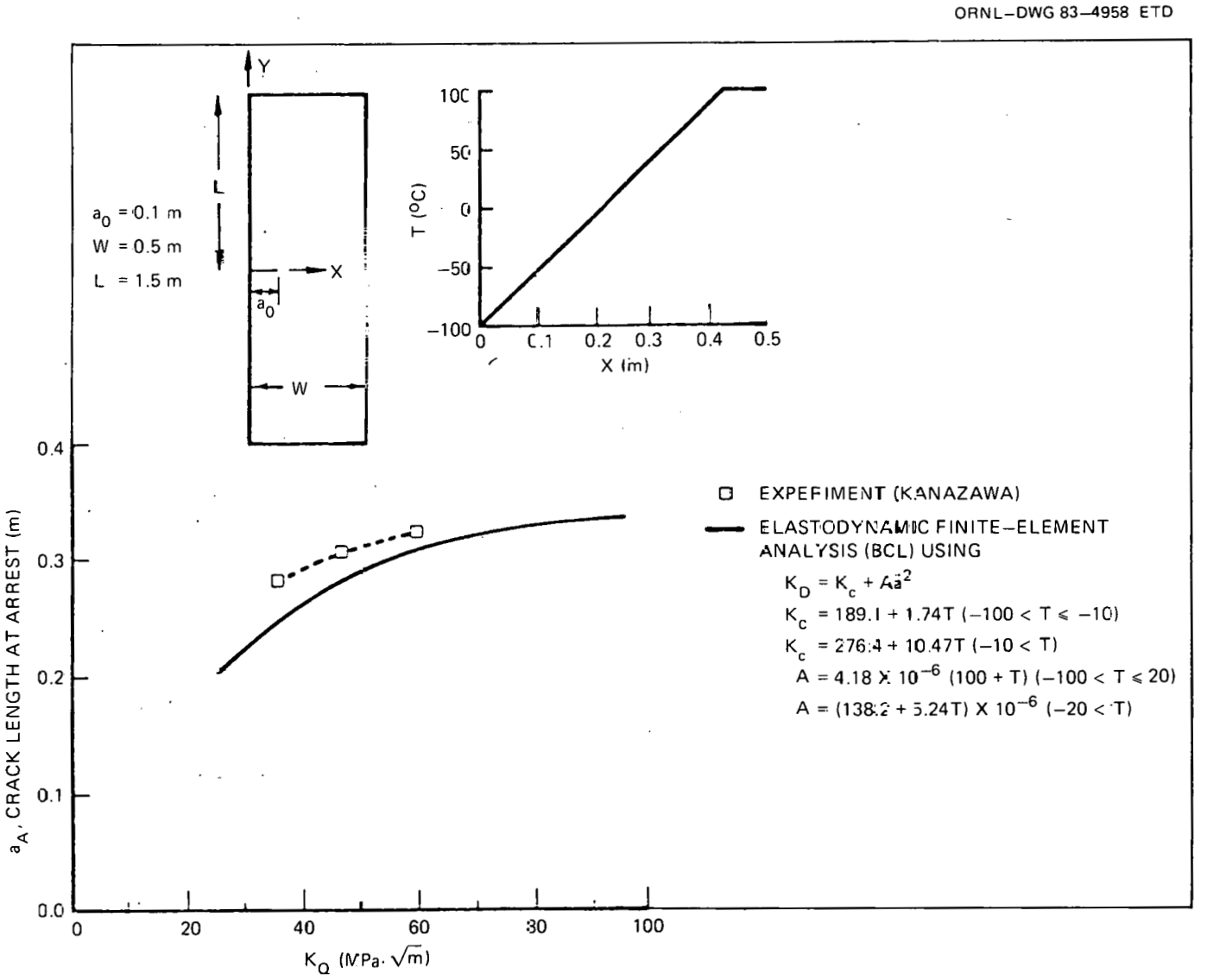

Fig. 2.25. Results of application-phase computations.

application-phase analyses, the accuracy of the predictions can be expected to be about the same.

Overall, the work performed in this task leads to the conclusion that the experimental data obtained from the DT test conducted in Ref. 29 appears to be quite accurate. What is in doubt is their analytical interpretation of the data. Some of the difficulties in the analysis of the data can be alleviated if an experimental record of strain variation at the boundaries of the test piece throughout the crack propagation test can be obtained. Then, in the finite-element analysis, only the test piece (with stress boundary conditions) will need to be modeled, thus avoiding the necessity to include the pulling plates and the loading fixture in the analyses and circumventing the concern for the thickness changes.

2.3.3 Preliminary test procedure

Based on the analysis conclusions, and to address some other aspects of the problem, a preliminary plan has been made for instrumenting the wide-plate specimens for tests proposed to be conducted in Japan. For the most part, the specimen instrumentation will consist of timing wires, strain gages, and thermocouples. The timing wires will be used to determine crack speed for the brittle portion of crack propagation and to verify the crack speed monitoring capability of strain gages applied to one side of the projected crack path. This procedure will establish a degree of credibility for strain gage readings during the ductile portion of crack propagation and subsequent crack arrest. Strain gages will also be used to measure specimen boundary strains during crack propagation. The thermocouples will be used to monitor the specimen temperature gradient.

It has been suggested that the test specimens in this program could serve a dual purpose. The first purpose could be to provide crack initiation, propagation, and arrest data. A second test procedure could be used to establish material J resistance behavior on completion of the first test. This would consist of reloading the specimen until the crack reinitiates and extends. This reinitiation and growth could be monitored using the dc electrical potential technique.

In principle, this is a relatively straightforward procedure. However, there are bothersome details that cannot be addressed without a detailed examination of the test machine. This examination is necessary to devise a method of insulating the test specimen from the machine (or alternatively of insulating the entire machine from ground). The viability of the electric potential technique depends on the electrical isolation of the test specimen. Planning will continue for this activity.

2.4 Investigation of Damping and Cleavage-Fibrous Transition in Reactor-Grade Steel*

W. L. Fourney† G. R. Irwin†
K. Ogawa† X-J. Chang†
R. Chona†

2.4.1 Introduction

The research program at the University of Maryland is aimed at increasing the understanding of crack run-arrest events in nuclear RPV steels. An intensive study is being conducted of the behavior of various steels or heats of steels in the transition temperature range. That is, SEM and metallographic studies are being conducted to investigate the transition from pure ductile fracturing at high temperatures to brittle cleavage at lower temperatures. In particular, we are trying to assess what is responsible for the conversion of slow fibrous fracturing into rapid cleavage.

This study is being conducted by examining specimen halves obtained from tests conducted in very compliant loading machines. Single- and double-width Charpy testing is also being used to evaluate fracture toughness and determine the temperature above which slow fibrous fracturing could be expected for the steels under investigation. This research into transition behavior is aimed at formulating a mechanistic model.

Dynamic calculations are also being performed with a dynamic finite-element computer code (SAMCR) to predict run-arrest events in standard specimen geometries and thermal-shock cylinders. We are also supporting crack-arrest studies with our stress analysis capabilities by testing transparent models or opaque models covered with photoelastic coatings.

During the past report period, progress has been made in Charpy testing of A508 materials obtained from ORNL, in topology and microstructure examinations of an A533B material, in improvements made to the SAMCR code, and in analysis performed to support ESSO-type testing that may be conducted in cooperation with the Japanese.

2.4.2 Toughness in relation to small inhomogeneities

In this report period, additional attention was given to the significance of carbide density bands in A508 and A533 heavy-section steels. As noted in the last quarterly report,[30] the carbide density bands in specimens taken from a 600-mm-thick A533 plate show considerable similarity to those observed in A508 specimens taken from 300-mm-wall cylinder forgings. In appearance, the carbide density bands were closely related to dendritic solidification and showed orientation differences when viewed on orthogonal surfaces.

---

*Work sponsored by HSST Program under UCC-ND Subcontract 7778 between UCC-ND and the University of Maryland.

†Department of Mechanical Engineering, University of Maryland, College Park.

Five Charpy V-notch specimens in each of six orientations were made from the above A508 cylinder material and tested to determine the influence of carbide density bands on toughness. A section from one end of a large three-point-bend specimen blank was used for this purpose. The position of the specimen blank relative to the ORNL cylinder is shown in Fig. 2.26. Figure 2.27 shows the six Charpy V-notch specimen orientations relative to the specimen blank. The orientation tendency of observed segments of carbide density bands are indicated in Fig. 2.27 in schematic fashion. The number of small line segments across the line representing a carbide density band is intended to suggest visual width of the band. Thus the band lengths and widths are, on the average, largest on a section which, when extended, would include the cylinder axis.

The Charpy V-notch results are summarized in Fig. 2.28 and in Tables 2.14 and 2.15. Figure 2.28 also shows the results for Charpy V-notch

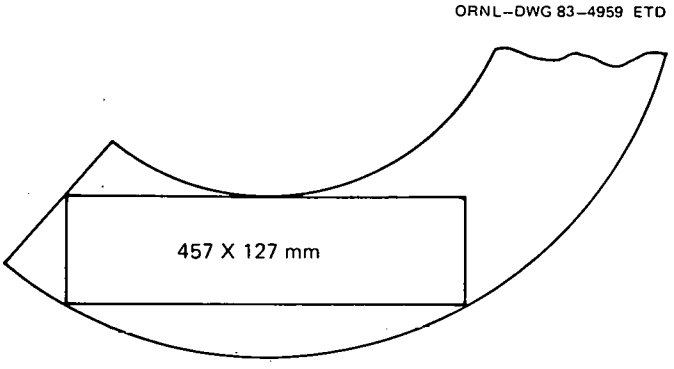

Fig. 2.26. Location of three-point bend specimen blanks relative to ORNL test cylinder.

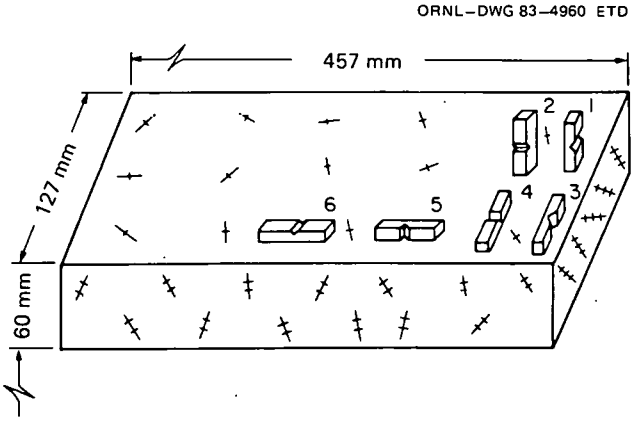

Fig. 2.27. Orientations of A508 Charpy V-notch specimens taken from the TPB specimen blank. Carbide density band widths and orientations are indicated in schematic fashion.

Table 2.14. Charpy V-notch test results at 15 ± 2°C for A508 steel tempered at 613°C

Specimen orientation[a]	Specimen No.	Impact energy (N/m)	Average impact energy (N/m)
1	1-3	56.7	68.4
	1-4	89.0	
2	2-3	62.4	52.4
	2-4	42.0	
4	4-3	47.5	46.8
	4 4	46.1	
5	5-3	54.2	48.1
	5-4	42.0	
6	6-3	40.7	35.3
	6-4	29.8	

[a]See Fig. 2.27.

Table 2.15. Charpy V-notch test results at 50 ± 2°C for A508 steel tempered at 613°C

Specimen orientation[a]	Specimen No.	Impact energy (N/m)	Average impact energy (N/m)
1	1-1	75.9	87.4
	1-2	98.9	
2	2-1	86.8	77.7
	2-2	80.0	
	2-5	66.4	
3	3-1	47.5	48.8
	3-2	61.0	
	3-3	37.9	
4	4-1	61.0	56.9
	4-2	70.5	
	4-5	39.3	
5	5-1	71.9	64.2
	5-2	51.5	
	5-2	69.2	
6	6-1	50.2	58.8
	6-2	61.0	
	6-3	65.1	

[a]See Fig. 2.27.

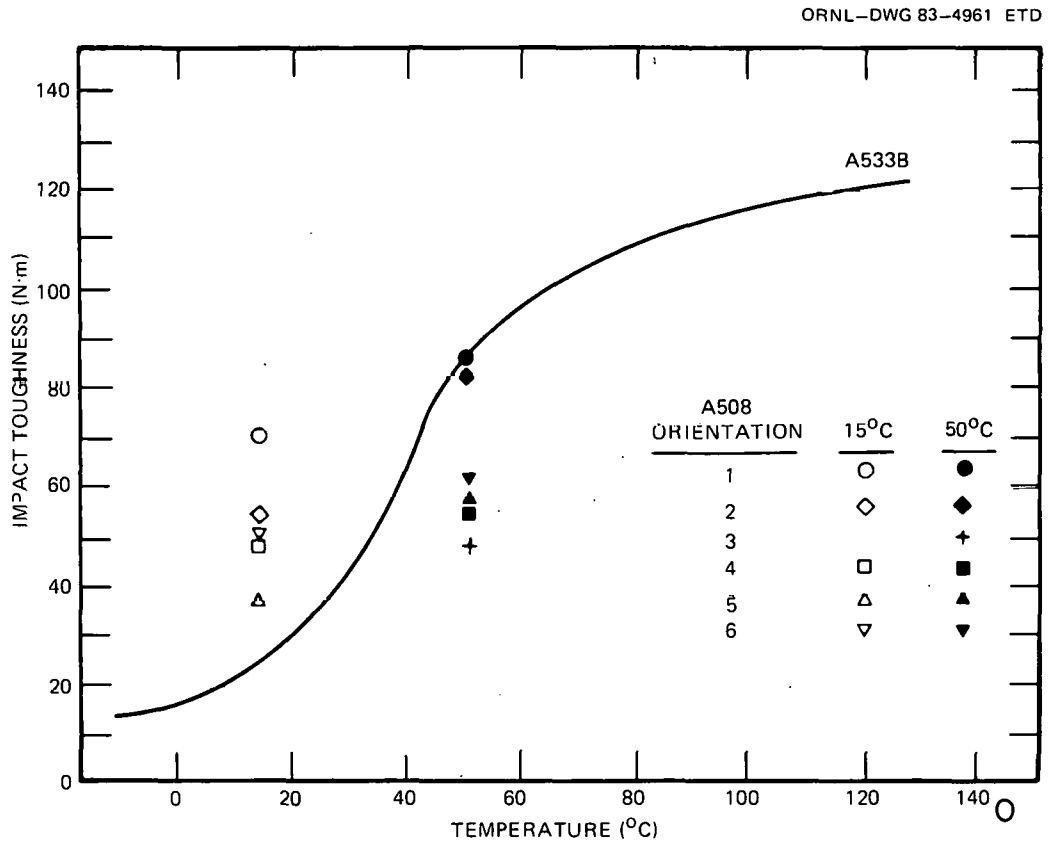

Fig. 2.28. Charpy V-notch impact energy as function of test temperature and specimen orientation for A508 specimens tested at 15 and 50°C.

specimens of A533B steel tested at the Naval Ship Research and Development Center, Annapolis. With some exceptions, of the five specimens available in each of the six orientations, two were tested at 15 ± 2°C, and three were tested at 50 ± 2°C. From inspections prior to testing, the tool used for notching the A508 Charpy V-notch specimens may have been overly worn. This feature was probably unimportant at the 50°C test temperature, but it should be considered with regard to the results at 15°C.

The results indicate that the fracture plane and direction for orientations 1 and 2 correspond to the largest toughness. The plane and direction of fracture for orientations 5 and 6 correspond, respectively, to through-the-thickness and lengthwise extension of an axial surface crack in the ORNL test cylinder. Relative to the carbide density bands, the A533B specimen corresponded to orientation 2 in Fig. 2.27. The results for orientations 3–6 correspond to a substantial transition temperature increase in comparison to results for orientations 1 and 2 and for A533B steel. Although the A508 Charpy V-notch results suggest existence of a relationship between toughness and carbide density bands, the fracture mechanisms basic to this relationship will require further study.

Microhardness tests were used to compare resistance with plastic deformation within and between carbide density bands. These tests were made on the surface having the orientation of the right face of the block shown in Fig. 2.27 and have been mentioned in previous reports. The results of these tests for A533B steel (679°C temper) and A508 steel (613°C temper) are given in Table 2.16.

Table 2.16. The comparison of hardnesses between A508 (tempered at 613°C) and A533B (tempered at 679°C)

A533B steel			A508 steel		
Microhardness (DPH)		Macrohardness (Knoop)	Microhardness (DPH)		Macrohardness (Knoop)
Dark band	Light band		Dark band	Light band	
266	197	212	375	307	279
282	225	226	380	293	285
260	205	235	390	323	278
261	220	206	377	315	292
		194			270
		227			285
		220			279
		227			280
		223			278
		225			291
		233			291
		227			289
		Mean values			
267	212	221	380	310	282

2.4.3 Fracture topology and microstructure

Additional comparison of fracture topology and microstructure were made using an A533B specimen fractured at 4°C. Figure 2.29 shows an SEM photograph of a portion of the fracture surface adjacent to the fatigue precrack. A cleavage initiation region is indicated by the circle A. After nickel plating, the specimen was sectioned normal to the fracture surface. The cut section was polished and etched to show both topology and microstructure appearance along the line E-E in Fig. 2.29. This result is shown in Fig. 2.30. The topology and microstructure along the line G-G were obtained in a similar manner, and this result is shown in Fig. 2.31. The fracture surface irregularities in this A533B specimen occur on a much smaller scale than those observed in specimens from a plate of 50-mm-thick A36 bridge steel, which has been used in this program for comparison purposes. This would be caused by the smaller grain size and carbide colonies in the A533B material.

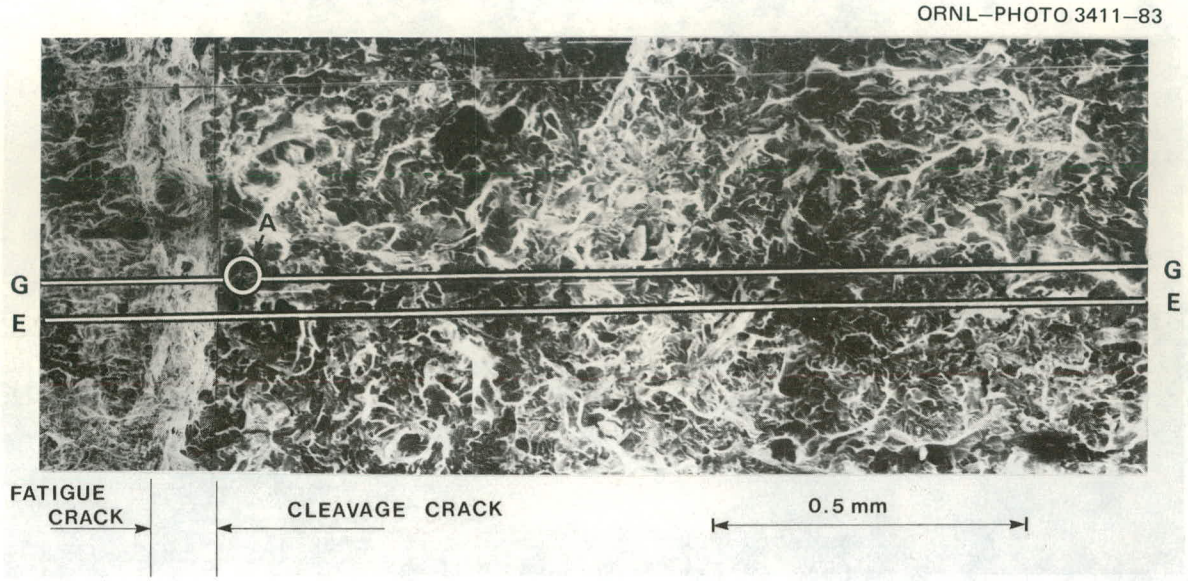

Fig. 2.29. SEM photograph of fracture surface near an apparent cleavage initiation site A. (A533B CT specimen tested at 4°C.)

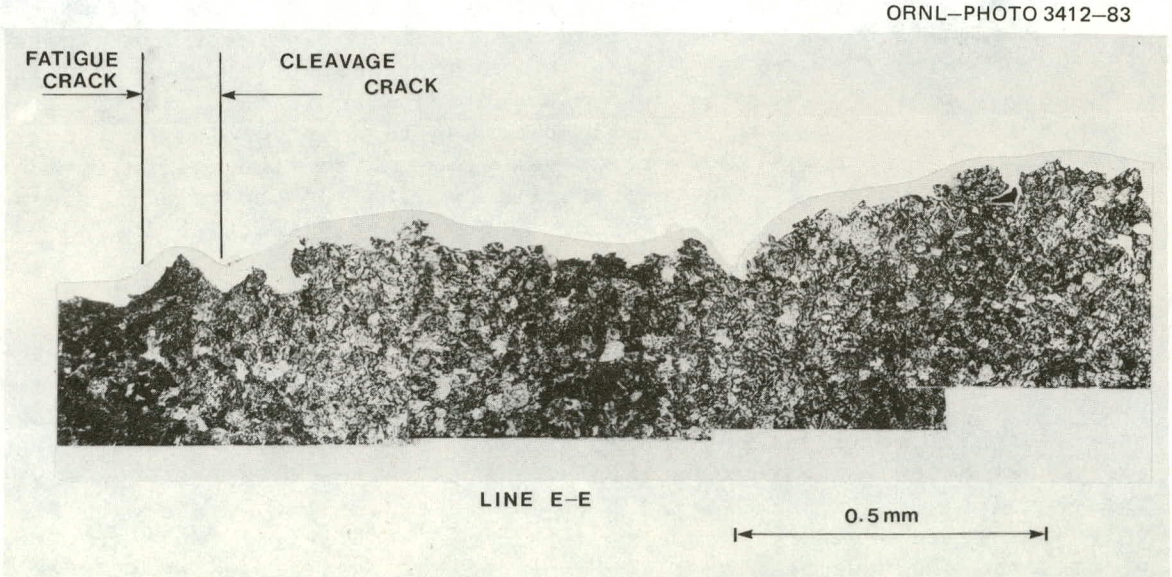

Fig. 2.30. Microstructure appearance on section along line E–E normal to fracture surface of Fig. 2.29.

In Figs. 2.30 and 2.31, one can see dark and light bands, corresponding to different levels of carbide density. Within these bands, carbide clusters occur in different sizes, often in a network formation. Numerous small-scale ductile fractures are observed in these section views, although the appearance of the fracture surface (Fig. 2.29) seems to be dominated by cleavage elements. From the section views, the fracture elements, which separated after substantial plastic deformation, are seen to

ORNL–PHOTO 3413–83

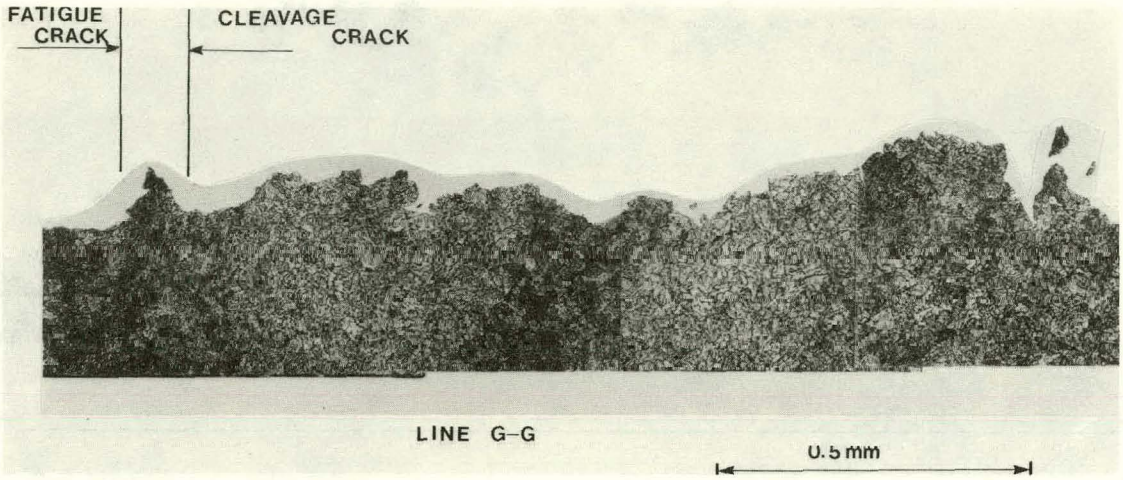

Fig. 2.31. Microstructure appearance on section along line G–G normal to fracture surface of Fig. 2.29.

be associated mainly with dark band regions and large carbide clusters. Figure 2.32(*a*) shows a region of fracture topology on line E–E close to region A of Fig. 2.29. This figure shows the undercutting cleavage (indicated as C) that subsequently deformed and resulted in the late-breaking regions (indicated by L.B.). A late-breaking ligament of larger size is shown in Fig. 2.32(*b*). This section was at 2 mm from the fatigue precrack on line E–E. Presumably the undercutting by adjacent cleavage elements, which produces a late-breaking ligament, occurs by preference in the regions of this nature.

To further understand cleavage fracture, it is of interest to observe the small cracks beneath the fracture surface. With the A36 steel fracture specimens, it was not difficult to find relatively tight cleavage cracks near but beneath the exposed fracture surface. A similar investigation with this A533B fracture specimen was less successful. However, in the lower right portion of Fig. 2.32(*b*), one can see small cleavage cracks extending through several ferritic grains. This is shown at larger scales in Fig. 2.33(*a* and *b*). The interruptions of cleavage, not only at a grain boundary, but also within a single grain, are indicative of the enhanced toughness of the microstructure relative to that of coarse-grained A36 steel. Presumably, the cleavage openings shown may have been substantially enlarged by plastic deformation during fracture of the large late-breaking ligament shown in Fig. 2.32(*b*).

2.4.4 Dynamic run-arrest calculations

Efforts towards improving our two-dimensional, dynamic finite-element code SAMCR have continued during the current report period. Sources of particular concern in the computer code results have been identified previously,[31,32] namely, the oscillations with time in the computed K values and the discontinuous changes in K that were associated with the shift of

ORNL–PHOTO 3414–83

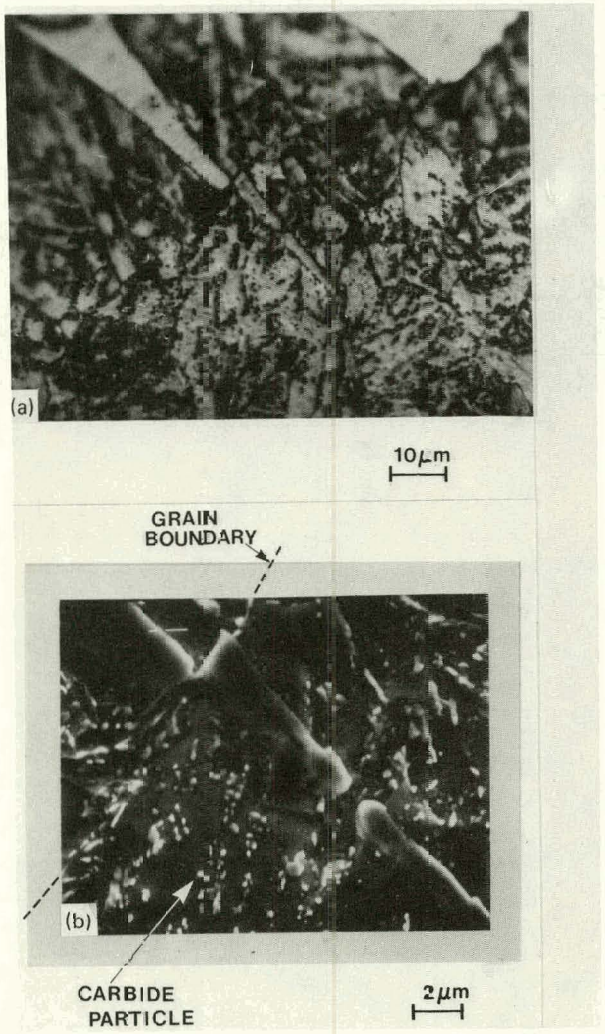

Fig. 2.32. Section along line E–E showing late-breaking ligament (L.B.) (*a*) near apparent cleavage initiation site shown in Fig. 2.29 and (*b*) approximately 2 mm from end of fatigue precrack.

ORNL–PHOTO 3415–83

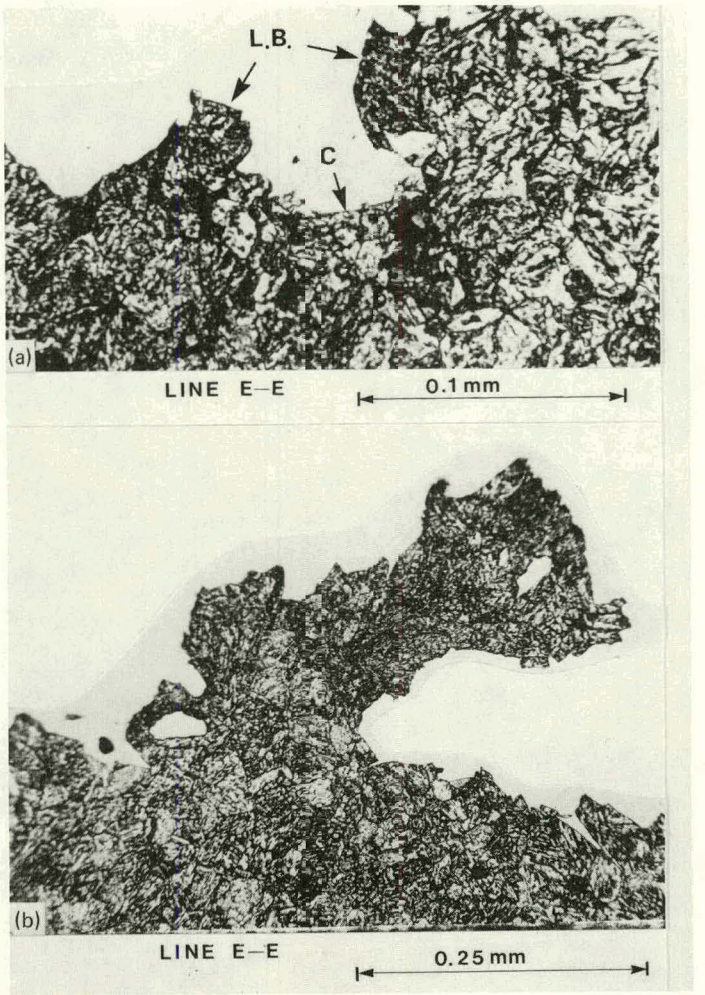

Fig. 2.33. Enlargement of lower right corner of Fig. 2.32(*b*): (*a*) showing an interrupted cleavage crack passing through ferritic grains below fracture surface and (*b*) further enlargement of Fig. 2.33(*a*).

the J-integral contour as the crack tip completed its advance from one node to the next.

The oscillatory value of the results was initially felt to be caused by the presence of countercyclical "keystone" or hourglass modes of deformation that were partially restrained in the original formulation by using an artificial keystone viscosity. This scheme was replaced by a stiffness correction method[33] that was found to work better. Figure 2.34(*a*) shows the K value computed at every time step for the first 150 μs of crack

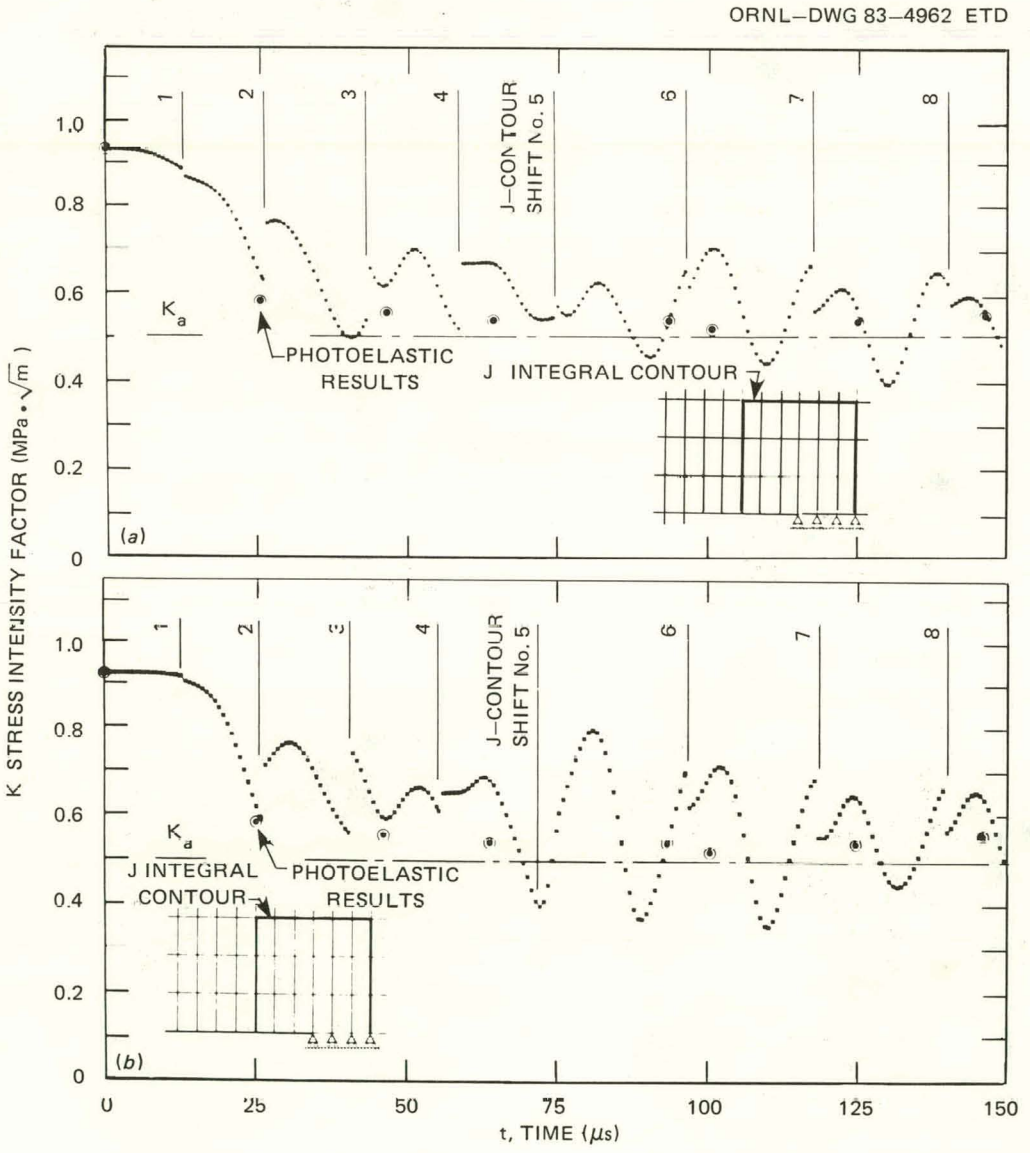

Fig. 2.34. K values calculated for test MCT1 (*a*) using original formulation of SAMCR (keystone and bulk viscosities) and J-contour shown and (*b*) using revised formulation of SAMCR (stiffness corrections, no bulk viscosity) and J-contour shown.

propagation in test MCT1, using the original formulation of SAMCR. Several such figures will be presented in this report, and in all cases, the times at which the J contour was shifted have been indicated. The photoelastically obtained results for the same test have also been shown. The K-t information obtained after incorporation of the stiffness correction (and elimination of the keystone viscosity) is shown in Fig. 2.34(*b*). In both cases, the K values follow essentially the same pattern of abrupt changes in K as the J contour moves, as well as an underlying oscillatory behavior. Figure 2.35(*a* and *b*) compares the predicted and observed crack extension behavior for the two cases, and there appears to be little difference in the results.

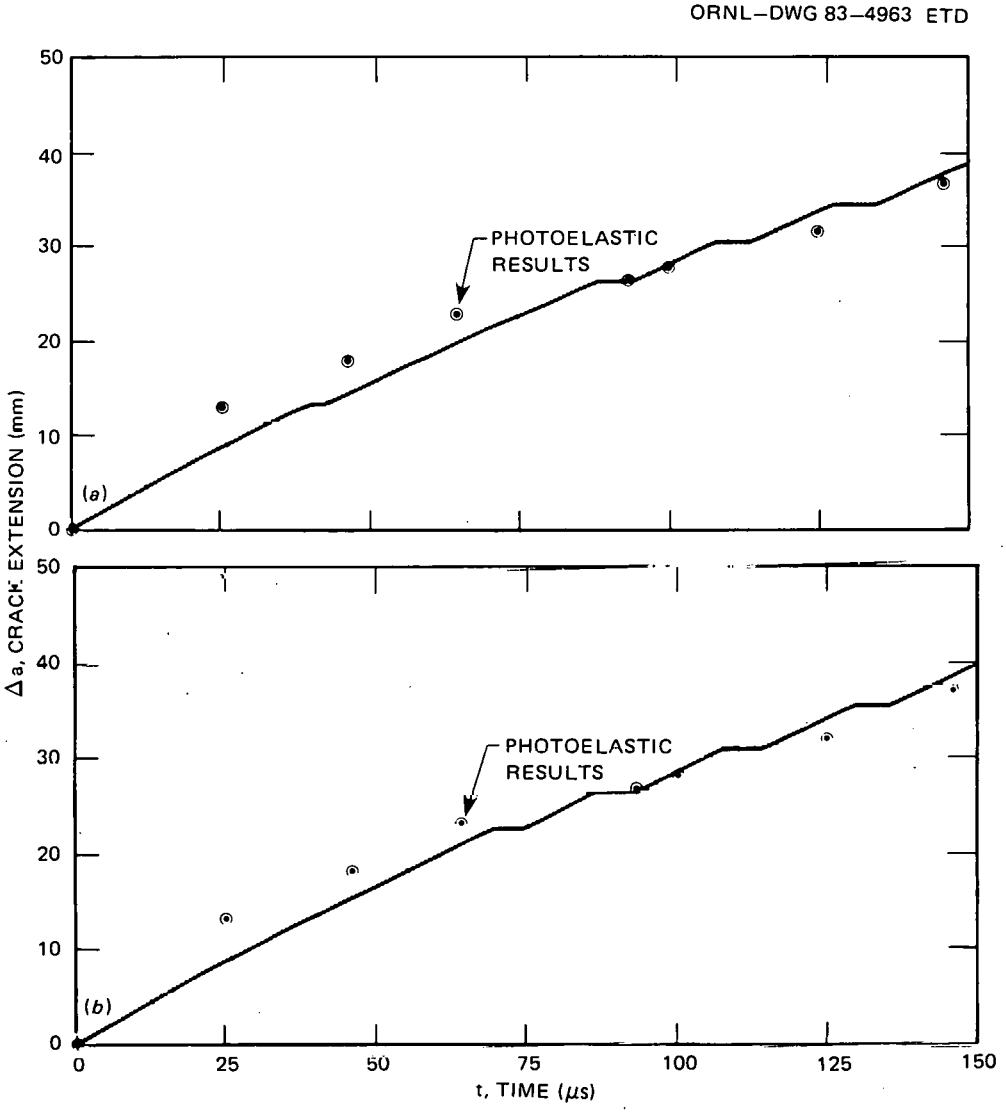

Fig. 2.35. Predicted crack-extension history (*a*) corresponding to Fig. 2.34(*a*) and (*b*) corresponding to Fig. 2.34(*b*).

A careful examination of the J integral computations led to a revision of the contour used,[30] and the corresponding K-t data are shown in Fig. 2.36(*a*). The abrupt changes in K with contour shift are seen to have decreased substantially in magnitude. However, the oscillations in K are still present, with larger amplitude but a visible period. Next, the bulk viscosity in the SAMCR formulation was reintroduced because this would help damp out any unwanted vibrations of the elements. (The bulk viscosity had been eliminated from the code at the same time that keystone viscosity was replaced with a stiffness correction.) The results obtained

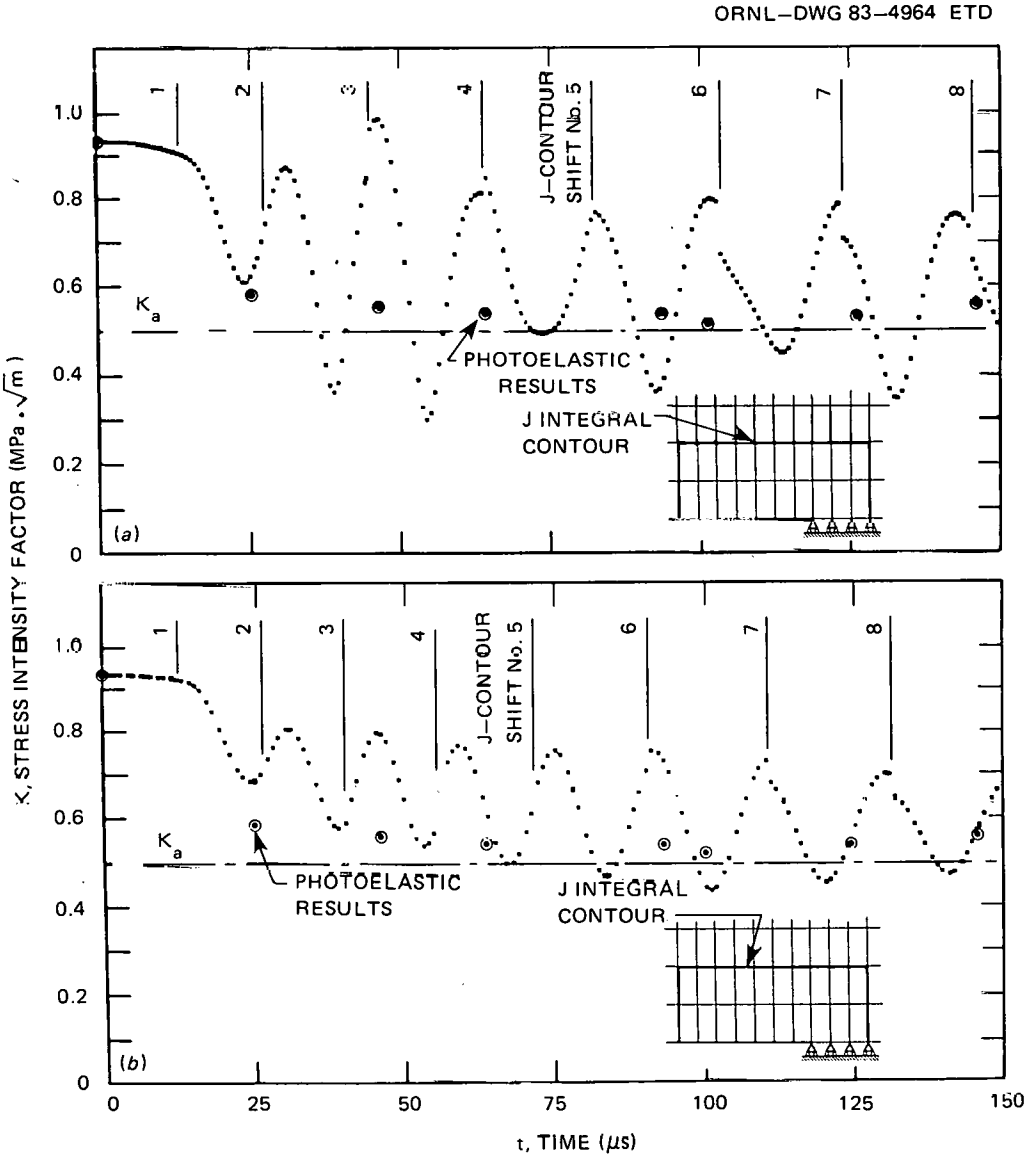

Fig. 2.36. K values calculated for test MCT1 using revised formulation of SAMCR (stiffness corrections) and revised J-contour shown (*a*) without bulk viscosity and (*b*) with bulk viscosity.

after this latest modification are shown in Fig. 2.36(*b*). Figure 2.37 (*a* and *b*) shows the crack extension predictions corresponding to Fig. 2.36 (*a* and *b*).

The results shown in Fig. 2.36(*b*) represent a substantial improvement over those presented previously. The K-t data show a much more regular behavior, with near-constant amplitude and period. It is still felt, however, that such oscillations do not represent physical reality, in particular, because we have seen little evidence of such phenomena in the many plastic model tests conducted in our dynamic photoelastic studies of run-arrest fracturing. Therefore, we intend to continue our critical appraisal of the formulations used in SAMCR and other finite-element codes to develop a computer code that will give reliable predictions of run-arrest phenomena.

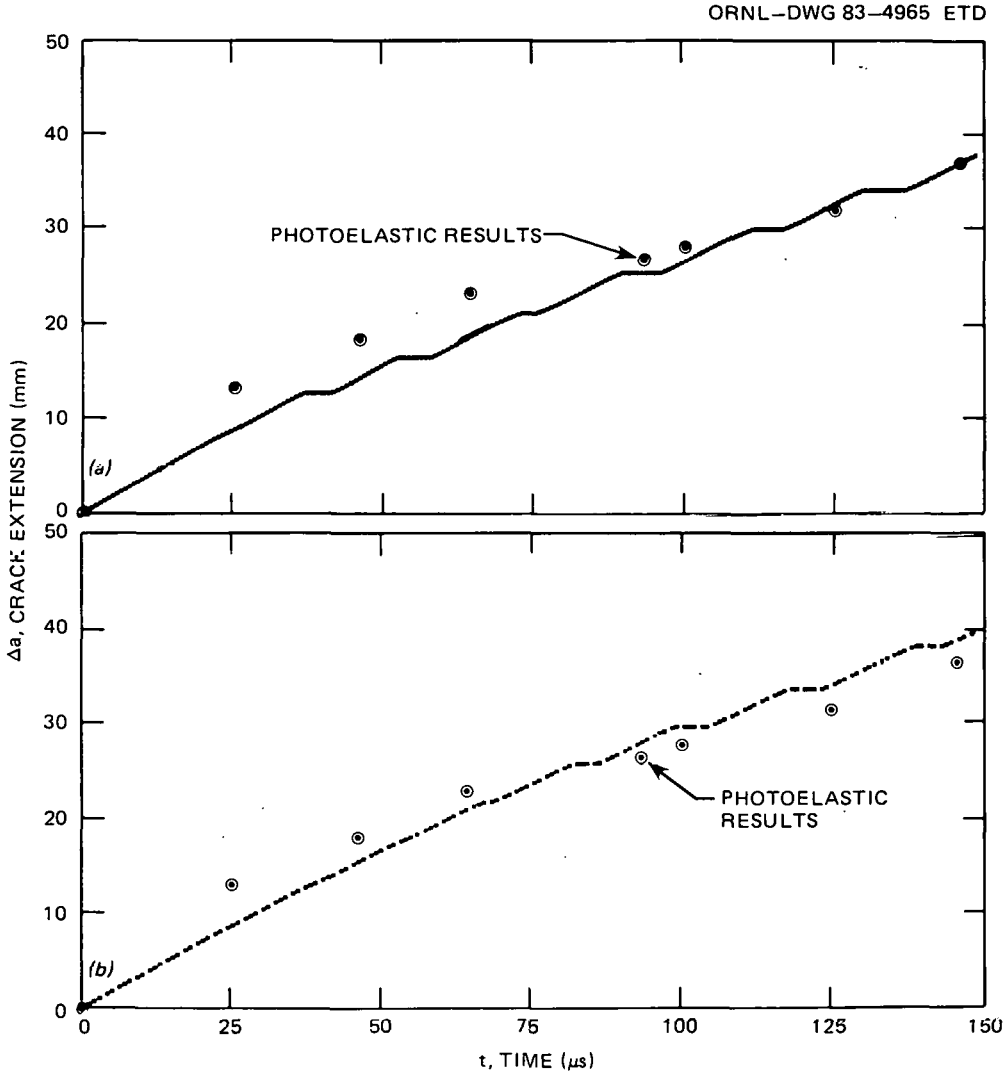

Fig. 2.37. Predicted crack-extension history (*a*) corresponding to Fig. 2.36(*a*) and (*b*) corresponding to Fig. 2.36(*b*).

2.4.5 Analysis in support of ESSO tests

Preliminary work has been started towards performing an analysis of ESSO-type tests, which are currently being investigated as a means of obtaining upper-shelf arrest-toughness data in a rising K_I field. The geometry analyzed using static finite elements was a single-edge-notched, center-pin-loaded specimen shown in Fig. 2.38. The basic features of this specimen geometry are the same as the ESSO specimen in that it is relatively long compared with its width, and it is usually tested in tension with a constant load applied remotely from the crack line.

Figure 2.39 shows the near-crack-tip portion of the finite-element mesh employed. Crack lengths ranging from a/w = 0.08 to a/w = 0.64 were studied with the same load being applied in all cases. The normalized y direction strain ε_{yy} was plotted for the first six rows of elements parallel to the crack line, and typical results from three crack lengths are shown in Fig. 2.40(*a*) (a/w = 0.167), (*b*) (a/w = 0.333), and (*c*) (a/w = 0.50). It was observed that the strain distributions showed a noticeable peak in the vicinity of the crack tip, with the sharpness of the peak diminishing as one moved away from the crack line.

These data were used to construct Fig. 2.41, which shows the strain read by two gages at fixed locations as the crack is extended past the gages in a quasi-static fashion. From these results it appears possible to use a double row of strain gages parallel to the crack line to obtain both crack-tip position and stress-intensity information in the ESSO tests. In the forthcoming quarter, we plan to (1) investigate other strain gage measuring schemes in an effort to optimize the sensitivity of the method and (2) utilize previously obtained dynamic photoelastic data to study the dynamic counterpart of the results described in this progress report.

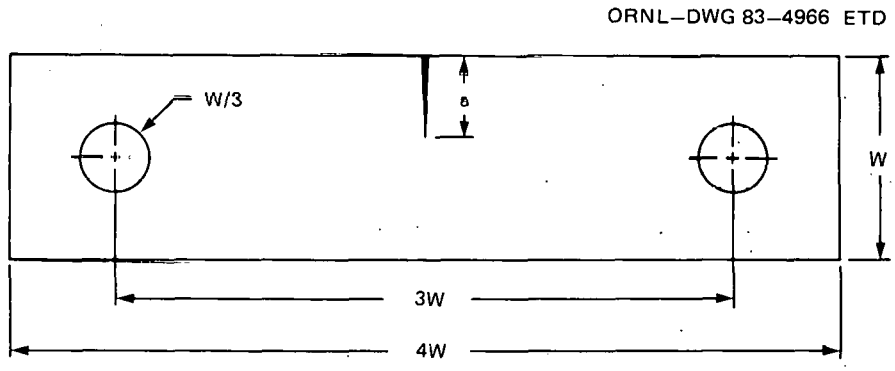

Fig. 2.38. Geometry of single-edge-notched specimen similar to ESSO specimen.

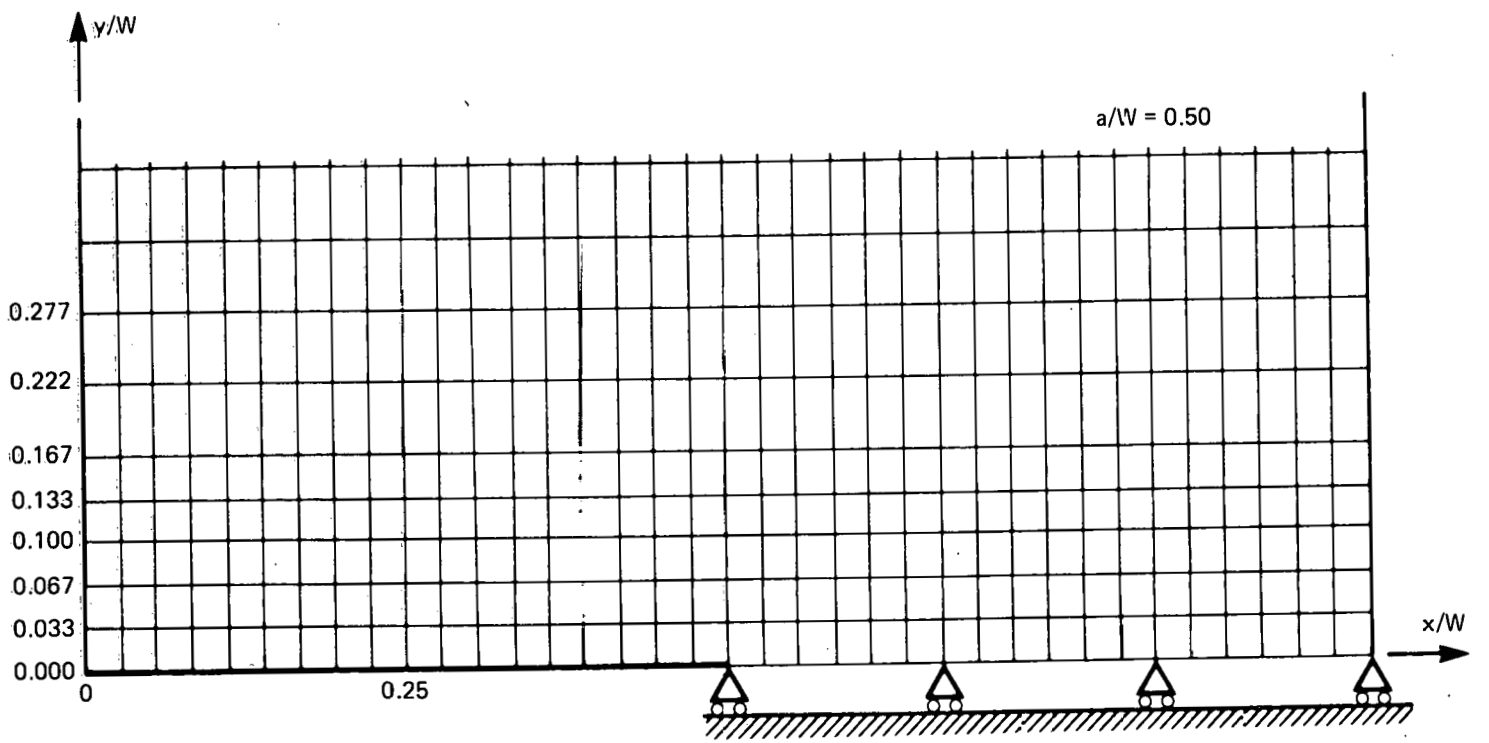

Fig. 2.39. Near-crack-tip portion of static finite-element mesh used to study strain distributions in SEN specimen.

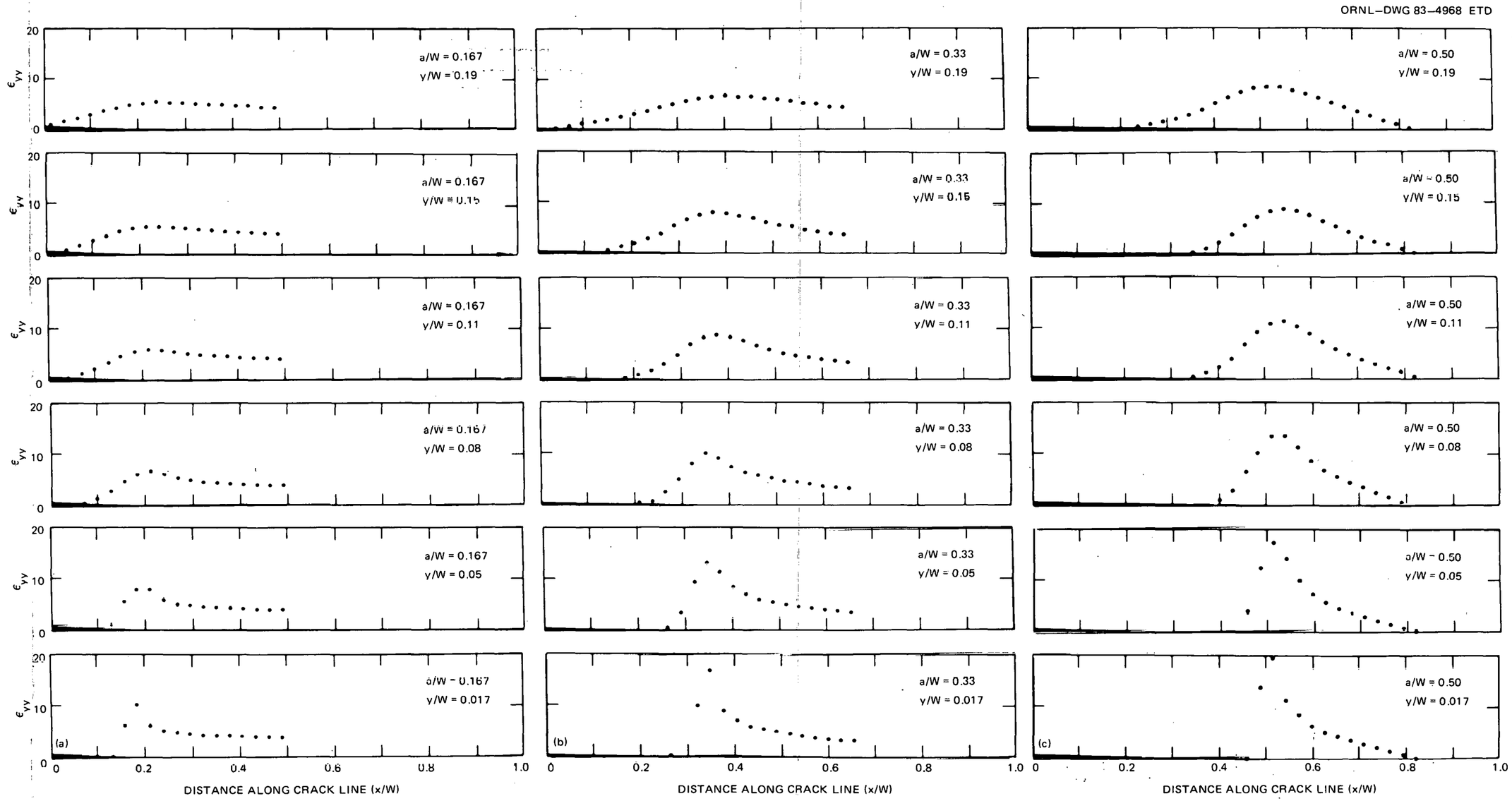

Fig. 2.40. Normal strain ε_{yy} at different distances from crack line (*a*) for a/w = 0.17, (*b*) for a/w = 0.33, and (*c*) for a/w = 0.50.

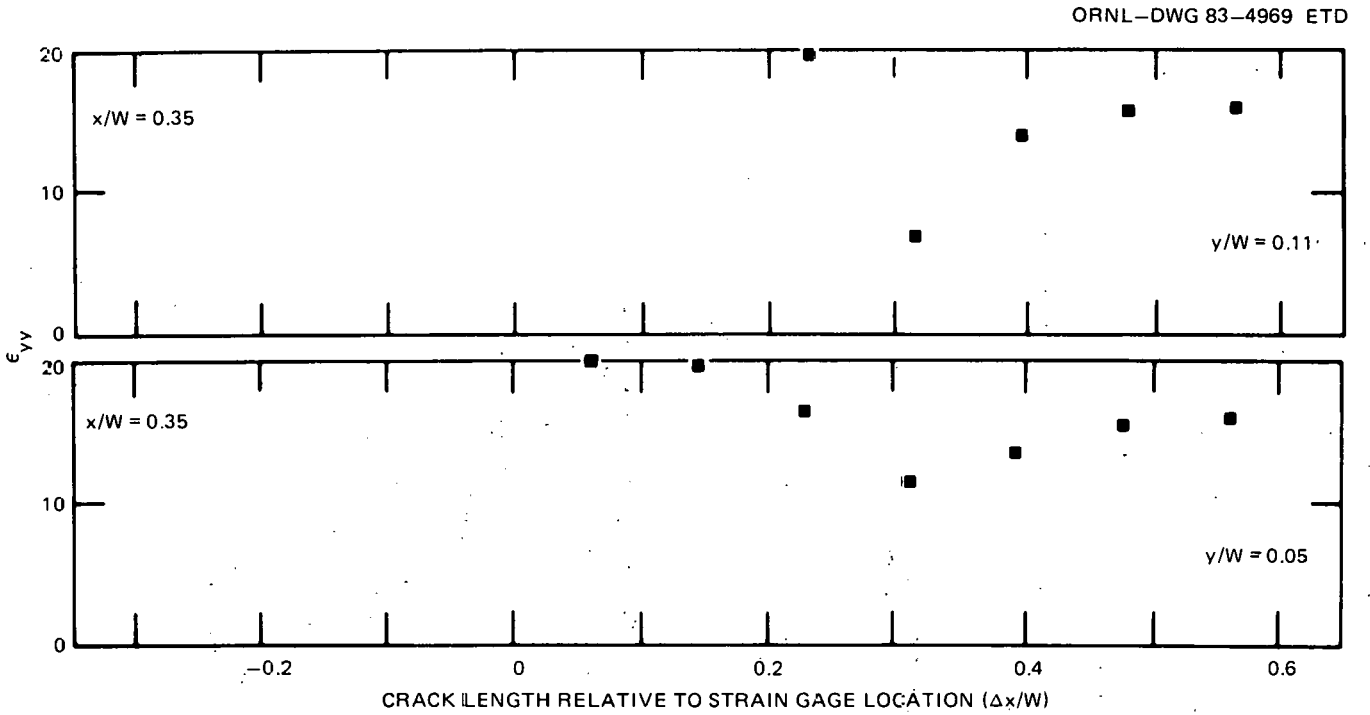

Fig. 2.41. Strains read by two gages located at x/w = 0.35 as crack extends past gage in a quasi-static fashion.

References

1. B. R. Bass et al., "Computational Methods for 3-D Nonlinear Fracture Mechanics," in *Heavy-Section Steel Technology Program Quart. Prog. Rep. January–March 1982*, NUREG/CR-2751, Vol. 1 (ORNL/TM-8369/V1), Union Carbide Corp. Nuclear Div., Oak Ridge Natl. Lab.

2. K. J. Bathe, *ADINA: A Finite Element Program for Automatic Dynamic Incremental Nonlinear Analysis*, Report 82448-1, Massachusetts Institute of Technology, 1975, revised 1978.

3. B. R. Bass and J. W. Bryson, *Applications of Energy Release Rate Techniques to Part-Through Cracks in Plates and Cylinders, Volume 2. ORVIRT: A Finite Element Program for Energy Release Rate Calculations for 2-D and 3-D Crack Models*, NUREG/CR-2997, Vol. 2 (ORNL/TM-8527/V2), Union Carbide Corp. Nuclear Div., Oak Ridge Natl. Lab., February 1983.

4. H. G. deLorenzi and C. F. Shih, *Finite Element Implementation of the Deformation Theory of Plasticity*, TIS Report 80CRD058, General Electric Company, April 1980.

5. R. A. Ainsworth, B. K. Neale, and R. H. Price, *Fracture Behavior in the Presence of Thermal Strains*, Report RD/B/N4152, Central Electricity Generating Board, Research Division, Berkeley Nuclear Laboratories, November 1977.

6. R. S. Barsoum, "Triangular Quarter-Point Elements as Elastic and Perfectly Plastic Crack Tip Elements," *Int. J. Numer. Methods Engr.* 11, 85–98 (1977).

7. A. R. Rosenfield and P. N. Mincer, "Reinitiation of an Arrested Cleavage Crack," in *Engineering Fracture Mechanics*, in press (1983).

8. A. R. Rosenfield et al., "BCL HSST Support Program," in *Heavy-Section Steel Technology Program Quart. Prog. Rep. April–June 1982*, NUREG/CR-2751, Vol. 2 (ORNL/TM-8369/V2), Union Carbide Corp. Nuclear Div., Oak Ridge Natl. Lab.

9. A. R. Rosenfield et al., "BCL HSST Support Program," in *Heavy-Section Steel Technology Program Quart. Prog. Rep. July–September 1982*, NUREG/CR-2751, Vol. 3 (ORNL/TM-8369/V3), Union Carbide Corp. Nuclear Div., Oak Ridge Natl. Lab.

10. F. M. Beremin, "Numerical Modelling of Warm Prestress Effect Using a Damage Function for Cleavage Fracture," *Advances in Fracture Research* 2, 825–32 (1981).

11. R. O. Ritchie, J. F. Knott, and J. R. Rice, "On the Relationship Between Critical Tensile Stress and Fracture Toughness in Mild Steel," *J. Mech. Phys. Solids* 21, 395–410 (1973).

12. K. Ogawa et al., "Microstructural Aspects of the Fracture Toughness Cleavage-Fibrous Transition for Reactor Grade Steel," presented at the 15th National Fracture Mechanics Symposium, University of Maryland, College Park, Md., 1982.

13. A. Melander and J. Steninger, "The Role of Sulphides, Oxides, and Pearlite in the Ductile Fracture of a Niobium Microalloyed Steel," *Mater. Sci. Eng.* 52, 239–48 (1982).

14. D. A. Curry and J. F. Knott, "Effect of Microstructure on Cleavage Fracture Toughness of Quenched and Tempered Steels," *Met. Sci.* 13, 341–45 (1979).

15. A. R. Rosenfield et al., "BCL HSST Support Program," in *Heavy-Section Steel Technology Program Quart. Prog. Rep. October–December 1982*, NUREG/CR-2751, Vol. 4 (ORNL/TM-8369/V4), Union Carbide Corp. Nuclear Div., Oak Ridge Natl. Lab.

16. G. T. Hahn et al., "Fast Fracture Toughness and Crack Arrest Toughness of Reactor Pressure Vessel Steel," pp. 289–320 in *Crack-Arrest Methodology and Applications: A Symposium*, ASTM STP 711, 1980.

17. W. L. Fourney, "Investigation of Damping and of Cleavage-Fibrous Transition in Reactor Grade Steel," in *Heavy-Section Steel Technology Program Quart. Prog. Rep. October–December 1981*, NUREG/CR-2141, Vol. 4 (ORNL/TM-8252), Union Carbide Corp. Nuclear Div., Oak Ridge Natl. Lab.

18. P. B. Crosley and E. J. Ripling, "Crack-Arrest Studies," NP-1225, Electric Power Research Institute, 1979.

19. R. D. Cheverton et al., "Application of Crack Arrest Theory to a Thermal Shock Experiment," pp. 392–421 in *Crack Arrest Methodology and Applications: A Symposium*, ASTM STP 711, 1980.

20. F. J. Witt, *Static Crack Arrest, K_{Ia}, Determined from Pop-In Arrest and Tearing Arrest*, WCAP 9786, Westinghouse Electric Corporation, 1980.

21. P. B. Crosley et al., *Final Report on the Cooperative Test Program on Crack-Arrest Toughness Measurement*, to be issued by NRC (1983).

22. A. R. Rosenfield et al., *Critical Experiments, Measurements, and Analyses to Establish a Crack Arrest Methodology for Nuclear Pressure Vessel Steels*, NUREG/CR-1887 (BMI-2071), Battelle Memorial Institute, 1981.

23. A. R. Rosenfield et al., "BCL HSST Support Program," in *Heavy-Section Steel Technology Program Quart. Prog. Rep. January–March 1982*, NUREG/CR-2751, Vol. 1 (ORNL/TM-8369/V1), Union Carbide Corp. Nuclear Div., Oak Ridge Natl. Lab.

24. A. R. Rosenfield et al., "BCL HSST Support Program," in *Heavy-Section Steel Technology Program Quart. Prog. Rep. July–September 1981*, NUREG/CR-2141, Vol. 3 (ORNL/TM-8145), Union Carbide Corp. Nuclear Div., Oak Ridge Natl. Lab.

25. T. A. Bishop, A. J. Markworth, and A. R. Rosenfield, "Analyzing Statistical Variability of Fracture Properties," *Metallurgical Transactions A* (in press).

26. T. A. Bishop, "Estimation of Weibull Percentiles Using the Method of Iterated Least Squares," submitted to *Technometrics* (1983).

27. R. D. Cheverton et al., "Fracture Mechanics Data Deduced from Thermal Shock and Related Experiments with LWR Pressure Vessel Material," pp. 1–15 in *Aspects of Fracture Mechanics in Pressure Vessels and Piping*, ASME Publ. PVP 58, 1982.

28. A. R. Rosenfield et al., *Critical Experiments, Measurements, and Analyses to Establish a Crack-Arrest Methodology for Nuclear-Pressure-Vessel Steels*, NUREG/CR-1555 (BMI-2064), Battelle Memorial Institute, 1980.

29. T. Kanazawa et al., "Study on Fast Fracture and Crack Arrest," *Exp. Mech.* 21, 78–88 (February 1981).

30. W. L. Fourney et al., "Investigation of Damping and of the Cleavage-Fibrous Transition in Reactor-Grade Steel," pp. 29–55 in *Heavy-Section Steel Technology Program Quart. Prog. Rep. October–December 1982*, NUREG/CR-2751, Vol. 4 (ORNL/TM-8369/V4), Union Carbide Corp. Nuclear Div., Oak Ridge Natl. Lab.

31. W. L. Fourney, "Dynamic Run-Arrest Calculations," pp. 53–59 in *Heavy-Section Steel Technology Program Quart. Prog. Rep. April–June 1982*, NUREG/CR-2751, Vol. 2 (ORNL/TM-8369/V2), Union Carbide Corp. Nuclear Div., Oak Ridge Natl. Lab.

32. W. L. Fourney, "Dynamic Run-Arrest Calculations," pp. 49–55 in *Heavy-Section Steel Technology Program Quart. Prog. Rep. July–September 1982*, NUREG/CR-2751, Vol. 3 (ORNL/TM-8369/V3), Union Carbide Corp. Nuclear Div., Oak Ridge Natl. Lab.

33. D. Kosloff and G. A. Frazier, "Treatment of Hourglass Patterns in Low Order Finite Element Codes," *Int. J. Num. Anal. Meth. Geomech.* 2, 57–72 (1978).

3. INVESTIGATION OF IRRADIATED MATERIALS

3.1 Fourth HSST Irradiation Series

R. G. Berggren R. K. Nanstad
T. N. Jones

The cooperative testing program[1] on specimens from the first three capsules of the Fourth Heavy-Section Steel Technology (HSST) Irradiation Study is in progress. In this program, Charpy V-notch impact tests and fracture-toughness tests on 1TCS specimens are divided between two organizations — Oak Ridge National Laboratory (ORNL) and Materials Engineering Associates (MEA). The Charpy V-notch tests on unirradiated (control) specimens by the two organizations are essentially completed. Charpy V-notch tests of "unassigned" unirradiated specimens will be conducted after the results obtained to date have been studied. Scoping tests on irradiated Charpy V-notch specimens have been completed at the two facilities, and test temperatures for the main test series have been assigned. These tests should be completed during the next quarter. Scoping tests on unirradiated fracture-toughness (1TCS) specimens should also be completed in the next quarter. Irradiated Charpy V-notch specimens (84) and some irradiated 1TCS specimens (20) were delivered to MEA in January, and the remainder of the irradiated specimens should be shipped to MEA in April 1983. Staff members from ORNL and MEA will meet in April to agree on test procedures and data analysis methods for the fracture-toughness testing.

Statistical analyses have been conducted for the Charpy V-notch test results obtained at the two facilities on unirradiated specimens of the SA533 grade B class 1 plate (HSST plate 02) and on three submerged-arc welds (HSST welds 69W, 70W, and 71W), and there is excellent agreement between the two data sets.[1] Unirradiated HSST weld 68W was not included in this comparison because of insufficient specimens for statistical analysis. ORNL is considering the possibility of reconstituting tested specimens to provide sufficient test data for statistical analysis.

Results of the statistical analyses are presented in Table 3.1. Mean energy values and standard deviations (σ) for each material and test temperature were calculated for each facility and for the combined data sets. The differences in mean energies ($\bar{x}$) for the two facilities were $<1\ \sigma$ from the combined mean energy in each case. Mean energies for the Charpy V-notch transition region tended to be higher (0 to 7 J) in ORNL results than in MEA results, but MEA results tended to be higher (up to 15 J) than ORNL results for the Charpy V-notch upper-shelf region. However, these differences are probably not statistically significant. There is no apparent pattern of standard deviations in the data from the two facilities. In the transition region, the largest standard deviations were for weld metals tested high in the transition region. This was expected because the Charpy V-notch curve is steepest in this region. In the upper-shelf region, the largest standard deviations were for weld metals tested at 288°C.

Hyperbolic tangent curves were fitted to the Charpy data (including data from scoping tests), and the results are presented in Figs. 3.1–3.4.

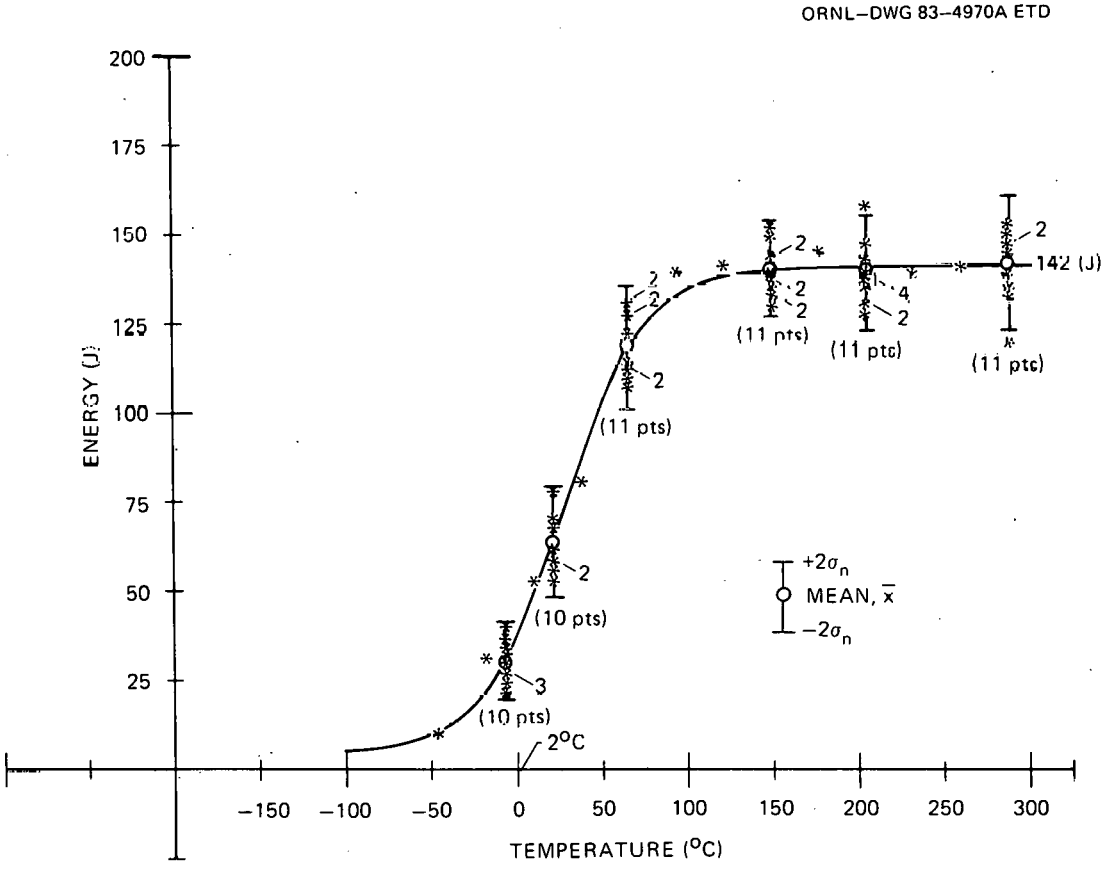

Fig. 3.1. Charpy V-notch impact test results for unirradiated SA533 grade B class 1 steel plate (HSST plate 02).

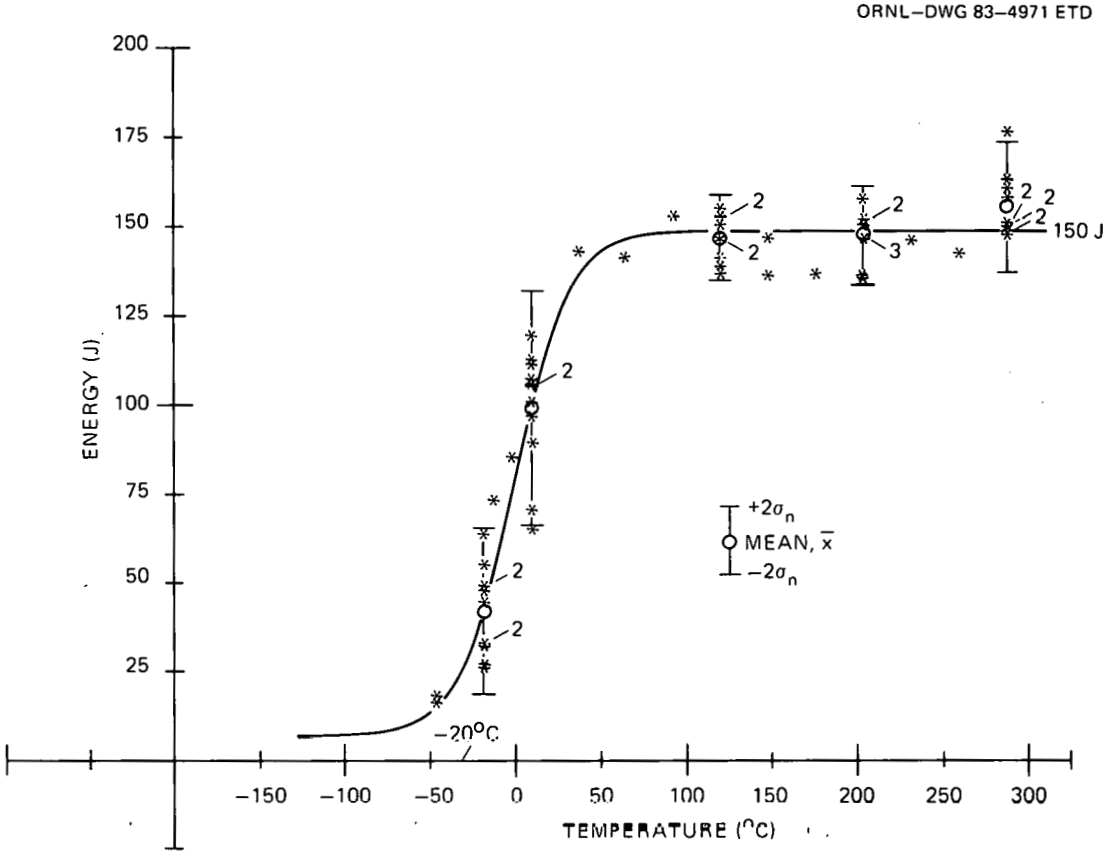

Fig. 3.2. Charpy V-notch impact test results for unirradiated submerged-arc weld (HSST weld 69W): 0.12% Cu, Linde 091 flux.

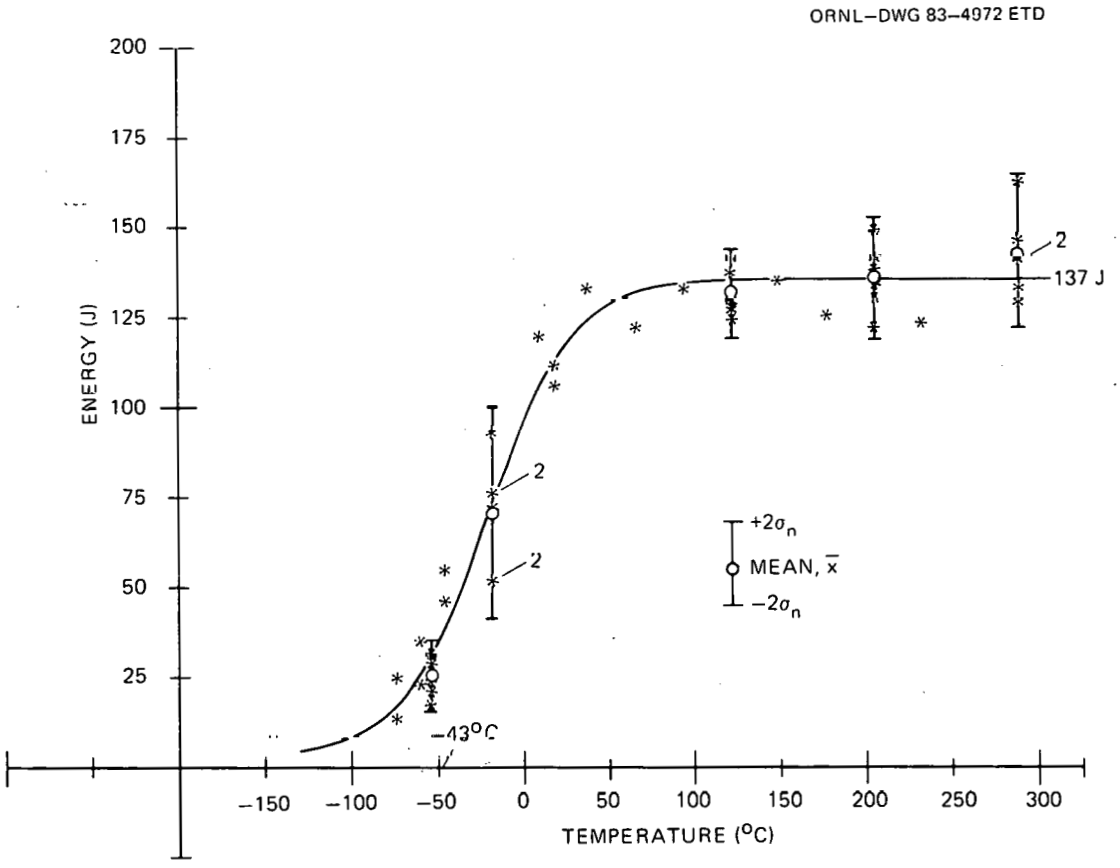

Fig. 3.3. Charpy V-notch impact test results for unirradiated submerged-arc weld (HSST weld 70W); 0.056% Cu, Linde 0124 flux.

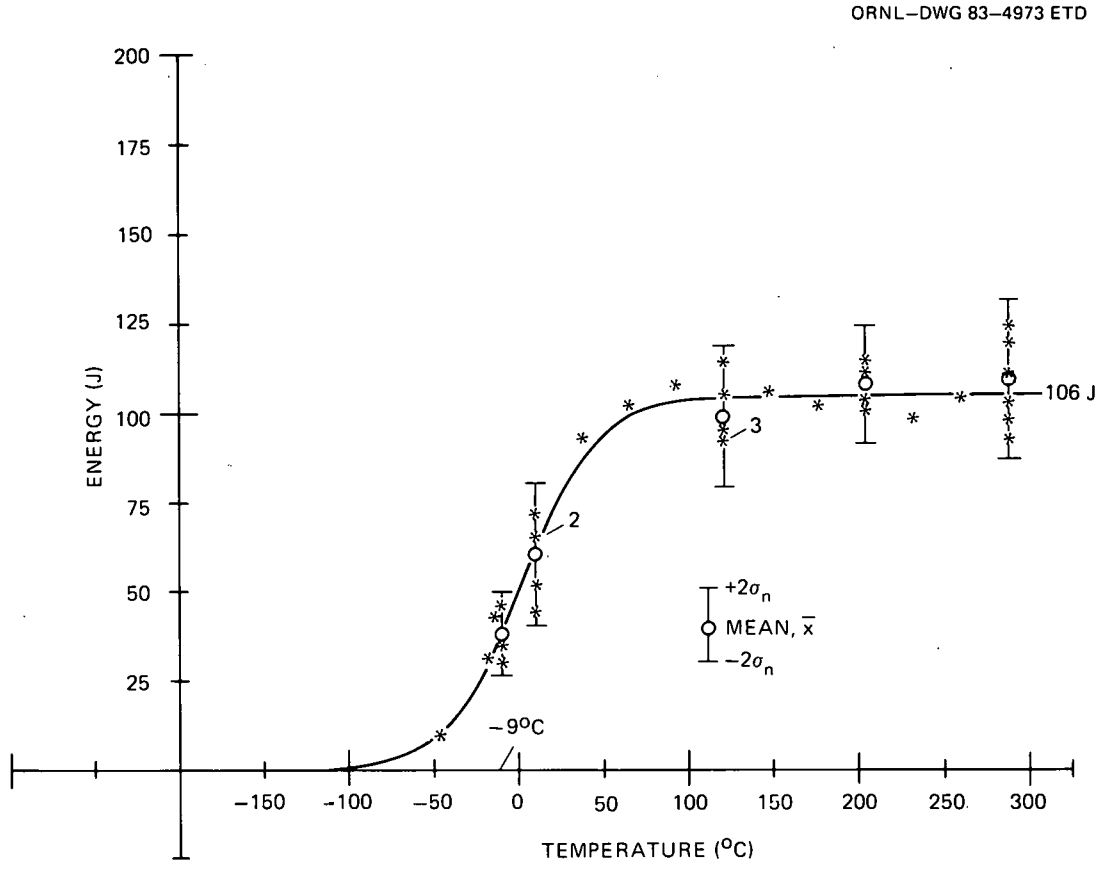

Fig. 3.4. Charpy V-notch impact test results for unirradiated submerged-arc weld (HSST weld 71W); 0.040% Cu, Linde 0.80 flux.

Table 3.1. Comparison of Charpy impact test results for unirradiated pressure vessel plate and submerged-arc welds from ORNL and MEA

Material	Test temperature (°C)	Mean energy ($\bar{x}$) (J)			Standard deviation (σ_n) (J)			Number of tests	
		ORNL	MEA	Combined	ORNL	MEA	Combined	ORNL	MEA
A533 grade B class 1 (HSST 02)	−7	31.5	28.7	30.1	5.0	5.7	5.5	5	5
	21	64.8	61.3	63.0	7.9	7.2	7.7	5	5
	66	119.7	116.9	118.5	8.2	8.9	8.6	6	5
	149	143.0	135.6	139.6	5.8	4.9	6.6	6	5
	204	138.4	138.3	138.3	5.1	10.6	8.1	6	5
	288	137.9	145.9	141.5	10.6	3.9	9.2	6	5
Submerged-arc weld (HSST 69W)	−18	41.9	41.2	41.6	12.7	10.5	11.7	6	5
	10	98.7	98.2	98.4	14.5	17.8	16.4	5	6
	121	144.0	148.9	146.4	6.1	4.7	6.0	5	5
	204	143.0	151.2	146.7	6.7	4.0	6.9	5	4
	288	147.8	161.3	154.6	1.5	8.5	9.1	5	5
Submerged-arc weld (HSST 70W)	−54	25.8	24.4	24.9	4.1	5.5	5.0	2	3
	−18	73.5	66.4	70.0	16.9	10.7	14.6	3	3
	121	131.9	129.8	130.8	6.5	5.2	6.0	3	3
	204	131.9	140.1	136.0	7.1	7.8	8.5	3	3
	288	134.2	150.1	142.1	5.1	9.2	10.9	3	3
Submerged-arc weld (HSST 71W)	−9	38.0	37.3	37.7	8.1	2.0	5.9	2	2
	10	60.6	58.3	59.7	11.5	6.8	10.0	3	2
	121	99.4	97.2	98.3	10.2	5.2	8.2	3	3
	204	102.6	111.6	107.1	1.7	1.7	4.8	3	3
	288	99.9	115.2	107.5	7.4	8.8	11.2	3	3

In these figures we have also indicated mean energies and 2-σ limits for the combined data sets. Several observations, based on these figures, may be made: (1) Mean energies for all sets are within 1 σ of the hyperbolic tangent curves. (2) Straight-line interpolation between mean energies near 40.7 J gave 40.7-J transition temperatures within 2.6°C of those obtained from the hyperbolic tangent curve. (3) The 2-σ limits for data sets around a 40.7-J transition temperature represent 2-σ limits of ±10 to ±15°C in determining the 40.7-J transition temperature. This should represent the probable error in determining transition temperature with a limited number of tests. (4) Probable errors (2 σ) in determining upper-shelf energy could be 23 J (or 20%).

Similar analyses of the results of tests on irradiated specimens are planned when the data become available.

3.2 Irradiation-Induced K_{Ic} Curve Shift

R. G. Berggren R. K. Nanstad

The philosophy, materials, and specimen complements for this study were presented in previous reports.[2,3] Negotiations for weldment fabrication are essentially complete, and placement of the purchase order is expected in April.

Work on the prototype 4TCS capsule is proceeding, with a June date set for tests at the Oak Ridge Research Reactor.

3.3 Irradiated Stainless Steel Cladding

R. G. Berggren R. K. Nanstad
W. R. Corwin

This task, discussed previously,[4,5] is to determine the fracture-toughness properties of irradiated stainless steel vessel cladding. The first experiment will be the irradiation of Charpy V-notch specimens from type 309/308 three-layer cladding deposited by the single-wire series-arc process. Both the first-layer (type 309) and the upper-layer (type 308) material is to be irradiated. A contract has been placed with MEA for capsule construction and irradiation at the Nuclear Science and Technology Facility at the State University of New York in Buffalo. Specimens for this irradiation experiment have been prepared and will be shipped to MEA in April 1983.

During preliminary Charpy impact testing of unirradiated specimens, differences were found between two sets of specimens that were supposedly cut from the top layer (type 308) of weld material (see Fig. 3.5). The

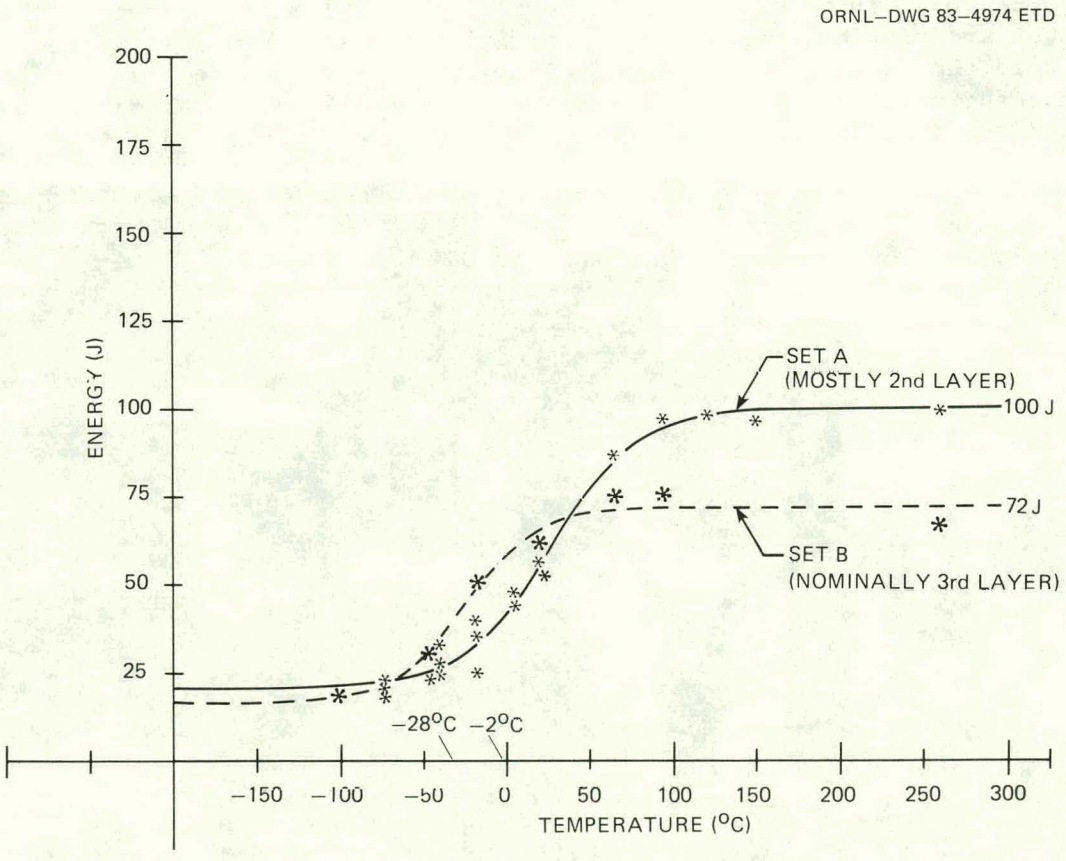

Fig. 3.5. Charpy V-notch impact test results for unirradiated upper layers of three-layer stainless steel cladding (type 309/308, single-wire series-arc process).

preparation of these specimens differed only in the sequence of machining operations. One group of specimens, set A, was prepared by machining the cladding surface to eliminate surface irregularities; cutting a slab of cladding, of Charpy V-notch thickness, parallel to the surface; and machining Charpy specimens. The second group of specimens, set B, was prepared by cutting slabs perpendicular to the cladding surface, etching to reveal the weldment structure, and marking and machining specimens as close to the original top surface as possible. Figure 3.5 shows the differences in Charpy impact test results for the two sets of specimens when hyperbolic tangent curves are fitted to the data. Differences were also noted in the appearance of the fracture faces for the two sets of specimens (see Fig. 3.6). Specimens from set A appeared to consist of two layers of weld cladding, while set B appeared to consist primarily of a single layer of cladding. Metallographic examinations have been carried out on the specimens shown in Fig. 3.6, which had been tested at −18°C. The fracture path in the specimen from set A started in second-layer material and ended in third-layer material, with most of the fracture being in the second-layer material. However, the fracture path in the specimen from set B lay entirely in the third-layer (top) material. All top-layer (type 308) cladding specimens for the irradiation experiment were prepared by the same method used for preparing set B specimens.

Specimens representing first-layer (type 309) material were machined by the same procedure described above for set B specimens, with care taken to avoid the juncture of adjacent first-layer passes where a cusp occurs at the fusion line with the base metal. The results of preliminary Charpy impact tests on this material are presented in Fig. 3.7, and a hyperbolic

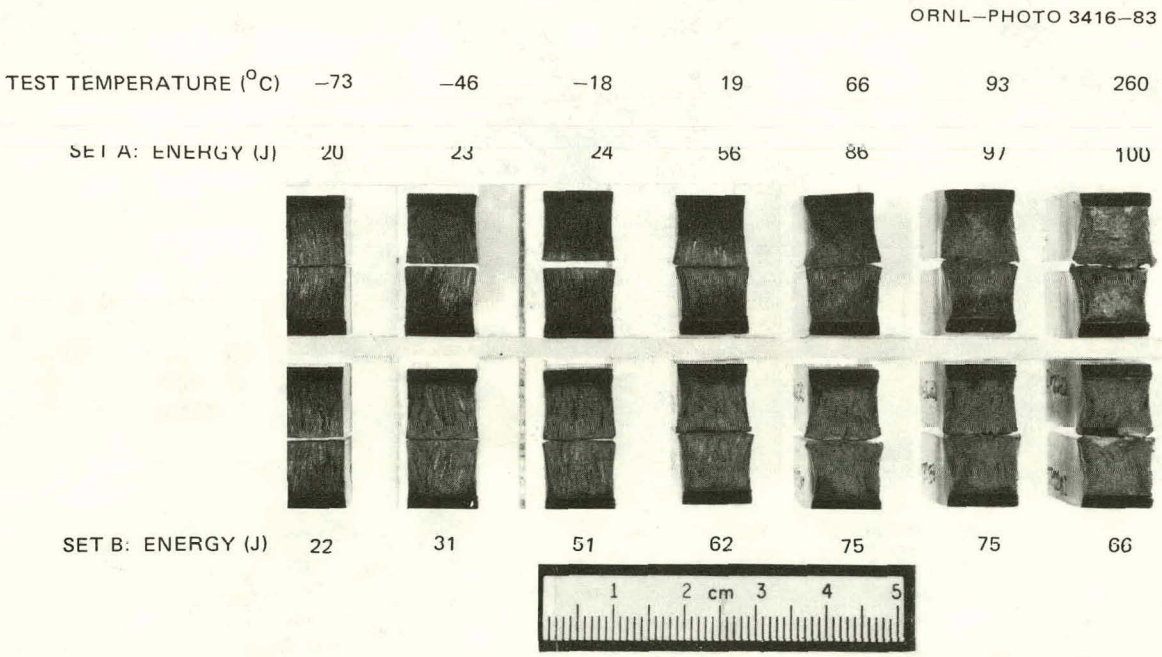

Fig. 3.6. Fracture appearance of Charpy impact test specimens from upper layer of three-layer stainless steel cladding (type 309/308, single-wire submerged-arc process).

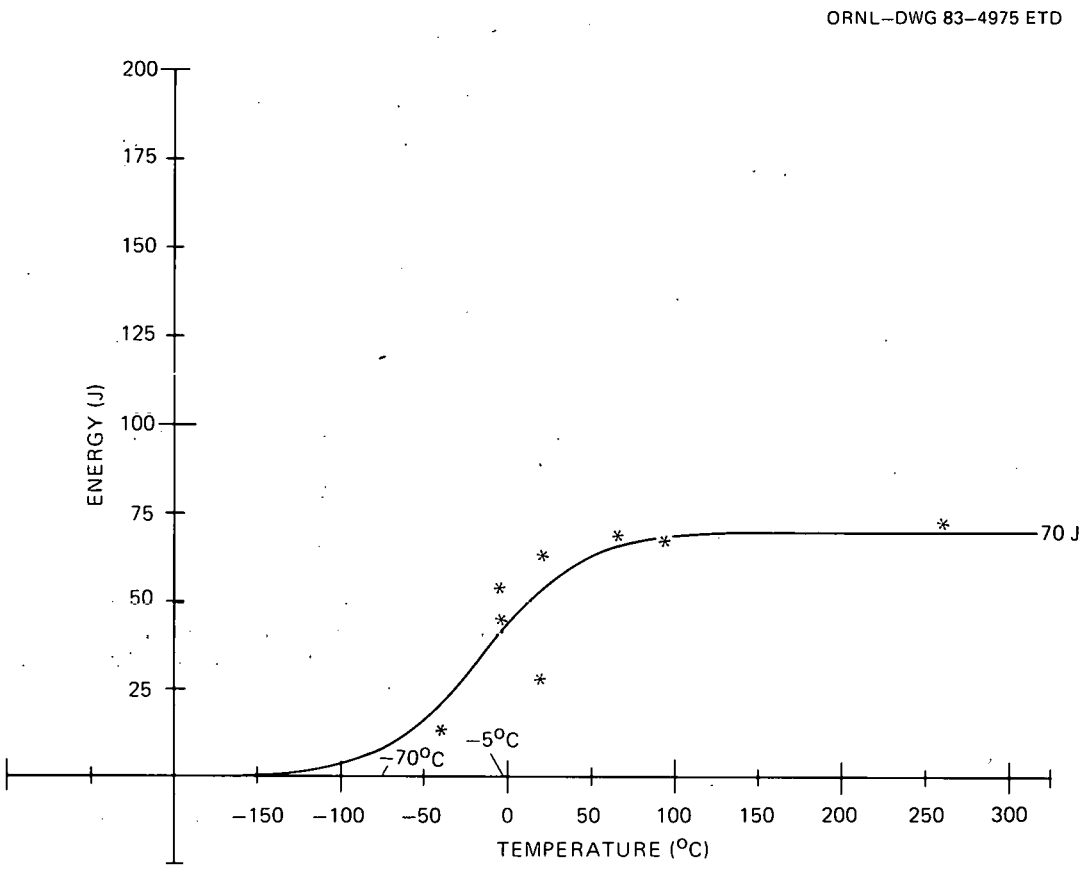

Fig. 3.7. Charpy V-notch impact test results for unirradiated first layer of three-layer stainless steel cladding (type 309/308, single-wire series-arc process).

tangent curve was fitted to the data (a fictitious data point was added at −184°C and 8 J to prevent the curve from showing negative energies below −70°C). Because of the large difference in fracture energy for the two specimens tested at 20°C, these specimens were metallographically examined. In both specimens the fracture started in the first-layer (type 309) material and propagated through both first- and second-layer material. However, crack propagation in the specimen with a fracture energy of 63 J was ~10% in first-layer material and ~90% in second-layer material; in the specimen with a fracture energy of 28 J, crack propagation was ~40% in first-layer material and ~60% in second-layer material. The metallurgical structure of this multilayer stainless steel weld cladding is discussed in greater detail in Chap. 6. It appears that considerable care will have to be taken in interpreting results of this irradiation experiment.

References

1. R. G. Berggren, T. N. Jones, and R. K. Nanstad, "Fourth HSST Irradiation Series," in *Heavy-Section Steel Technology Program Quart. Prog. Rep. October–December 1982*, NUREG/CR-2751, Vol. 4 (ORNL/TM-8369/V4), Union Carbide Corp. Nuclear Div., Oak Ridge Natl. Lab.

2. R. G. Berggren and R. K. Nanstad, "Irradiation-Induced K_{Ic} Curve Shift," in *Heavy-Section Steel Technology Program Quart. Prog. Rep. April–June 1982*, NUREG/CR-2751, Vol. 2 (ORNL/TM-8369/V2), Union Carbide Corp. Nuclear Div., Oak Ridge Natl. Lab.

3. R. G. Berggren and R. K. Nanstad, "Irradiation-Induced K_{Ic} Curve Shift," in *Heavy-Section Steel Technology Program Quart. Prog. Rep. October–December 1982*, NUREG/CR-2751, Vol. 4 (ORNL/TM-8369/V4), Union Carbide Corp. Nuclear Div., Oak Ridge Natl. Lab.

4. R. G. Berggren, R. K. Nanstad, and W. R. Corwin, "Irradiated Stainless Steel Cladding," in *Heavy-Section Steel Technology Program Quart. Prog. Rep. April–June 1982*, NUREG/CR-2751, Vol. 2 (ORNL/TM-8369/V2), Union Carbide Corp. Nuclear Div., Oak Ridge Natl. Lab.

5. R. G. Berggren, R. K. Nanstad, and W. R. Corwin, "Irradiated Stainless Steel Cladding," in *Heavy-Section Steel Technology Program Quart. Prog. Rep. October–December 1982*, NUREG/CR-2751, Vol. 4 (ORNL/TM-8369/V4), Union Carbide Corp. Nuclear Div., Oak Ridge Natl. Lab.

4. THERMAL-SHOCK INVESTIGATIONS

R. D. Cheverton

During this report period, provisions were made to include finite-length flaws in the computer program OCA-II, and a parametric analysis was conducted to determine the advantage, in terms of vessel integrity, in replacing two-dimensional (2-D) flaws in the fracture-mechanics (FM) model with specific finite-length flaws. Material properties continued to be gathered in support of TSE-7, and a preliminary thermal-shock experiment TSE-7-1 was performed to be sure that an appropriate shock can be achieved.

4.1 Inclusion of Finite-Length Flaws in OCA-II

R. D. Cheverton D. G. Ball

Flaws in a pressurized-water reactor (PWR) vessel are most likely to be located in the welds that join the segments of the vessel, and for most of the vessels in operation today, radiation embrittlement is greater in the welds than in the base material because of higher concentrations of copper in the welds. Thus, although a flaw may extend in length as the result of an overcooling accident (OCA), the length of the flaw tends to be limited to the length of the weld. For plate-type vessels, which have both axial and circumferential welds in the belt-line region, the length of the axial welds is ~2 m, which is equal to the height of a shell course. Recent calculations[1] indicate that the stress-intensity factor for a deep axial flaw of this length is substantially less than for an infinitely long (2-D) flaw, which is usually used in the evaluation of vessel integrity during OCAs. Thus, replacement of the 2-D axial flaw with the 2-m axial flaw in the FM model could represent a benefit in terms of projected vessel lifetime. For this reason, a 2-m semielliptical axial flaw was included as an option in OCA-II (Ref. 2).

Another finite-length flaw of interest, particularly for initial flaws, is a semielliptical flaw with a length-to-depth ratio of 6:1. There is no particular technical justification for using this specific initial flaw in the analysis of OCAs except that, presumably, initial flaws are much more likely to be short than long. With this in mind, and also because other investigators have included the 6:1 flaw in their studies, a 6:1 flaw was included as an option in OCA-II.

To include the 6:1 and 2-m flaws in OCA-II and still retain the rapid-computation capability, it is necessary to use superposition techniques for calculating K_I, and this requires the availability of influence coefficients for these flaws. Several sets of coefficients have been published,[3-5] but there is some question regarding their accuracy, particularly because extrapolation is required in several cases. Thus, influence coefficients were calculated specifically for the 6:1 and 2-m flaws of interest to our studies.

Application of the superposition technique is discussed in detail in Refs. 6. and 7. It suffices to say here that it was implemented by fitting a third-order polynomial to the stress distribution that would exist in the absence of the flaw, as indicated in Eq. (4.1):

$$\sigma(a') = C_0 + C_1 \left(\frac{a'}{a}\right) + C_2 \left(\frac{a'}{a}\right)^2 + C_3 \left(\frac{a'}{a}\right)^3 , \tag{4.1}$$

where $\sigma(a')$ is the circumferential stress at radial position a', and a' and a are defined in Fig. 4.1. K_I values are calculated for each of the individual terms (stress distributions) in Eq. (4.1) and then added to obtain the total K_I value, as indicated by Eq. (4.2):

$$K_I(a) = \sum_{j=0}^{3} K_{Ij}(a) = \sum_{j=0}^{3} C_j \sqrt{a}\, K_j^*(a) , \tag{4.2}$$

where

$$K_j^*(a) = K'_{Ij}(a)/C'_j \sqrt{a} . \tag{4.3}$$

Values of $K'_{Ij}(a)/C'_j$ are calculated using a three-dimensional (3-D) finite-element analysis[8] and an arbitrary value of C'_j, such as unity. The quantity $K_j^*(a)$ is referred to as the influence coefficient and, as indicated

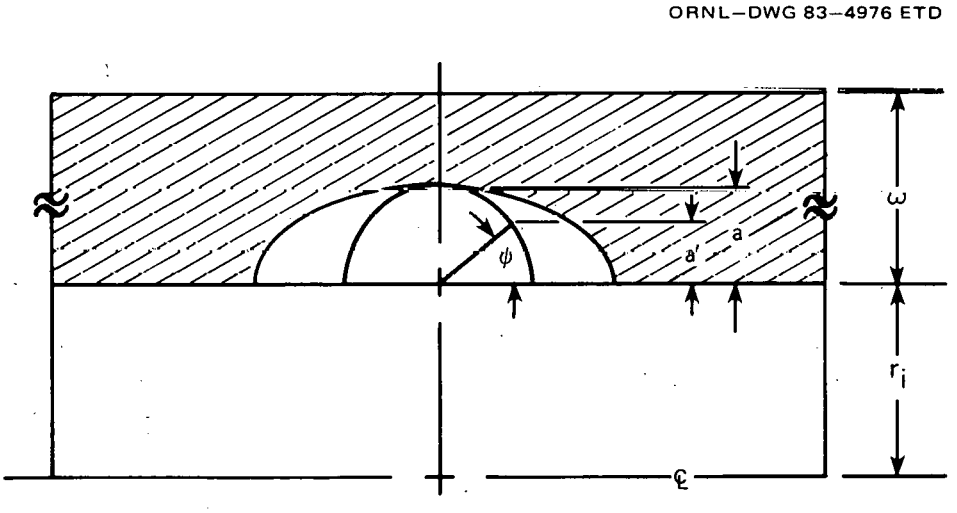

Fig. 4.1. Axially oriented semielliptical flaw on inner surface of cylinder.

by Eq. (4.3), is dimensionless. Once the influence coefficients are obtained, they can be used with any values of C_j to obtain corresponding values of $K_I(a)$.

For 3-D flaws, $K_j^*(a)$ values can be calculated for several points along the crack front, in which case Eq. (4.2) becomes

$$K_I(\phi) = \sum_{j=0}^{3} C_j \sqrt{a}\, K_j^*(\phi) , \qquad (4.4)$$

where ϕ is the elliptic angle denoting the point on the crack front, and the crack-depth notation (a) has been dropped.

The influence coefficients included in OCA-II at this time for the 6:1 and 2-m axial flaws were calculated for the conditions described in Table 4.1. As indicated, only a 90° segment of the cylinder (see Fig. 4.2) was used in the analysis, and this corresponds to having flaws at 0° and 180° (two flaws opposite each other). A single flaw (180° segment) was preferred, but from a practical point of view, the computer requirements were excessive. Fortunately, for the flaws being considered, the difference between the K_I values is quite small.

Table 4.1. Details of calculational model pertaining to influence coefficients for 6:1 and 2-m axial flaws

Dimensions	Flaw type	
	2-m	6:1
Cylinder dimensions		
ID, mm	4370	4370
OD, mm	4800	4800
Length, mm	7010	4674
Segment, deg	90	90
Length of flaw, mm	1828	32–321
Depth of flaw (a/w)	0.2–0.9	0.025–0.25

The difference in K_I values associated with the 90° and 180° models increases with the length and depth of the flaw. Reference 4 states that the difference for a two-dimensional (2-D) flaw with a/w = 0.8 was only 2%, but this conclusion appears to be based on an analysis using an inappropriate model. Thus, we analyzed the 2-D flaw using the model in

ORNL-DWG 83-4977 ETD

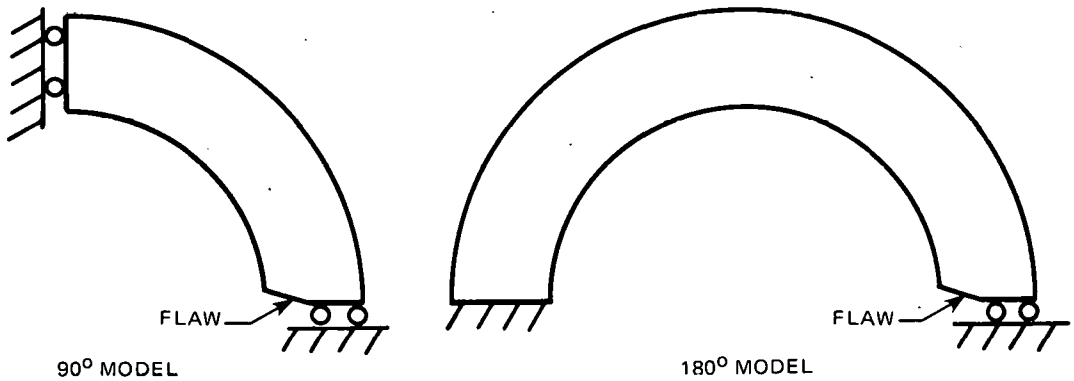

Fig. 4.2. 90° and 180° models used for determining difference in K_I values for single axial flaw and two opposite flaws.

Table 4.1 and a very severe thermal-shock loading large-break loss-of-coolant accident (LBLOCA). The results in Table 4.2 show that for a/w = 0.8, the 90° model results in a 30% higher value of K_I. Because this value is rather large, a similar comparison was made for the 2-m flaw with a/w = 0.8. For this case, the K_I value for the 90° model was <4% higher. Because the difference would be even less for the shallow 6:1 flaws considered, the influence coefficients obtained for the 6:1 and 2-m flaws are appropriate for both the 90° and 180° models.

In the process of calculating the coefficients, careful attention was paid to using converged meshes and appropriate cylinder lengths. Mesh convergence studies were conducted to reduce the apparent error in K_I to <1%. With regard to cylinder lengths, a minimum incremental length of

Table 4.2. Comparison of K_I values for 2-D flaws in 90° and 180° models, using the large-break LOCA transient

a/w	$\{[K_I(90°) - K_I(180°)]/K_I(180°)\}\ 10^2$ (%)
0.1	0.4
0.4	3.5
0.8	30.4

cylinder that could be added to the length of the flaw to negate end effects was estimated from Eq. (4.5):[9]

$$\ell = \frac{2\pi}{\beta} , \tag{4.5}$$

where

$$\beta^4 = \frac{3(1 - \nu^2)}{r_i^2 w^2} ,$$

r_i = radius of cylinder,
w = wall thickness,
ν = Poisson's ratio.

For the model described in Table 4.1, $\ell \cong 3300$ mm. A 3-D analysis, using the 2-m flaw and a typical transient, indicated that this added length was not sufficient to reduce end effects below ~5% and that the required length to reduce end effects below 2% would be greater than the length of a PWR vessel between the lower head and the nozzle ring. It was decided that for the 2-m flaw, a cylinder length of 7510 mm would be appropriate. A similar analysis for the 6:1 flaw indicated an appropriate length of 4670 mm. In both cases, the ends of the cylinder were free.

As discussed in Sect. 4.2, only the K_I values corresponding to $\phi = 90°$ are being used in the OCA analysis at the present time. Influence coefficients for $\phi = 90°$ are plotted as a function of a/w in Figs. 4.3 and 4.4 for the 2-m and 6:1 flaws, respectively.

Coding has been added to OCA-II to permit calculation of K_I values along the crack front for the 6:1 and 2-m flaws. The type of flaw used in an OCA-II analysis is selectable; that is, both the above finite flaws and/or the infinite flaw can be included. For each time step and each crack depth of interest, a least-squares fit is made to the circumferential stresses from the crack mouth to the crack tip, in accordance with Eq. (4.1).

OCA-II performs the same type of calculations for the two finite flaws as for the infinite flaw. These include determination of K_I/K_{Ic} and K_I/K_{Ia} at all times and for all crack depths. Additional digital output for the finite flaw is provided as well as inclusion of the finite flaws in the critical crack-depth plot (see Fig. 4.5). Also, for the 6:1 flaw as well as for the 2-D flaws, it is possible to search for the critical value of ΔRTNDT on the inner surface corresponding to incipient initiation without warm prestressing.

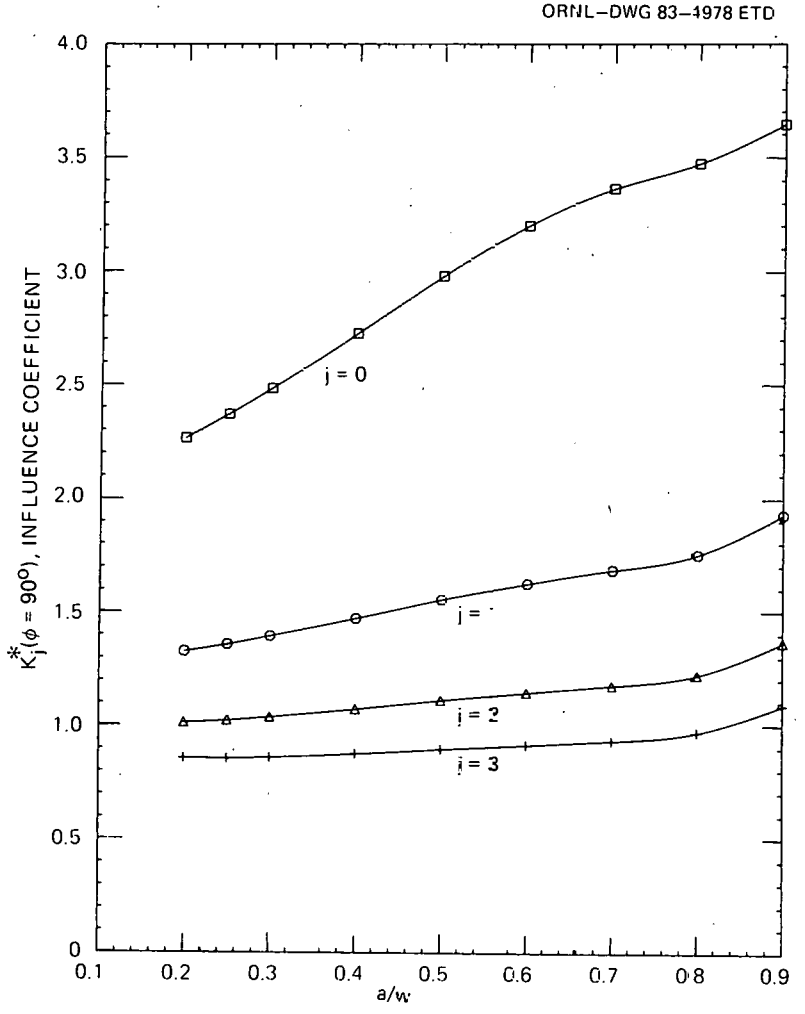

Fig. 4.3. Influence coefficients for 2-m flaw.

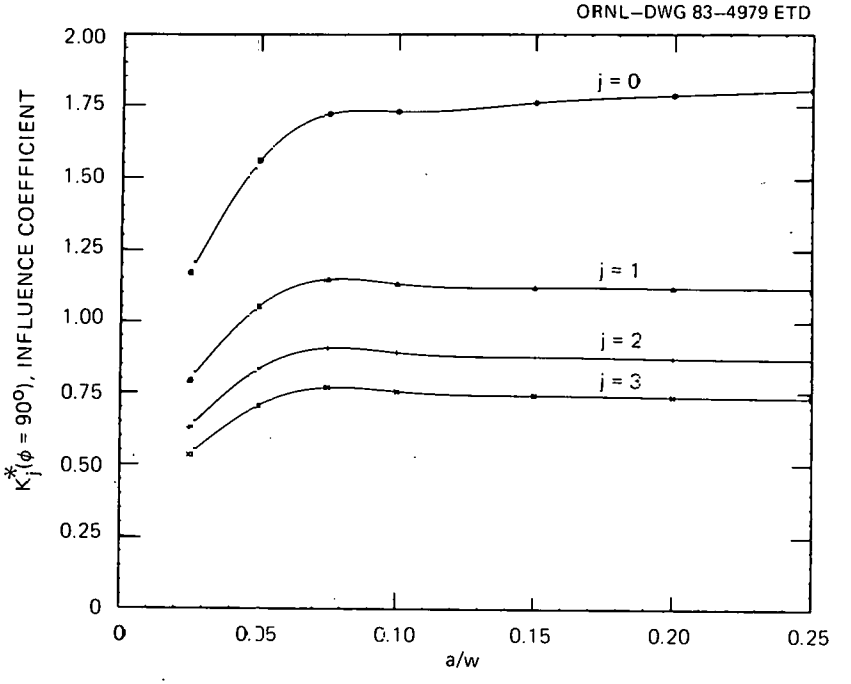

Fig. 4.4. Influence coefficients for 6:1 flaw.

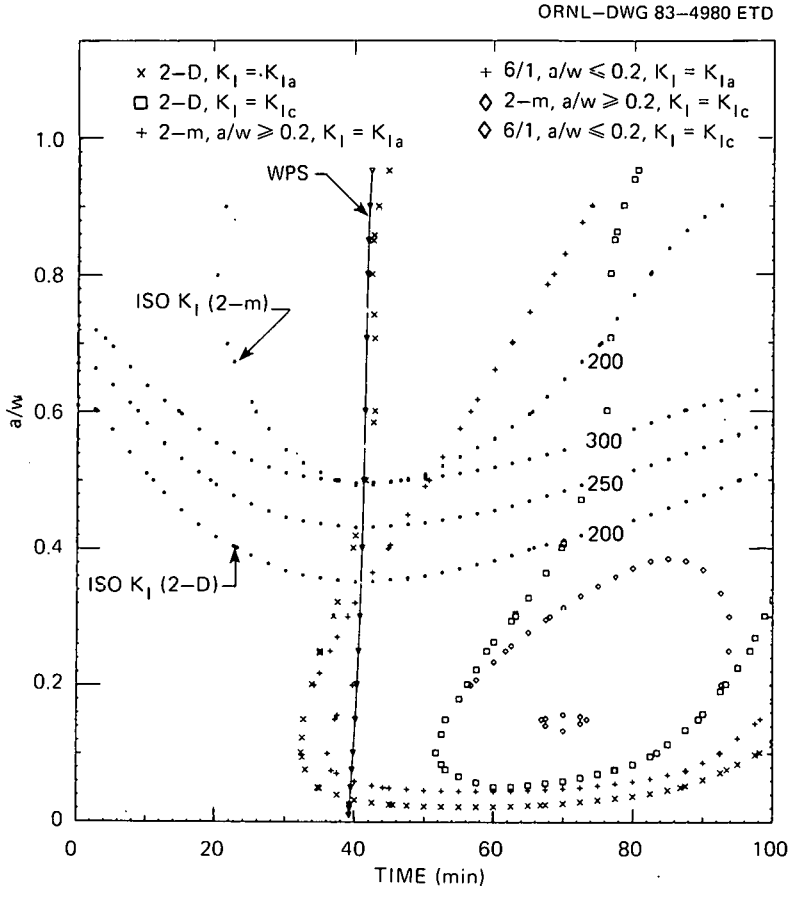

Fig. 4.5. Typical set of critical-crack-depth curves that includes 2-D flaws for incipient initiation and subsequent events, a 6:1 flaw for incipient initiation, and a 2-m flaw for first arrest and subsequent events.

4.2 OCA Parametric Analysis Using Finite-Length Flaws

R. D. Cheverton D. G. Ball

An OCA parametric analysis was conducted to determine the benefit of using two specific combinations of 2-D, 2-m, and 6:1 flaws in place of 2-D flaws only. Because a very shallow flaw does not have to be very long to be effectively infinitely long and because the flaw tends to grow in length before growing radially, one combination of axial flaws considered was a shallow ($a/w \leq 0.15$) 2-D flaw for the first initiation event and a 2-m flaw for the first arrest and subsequent events. The other combination consisted of a shallow ($a/w \leq 0.15$) 6:1 flaw for the first initiation and a 2-m flaw for subsequent events.

For both the 6:1 and 2-m flaws, radial propagation of the flaw, in terms of both initiation and arrest, was assumed to be governed by the K_I, K_{Ic}, and K_{Ia} values at the deepest point (midlength) of the flaw. This is

a reasonable assumption for the 2-m flaw because it cannot grow in length. However, the assumption tends to result in an underestimation of the potential for radial propagation of the 6:1 flaw because K_I/K_{Ic} tends to be greater near the surface than at the bottom of the flaw, and as the flaw grows in length, K_I/K_{Ic} at the deepest point increases. The amount of axial extension and the change in crack shape are not known. Thus, one has a choice of considering one of two extremes: a 2-D flaw, which, barring dynamic effects, has the greatest potential for radial propagation, or the 6:1 flaw, using K values at the deepest point. If the maximum value of K_I/K_{Ic} were used on the crack front of the 6:1 flaw, the computed potential for radial propagation would be greater than that for the 2-D flaw; thus, the 2-D flaw should be used instead.

Fracture-toughness data (K_{Ic} and K_{Ia} vs T − RTNDT) were taken from ASME Code Sect. XI (Ref. 10), and the reduction in toughness due to radiation damage was estimated using Eq. (4.1), which was recently proposed by Randall[11] as a revision to Regulatory Guide 1.99, Rev. 1:[12]

$$\Delta RTNDT = 0.56\ (-10 + 470\ Cu + 350\ Cu\ Ni)(F \times 10^{-19})^{0.27}\ , \qquad (4.6)$$

where

$2 \times 10^{17} \leq F \leq 6 \times 10^{19}$ neutrons/cm²,
F = fast neutron fluence (E ≥ 1 MeV) at tip of flaw,
ΔRTNDT = change in RTNDT at tip of flaw due to fast neutron exposure, °C,
RTNDT = $RTNDT_o$ + ΔRTNDT,
$RTNDT_o$ = initial (zero fluence) value of RTNDT,
Cu, Ni = copper and nickel concentrations, wt %.

For comparing the calculated effects of the choice of flaw combination on vessel integrity, threshold or critical values of RTNDT corresponding to incipient initiation of a flaw and incipient failure of the vessel (extension of the flaw through the wall) were calculated. For convenience, the particular values of RTNDT that are compared with each other are the values corresponding to the inner surface of the vessel wall and are referred to here as $(RTNDT_s)_{ci}$ for incipient initiation and $(RTNDT_s)_{cf}$ for incipient failure.

Failure of the vessel was judged by application of two criteria: (1) $K_I > K_{Ia}$ (no arrest) and (2) plastic instability. The largest measured value of dynamic fracture toughness included in the ASME Code (Sect. XI) (Ref. 10) for PWR pressure vessel material is 220 MPa·$\sqrt{m}$, while more recent data[13] indicate that appropriate K_{Ia} values could be as high as 330 MPa·$\sqrt{m}$. Previous studies[14] demonstrated that for some postulated OCAs, this range of $(K_{Ia})_{max}$ values could make a substantial difference in the calculated behavior of a flaw; thus, both values were included in this study. With regard to plastic instability, a critical crack depth corresponding to this failure condition was specified for each pressure, assuming no 3-D or thermal-stress effects, a uniform pressure stress in the ligament, and a failure stress of 550 MPa.

Most of the other details concerning the fracture-mechanics model used for this study are the same as those included in a previous OCA parametric analysis.[14] One notable exception is the complete absence of cladding for this study. (Appropriate finite-length-flaw influence coefficients for a clad vessel were not yet available.) This has little effect on the results, however, because complete omission of the cladding yields about the same values of $(RTNDT_s)_c$ as obtained when cladding is included as a discrete region (both thermal and stress effects considered).[15]

Results of the previous parametric study,[14] which considered only 2-D flaws, indicated that changing from 2-D to 2-m flaws for crack arrest would not necessarily result in an increase in $(RTNDT_s)_{cf}$ for all postulated OCAs. It was found that for primary-system pressures above some critical value p_c, $(RTNDT_s)_{cf} = (RTNDT_s)_{ci}$, a condition depicted in Fig. 4.6. For pressures less than p_c, a higher value of $RTNDT_s$ is required for failure than for incipient initiation; that is, the crack will arrest following incipient initiation and will not reinitiate, as shown in Fig. 4.7. For this case, it was apparent that replacing the 2-D axial flaw with a 2-m flaw (for crack arrest) would increase p_c, and that only for pressures less than p_c would the change in flaw type result in an increase in $(RTNDT_s)_{cf}$. A point of interest was whether p_c would be high enough relative to expected pressures during OCAs for the change in flaw type 2-D to 2-m to have a significant effect on vessel integrity.

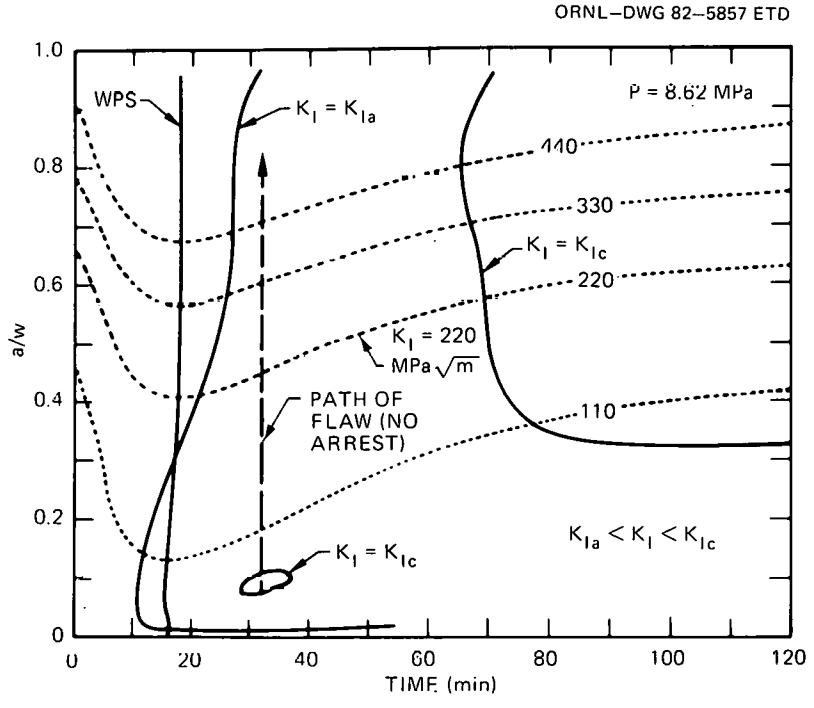

Fig. 4.6. Critical-crack-depth curves for an OCA illustrating incipient initiation and failure (no arrest unless on upper shelf).

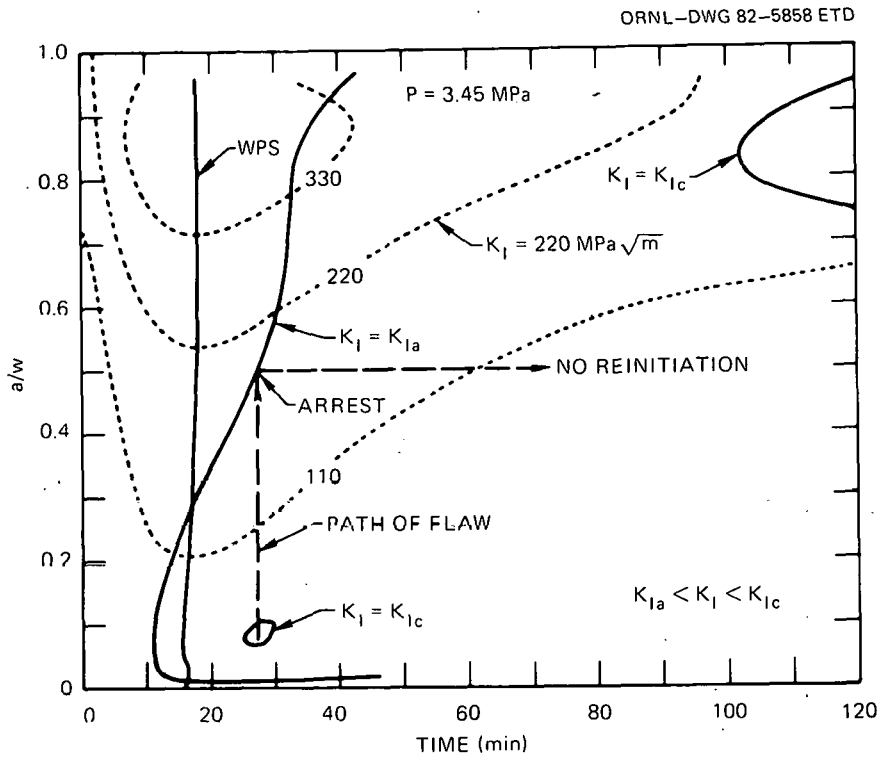

Fig. 4.7. Critical-crack-depth curves for OCA illustrating incipient initiation followed by arrest and no reinitiation.

A quantitative evaluation of the effect of the different assumed flaw types on vessel integrity was obtained by comparing values of $(RTNDT_s)_{cf}$ for several postulated OCAs and for the Rancho Seco transient that occurred in 1978 (see Fig. 4.8). The postulated transients consisted of a constant primary-system pressure p and a temperature transient defined by

$$T_c = T_f + (T_i - T_f)\, e^{-nt}\ , \qquad (4.7)$$

where

T_c = downcomer coolant temperature,
T_f^i = initial temperature of vessel wall and coolant,
T_f = final (asymptotic) temperature of coolant,
n = decay constant,
t = time in transient.

The duration of the transient t_{max} was varied to determine the sensitivity of vessel integrity to this parameter. Input data for the various cases calculated are summarized in Table 4.3.

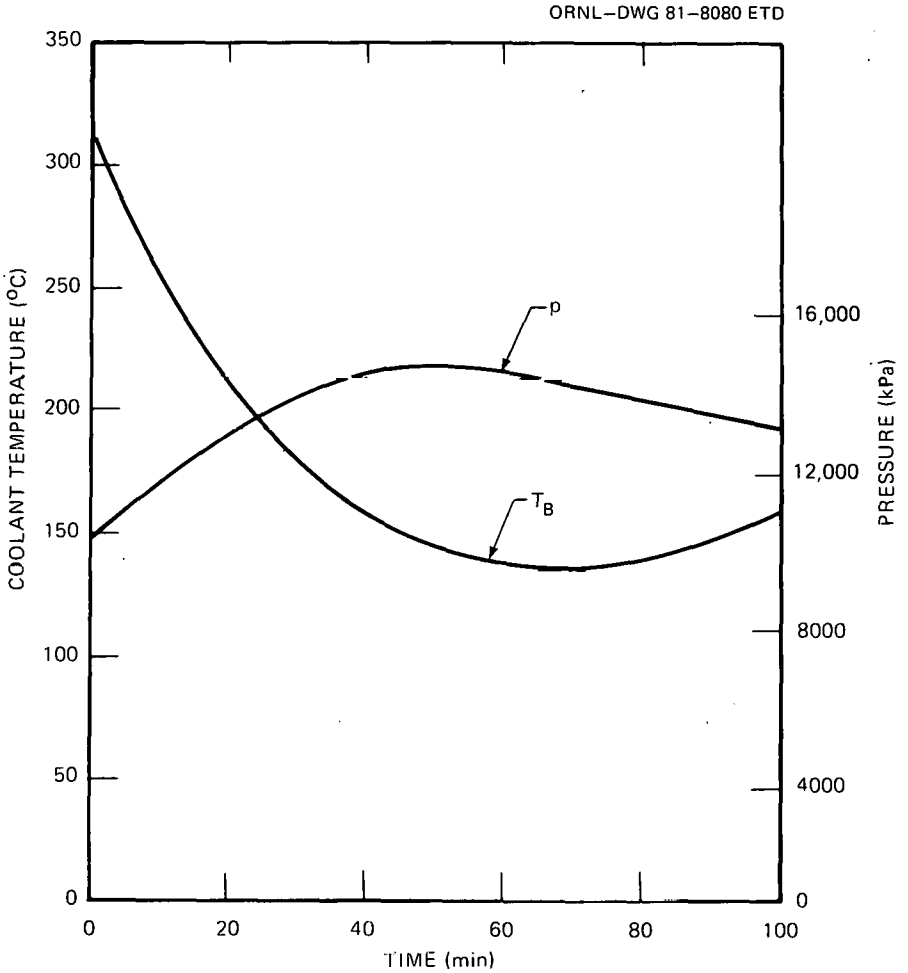

Fig. 4.8. Rancho Seco 1978 OCA coolant temperature and pressure transients (smoothed).

Calculated values of $(RTNDT_s)_{cf}$ for the 2-D, 2-D axial flaw combination are presented in Fig. 4.9 and the increases resulting from replacement of the (2-D, 2-D) combination with the (2-D, 2-m) and (6:1, 2-m) combinations are illustrated in Figs. 4.10 and 4.11 for T_f = 66 and 121°C, respectively. As indicated by Figs. 4.10 and 4.11, there can be an advantage associated with the 2-m flaw, and as expected, it decreases with increasing pressure. The critical pressure p_c (the maximum pressure for which the 2-m flaw has an advantage over the 2-D flaw) ranges from ~7 MPa for t_{max} = 120 min to 17.2 MPa for t_{max} = 45 min, indicating a greater advantage of the 2-m flaw for a shorter duration of the transient, although as indicated in both figures, there can be a small reversal of this trend for some combinations of t_{max} and $(K_{Ia})_{max}$. The results also show that the advantage of the 2-m flaw is greater for a $(K_{Ia})_{max}$ value of 330 than for 220 MPa·$\sqrt{m}$, provided t_{max} is somewhat less than 60 min and the pressure is greater than ~10 MPa. For $t_{max} \geq 60$ min, there is no effect of increasing $(K_{Ia})_{max}$ from 220 to 330 MPa·$\sqrt{m}$.

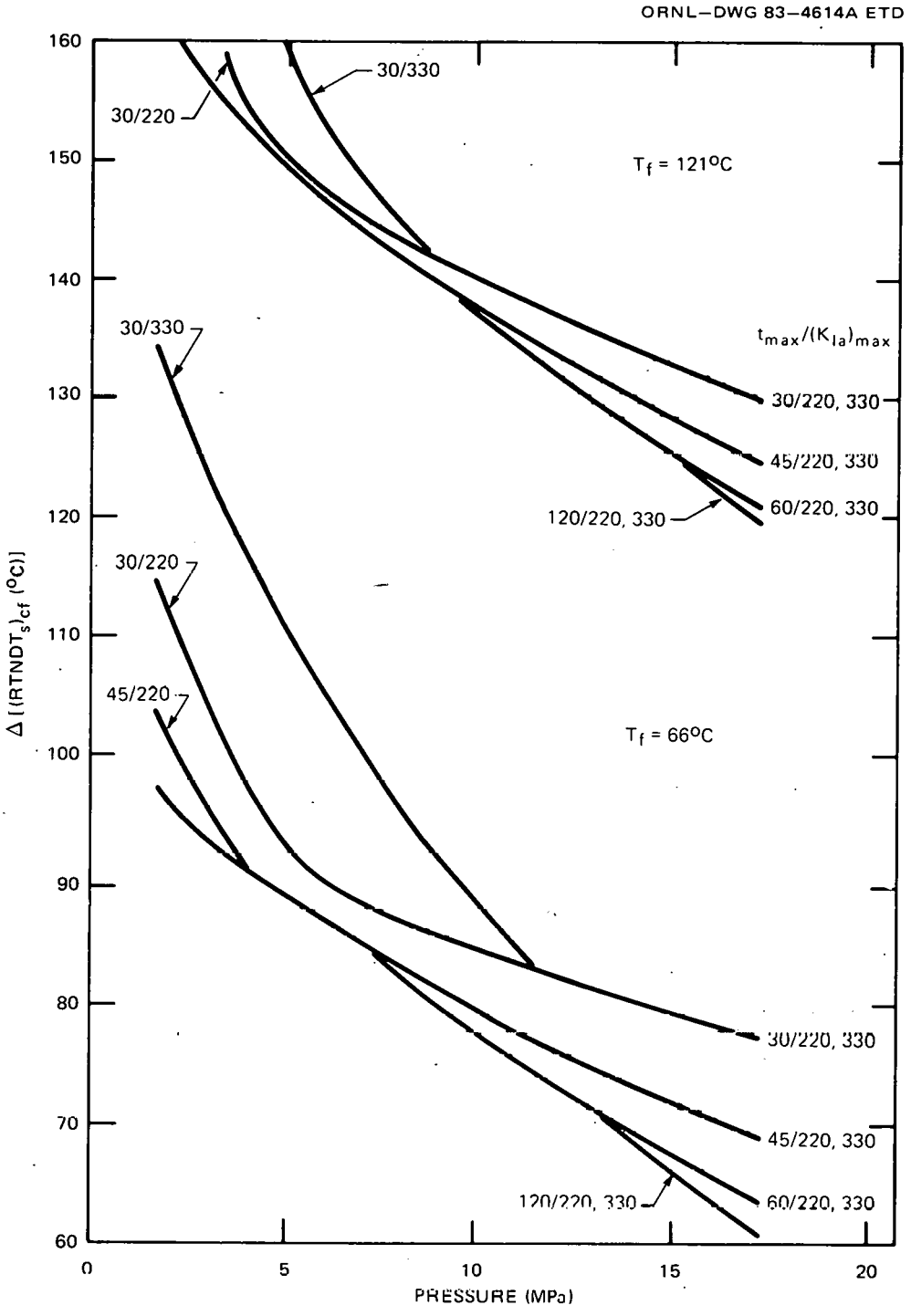

Fig. 4.9. $(RTNDT_s)_{cf}$ vs pressure for several values of T_f, $(K_{Ia})_{max}$, and t_{max}.

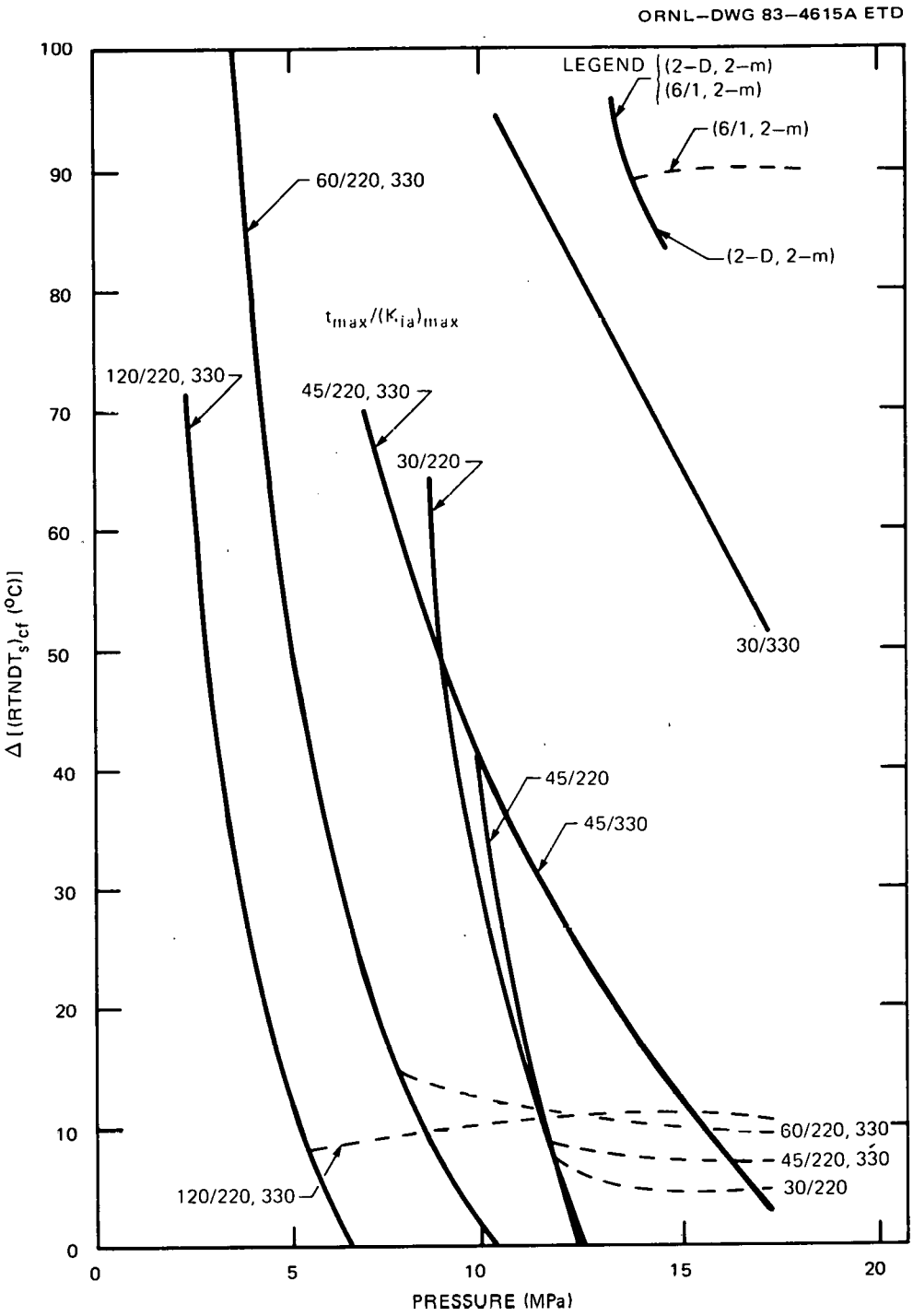

Fig. 4.10. Increase $\Delta(RTNDT_s)_{cf}$ in $(RTNDT_s)_{cf}$ for (2-D, 2-m) and (6:1, 2-m) flaw combinations relative to (2-D, 2-D) combination for T_f = 66°C.

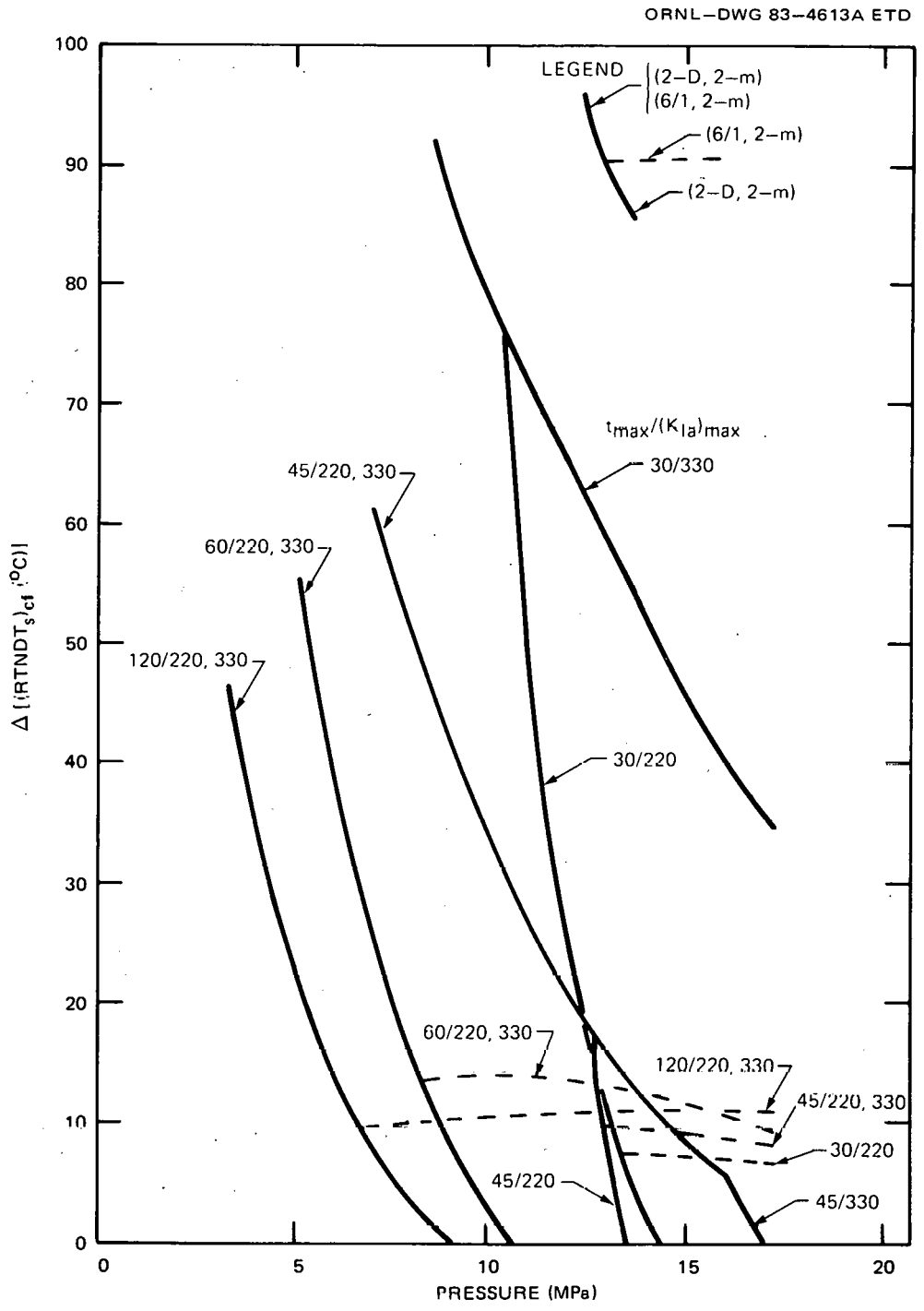

Fig. 4.11. Increase $\Delta(RTNDT_s)_{cf}$ in $(RTNDT_s)_{cf}$ for (2-D, 2-m) and (6:1, 2-m) flaw combinations relative to (2-D, 2-D) combination for T_f = 121°C.

Table 4.3. Input data for OCA cases calculated

Vessel OD, mm	4800
Vessel ID, mm	4370
T_f, °C	66, 121
T_i, °C	288
n, min^{-1}	0.15
t_{max}, min[a]	30, 45, 60, 120
h_f, $W \cdot m^{-2} \cdot °C^{-1}$[b]	1870[c,d]
p, MPa	0–17.2
$RTNDT_o$, °C	−18[d]

[a] Duration of transient.

[b] Fluid-film heat transfer coefficient.

[c] Corresponds to main pumps off.

[d] Used for both Rancho Seco and postulated OCAs.

From a quantitative point of view, the advantage in replacing the 2-D, 2-D flaw combination with the 2-D, 2-m combination for T_f = 121°C and p = 10 MPa corresponds to an increase in $(RTNDT_s)_{cf}$ of 76, 31, and 0°C for t_{max} = 30, 45, and ≥60 min, respectively, and the increase is independent of the value of $(K_{Ia})_{max}$ (220–330 MPa·$\sqrt{m}$). At a pressure of 17.2 MPa, there is no advantage except for t_{max} = 30 min and $(K_{Ia})_{max}$ = 330 MPa·$\sqrt{m}$, and for this case the increase in $(RTNDT_s)_{cf}$ is ~34°C.

As shown in Figs. 4.10 and 4.11, replacement of the 2-D initial flaw with the 6:1 flaw increases $(RTNDT_s)_{cf}$ for pressures that are greater than a value that is a little less than p_c. This increase is nearly independent of pressure and is greater for larger values of t_{max}. For t_{max} = 30 min, the increase in $(RTNDT_s)_{cf}$ is ~6°C, and for t_{max} = 120 min, it is ~12°C.

A comparison of Figs. 4.10 and 4.11 indicates that the advantage of the 2-D, 2-m and 6:1, 2-m flaw combinations over the 2-D, 2-D combination is about the same for T_f = 66 and 121°C, although there are some significant differences for t_{max} = 30 min.

Estimates of the extension in calculated lifetime of a PWR pressure vessel due to increases in $(RTNDT_\varepsilon)_{cf}$ can be obtained using Eq. (4.6) and

typical PWR fluence rates ($\dot{F}_o$). As an example, estimates corresponding to a change in flaw combination from 2-D, 2-D to 2-D, 2-m were made for a case in which T_f = 121°C, n = 0.15 min^{-1}, p = 10 MPa, $RTNDT_o$ = −18°C, Cu = 0.3%, Ni = 0.8%, and $(K_{Ia})_{max}$ = 220 MPa·$\sqrt{m}$. The results are presented in Table 4.4 for t_{max} = 30, 45, and ≥60 min and for the approximate extremes in fluence rates among the existing PWRs for the effective full power years (EFPY) (0.3 and 1.5 x 10^{18} neutrons·cm^{-2}·$EFPY^{-1}$). As shown in the table, there is no extension of the lifetime for $t_{max} \geq 60$ min. However, if the 2-D initial flaw were replaced with a 6:1 flaw, there would be an extension for $t_{max} \geq 60$ min of 9 and 2 EFPY for $\dot{F}_o$ = 0.3 and 1.5 x 10^{18} neutrons·cm^{-2}·$EFPY^{-1}$.

Table 4.4. Estimates of the extension in calculated vessel lifetime due to changing the assumed flaw combination from 2-D, 2-D to 2-D, 2-m

(Sample case described in text)

t_{max} (min)	$(RTNDT_s)_{cf}$[a] (°C)	F_o x 10^{-19}[b] (neutrons/cm^2)	ΔEFPY[c] $\dot{F}_o$ x 10^{-18}[d] 0.3	ΔEFPY[c] $\dot{F}_o$ x 10^{-18}[d] 1.5
30	214	2.45	49	10
45	169	1.65	22	4
≥60	138	0.98	0	0

[a] Values for 2-D, 2-m flaw combination.

[b] Inner-surface fluence to achieve indicated $(RTNDT_s)_{cf}$.

[c] Extension in vessel life due to change in flaw combination.

[d] Fluence rate at inner surface (neutrons·cm^{-2}·$EFPY^{-1}$).

Analysis of the Rancho Seco transient described in Fig. 4.8 indicated no increase in $(RTNDT_s)_{cf}$ as a result of changing the flaw combination from 2-D, 2-D to 2-D, 2-m. However, changing the combination from 2-D, 2 D to 6:1, 2-m increased $(RTNDT_s)_{cf}$ by ~11°C.

Circumferential flaws were analyzed in a similar fashion to the extent of determining whether the circumferential flaw might have a lower value of $(RTNDT_s)_{cf}$ than the axial flaw. The comparison was made between

the 2-D, 2-D circumferential-flaw combination and the 2-D, 2-m axial-flaw combination; for none of the cases considered was the circumferential flaw limiting.

4.3 Thermal-Shock Materials Characterization

W. J. Stelzman R. K. Nanstad
R. L. Swain

Characterization of prolongation TSP-4 from test cylinder TSC-4 was continued in support of TSE-7 with emphasis on fracture toughness. Drop-weight and Charpy V-notch impact results have been reported previously.[16] Test results from 1T compact specimens (1TCS) from a segment tempered for 4 h at 676°C followed by cooling in air[16] are listed in Table 4.5. A total of ten CT-oriented[17] 1TCS were tested. All specimens were machined so that the fatigue crack would be located at the 0.23 and 0.58t depth locations from the inner surface of the 203-mm-thick wall. The specimens were precracked to an average crack length-to-width ratio (a/w) of 0.560 and tested in the stroke control mode. The crack opening displacement

Table 4.5. Static fracture-toughness properties from CT-oriented 1T compact specimens from prolongation TSP-4 (SA508) after tempering at 676°C for 4 h, cooling in air, and testing at 21°C

Static fracture toughness (MPa·√m)		J integral (K_J/m^2)	Average ductile crack extension (mm)
K_J	β_{Ic} adjusted		
131	82	85	0.08
114[a]	77	64	0.07
248	106	304	0.42
153	88	117	0.11
146	86	106	0.11
257	108	327	0.14
264	109	247	0.64
255	107	324	0.43
174	92	150	0.11
270[b]	110	363	0.56

[a] Lowest measured toughness.

[b] Highest measured toughness.

(COD) was measured at the specimen load line, and the calculation of the J integral was made using the area-to-maximum load and the Merkle-Corten correction for the tensile component.[18] The static fracture toughness K_J was calculated from the relationship $K_J^2 = EJ$, where E = 201 GPa (29.2 x 10^6 psi). The β_{Ic} adjustment was made using the Merkle method.[19] Values of K_J at 21°C ranged from 114 to 270 MPa·$\sqrt{m}$ and from 77 to 110 MPa·$\sqrt{m}$ after the β_{Ic} adjustment. All specimens experienced some stable ductile crack extension prior to failure by cleavage, and all specimens failed prior to attainment of limit load. Ductile crack extension was measured on each specimen fracture surface using a three-point average. The results are given in Table 4.5 and show a wide range of stable crack growths from 0.07 to 0.64 mm.

We are presently (1) fatigue precracking 1TCS from TSP-4 material tempered for 4 h at 702°C followed by cooling in air[16] and (2) machining tensile specimens from the 675 and 702°C tempered TSP-4 material.

4.4 TSE-7 Thermal-Hydraulic Experiment

R. D. Cheverton

Prior to conducting each thermal-shock experiment, a preliminary thermal-shock experiment is conducted with the actual test cylinder to be sure that the desired thermal shock can be achieved. The test is conducted without the intended initial flaw present and with the cylinder in a quench-only condition. The latter condition is specified to minimize yielding at the inner surface.

Prior to the thermal-hydraulic test, the test cylinder is equipped with 180 thermocouples that are used for measuring the temperature distribution in the wall at 15 different locations, and then the inner surface of the cylinder is coated with the appropriate layer of rubber cement. This inner-surface coating suppresses film boiling and promotes transitional nucleate boiling during the thermal-shock quench in liquid nitrogen. Preparation of this coating to achieve the desired heat removal rate for each experiment is somewhat of a black art; thus, the thermal-hydraulic experiment is needed.

For this particular experiment, 24 coats of rubber cement were applied to achieve a total surface density of 273 g/m². The first five coats were sprayed with 3M Company type 3M-34 material (total surface density ~20 g/m²), and the remaining coats were sprayed with 3M-NF34.

The thermal-shock experiment consisted of first heating the appropriately insulated test cylinder to 93°C and then effectively dunking the test cylinder assembly in liquid nitrogen to achieve the desired thermal shock. Results of the experiment (TSF-7-1) in terms of the temperature close to the inner surface (radial depth = 1.3 mm) as a function of time are shown in Fig. 4.12 along with similar curves for thermal-shock experiments TSE-5 and -5A. The desired quench rate for TSE-7 is the one achieved for TSE-5A or somewhat more severe. As indicated in Fig. 4.12, the transient achieved during TSF-7-1 fits the latter category and provides some margin for a possibly less severe transient as a result of having to respray the test cylinder for TSE-7.

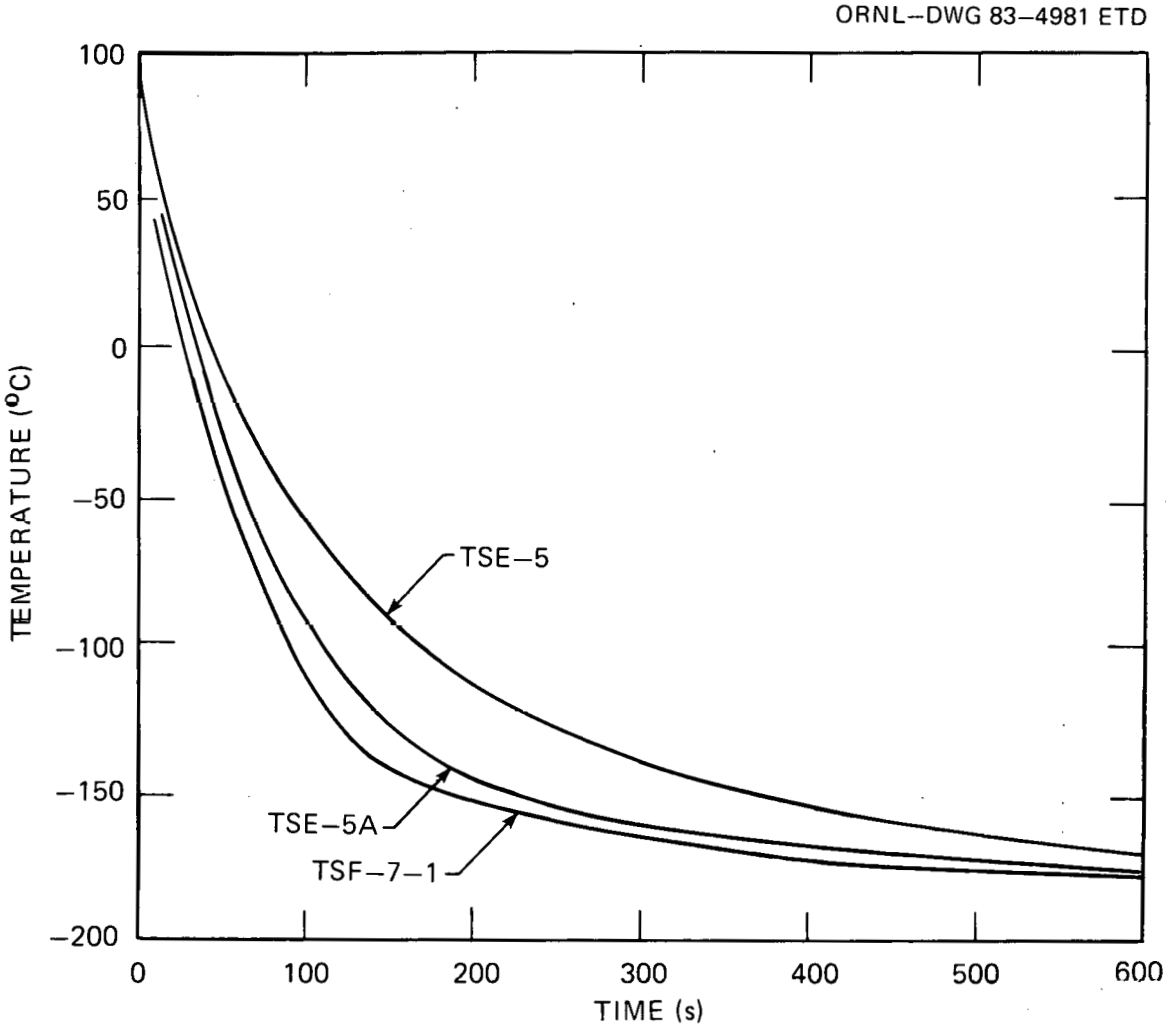

Fig. 4.12. Comparison of TSE-5, TSE-5A, and TSF-7-1 temperature transients for position in wall of test cylinders located 1.3 mm from inner surface.

The curves in Fig. 4.12 represent averages of 15 thermocouples at the same depth in the wall but at different locations so that the degree of uniformity of the quench over the entire inner surface can be established. For TSF-7-1, the scatter in the 15 readings was $\leq \pm 6°C$, and there was no specific significant trend in the axial or circumferential direction. This is a very acceptable situation.

References

1. J. G. Merkle et al., "Fracture Mechanics Analysis and Investigations," in *Heavy-Section Steel Technology Program Quart. Prog. Rep. July–September 1982*, NUREG/CR-2751, Vol. 3 (ORNL/TM-8369/V3), Union Carbide Corp. Nuclear Div., Oak Ridge Natl. Lab.

2. D. G. Ball, R. D. Cheverton, and S. K. Iskander, *OCA-II, A Code for Calculating the Behavior of 2-D and 3-D Surface Flaws in a Pressure Vessel Subjected to Temperature and Pressure Transients*, ORNL-5934, Union Carbide Corp. Nuclear Div., Oak Ridge Natl. Lab., to be published.

3. J. Heliot, R. C. Labbens, and A. Pellissier-Tanon, "Semi-Elliptical Cracks in a Cylinder Subjected to Stress Gradients," pp. 342–64 in *Fracture Mechanics*, ASTM STP 677, American Society for Testing and Materials, 1979.

4. I. S. Raju and J. C. Newman, Jr., "Stress-Intensity Influence Coefficients for Internal and External Surface Cracks in Cylindrical Vessels," pp. 37–48 in *Aspects of Fracture Mechanics in Pressure Vessels and Piping*, PVP-Vol. 58, American Society of Mechanical Engineers, 1982.

5. J. J. McGowan and M. Raymund, "Stress Intensity Factor Solutions for Internal Longitudinal Semi-Elliptical Surface Flaws in a Cylinder Under Arbitrary Loadings," pp. 365–80 in *Fracture Mechanics*, ASTM STP 677, American Society of Mechanical Engineers, 1979.

6. S. K. Iskander, R. D. Cheverton, and D. G. Ball, *OCA-I, A Code for Calculating the Behavior of Flaws on the Inner Surface of a Pressure Vessel Subjected to Temperature and Pressure Transients*, ORNL/NUREG-84, Union Carbide Corp. Nuclear Div., Oak Ridge Natl. Lab., August 1981.

7. D. G. Ball et al., "Superpositive Methods in Three-Dimensional Computational Fracture Machines," in *Heavy-Section Steel Technology Program Quart. Prog. Rep. October–December 1982*, NUREG/CR-2751, Vol. 4 (ORNL/TM-8369/V4), Union Carbide Corp. Nuclear Div., Oak Ridge Natl. Lab., to be published.

8. B. R. Bass and J. W. Bryson, *Applications of Energy Release Rate Techniques to Part-Through Cracks in Plates and Cylinders, Vol. 2, ORVIRT: A Finite Element Program for Energy Release Rate Calculations for 2-Dimensional and 3-Dimensional Crack Models*, NUREG/CR-2997, Vol. 2 (ORNL/TM-8527/V2), Union Carbide Corp. Nuclear Div., Oak Ridge Natl. Lab., February 1983.

9. S. Timoshenko, *Theory of Plates and Shells*, McGraw-Hill, New York, 1940, pp. 389–96.

10. T. U. Marston, ed., *Flaw Evaluation Procedures: ASME Section XI*, EPRI NP-719-SR, Electric Power Research Institute, August 1978.

11. P. N. Randall, U.S. Nuclear Regulatory Commission, personal communication to R. D. Cheverton, Oak Ridge National Laboratory, 1983.

12. U.S. Nuclear Regulatory Commission, "Effects of Residual Elements on Predicted Radiation Damage to Reactor Pressure Vessel Materials," *Reg. Guide 1.99*, Rev. 1 (September 16, 1976).

13. Yoshifume Nakawa et al., *Assessment of Fracture Toughness of Heavy-Section Steels for Nuclear Pressure Vessels*, Research Laboratories, Kawasaki Steel Corporation (September 1980).

14. R. D. Cheverton, S. K. Iskander, and D. G. Ball, *PWR Pressure Vessel Integrity During Overcooling Accidents: A Parametric Analysis*, NUREG/CR-2895 (ORNL/TM-7931), Union Carbide Corp. Nuclear Div., Oak Ridge Natl. Lab., February 1983.

15. A. Sauter, R. D. Cheverton, and S. K. Iskander, *Modification of OCA-I for Application to a Reactor Pressure Vessel with Cladding on the Inner Surface*, NUREG/CR-3155 (ORNL/TM-8649), Union Carbide Corp. Nuclear Div., Oak Ridge Natl. Lab., April 1983.

16. W. J. Stelzman and R. K. Nanstad, "Thermal-Shock Characterization," in *Heavy-Section Steel Technology Program Quart. Prog. Rep. October-December 1982*, NUREG/CR-2751, Vol. 4 (ORNL/TM-8369/V4), Union Carbide Corp. Nuclear Div., Oak Ridge Natl. Lab.

17. W. J. Stelzman and D. A. Canonico, "Thermal Shock-Temper Study," in *Heavy-Section Steel Technology Program Quart. Prog. Rep. January-March 1979*, NUREG/CR-0818 (ORNL/NUREG/TM-324), Union Carbide Corp. Nuclear Div., Oak Ridge Natl. Lab.

18. J. G. Merkle and H. T. Corten, "A J-Integral Analysis for the Compact Specimen, Considering Axial Force as Well as Bending Effects," *J. Press. Vessel Technol.*, Series J, *Trans. ASME* 96(4), 286-92 (1974).

19. J. G. Merkle, "New Method for Analyzing Small Scale Fracture Specimen Data in the Transition Zone," pp. 307-15 in *Proceedings of the U.S. Nuclear Regulatory Commission 10th Water Reactor Safety Research Information Meeting*, NUREG/CP-0041, Vol. 4, 1982.

5. PRESSURE VESSEL INVESTIGATIONS

R. H. Bryan

Posttest evaluation of intermediate test vessel (ITV) V-8A continued with measurement of properties of the low-upper-shelf weld seam and determination of flaw geometry. Preparations are being made for the first pressurized-thermal-shock experiment (PTSE-1). Two test vessels are being fabricated, one to be used for testing of the PTS experimental facility and the other for the first experiment PTSE-1. Fracture-mechanics (FM) analyses were made with candidate transients for the PTSE-1 and with upper-shelf behavior being considered explicitly for the first time. Further developmental tests of seals, thermocouples, and other apparatus were conducted; and test facility construction was nearly completed. Material property studies were continued to define the desired heat treatment of the vessel for PTSE-1.

5.1 Posttest Study of ITV V-8A

R. H. Bryan

Vessel V-8A was tested with a flaw in a special seam weld having low-upper-shelf toughness similar to that of irradiated high-copper weld metal.[1-3] After the test, the entire seam weld was removed and sectioned to separate the flawed region from the unbroken segments. The flaw geometry is being determined precisely, and the unbroken pieces of the weld seam are being used in studies related to both the V-8A test and preparations for a PTS test with low-upper-shelf material, possibly in PTSE-2.

Properties of the V-8A seam were investigated because the four characterization welds, which were prepared with the same materials and procedures as the V-8A seam, exhibited a remarkable scatter in upper-shelf toughness.[4]

5.1.1 Fracture surfaces of V-8A flaw

A block of material containing the V-8A flaw was removed from the test vessel, chilled in liquid nitrogen, and split along the fracture plane by wedge-loading the machine opening of the flaw. As indicated by photographs previously published, this splitting did not uncover the fracture surfaces at the two ends of the flaw.[5] Therefore, it was necessary to resection the two halves of the split block, chill the pieces in liquid nitrogen, and wedge apart the unopened portions of the fracture surfaces. This process produced about 20 fragments containing some portion of the fracture surfaces developed during the V-8A test.

The two complete fracture surfaces were reconstructed so that precise measurements of the flaw could be made. Photographs of the surfaces are shown in Figs. 5.1 and 5.2. The widths of saw cuts were measured and accounted for in reassembly of the surfaces. The V-8A flaw attained a depth of 102 mm and a length of 456 mm. This length is about 30 mm greater than

ORNL–PHOTO 6782–83 ETD

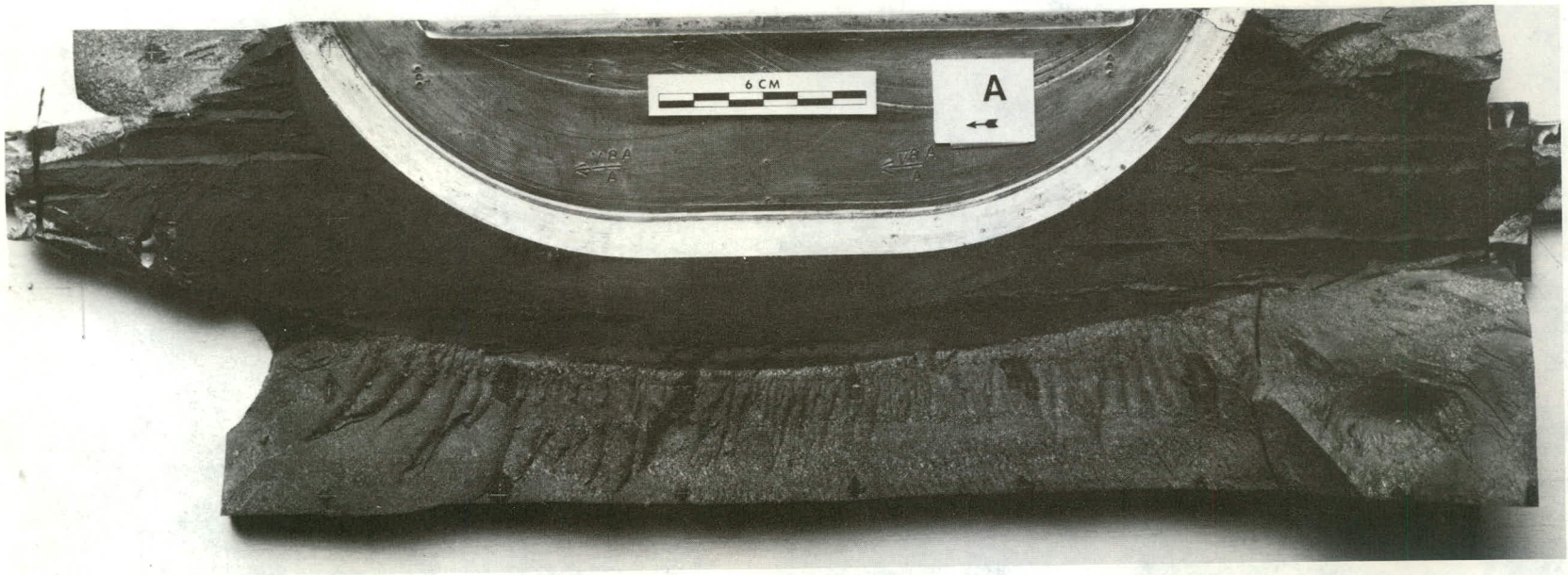

Fig. 5.1. Fracture surface A of V-8A flaw. Arrow points toward closure flange of test vessel. Pieces reattached to central part of flaw block were spaced to account for width of cuts.

ORNL–PHOTO 6781–83 ETD

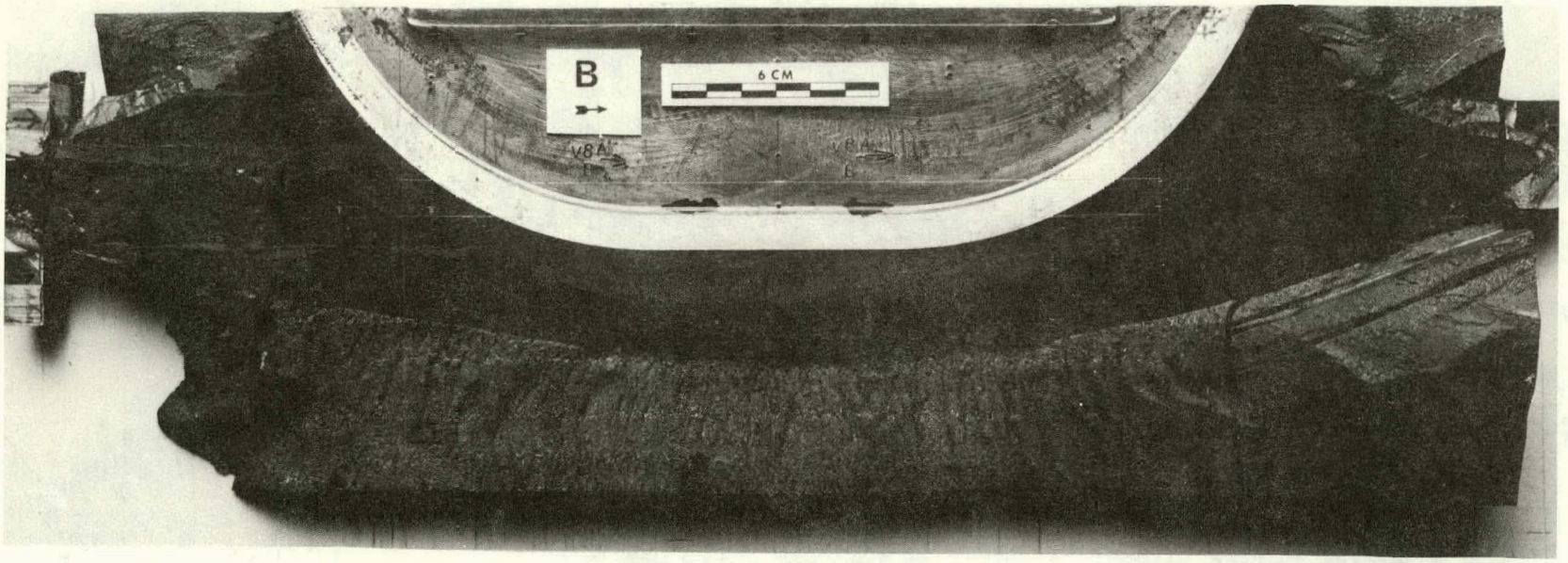

Fig. 5.2. Fracture surface B of V-8A flaw. The arrow points toward closure flange of test vessel. Pieces reattached to central part of flaw block were spaced to account for width of cuts.

that reported earlier on the basis of an ultrasonic scan of the flaw block.[5]

5.1.2 Tearing resistance of low-upper-shelf seam weld in vessel V-8A

A portion of the seam weld from vessel V-8A (piece V8A-CA) was sent to the Babcock & Wilcox Company (B&W) Alliance Research Center for determination of the tearing resistance J_R of the material. B&W had measured J_R of four characterization seam welds made of the same welding wire and flux and with the same welding procedure as the V-8A seam weld.[3,6] The four characterization welds, although nominally identical, indicated considerable scatter, as shown by their average J_R properties[4] (Fig. 5.3).

B&W tested ten nominally 25-mm-thick side-grooved compact specimens at 149°C. Eight specimens were of the WL orientation and two of WT orientation. The results reported by Domian and Futato[7] are summarized in Fig. 5.3 and Table 5.1. The WT data fall within the scatter band of WL data.

Table 5.1. J-integral average properties of V-8A characterization and vessel welds at 149°C

Weld	Number of specimens	J_{Ic} (kJ/m²)
V852	5	70.8
V862	6	61.5
V882	2	59.0
V8102	10	43.2
Vessel V-8A		
WT orientation	2	41.2
WL orientation	8	47.9

5.2 Pressurized-Thermal-Shock Studies

R. H. Bryan R. W. McCulloch

The principal effort in the experimental pressurized-thermal-shock (PTS) studies is toward performance of a test (PTSE-1) of an ITV.[8] Two test vessels are being fabricated from used ITVs. One of the two vessels is to be used for PTS test facility checks and preliminary thermal-hydraulic tests (PTSE-0) and the second for the fracture test PTSE-1. The PTSE-0 vessel will eventually be used for a fracture test.

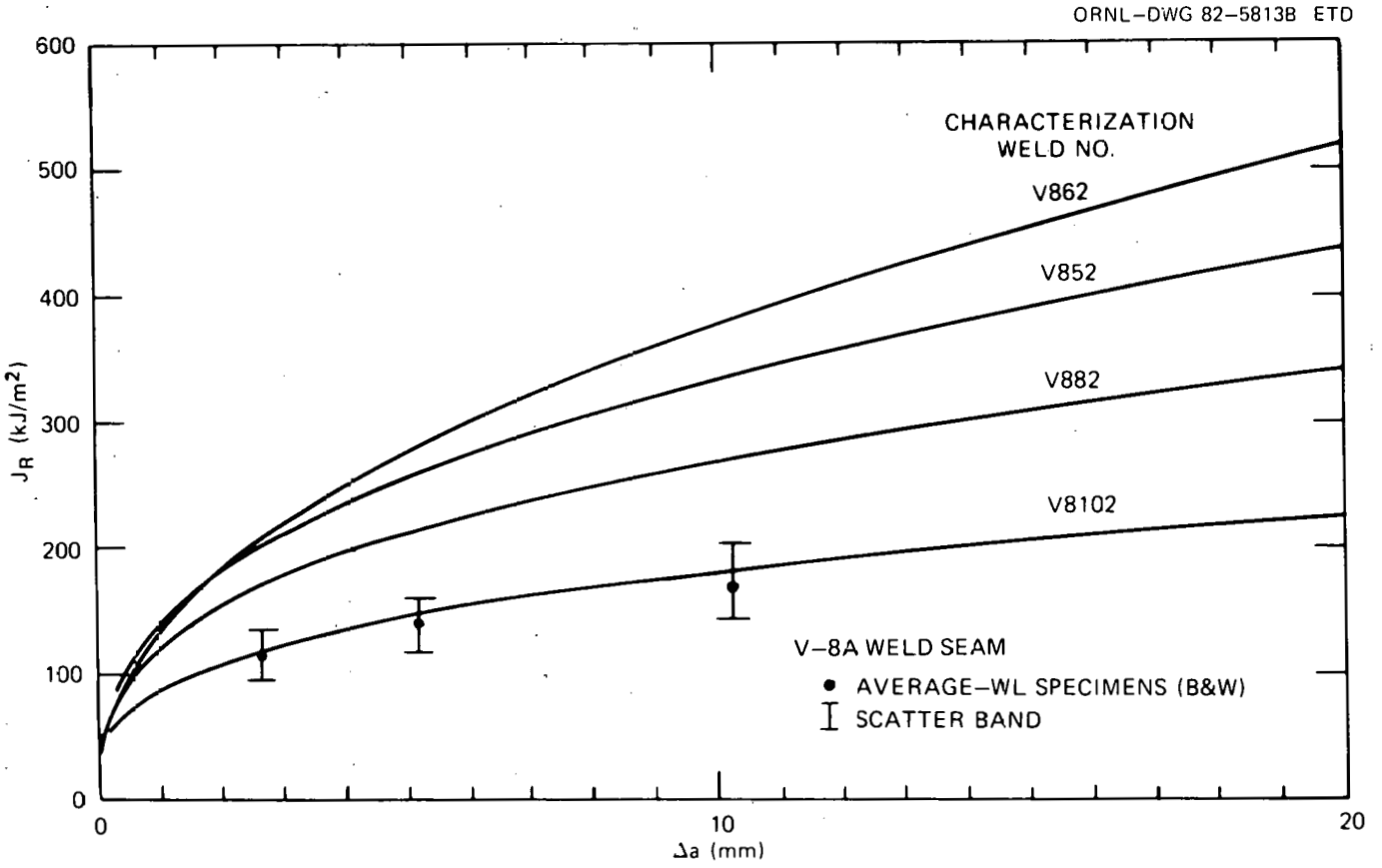

Fig. 5.3. J_R curves for average power law parameters for each of four V-8A characterization welds at 149°C. Additional data points are from posttest J_R measurements by B&W of vessel V-8A seam weld.

Some investigations pertaining to PTSE-2, which is tentatively planned as a test of low-upper-shelf material, are also being conducted. Materials available from the vessel V-8A test program are being studied. A piece of the V-8A seam weld will be used for crack-arrest toughness measurements in preparation for PTSE-2 and, perhaps, ESSO tests.

Construction of the PTS test facility was almost completed during the quarter. Conceptual designs were adopted for essential testing apparatus: the pressurization system, the data acquisition system (DAS), and seals. Some features of the testing system were abandoned because of cost or schedule constraints: principally automatic pressure controls, real-time fracture analysis from test data, and ultrasonic crack-depth measurements.

Development and application of methods of fracture analysis for investigating pressure-temperature transients in test vessels were pursued in two directions. In the first, a computer code (PTSUSA) was developed to determine J-integral-controlled fracture behavior on the upper shelf. A series of upper-shelf arrest analyses has been performed using PTSUSA to demonstrate the influence of test conditions on the outcome of a PTS test. In the second direction, 3-D ADINA-ORVIRT studies were performed as a basis for developing a version of the OCA code that will account for the effects of finite flaw, finite cylinder, and uncooled heads on the PTS test vessel. This modified OCA analysis capability is being used to carry out parametric analyses covering potential ranges of PTSE variables.

A study of the effects of various temper treatments on toughness is being conducted to determine the heat treatment to be applied to the vessels for PTSE-0 and -1, in which the selected test material has been plug welded.

5.2.1 Elastic-ideally-plastic PTS analysis for a deep continuous external longitudinal crack in a cylinder (J. G. Merkle)

In previous progress reports, closed-form solutions were presented for analyzing the effects of thermal-shock loading, under elastic conditions, on deep continuous internal longitudinal[9] and circumferential[10] surface cracks in pressure vessels, and the effects of complete ligament yielding without strain hardening in the case of internal longitudinal cracks.[11] More recently it has become necessary to consider the effects of vessel internal pressure as well as those of thermal-shock loading, with specific attention being given to the design of ITV experiments using internal pressure, external flaws, and external thermal-shock loading. The objective of the analysis to be presented here is to extend the previous analyses to cover deep, continuous, external, longitudinal surface cracks subjected to pressure as well as thermal loading, with complete ligament yielding, but without strain hardening.

Because the crack is assumed to be deep, it is reasonable to adopt the strip-yield-model philosophy by assuming that yielding occurs only on the plane ahead of the crack tip. When the ligament is completely yielded, the stress distribution directly ahead of the crack is an ideally plastic stress distribution, and the crack-plane displacements are the elastic ring bending displacements corresponding to the applied loading and the crack-plane tractions.[11]

To calculate the elastically induced displacements of the crack faces, a section of the cylinder is modeled as a cut ring, with one end fixed and the other end free (Fig. 5.4). For $\phi_{max} = 2\pi$ and radially symmetric loading, $X_a = 0$, and the total relative displacements of the crack faces are equal to the elastically calculated displacements of the free end, given by

$$\begin{Bmatrix} \theta \\ \Delta_y \end{Bmatrix} = \frac{1}{EI} \begin{bmatrix} 2\pi r & -2\pi r^2 \\ -2\pi r^2 & 3\pi r^3 \end{bmatrix} \begin{Bmatrix} M_a \\ Y_a \end{Bmatrix} , \tag{5.1}$$

where positive displacements and rotations are defined as those occurring in the directions of the positive tractions.

Referring to Fig. 5.5, the moment causing bending deflections that act on the crack plane is given by

$$M_a = -M_B - \sigma_Y \left[-d^2 + dw - \left(\frac{bw}{2} - \frac{b^2}{2} \right) \right] , \tag{5.2}$$

where M_B is the moment of the total stress distribution acting in the uncracked ring. The moment M_B can be represented by

$$M_B = \frac{\sigma_B w^2}{6} , \tag{5.3}$$

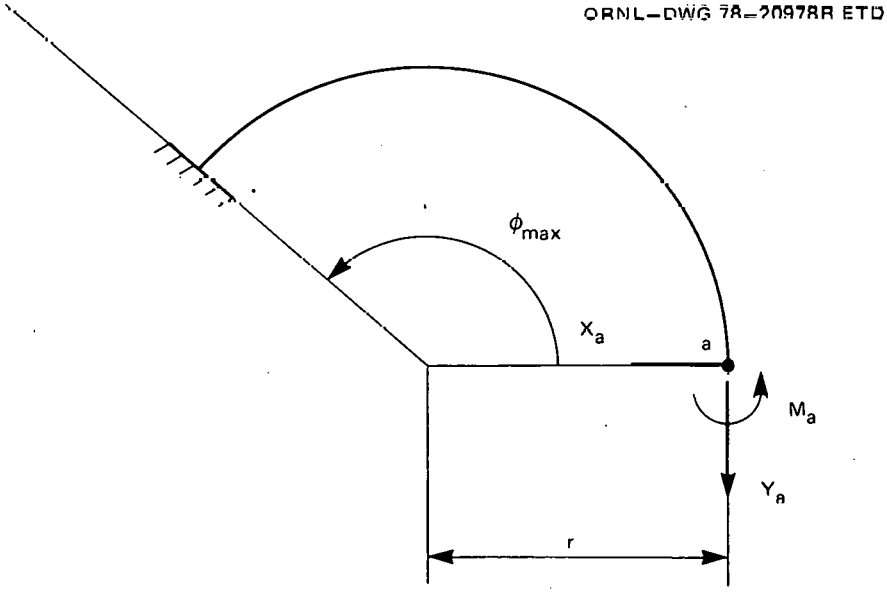

Fig. 5.4. Cut ring model of cylinder containing continuous longitudinal surface crack.

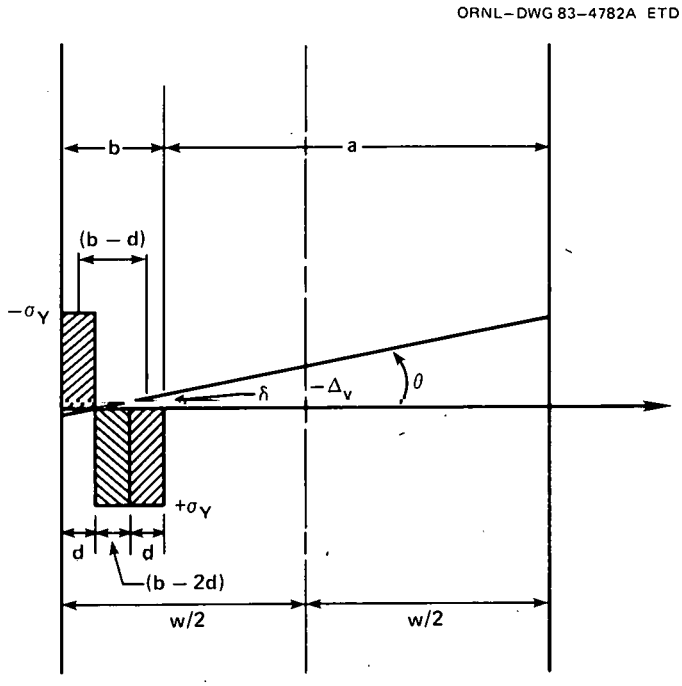

Fig. 5.5. Ideally plastic model of uncracked ligament in cylinder containing continuous external longitudinal surface crack.

where σ_B is the linearized inside surface thermal stress. The force causing bending deflections that acts on the crack plane is given by

$$Y_a = -\sigma_Y (2d - b) - \sigma_p w , \tag{5.4}$$

where

$$\sigma_p = p\left(\frac{r_i}{w}\right) . \tag{5.5}$$

Referring again to Fig. 5.5, the crack-plane displacement-rotation relations are given by

$$-\Delta_y = \theta\left(\frac{w}{2} - d\right) , \tag{5.6}$$

and

$$\delta = \theta(b - d) . \tag{5.7}$$

Note that the sign convention adopted here results in the crack-tip-opening displacement (COD) δ being positive when the crack-opening angle θ is positive for an external surface crack.

The problem solution is obtained by using Eq. (5.6) to eliminate Δ_y in Eq. (5.1), then eliminating θ and solving Eq. (5.1) for (d/b). This locates the hinge point, which is the point of stress reversal in the fully yielded remaining ligament. The resulting equation for (d/b) is

$$\left(\frac{b}{w}\right)^2 \left(\frac{d}{b}\right)^3 + C_2 \left(\frac{d}{b}\right)^2 + C_1 \left(\frac{d}{b}\right) - C_0 = 0 \ , \tag{5.8}$$

where

$$C_0 = \left[1 - \frac{\left(\frac{\sigma_p}{\sigma_Y}\right)}{\left(\frac{b}{w}\right)}\right] \frac{1}{2} \left(\frac{r}{w}\right) \left(3 \frac{r}{w} - 1\right) - \left(\frac{r}{w} - \frac{1}{2}\right) \left[-\frac{1}{6} \frac{\left(\frac{\sigma_T}{\sigma_Y}\right)}{\left(\frac{b}{w}\right)} + \frac{1}{2} \left(1 - \frac{b}{w}\right)\right] \ , \tag{5.9}$$

$$C_1 = 3 \left(\frac{r}{w}\right)^2 - \left(2 + \frac{b}{w} - \frac{\sigma_p}{\sigma_Y}\right) \left(\frac{r}{w}\right) + \frac{1}{2} - \frac{1}{6} \left(\frac{\sigma_T}{\sigma_Y}\right) + \frac{1}{2} \left(\frac{b}{w}\right) \left(1 - \frac{b}{w}\right) \ , \tag{5.10}$$

and

$$C_2 = 3 \left(\frac{b}{w}\right) \left(\frac{r}{w} - \frac{1}{2}\right) \ . \tag{5.11}$$

For the case of (d/b) > 0, corresponding to the hinge point located inside the remaining ligament, Eq. (5.8) can be solved by iteration, using the rearranged form

$$\left(\frac{d}{b}\right) = \frac{C_0 - C_2 \left(\frac{d}{b}\right)^2 - \left(\frac{b}{w}\right)^2 \left(\frac{d}{b}\right)^3}{C_1} \ . \tag{5.12}$$

The crack-plane moment can be obtained by noting that

$$\left(\frac{d}{w}\right) = \left(\frac{d}{b}\right) \left(\frac{b}{w}\right) \ , \tag{5.13}$$

and then combining Eqs. (5.2) and (5.3) to read

$$\frac{M_a}{M_B} = -1 + \frac{6}{(\sigma_B/\sigma_Y)} \left[\left(\frac{d}{w}\right)^2 - \left(\frac{d}{w}\right) + \frac{1}{2} \left(\frac{b}{w}\right) \left(1 - \frac{b}{w}\right)\right] \ . \tag{5.14}$$

The crack plane bend angle and centerline vertical displacement are given by

$$\frac{\theta}{2\pi\varepsilon_Y} = 2\left(\frac{r}{w}\right)\left(\frac{\sigma_B}{\sigma_Y}\right)\left(\frac{M_a}{M_B}\right) + 12\left(\frac{r}{w}\right)^2\left[-\left(\frac{b}{w}\right) + 2\left(\frac{d}{w}\right) + \left(\frac{\sigma_p}{\sigma_Y}\right)\right] \tag{5.15}$$

and

$$\frac{-\Delta_y}{2\pi\varepsilon_Y r} = 2\left(\frac{r}{w}\right)\left(\frac{\sigma_B}{\sigma_Y}\right)\left(\frac{M_a}{M_B}\right) + 18\left(\frac{r}{w}\right)^2\left[-\left(\frac{b}{w}\right) + 2\left(\frac{d}{w}\right) + \left(\frac{\sigma_p}{\sigma_Y}\right)\right] . \tag{5.16}$$

Finally, the COD is calculated by rearranging Eq. (5.7) to read

$$\delta = \theta w\left(\frac{b}{w}\right)\left(1 - \frac{d}{b}\right) . \tag{5.17}$$

Referring to Fig. 5.5, when the distance d is reduced to zero, the remaining ligament becomes completely yielded in tension, even though a strain gradient still exists in the ligament. For this condition, Eq. (5.8) reduces to

$$C_o = 0 . \tag{5.18}$$

Consequently, using Eq. (5.9), the ligament size for a given loading at which the ligament becomes completely yielded in tension is given by

$$\left(\frac{b}{w}\right)^2 + \left(\frac{b}{w}\right)\left[\frac{\left(\frac{r}{w}\right)\left(3\,\frac{r}{w} - 1\right)}{\left(\frac{r}{w} - \frac{1}{2}\right)} - 1\right] + \left[\frac{1}{3}\left(\frac{\sigma_B}{\sigma_Y}\right) - \left(\frac{\sigma_p}{\sigma_Y}\right)\frac{\left(\frac{r}{w}\right)\left(3\,\frac{r}{w} - 1\right)}{\left(\frac{r}{w} - \frac{1}{2}\right)}\right] = 0 . \tag{5.19}$$

Also, by rearranging Eq. (5.19), the pressure at the onset of complete tensile yielding in the remaining ligament, for a given ligament size and thermal loading, is given by

$$\frac{\sigma_p}{\sigma_Y} = \frac{b}{w} - \frac{\left(\frac{r}{w} - \frac{1}{2}\right)}{\left(\frac{r}{w}\right)\left(3\,\frac{r}{w} - 1\right)}\left[\left(\frac{b}{w}\right) - \left(\frac{b}{w}\right)^2 - \frac{1}{3}\left(\frac{\sigma_T}{\sigma_Y}\right)\right] . \tag{5.20}$$

For the case of (d/b) = 0, the crack plane moment, bend angle, centerline vertical displacement, and the COD can all be obtained from Eqs. (5.14)–(5.17) by setting (d/b) = 0.

For the case of the remaining ligament fully yielded in tension, with the hinge plot located outside the ligament, the stress distribution in the ligament is independent of the hinge point location, being the same as for d = 0. Therefore, using Eq. (5.14), the crack-plane bending movement is given by

$$\frac{M_a}{M_B} = \frac{3\left(\frac{b}{w}\right)\left(1 - \frac{b}{w}\right)}{\left(\frac{\sigma_B}{\sigma_Y}\right)} - 1 \ . \tag{5.21}$$

The crack-plane bend angle and vertical centerline displacement are given by

$$\frac{\theta}{2\pi\varepsilon_Y} = 2\left(\frac{r}{w}\right)\left(\frac{\sigma_B}{\sigma_Y}\right)\left(\frac{M_a}{M_B}\right) + 12\left(\frac{r}{w}\right)^2\left(\frac{\sigma_p}{\sigma_Y} - \frac{b}{w}\right) , \tag{5.22}$$

and

$$\frac{-\Delta_y}{2\pi\varepsilon_Y r} = 2\left(\frac{r}{w}\right)\left(\frac{\sigma_B}{\sigma_Y}\right)\left(\frac{M_a}{M_B}\right) + 18\left(\frac{r}{w}\right)^2\left(\frac{\sigma_p}{\sigma_Y} - \frac{b}{w}\right) . \tag{5.23}$$

Finally, using Fig. 5.5, the COD δ is given by

$$\delta = -\Delta_y - \theta w\left(\frac{1}{2} - \frac{b}{w}\right) . \tag{5.24}$$

These equations were initially used to investigate the effects of ligament yielding on the COD for a deep external thermally loaded surface crack in an ITV. A comparison, based on elastic analysis, had previously been made between the effects of the same thermal-shock loading on outside vs inside surface cracks in an ITV.[12] From those studies, it was concluded that for flaw depths less than half the vessel wall thickness, there is little difference between the stress-intensity factors for the two flaw locations.[12] Using a yield stress of 517 MPa (75 ksi) and a linearized thermal stress loading of $\sigma_B/\sigma_Y = -1$, calculations were made to determine the effects of ligament yielding for the external flaw. The results, shown in Fig. 5.6, indicate that for thermal loading only, the effects of yielding are negligible until the ligament becomes fully

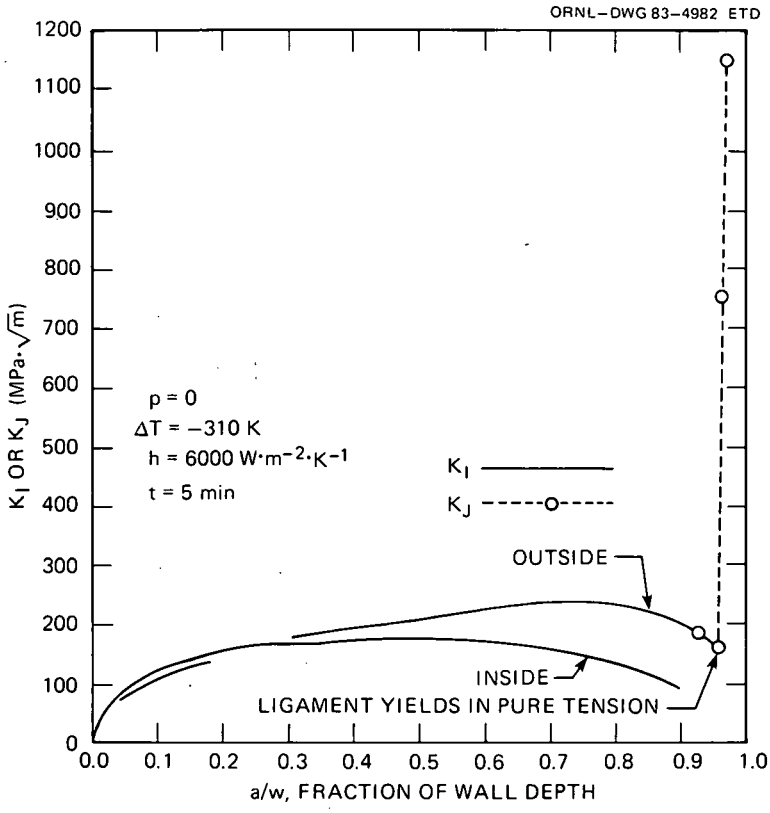

Fig. 5.6. Effects of yielding, without strain hardening, on crack driving force for continuous external longitudinal surface crack in thermally shocked cylinder.

yielded in tension, after which the stretching of the ligament causes large increases in the COD. For purposes of comparison with elastic analysis, the calculated CODs are expressed in terms of equivalent stress-intensity factors by using the conversions

$$J = \sigma_Y \delta \ , \tag{5.25}$$

and

$$K_J = \sqrt{EJ} \ . \tag{5.26}$$

The results shown in Fig. 5.6 illustrate some fundamental differences between the behavior of very deep flaws subject to thermal loading only, because of yielding and flaw location. Whereas elastic analysis indicates that the stress-intensity factors for both deep external and internal

cracks approach zero as a/w approaches unity, uniform tensile yielding eventually causes the remaining ligament ahead of a very deep external surface crack to stretch, producing large crack openings. As pointed out in Ref. 11, the opposite happens in the case of a very deep internal surface crack; that is, the ligament eventually yields in uniform compression and the COD becomes zero. However, for thermal loading only, these effects do not occur until the crack has penetrated more than 90% of the vessel wall.

A second application of the analysis was made to determine the effects of ligament yielding in an ITV containing a continuous external surface crack and subjected to internal pressure as well as external thermal shock. The analysis was based on a linear fit to the stress distribution determined by the OCA code, for p = 82.7 MPa, ΔT = 213.9 K, h = 5675 $W \cdot m^{-2} \cdot K^{-1}$, and t = 6 min. The total stress distribution was fit with a straight line, and the results were separated to give a bending stress represented by $\sigma_B/\sigma_Y = -0.430$ and a uniform stress represented by $\sigma_p/\sigma_Y = 0.266$. The yield stress σ_Y was assumed to be 700 MPa. Based on Eq. (5.19), it was determined that the relative crack depth a/w at which the remaining ligament would become fully yielded in tension would be 0.694. Figure 5.7 shows a comparison between the ideally plastic ligament analysis and a completely elastic analysis. The lower intersection

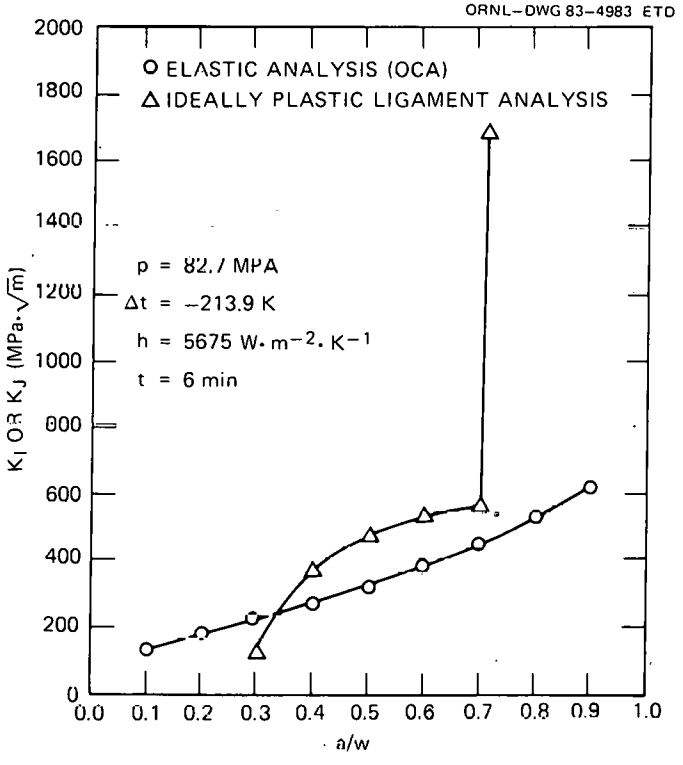

Fig. 5.7. Effects of yielding, without strain hardening, on crack driving force for continuous external longitudinal surface crack in cylinder subjected to internal pressure and external thermal shock.

of the two curves identifies the crack depth below which the ideally plastic analysis should be disregarded because the remaining ligament is not yet completely yielded. At a/w = 0.694, the ligament becomes completely yielded in tension, causing large increases in the COD. By comparing Figs. 5.6 and 5.7, the effect of vessel internal pressure is to reduce the value of a/w at which the remaining ligament becomes completely yielded in tension. In addition, unlike the case of thermal loading only, ligament yield causes K_J to significantly exceed K_I prior to the development of complete tensile yielding in the remaining ligament. Thus, at least a plastic zone size correction is desirable for a PTS analysis.

It is expected that an elastic-plastic analysis considering strain hardening would produce K_J values lying between the two curves shown in Fig. 5.7. The results of such an analysis, using the ORGMEN-ADINA ORVIRT codes, are presented in Sect. 5.2.2 of this report.

5.2.2 Fully plastic ligament study of an ITV for combined pressure-thermal loading using ADINA-ORVIRT (J. W. Bryson, J. G. Merkle, B. R. Bass)

A fully plastic ligament study of an ITV under combined pressure-thermal loading was conducted using the ADINA-ORVIRT finite-element system.[13,14] The thermal loading represents a thermal shock on the outside surface of an ITV. The vessel is initially at a uniform temperature of 190.6°C and is suddenly exposed to a fluid at −23.3°C with a heat transfer coefficient of 5675 $W \cdot m^{-2} \cdot K^{-1}$. An internal pressure loading, p = 82.7 MPa, was applied. Outside surface longitudinal cracks were considered with a crack-depth-to-wall-thickness ratio in the range $0.5 \leq a/w \leq 0.8$. The ADINA-ORVIRT analysis represents a 2-D, plane-strain analysis using a deformation theory plasticity material model. A von Mises yield condition and isotropic strain hardening are employed.

Figure 5.8 shows the results of the study at t = 6 min into the thermal transient in the form of a pseudo K value vs a/w. In addition, an elastic-only analysis using OCA is shown as well as the simplified closed-form analysis discussed in Sect. 5.2.1, which does not account for strain hardening. The results indicate that yielding in the ligament ahead of a deep continuous longitudinal crack in a cylinder subjected to PTS loading causes the COD to exceed elastically calculated values. In addition, the ADINA-ORVIRT calculated crack-tip depth at which large increases in COD begin to occur because of yielding of the remaining ligament in uniform tension agrees with the ideally plastic closed-form analysis. These studies suggest that consideration of plastic instability in PTSE analyses is necessary because elastic analyses become unconservative for deep cracks.

5.2.3 Upper-shelf arrest analysis based on J_R-controlled tearing (R. H. Bryan and J. G. Merkle)

5.2.3.1 Development of method. One of the objectives of the series of PTS tests is to investigate the mechanisms of crack arrest initiated in cleavage and propagated into a region in which temperatures are high enough for the material to be considered completely ductile. One model for describing this type of upper-shelf arrest presumes that there is a

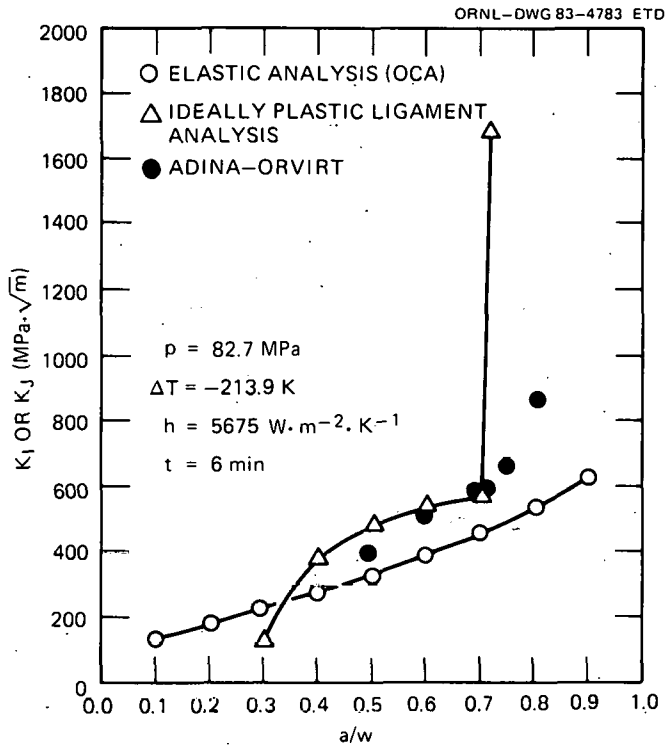

Fig. 5.8. A comparison of three methods of analyzing longitudinal outside cracks of uniform depth in test cylinder under combined pressure-thermal loading. The K_J values determined by ideally plastic ligament analysis and ADINA-ORVIRT analysis indicate crack depth at which plastic instability is approached.

temperature T_D above which ductile fracture (even though fast) will prevail and below which fracture will be entirely by a cleavage mode. This assumption is made in the present study, because there is some empirical evidence that there is a purely ductile regime, even though the transition admits mixed-mode fractures. Transitional behavior involving simultaneous cleavage and ductile fracture during a small increment of crack extension is ignored.

In PTS transient of practical interest, a growing crack runs into a monotonically increasing temperature field. Thus, one should ask what mechanism of fracture will control crack growth after the crack enters the ductile upper-shelf regime ($T > T_D$). As indicated by dynamic tests of large specimens, T_D is in the neighborhood of ~100 K higher than RT_{NDT};[15,16] and at such temperatures, crack-arrest toughness data are rare. Under these circumstances, the extrapolated K_{Ia} curve from Sect. XI of the ASME Code does not appear to be the most reliable basis for planning an upper-shelf arrest experiment. On the other hand, one can, with J_R data, investigate whether a crack in a region where $T > T_D$ would be stable in a quasi-static sense. ORNL has developed the computer program PTSUSA to analyze this stability question.

The procedure for determining upper-shelf stability points is illustrated in Fig. 5.9. Temperatures in the wall of a vessel during a transient can be represented as contours in a crack depth vs time (a vs t) graph [Fig. 5.9(*a*)]. At any given time t′ (less than some t_{max}), there is a crack depth a′ at which the temperature $T = T_D$. Suppose that, if a crack has a depth a′, its continued growth will be controlled by a tearing resistance J_R, which generally is a function of an increment in crack growth $\Delta a = a - a'$ and the temperature of the material at the crack tip. The condition for crack growth is

$$J_I\,(a) > J_R\,[a - a',\ T\,(a)]\ . \tag{5.27}$$

A crack of depth a will be stable when

$$J_I\,(a) \leq J_R\,[a - a',\ T\,(a)]\ . \tag{5.28}$$

These conditions are illustrated in Fig. 5.9(*b*) for t = t′.

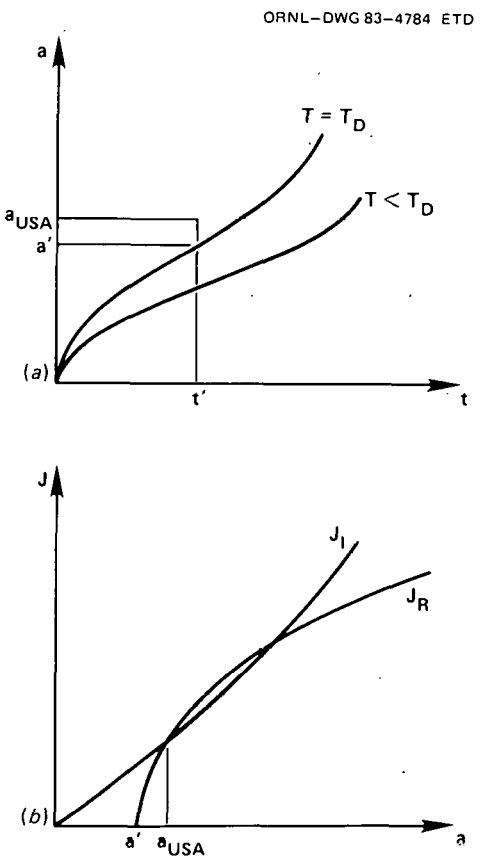

Fig. 5.9. Factors determining crack stability on upper shelf during pressurized-thermal-shock transient: (*a*) temperature contours in a-t plane; (*b*) J_I and J_R at t = t′.

The PTSUSA code uses temperature and K_I vs a and t calculated by the OCA-I code. The PTSUSA code makes a plastic zone size correction to the K_I values input from OCA, converts K_I to J_I, performs the computations of stable and unstable upper-shelf points, and plots results on an a/w-vs-t plot similar to an OCA critical-crack-depth plot. The point of incipient instability is defined as the last stable J_R-controlled crack depth with $a/w < (a/w)_m$, where $(a/w)_m$ is the greatest value of a/w for which K_I is defined by OCA. In OCA-I, values of K_I are not defined for $a/w > 0.9$, principally because there is little practical interest in deep crack behavior in a real vessel. The discussion of Fig. 5.6 in Sect. 5.2.1 identifies some of the difficulties of analyzing outside surface flaws with $a/w > 0.9$.

5.2.3.2 Application to PTSE-1. At this stage in the development of plans for PTSE-1, the material property data used for input to OCA or PTSUSA are either assumed on the basis of past thermal-shock experiments (as in earlier OCA studies of PTSE-1) or inferred from Charpy-V impact test data for material being considered for PTSE-1.

The first PTSUSA case illustrated here uses the same PTS transient as used in the plastic instability analyses discussed in Sects. 5.2.1 and 5.2.2. The parameters for this transient are given in Table 5.2. The upper-shelf arrest results are shown in Fig. 5.10 for two values of T_D.

Table 5.2. PTS parameters used in PTSUSA, OCA, and plastic instability analyses

Parameter	Value					
Constants						
Initial temperature, T_o (°C)	191					
RT_{NDT} (°C)	13					
Ductility temperature, T_D (°C)	120, 130					
J_R parameters[a]						
C	2.16					
n	0.359					
Variables (linear between time points)						
	Time (min)					
	0	3	4	5	6	20
Coolant temperature, T_c (°C)	−23					12
Pressure, P (MPa)	27.6	27.6	20.7	48.3	82.7	82.7

[a] $J_R = C(\Delta a)^n$; J_R in MJ/m^2, Δa in m.

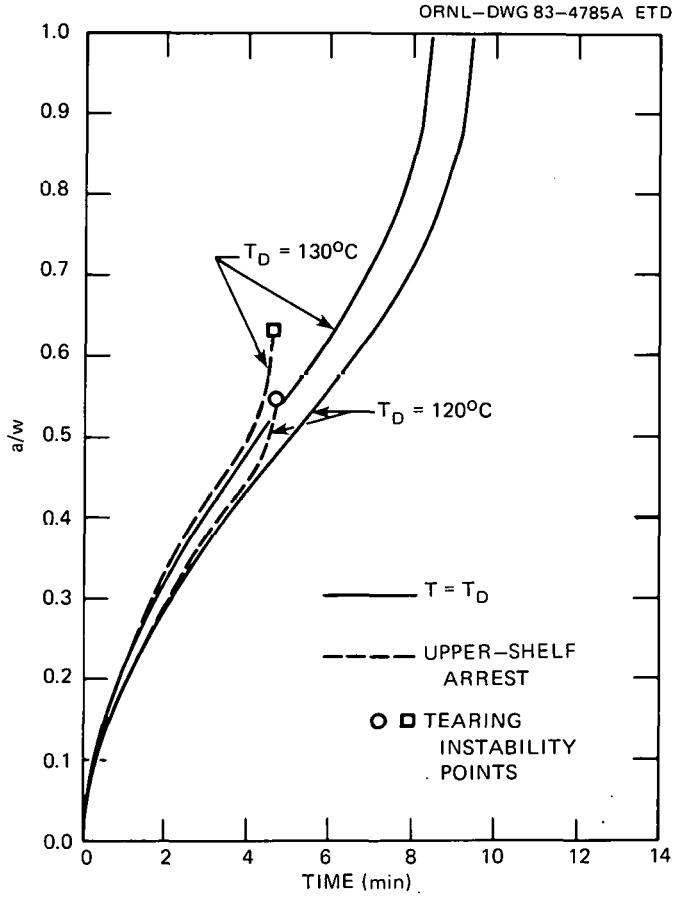

Fig. 5.10. Upper-shelf arrest curves from PTSUSA analysis of transient for which plastic instability was analyzed.

In this example, it can be seen that cracks initiating after ~4.9 min would be unstable on the upper shelf, if T_D = 120°C; for this case, the deepest crack that would be stable with respect to tearing would have a fractional crack depth a/w = 0.55. If T_D = 130°C, the deepest stable crack has a depth a/w = 0.64. Therefore, in this case a tearing instability would probably precede a plastic instability, which would not occur for a/w less than ~0.7 at t = 6 min, as indicated by Fig. 5.7.

The physical significance of an upper-shelf arrest curve in a PTS transient must be interpreted on the basis of the nature of the transient at the time of an upper-shelf arrest (see Fig. 5.11). In this example, a crack initiating at $t \geq T_I$ would not arrest. If a crack is initiated at some earlier time t_1 and arrests on the upper shelf at $a = a_1$ (point 1), it will or will not continue to tear depending on whether J_I continues to increase or decrease with time for crack depth a_1. If J_I increases, as in the PTS cases under discussion here, the crack would tear in a stable manner to point 2 and thereafter tear unstably. The secondary tearing instability (at point 2) will occur at a later time than the primary instability at t_I; that is, $t_2 > t_I$. The secondary instability would be prevented by changing the transient in such a way that J_I decreases after the

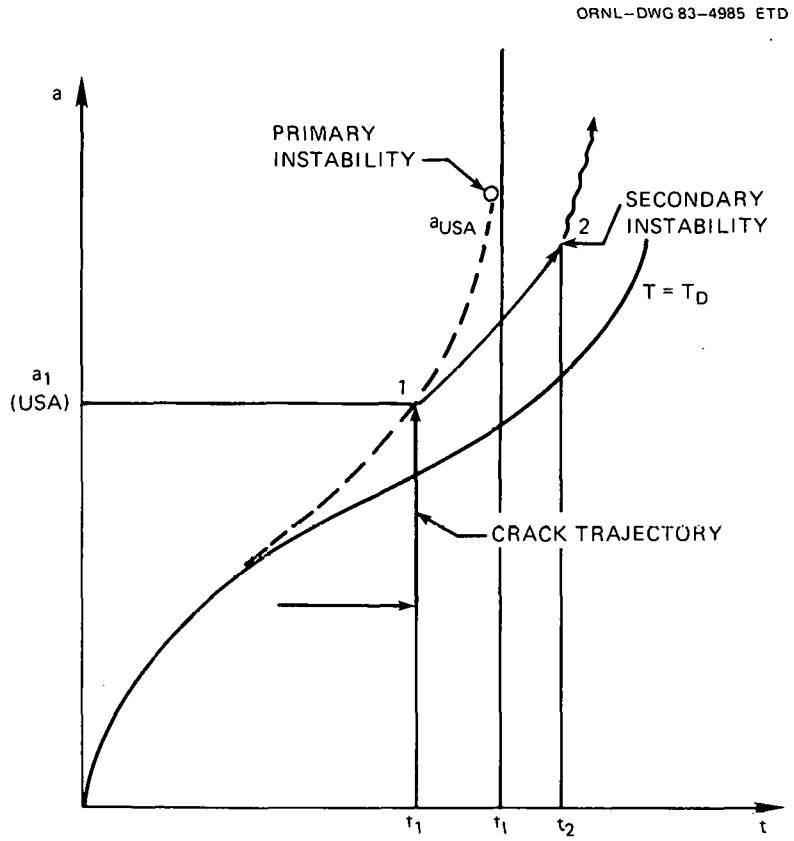

Fig. 5.11. Upper-shelf arrest and stable tearing trajectories for pressurized-thermal-shock transient with monotonically increasing pressure.

upper-shelf arrest, for example, by stopping pressure increases after time t_1. This aspect of the upper-shelf-arrest phase of PTSE-1 will be investigated further to determine the control measures that must be used during the test.

A series of PTSUSA and OCA analyses was studied to indicate the sensitivity of the results to variations of the following parameters: maximum pressure (p_{max}), T_O, T_D, C, and n. Base case values of the parameters are given in Table 5.3, and variation cases are defined in Table 5.4.

Until K_{Ic}, K_{Ia}, and J_R data are measured in FM specimen tests of the material used in the PTSE-1 vessel, estimates of these properties are being based on the best available data. Currently, these properties are being inferred from Charpy-V impact test data of material being investigated for determining the heat treatment process for the PTSE-1 vessel (see Sect. 5.2.5). The tentatively chosen material has an upper-shelf Charpy energy of ~110 J and a $T_{cv_{40}J} \simeq 40°C$. $T_{cv_{40}J}$ is a reasonable definition of RT_{NDT} for purposes of defining K_{Ic} and K_{Ia} as functions of temperature by use of the equations of Sect. XI of the ASME Code. This definition of an effective RT_{NDT} produces excellent agreement of OCA calculations and actual observations of four fracture initiations in TSE-5A (Ref. 17). The J_R power law parameters were determined by the Naval Research

Table 5.3. PTS parameters for base case PTSUSA-OCA analysis (Case C)

Parameter	Value
Constants	
T_o (°C)	200
RT_{NDT} (°C)	40
T_D (°C)	150
C^a	2.16
n^a	0.359

Variables (linear between time points)

	Time (min)			
	0	4	6	20
T_c (°C)	−23			12
p (MPa)	30	30	70^b	70^b

[a] $J_R = C(\Delta a)^n$; J_R in MJ/m², Δa in m.

[b] p_{max}.

Table 5.4. Definition of parameter variations for PTSUSA-OCA study

(Parameter values in units of Table 5.3)

Case	Parameter				
	p_{max}	T_o	T_D	C/C_c [a]	n/n_c [a]
C	70	200	150	1	1
D	70	200	130, 140, 150	1	1
E	70	200	150, 160, 170	1	1
F	70	200	150	0.8, 1.0, 1.2	1
G	70	200	150	1	0.8, 1.0, 1.2
H	60	200	150	1	1
I	80	200	150	1	1
J	70	240	150	1	1
K	70	280	150	1	1

[a] C_c, n_c = values for case C.

Laboratory and reported in Ref. 18 for material with a Charpy upper-shelf impact energy of 110 J.

Cases E, F, and G show the effects of varying the values of the upper-shelf parameters: T_D, C, and n, where C and n are the constants in the power-law expression for J_R,

$$J_R = C\,(\Delta a)^n \quad . \tag{5.29}$$

Figure 5.12 shows that a variation of the cleavage-ductile transition temperture makes a substantial difference in the extent of stable tearing

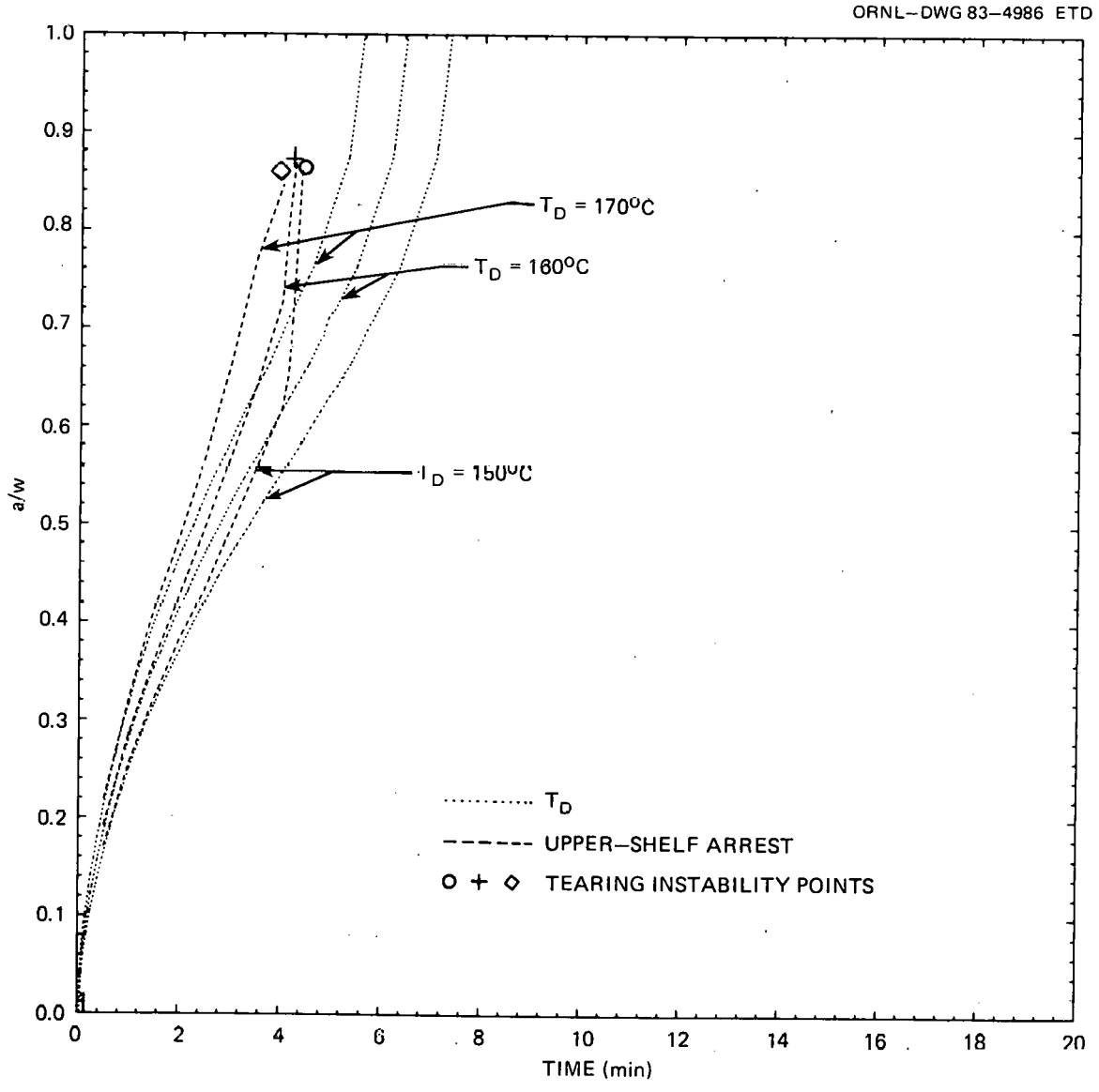

Fig. 5.12. Upper-shelf arrest and instability results from PTSUSA case E. Effects of different T_D values are shown.

that is possible and a slight difference in the times of instability. Similarly, Figs. 5.13 and 5.14 show the effects of ±20% variations in the J_R parameters C and n. These cases indicate that, in PTSE-1, it may be easier to tolerate uncertainties in upper-shelf toughness than an underestimate of T_D.

Figures 5.15 and 5.16 show the results of PTSUSA and OCA calculations for cases H and C, respectively, in which only p_{max} is different. Cleavage initiation (for small flaws) and arrest conditions are practically unaffected by the change in pressure. There is a time window, 2 min $\lesssim$ t

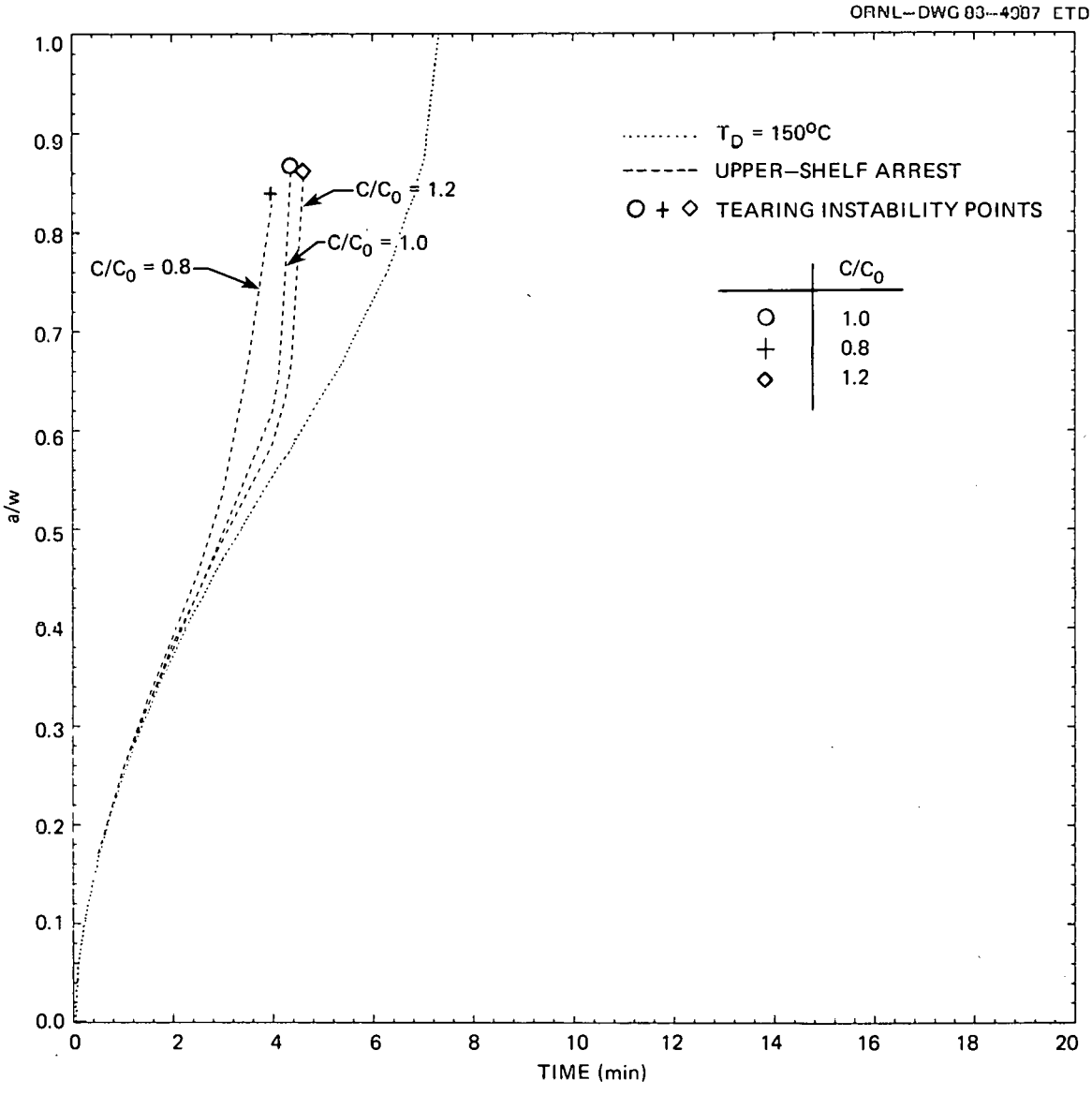

Fig. 5.13. Upper-shelf arrest and instability results for PTSUSA case F. Effects of different values of parameter C in $J_R = C\,(\Delta a)^n$ are shown.

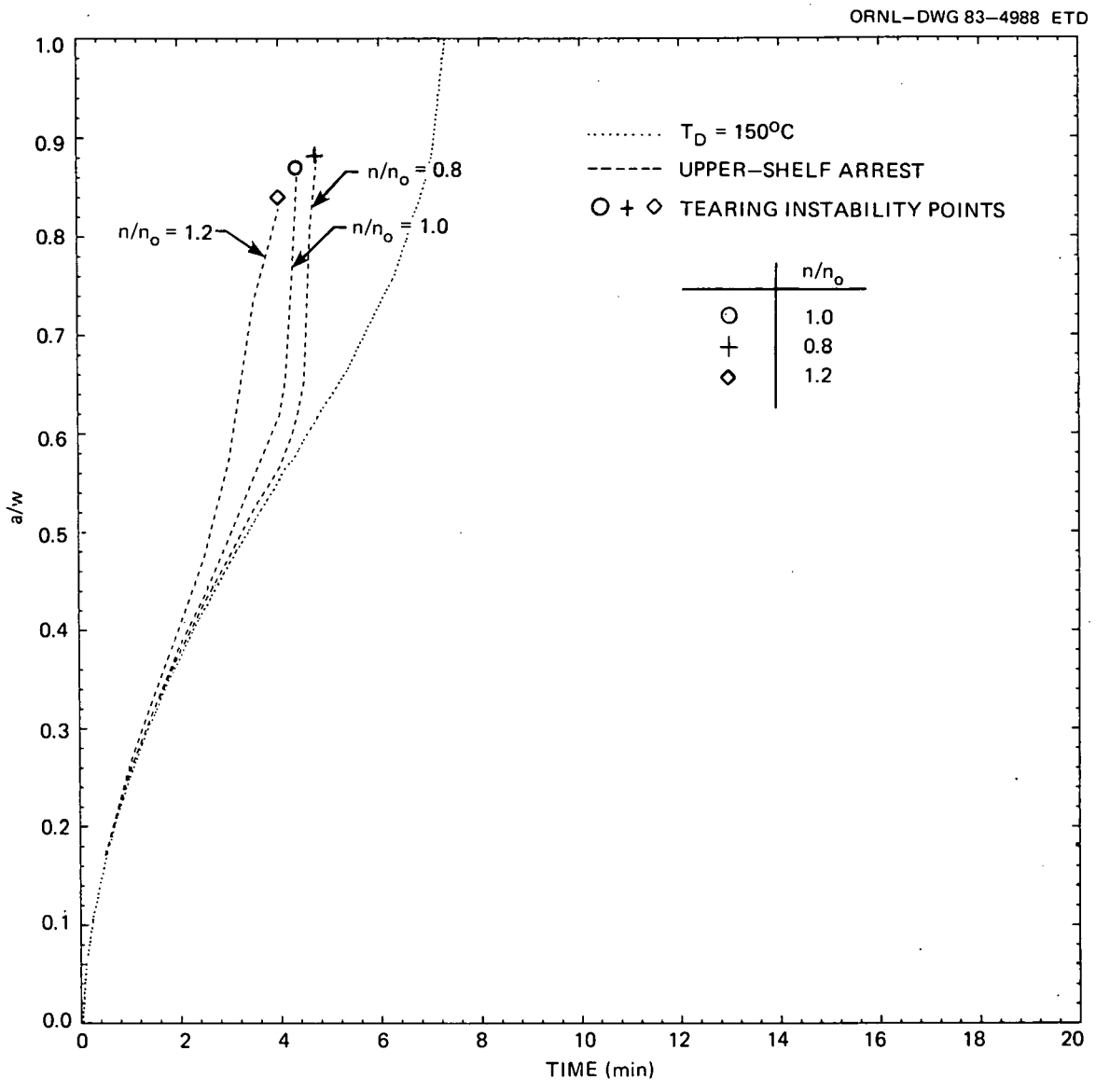

Fig. 5.14. Upper-shelf arrest and instability results for PTSUSA case G. Effects of different values of parameter n in $J_R = C\ (\Delta a)^n$ are shown.

$< t_I$, during which upper-shelf conditions would control the arrest of a crack initiated in cleavage. It is important to recognize that the $K_I = K_{Ia}$ arrest points above $a/w \simeq 0.2$ may be fictitious, because they are based on a $K_{Ia}(T)$ relationship at temperatures for which there are no crack-arrest data. These cases also indicate that an upper-shelf arrest could be achieved at a/w values from ~0.4 to 0.7 without interference from a net ligament instability, because the pressure for $t < t_I$ is less than ~42 MPa and at an a/w = 0.7 the pressure for ligament instability by Eq. (5.20) would be >80 MPa.

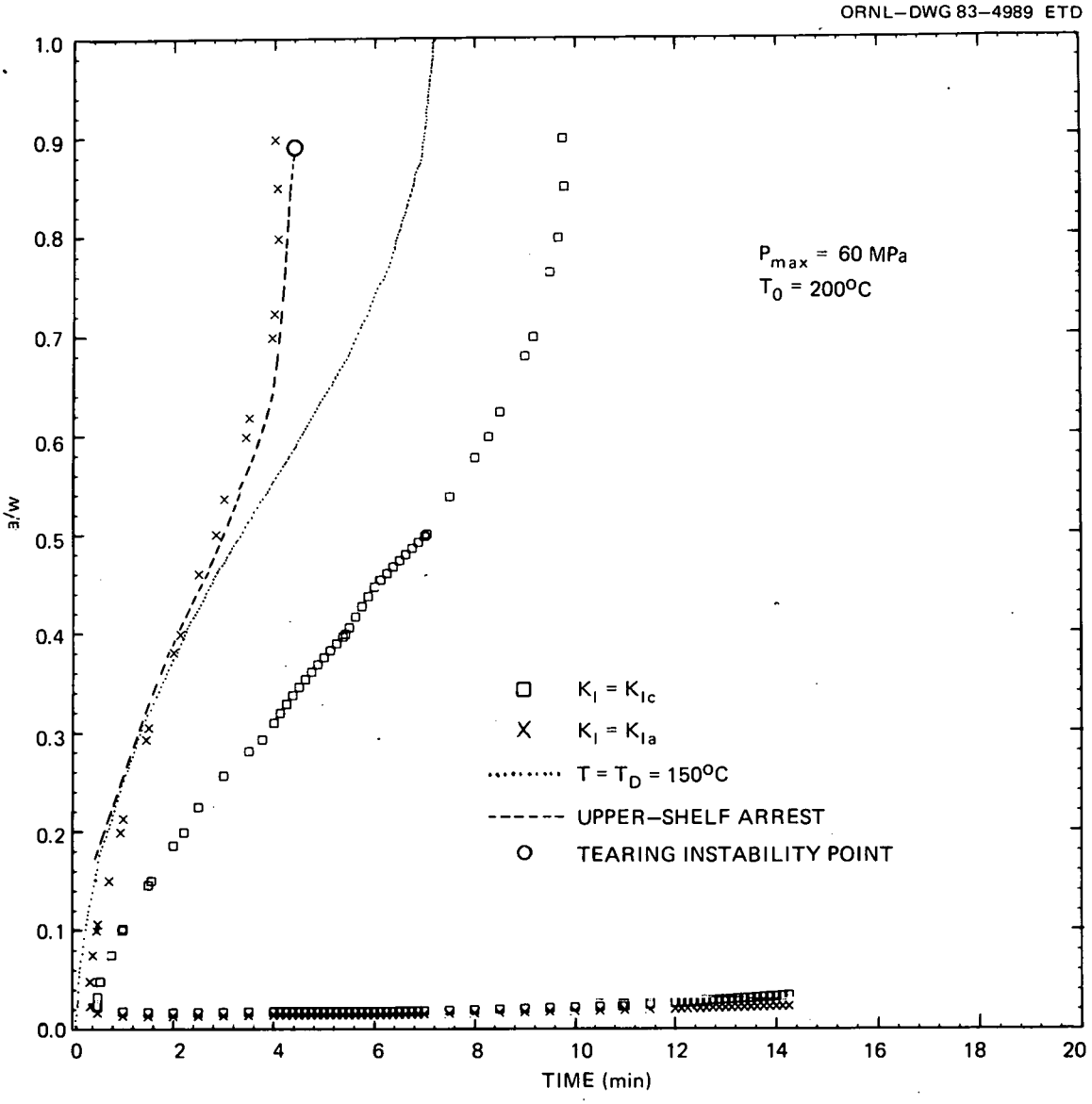

Fig. 5.15. PTSUSA-OCA case H (Table 5.5). Cleavage initiation and arrest and upper-shelf arrest and instability trajectories are shown. Results of this case and case C (Fig. 5.16), which differ only in p_{max}, are nearly the same.

The effects of variation of the initial temperature T_0 are shown in Figs. 5.16–5.18. Starting with a higher temperture makes the thermal stress contribution to K_I and J_I greater and shifts the points at which $T = T_D$ toward smaller a/w values. The latter effect will have an important role in the final selection of test conditions, because it has a strong influence on the depth of upper-shelf arrest. Upper-shelf arrest instability occurs at a/w values of ~0.60, 0.46, and 0.36 for T_0 = 200, 240, and 280°C, respectively.

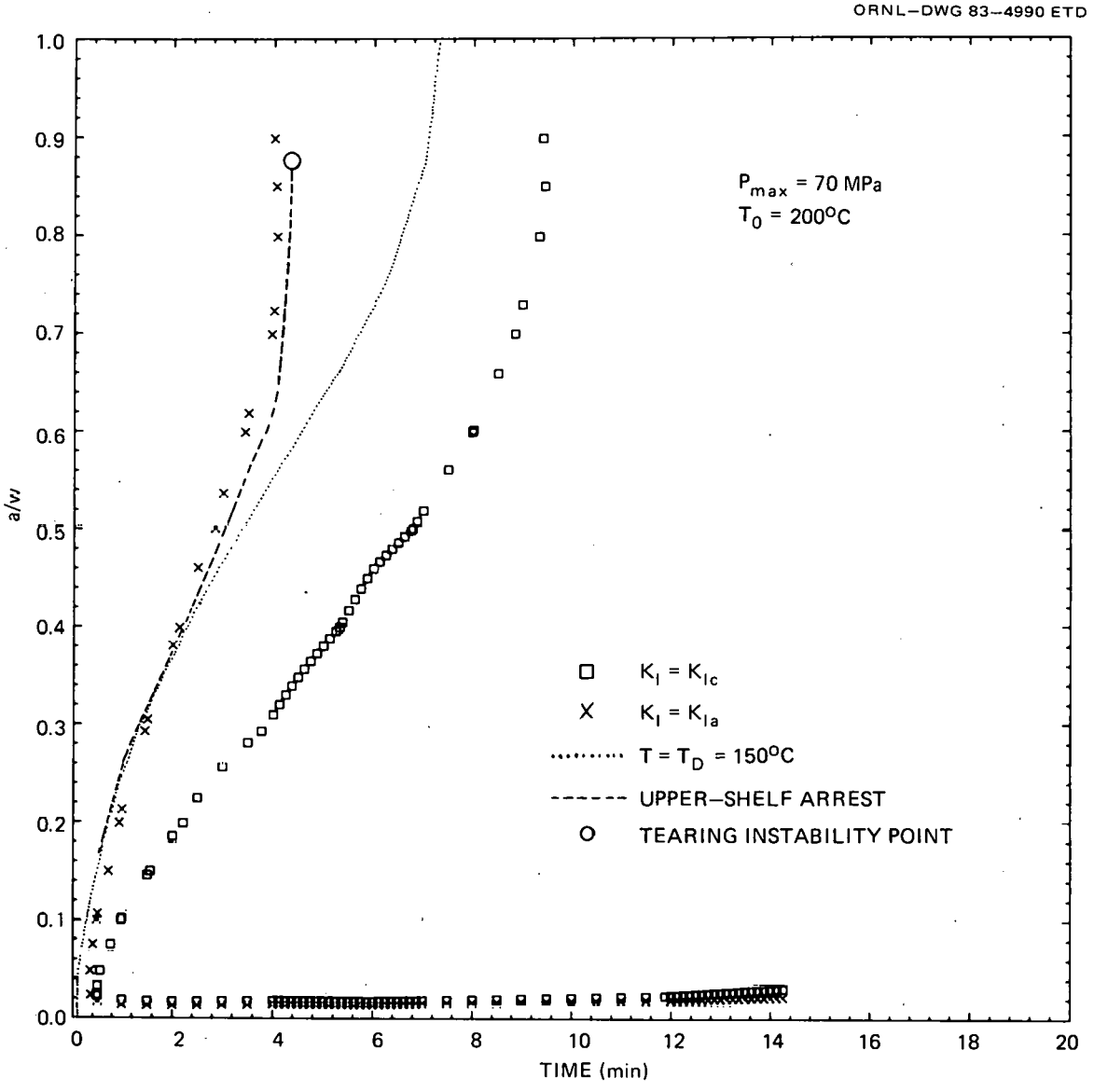

Fig. 5.16. PTSUSA–OCA case C. Cleavage initiation and arrest and upper–shelf arrest and instability trajectories are shown for comparison with Fig. 5.15 (for p_{max} variations) and Figs. 5.17 and 5.18 (for T_o variations).

5.2.3.3 Current developments. The PTSUSA code and an improved version of the OCA code will be used for planning PTSE–1 and defining specific test conditions. OCA has already been modified to handle the test vessel geometry by use of influence functions rather than unit-load K^* values for calculating K_I. These additional improvements are necessary for PTSE studies:

1. introduce a more general warm prestressing algorithm capable of handling PTSE transients,
2. make plastic zone size corrections in OCA,

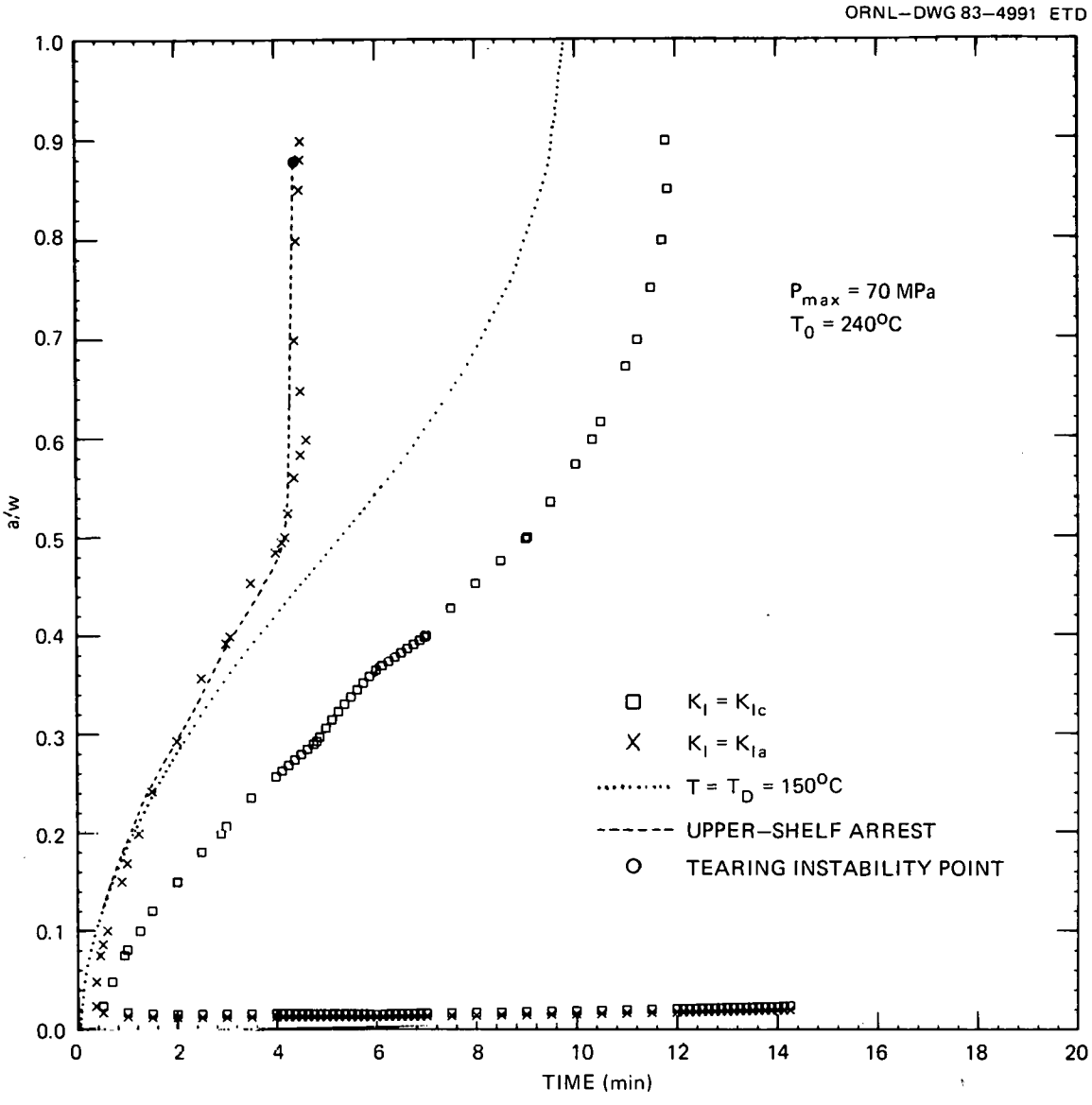

Fig. 5.17. PTSUSA–OCA case J. Cleavage initiation and arrest and upper-shelf arrest and instability trajectories are shown for comparison with Figs. 5.16 and 5.18 for different values of T_o.

3. link OCA and PTSUSA for plotting results together,
4. restructure input and output for efficient parameter studies, and
5. add ligament tensile instability calculations.

PTSUSA and OCA analyses described previously have all been based on the version of OCA that treats the test vessel and flaw as infinitely long. Further PTSE studies will use the 3-D version of OCA that accounts for the finite flaw, the finite cylinder, and the closed uncooled ends of the vessel. K_{Ic}, K_{Ia}, and J_R properties will continue to be inferred

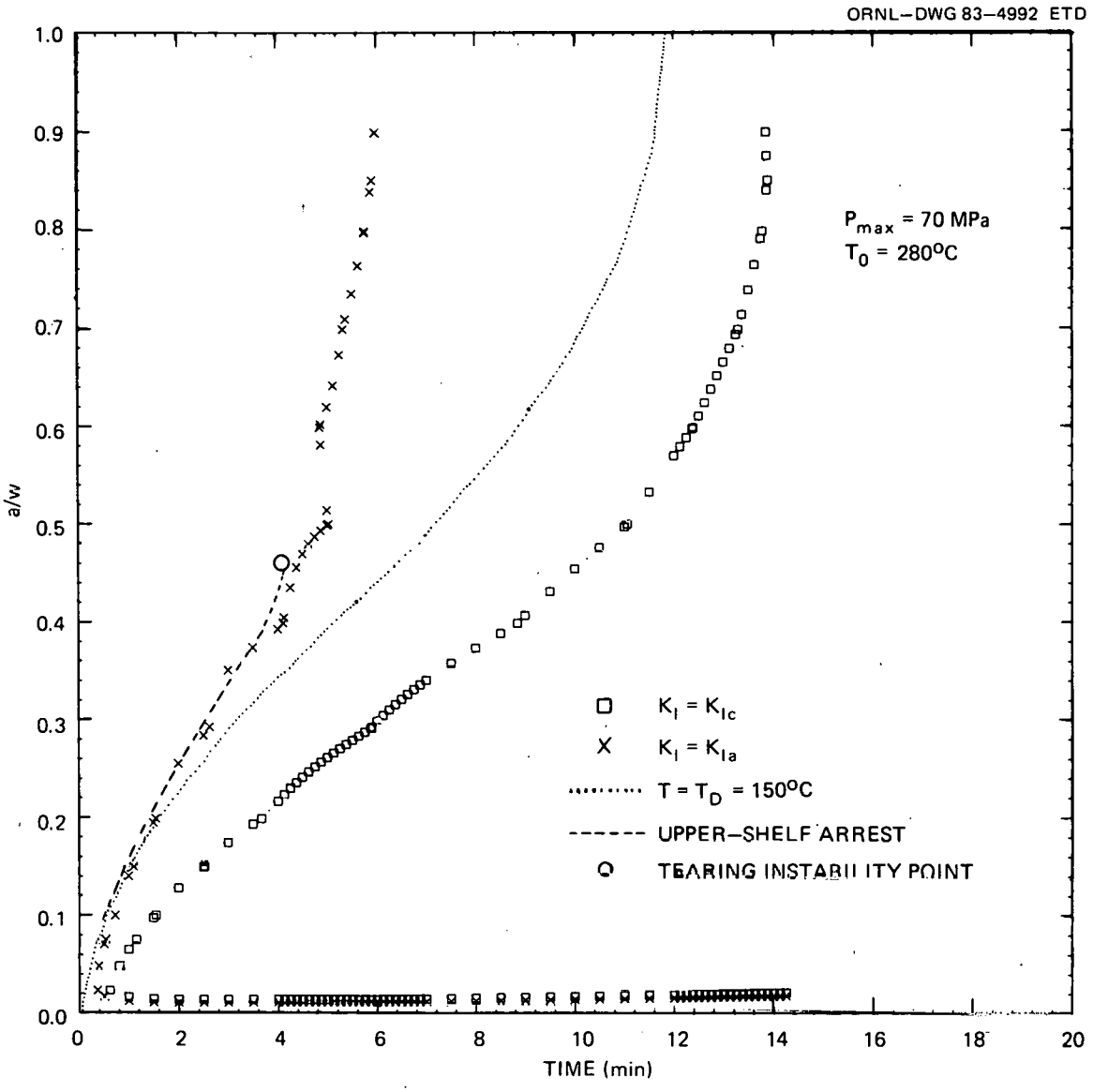

Fig. 5.18. PTSUSA-OCA case K. Cleavage initiation and arrest and upper-shelf arrest and instability trajectories are shown for comparison with Figs. 5.16 and 5.17 for different values of T_o.

principally from Charpy impact test data until extensive characterization tests are completed.

The emphasis of the near-term analyses will be to evaluate the impact on test plans of the new factors being introduced, namely upper-shelf arrest or instability and finite geometry. At present, it appears that upper-shelf behavior will limit maximum test pressures more than had been recognized previously. However, the capability of invoking a wide variety of pressure transients is still the best assurance of meeting the original PTSE-1 objectives.

5.2.4 Test vessel fabrication (K. R. Thoms)

Babcock & Wilcox is repairing two ITVs, V-7 and V-8, for use in shakedown tests, PTSE-0, and the first FM experiment, PTSE-1 (Ref. 19). The repair is being accomplished by welding a 1320-mm-long plug fabricated from TSC-6 into each of the vessels.

Early in this report period the cavities in each of the vessels were prepared for welding. During the inspection of the machined cavities, a potential problem was uncovered when high magnetic fields were discovered in both vessels. Magnetic flux densities as high as 0.0026 T (26 G) were observed in V-8 and as high as 0.0013 T (13 G) in V-7. This made magnetic particle inspection of the cavity surface impossible and suggested there may be a problem with the dc manual metal-arc (MMA) welding technique specified to weld the plugs into the vessels. Because B&W determined that the potential success of electrical degaussing of the vessels was questionable, it was decided to substitute dye penetrant inspection for the specified magnetic particle inspection throughout the repair process. Also, should the magnetism interfere with the dc MMA welding, B&W would attempt ac MMA welding prior to attempting schemes to degauss the vessels.

The TSC-6 cylinder was subjected to a temper of 523°C for 9.5 h prior to flame cutting a section from the cylinder to fabricate the plugs. After machining the plugs, they were also found to be significantly magnetized; however, the use of an electrical coil to degauss the plugs proved successful.

Both plugs have been welded into their respective vessels utilizing dc MMA welding with no problems encountered due to magnetism. During the next quarter, they will undergo inspection, postweld heat treatment (PWHT), further inspection, and machining of the outside diameter. The work remains on schedule for shipment of vessel V-8 approximately May 20 and V-7 approximately June 20, 1983.

Because of funding constraints, the awarding of a contract for the installation of a low-upper-shelf seam weld into vessel V-5 will be delayed ~1 year.

5.2.5 PTS materials characterizations (W. J. Stelzman, R. K. Nanstad, and T. D. Owings, Jr.)

Studies continued to determine the effect of tempering on the Charpy V-notch impact and drop-weight properties of the prolongation (TSP-4) from test cylinder TSC-4 after stress relieving for 8 h at 523°C and cooling in air. Characterization of the C_V toughness properties of the as-quenched prolongation TSP-6 was also begun to determine the variability of toughness through the thickness.

The cylinders (TSC) and prolongations (TSP) are forgings with the composition of SA508 class 2 steel procured in the quenched but untempered state. The test sections of the test vessels for PTSE-0 and -1 have been fabricated with segments of TSC-6. Preliminary tempering studies used TSP-4 material. The final determination of the heat treatment of the PTSE test vessels will be based on the studies of TSP-6.

Charpy V-notch and drop-weight test results from TSP-4 material that had been tempered have been reported.[20] Excess material from TSP-4, which

had been stress relieved for 8 h at 523°C and tempered for 6 h at 553°C, was given an additional 10 h at 553°C (16 h total). The cooling rate after the 6-h temper ranged from 1.1 to 0.55 K/min and after the 10-h temper from 0.44 to 0.16 K/min. The latter cooling rate was chosen to approximate the cooling rate anticipated for the PTSE-0 and -1 test vessels. Excess material from TSP-4, also previously stress relieved for 8 h at 523°C, tempered for 17 h at 563°C, and cooled at 0.92 to 0.68 K/min, was given an additional 10 h (27 h total) at 563°C, followed by cooling 0.43 to 0.16 K/min.

The Charpy V-notch and drop-weight results from both extended tempers are listed in Table 5.5 and presented in Figs. 5.19 and 5.20. Individual data are presented in Table 5.6. The Charpy V-notch fracture energy and lateral expansion results are also presented in Fig. 5.21, together with results previously reported.[20] Extending the hold time at 552°C for an

Table 5.5. Charpy V-notch impact (CT-oriented specimens) and drop-weight (Type P-3 specimens) results from 203-mm-thick prolongations TSP-4 and -6 as quenched and after stress relieving and tempering

Temper temperature (°C)	Depth[a] location (a/w)	Transition temperature (°C)			Upper-shelf energy (J)	Drop-weight NDT (°C)
		68-J Energy	0.89-mm Lateral expansion	Estimated 100% ductile fracture		
			TSP-4			
552[b,c]	0.24	82	74	149	105	-7
564[b,d]	0.24	63	63	149	110	-49
			TSP-6[e]			
	0.20	96	110	138	110[f]	
	0.26	121	113	149	90	
	0.28	118	107	143	93	
	0.40	116	104	127	105	
	0.54	102	88	129	115	66
	0.68	88	77	121	115	
	0.82	82	71	93	120	

[a] Fraction of depth from inside diameter of 203-mm-wall thickness.

[b] Stress relieved for 8 h at 523°C; cooled in air.

[c] Tempered 16 h at 553°C; cooled 0.44 to 0.16 K/min.

[d] Tempered 27 h at 563°C; cooled 0.43 to 0.16 K/min.

[e] As quenched.

[f] Minimum.

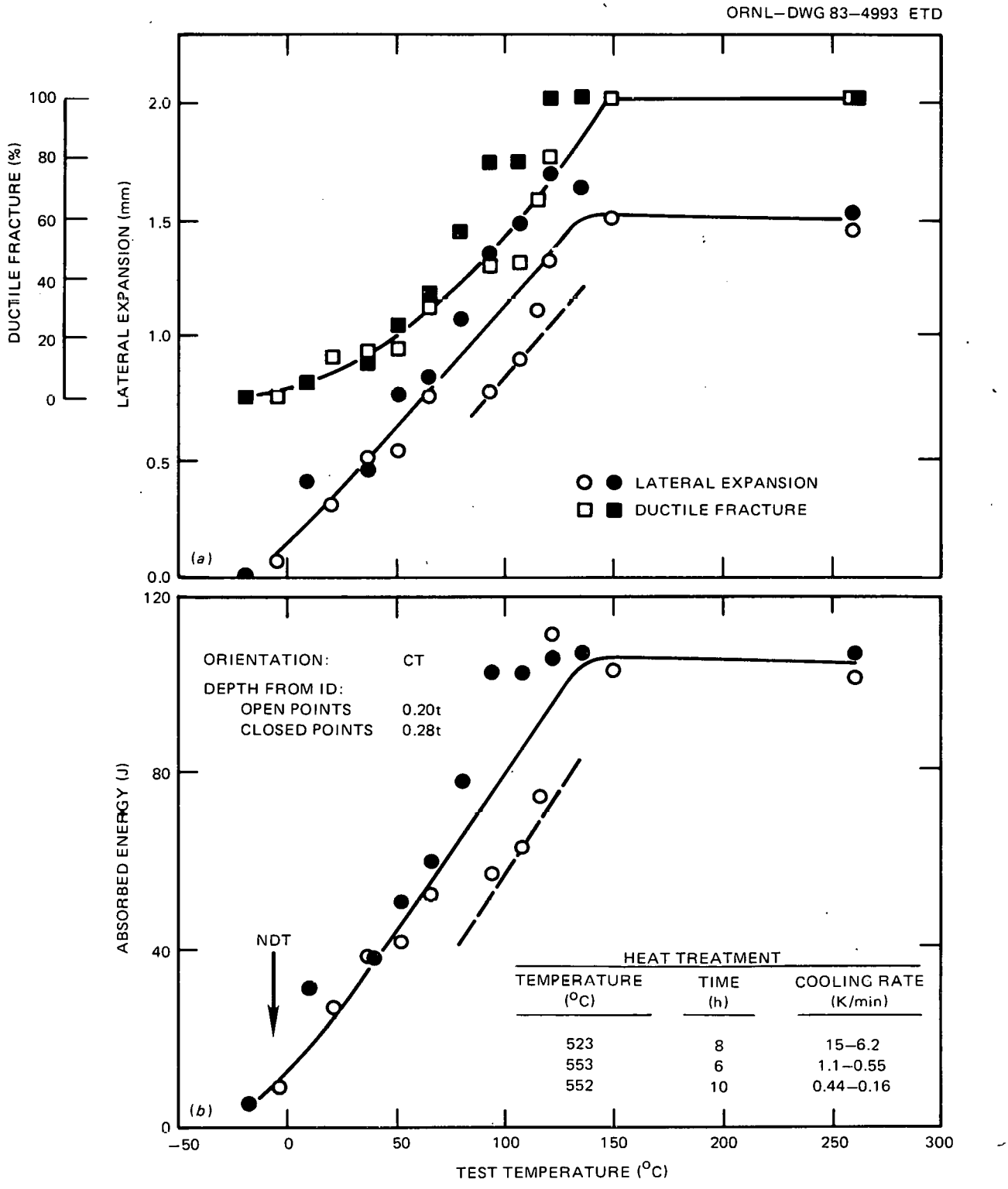

Fig. 5.19. Charpy V-notch impact properties of 203-mm-thick prolongation TSP-4 after stress relieving for 8 h at 523°C and tempering for 16 h at 552°C: (*a*) ductile fracture and lateral expansion and (*b*) absorbed energy.

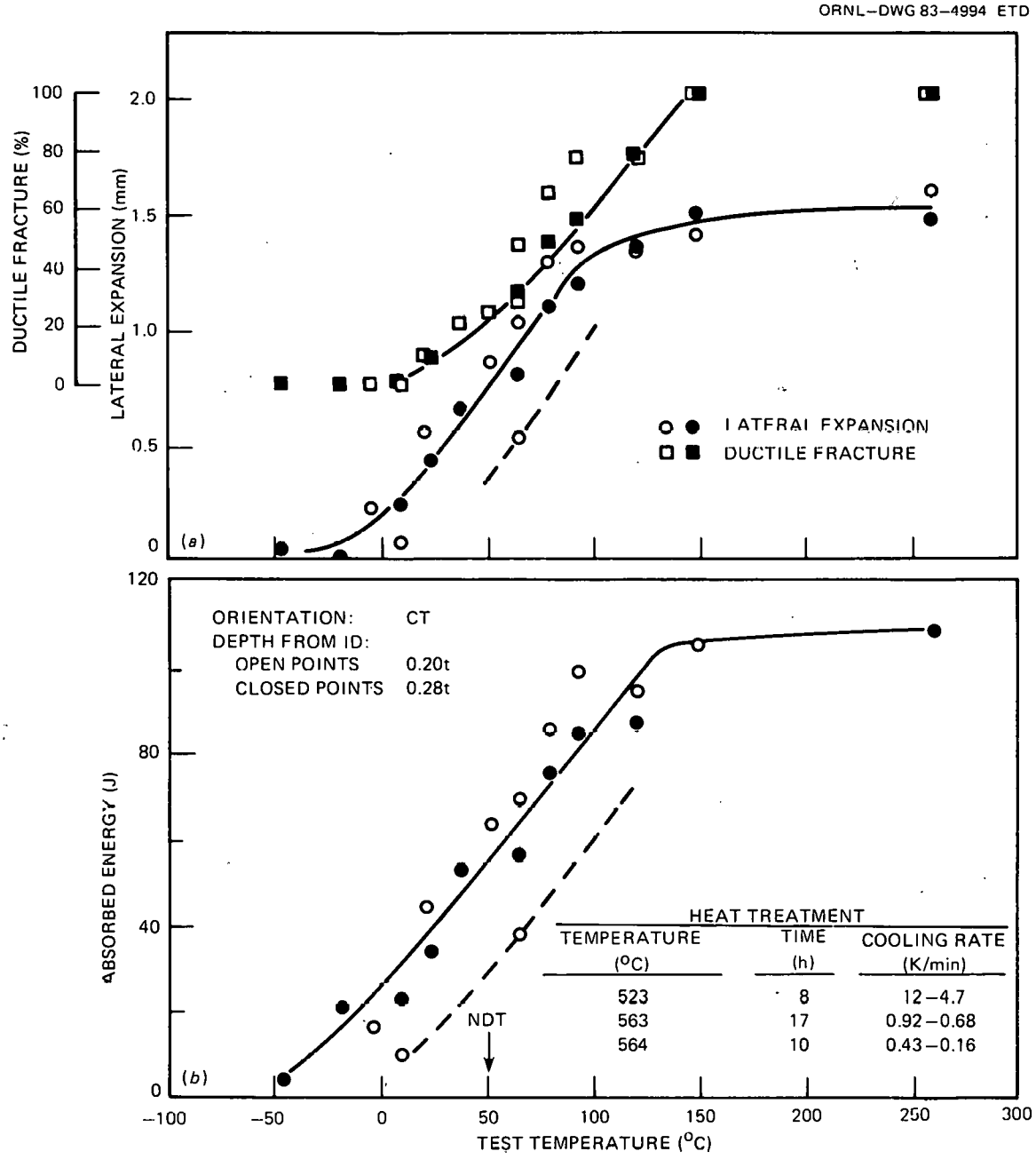

Fig. 5.20. Charpy V-notch impact properties of 203-mm-thick prolongation TSP-4 after stress relieving for 8 h at 523°C and tempering for 27 h at 563°C: (*a*) ductile fracture and lateral expansion and (*b*) absorbed energy.

Table 5.6. Charpy V-notch impact results (CT-oriented specimens) from prolongation TSP-4 after additional tempering at 552 and 564°C

Test temperature (°C)	Absorbed energy (J)	Lateral expansion (mm)	Shear (%)
Tempered at 552°C for additional 10 h[a]			
−18[b]	5.4	0	0
−4[b]	8.8	0.08	0
10[b]	32.0	0.41	5
21[b]	27.2	0.30	13
38[b]	38.6	0.51	5
38[b]	38.9	0.46	11
52[b]	42.2	0.53	16
52[b]	51.3	0.76	24
66[b]	53.0	0.75	30
66	60.5	0.86	35
79[b]	78.9	1.09	55
93[b]	57.8	0.79	44
93[b]	103.8	1.37	78
107[b]	63.9	0.91	45
107[b]	103.8	1.50	79
116[b]	75.3	1.14	66
121[b]	112.2	1.35	80
121	106.8	1.73	100
135[b]	108.1	1.65	100
149[b]	104.4	1.52	100
260[b]	102.7	1.50	100
260	108.4	1.55	100
Tempered at 564°C for additional 10 h[c]			
−46	4.1	0.05	0
−18[b]	20.9	0.03	0
−4[b]	16.3	0.23	0
10[b]	10.1	0.08	0
10[b]	23.5	0.25	0
21[b]	44.2	0.56	10
38[b]	53.0	0.66	21
52[b]	63.9	0.84	25
66[b]	38.1	0.53	28
66[b]	69.4	1.04	48
66[b]	56.7	0.81	32
79[b]	86.0	1.30	66
79[b]	75.5	1.09	49
93[b]	99.3	1.37	78
93[b]	84.7	1.19	57
121[b]	94.8	1.35	78
121[b]	87.4	1.37	79
149[b]	105.3	1.42	100
149[b]	106.1	1.52	100
260[b]	110.2	1.63	100
260	108.8	1.50	100

[a] Stress relieved 8 h at 523°C, tempered 6 h at 553°C, and retempered 10 h at 552°C.

[b] 0.20t depth in 203-mm-thick wall (inside diameter = 0t); remainder 0.28t.

[c] Stress relieved 8 h at 523°C, tempered 17 h at 563°C, and retempered 10 h at 564°C.

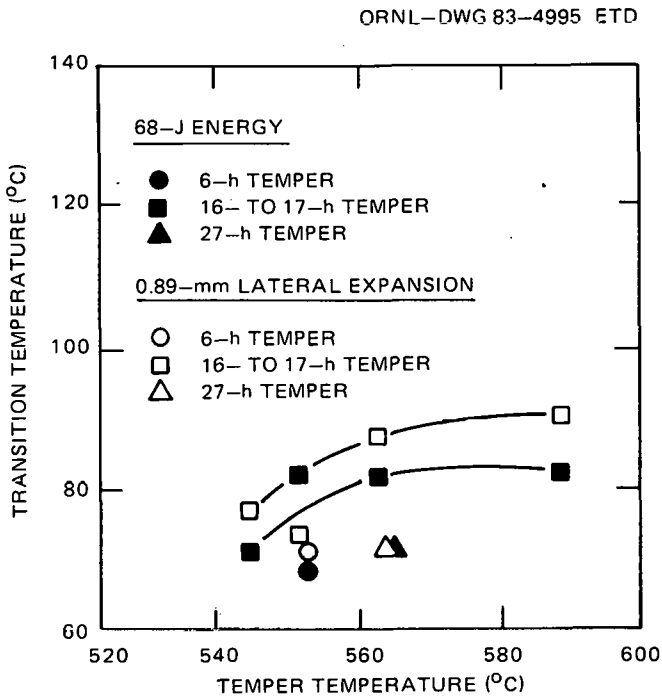

Fig. 5.21. Variation of Charpy V-notch transition temperature after stress relieving prolongation TSP-4 for 8 h at 523°C and tempering.

additional 10 h increased the transition temperature (reduced toughness) at the 68-J energy level from 68 to 82°C. After an additional 10 h at 563°C, the transition temperature decreased (increased toughness) from 82 to 63°C at the 68-J energy level. The extent of influence of the extended hold time or the slower cooling rate is not clear. Also unclear are the results from the drop-weight tests. A single-pass application of the weld bead was used instead of the two-pass bead. Either procedure is allowed in the ASTM E208 method for conducting drop-weight tests.[21] We also partially submerged the specimen in water during the application of the weld. Both procedures are intended to reduce the bulk temperature in the specimen during welding, thereby minimizing the possibility of retempering in the region near the heat-affected zone (HAZ). The test method assumes that the crack will advance from the brittle weld to the edges of the specimen within ~30°C of the nil-ductility temperature. In the present series of tests, the total crack extension occurs within 3°C of the nil-ductility temperature. The Japanese have also experienced similar problems with A508 classes 2 and 3 (Refs. 22 and 23). We are continuing to investigate the application of the E208 test method to testing of A508 steel.

We also examined the variability of as-quenched Charpy V-notch toughness properties through the thickness of the 203-mm-thick prolongation TSP-6 using CT-oriented specimens. The results from seven depth locations from the inner surface (0.20, 0.26, 0.28, 0.40, 0.54, 0.68, and 0.82t) are listed in Table 5.5. The results indicate that the minimum Charpy V-notch toughness occurs near the quarter-thickness depth from the inner surface.

A segment from TSP-6 was also stress relieved for 9 h at 521°C, tempered for 10 h at 566°C, and cooled 0.62 to 0.12 K/min. Charpy V-notch, drop-weight, tensile, and 1T compact specimens were then machined from this material. Testing of these specimens is under way.

5.2.6 PTS test facility (R. W. McCulloch and G. C. Robinson)

Design and construction of the Pressurized-Thermal-Shock Test Facility (PTSTF) are being accomplished under DOE Directive CL-523. Union Carbide Corporation-Nuclear Division is furnishing Titles I, II, and III engineering; procuring the ITV shroud or outer test vessel (OTV); providing instrumentation and controls (I&C) design, component procurement, and fabrication; performing utility tie-ins, instrument calibration, and preoperational testing; and providing support to the construction contractor. Mechanical components procurement and construction are being performed by Rust Engineering Company, the DOE construction contractor.

In addition to directive-controlled design and construction tasks, several peripheral facility-related tasks are in progress to enable PTS experimental testing. These include upgrading the data acquisition and pressurization systems, determining and installing needed test instrumentation, and providing reliable high-pressure high-temperature seals for instrumentation and pressurization penetration of the ITV.

5.2.6.1 Test facility construction. Site construction is ~95% completed and remains within projected costs. The ITV shroud or OTV was successfully modified to accept ITVs of slightly smaller diameter and was received on site 1 d ahead of the projected date of February 1, 1983. Receipt of the OTV completed the fourth of the planned six DOE Level II milestones and concluded procurement of major items for the facility. Figure 5.22 shows the completed OTV installed in the reinforced concrete cell. Electrical heaters beneath the insulation will be used to preheat the ITV prior to initiation of the thermal shock.

After installation of the OTV and completion of process piping, system hydrostatic tests were conducted. The initial hydrostatic tests revealed extensive piping gasket leaks. Investigations determined that the surface roughness of system flanges was too coarse for the flexitallic-type gasket to seal. Asbestos gaskets were substituted, and the hydrostatic tests were successfully performed on the OTV, system piping, and the coolant storage tank. Bellville washers will be retrofitted to the flange bolts prior to facility operation to preclude thermally induced seepage of the flanges.

Figure 5.23 shows the coolant storage tank and associated system piping. The large (20-cm-diam) pipes supply the coolant from the tank to the OTV housing the test vessel. The 15-cm-diam pipes provide bypass flow around the OTV, and the small lines are routed to the chiller for coolant refrigeration.

Installation of facility instrumentation and electrical systems is essentially complete; final insulation, painting, and cleanup are in progress.

UCC-ND, Rust Engineering, and DOE have agreed that Rust Engineering will complete facility constuction prior to the scheduled beneficial occupancy date of April 15. This change, in response to the better-than-

K–25 PHOTO 83–1306

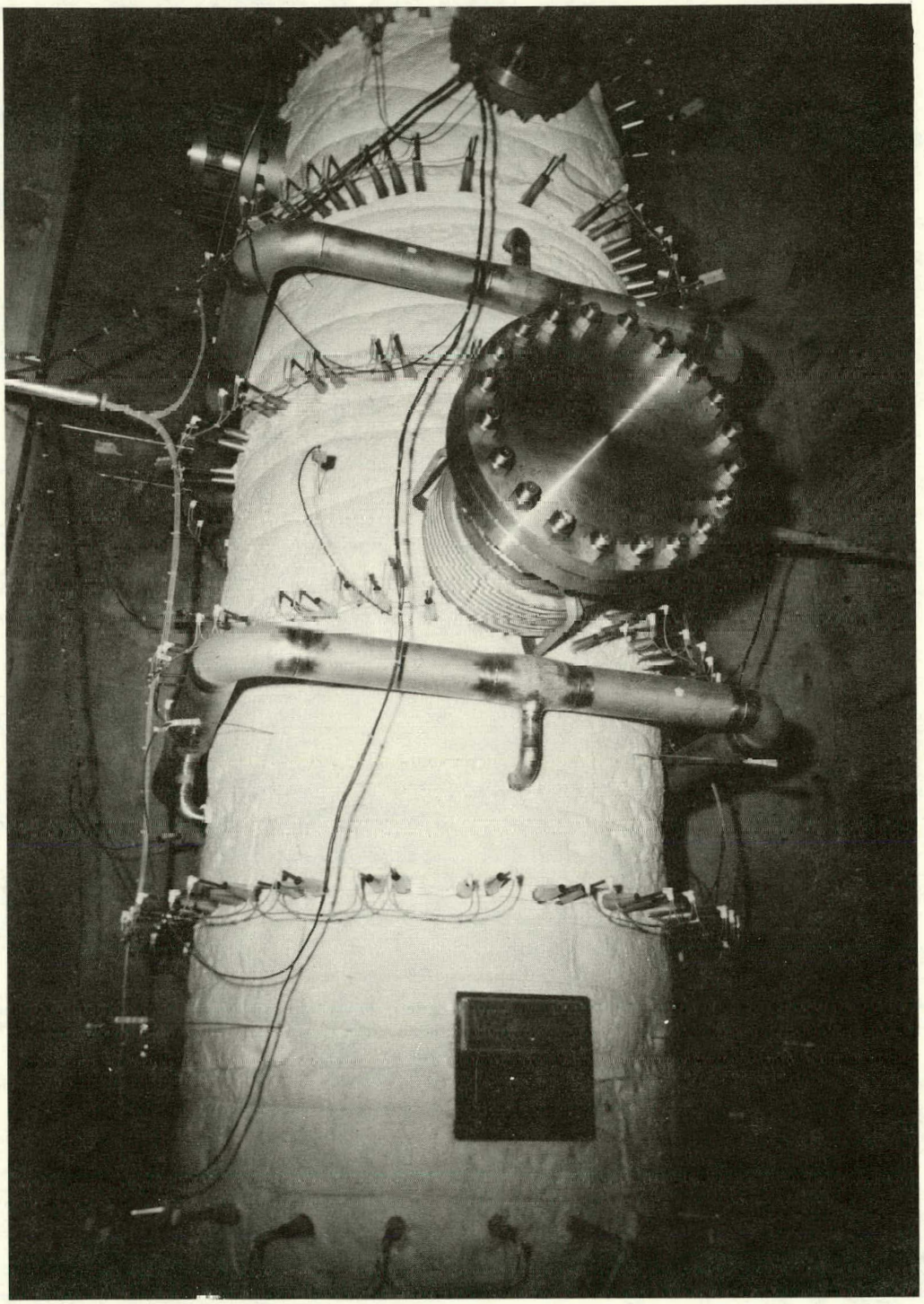

Fig. 5.22. Outer test vessel with associated heaters and insulation.

K–25 PHOTO 83–1307

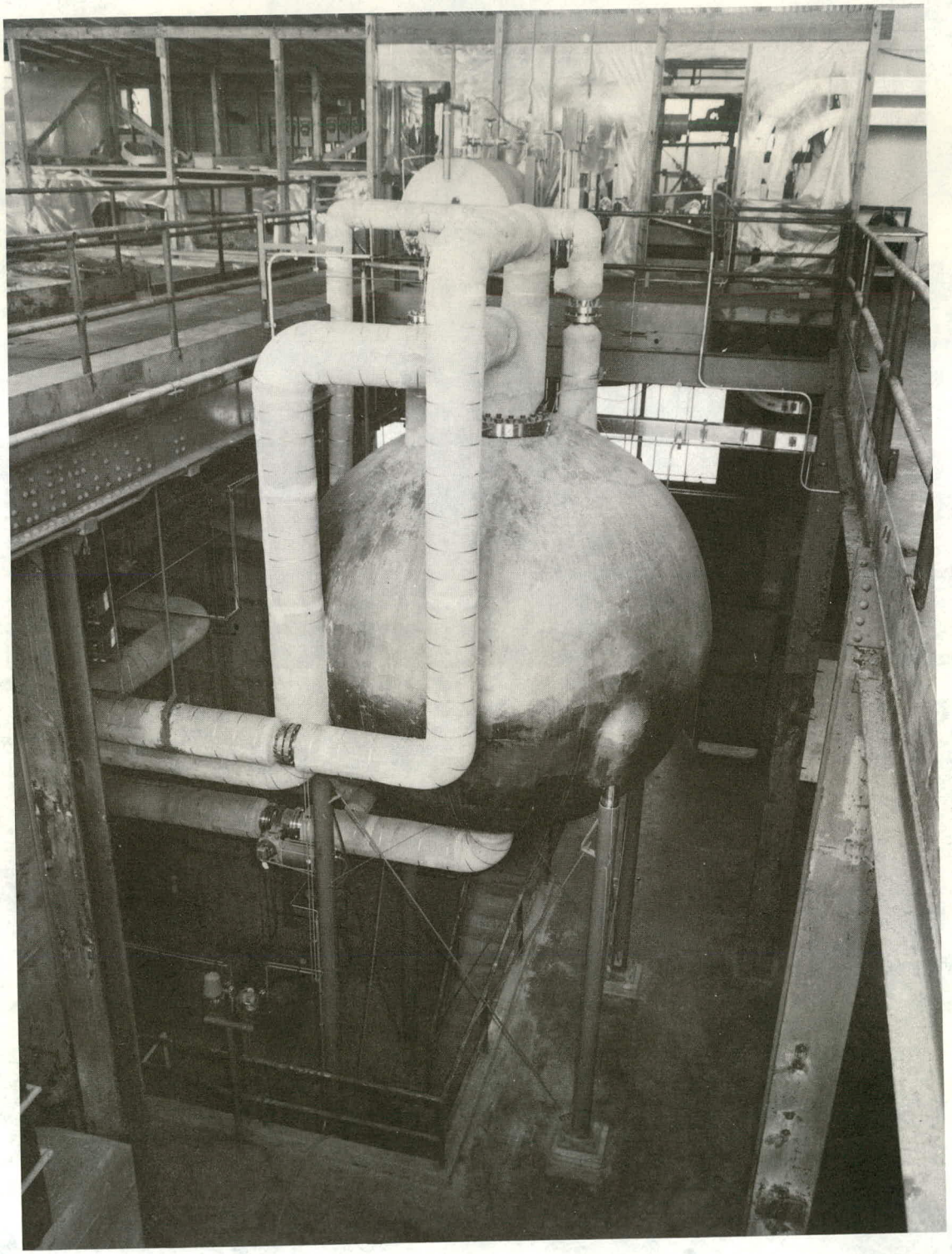

Fig. 5.23. Water–methanol coolant storage tank and associated piping system.

expected construction process, should result in facility completion by approximately mid-May, one month earlier than originally planned.

5.2.6.2 Data acquisition system. Definition of the detailed software and hardware requirements for the HSST DAS, and the PTSE needs in particular, have been proceeding. A completion date of July 1, 1983, has been agreed on for delivery of an assembled and checked DAS to the PTSTF. The trailer that will house the new DAS is being prepared, and all hardware components are on order.

Primary displays will consist of two plots: pressure vs time and average temperature vs time. Pressure is a single parameter and temperature is an average of up to seven thermocouple inputs from thimbles or surface thermocouples located at various positions on the I&V (see PTSE Instrumentation section). Each of the displays will also plot a calculated or predicted curve for comparison with the real-time generated test data. Thimble thermocouples, which are averaged, will be from a common a/w location within the vessel wall.

Additional graphic displays of test data or important variables calculated from test data were considered, but they were rejected for one or more reasons: (1) the cost of additional graphics terminals exceeded potential benefits; (2) data processing or computations could not be made quickly enough to influence control of the test; and (3) the displayed information could not be evaluated reliably by testing personnel in the short time available during the test.

Inclusion of a test-specific version of the OCA-I code will not be attempted for PTSE-1. However, a test-specific version of OCA-I will be prepared for possible posttest processing of PTSE-1 or use in subsequent PTS experiments. No attempt will be made to provide DAS control of the pressurization sequence during testing.

5.2.6.3 Pressurizing fluid investigation. During the qualification of seals for the V-8A test,[24] it was observed that the ethylene glycol in the pressurization fluid suffered chemical breakdown. Because of the decomposition of ethylene glycol under the even more severe PTS testing conditions, its use was considered inadvisable. Two serious problems would likely ensue if used: (1) the plugging of capillaries and/or low C_V orificed valves used for control letdown and (2) the formation of a freeze plug in the small-diameter pressurizing tubing. Consequently, dimethyl polysiloxane fluid, Dow Corning 210H, was tentatively selected as an alternative pressurizing medium.

As shown on Fig. 5.24, this fluid has a favorable compressibility (lower potential energy) compared with water at 288°C if it is assumed that the silicone oil's compressibility is relatively insensitive to temperature. Although no data are known to exist for the compressibility of silicone oil at elevated temperatures, the low voltility at elevated temperatures of silicone oil implies a low sensitivity of compressibility to temperature. Other favorable properties are high-flash-point temperature of 299°C, low-pour-point temperature of −50°C, and no established toxicity limits.

A change from the currently used 50% by weight ethylene glycol/water mixture to silcone oil could result in a minimal contamination due to residues. The ability of the Dow Corning 210H fluid to sustain prolonged heating and then chilling corresponding to PTS conditions was verified by autoclaving a sample in a vessel having a residue of ethylene glycol/water

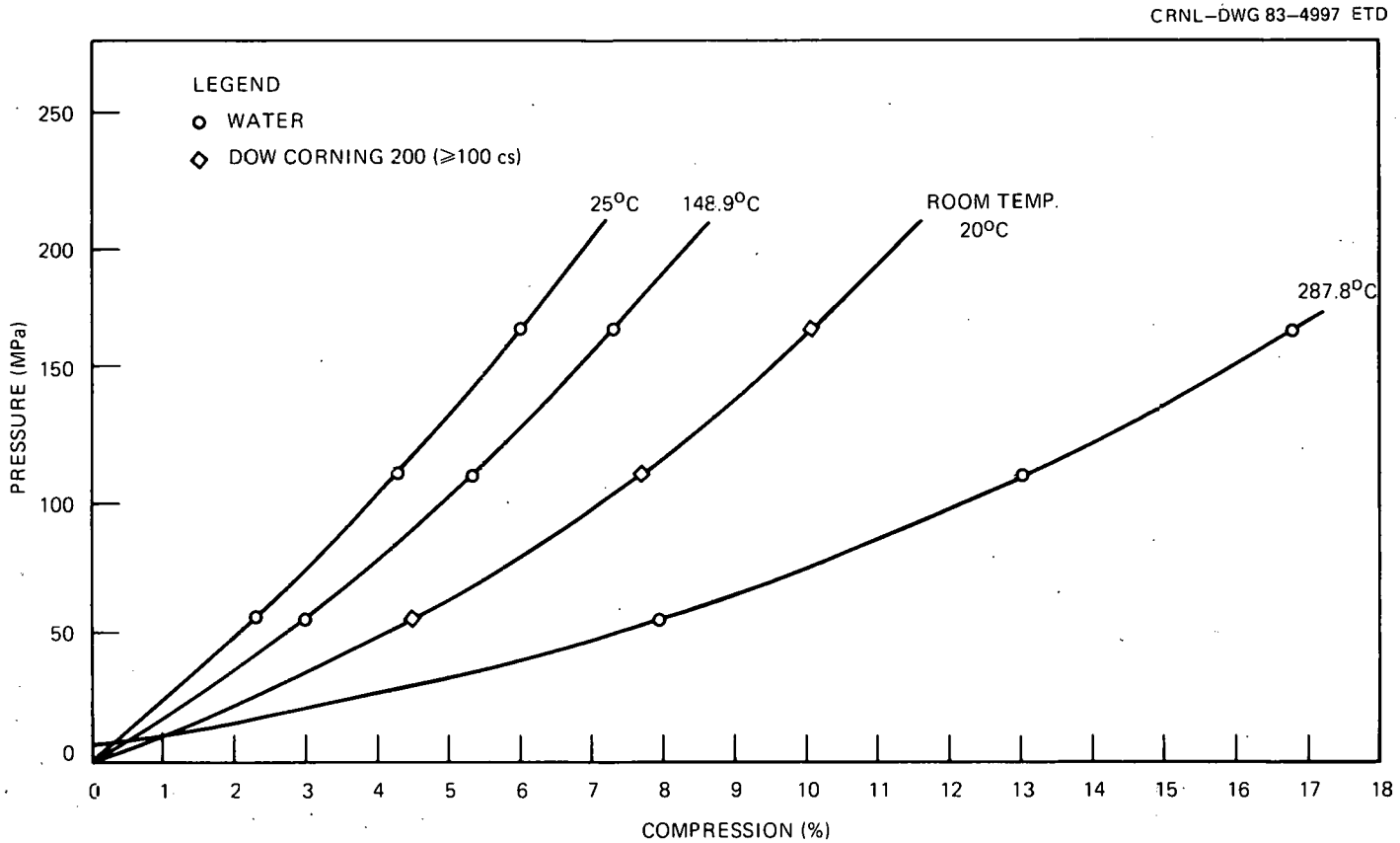

Fig. 5.24. Compressibility of water and Dow Corning 200 silicone fluid as function of pressure and temperature.

mixture as a film on the vessel wall for 22 d at 288°C and 20.7 MPa and then subjecting the fluid to pressure cycling as shown on Fig. 5.25. During the pressure cycling, the sample vessel's pressure indicator responsed in phase with the pressurizing-line pressure indicator, thereby indicating no significant change in viscosity. Also as shown on Fig. 5.25, the sample vessel was then cooled down to −50°C in an ethylene glycol-water CO_2 ice bath while being pressure cycled. Again, the pressure indicator on the sample vessel responded in phase with the pressurizing line pressure indicator. This simulation of PTS cooling verified that the viscosity changes were insignificant and that no freeze plug would form under PTS operating conditions.

5.2.6.4 Seal development. As previously reported,[25] instrument lead-through fittings having the configuration shown in Fig. 5.26 with both six- and three-hole designs of soapstone packing were subjected to severe simulations of PTS temperture and pressure conditions without leaking. In this design, the sleeves that are brazed to the instrument leads as shown in Fig. 5.26 restrain the leads from expulsion and eliminate any shear stresses between the leads and packing. The installation of these sleeves is a critical and painstaking operation that immediately precedes the installation of the fitting on the vessel cover flange and requires both a

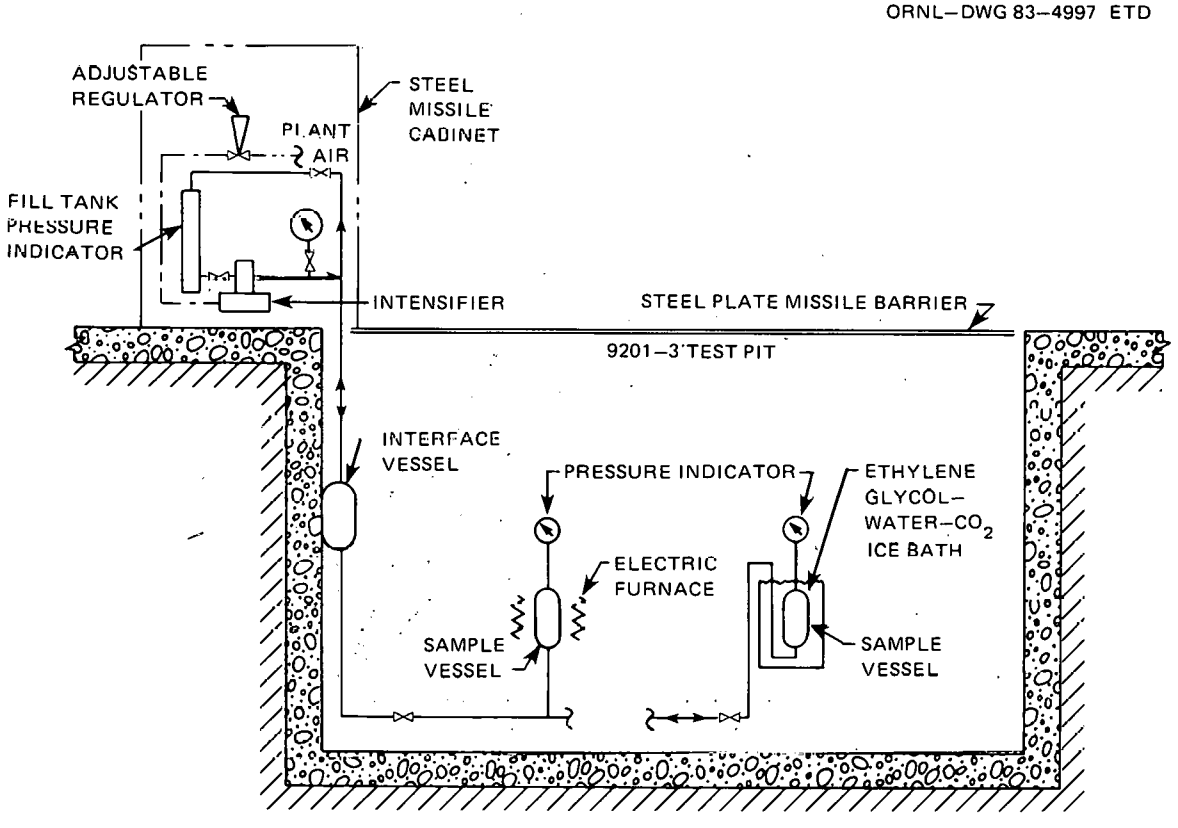

Fig. 5.25. Test setup for verification tests of silicone pressurizing fluid.

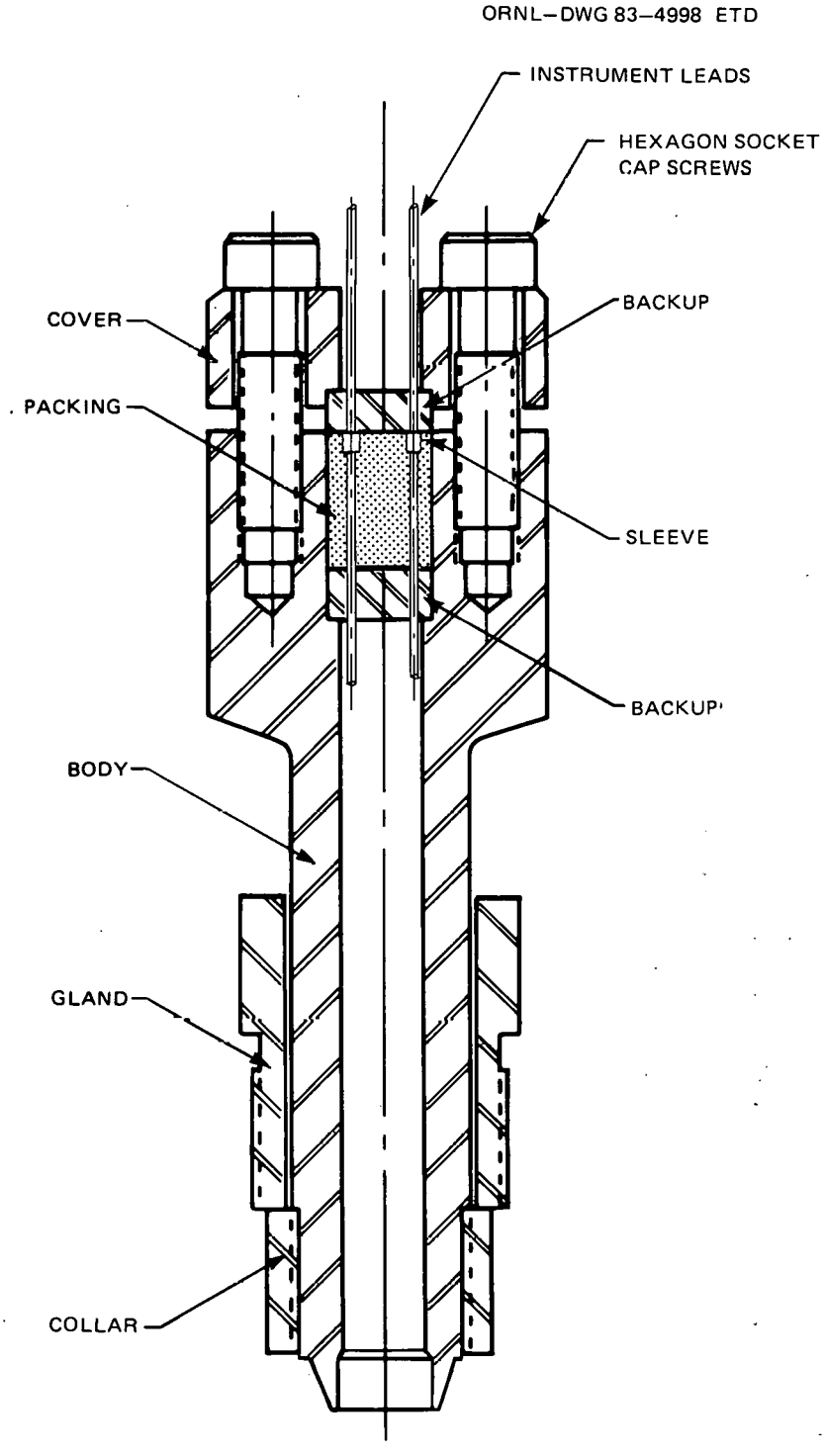

Fig. 5.26. Cross-sectional view of modified instrument lead-through fitting.

coiling of the leads internally for takeup at installation and an increased void volume in the graphite ballast to accommodate the required motion. The leads for the thermocouple thimbles in the PTS vessels are 0.32 cm in diameter and are very stiff compared with the previous designs incorporating 0.15-cm-diam leads. Consequently, it was anticipated that installation would be exceedingly difficult.

As an alternative approach, packing as shown in Fig. 5.26 was made from soapstone without the recesses to accommodate the sleeves; verification tests of the fittings have been made under severe simulated PTS conditions. While maintaining the fitting at 288°C (550°F), a six-hole version of the packing with solid stainless simulating the leads was cycled 25 times from 10 to 69 MPa and 25 times from 10 to 138 MPa without leakage. On the first cycle of pressurization to 207 MPa, the packing failed and a lead was expelled. A retest of this packing configuration was made except that the leads consisted of stainless-sheathed mgO-insulated 0.16-cm-diam thermocouple leads to improve the simulation of PTS service conditions. With the temperature held at 288°C, pressure was cycled in stages 25 times from 10 to 69 MPa, 25 times to 138 MPa, 75 times to 172 MPa, and 25 times to 207 MPa with no leakage. A three-hole version of the packing without the sleeve recesses and equipped with 0.32-cm-diam thermocouple thimble leads was tested at 288°C with pressure cycles in stages 25 times from 10 to 69 MPa, 25 times to 138 MPa, 75 times to 172 MPa, and 1 time to 200 MPa. At this point, failure occurred with one lead being expelled violently. Figure 5.27 shows a composite view of the backups, packing, retained leads, and the expelled lead. Three additional tests of the three-hole version packing with the same testing conditions were performed. Failure ensued at pressure levels of 131, 152, and 200 MPa.

It was then hypothesized that by careful routing of the thermocouple leads, sufficient restraint could be obtained from the spot-welded stainless foil supports for the leads to serve as anchors and limit the total slippage possible to ~0.5 cm. Two additional tests of the three-hole version packing were performed with a mechanical stop incorporated to limit the amount of movement of the leads. In the first test with the stop positioned to permit a maximum of 1.5-cm movement and with the temperature maintained at 288°C, pressure cycles in stages 25 times from 10 MPa to 69 MPa, 25 times to 103 MPa, 25 times to 138 MPa, and 25 times to 207 MPa were performed without leakage. However, after completion of the cycling and following a lapse of 15 min, sudden failure occurred. Two of the leads moved 1.5 cm, one violently, and although the third lead only moved 0.24 cm, leakage through the packing occurred near this lead as determined by a room-temperature repressurization. In the second test, the mechanical stop was positioned to prevent lead movement >0.69 cm. In addition, a prolonged soak period at 288°C and 138 MPa of 115 h was maintained prior to pressure cycling. Twenty-five pressure cycles were then performed from 10 to 138 MPa and from 10 to 207 MPa. After restoration to room temperature, the unit was pressurized to 207 MPa to verify its leaktightness. At disassembly it was found that all three leads had moved 0.11 cm without leakage occurring. These tests verified that if the leads are restrained to permit no more than ~0.1-cm movement, the penetration assemblies can function satisfactorily without the incorporation of brazed sleeves on the leads.

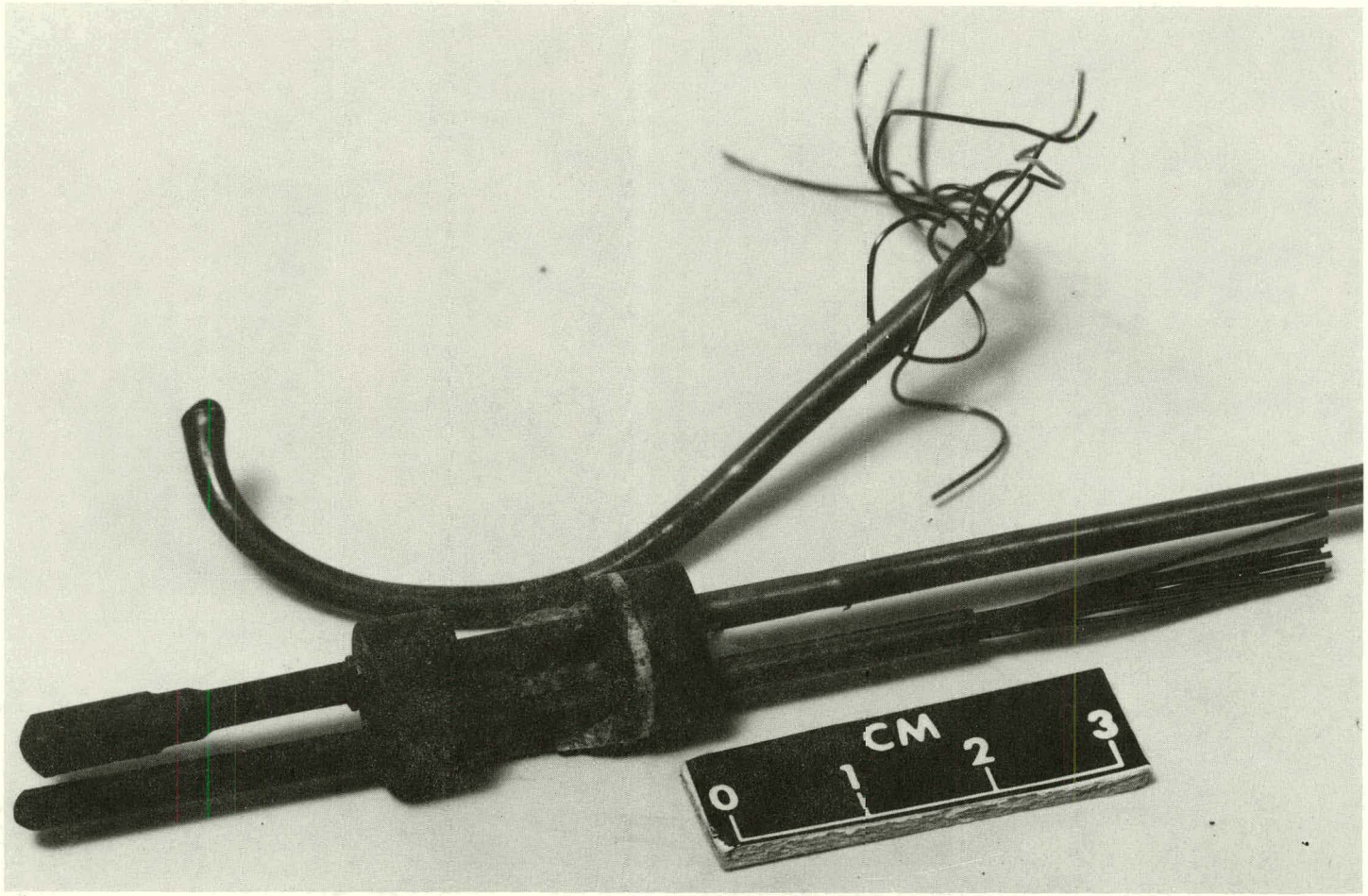

Fig. 5.27. Failed three-hole packing assembly without brazed sleeve to serve as anchor.

5.2.6.5 Elastomeric seals for cover flange of ITV for PTS conditions. A demonstration test of the ability of Viton to function acceptably in an ITV under PTS conditions was performed. The test fixture was heated slowly from room temperature to 260°C over a time interval of 144 h. The test fixture was then pressure cycled 25 times for 6.9 to 69 MPa, 25 times from 6.9 to 103 MPa, and 25 times from 6.9 to 138 MPa, while maintaining the temperature at 260°C. No leakage occured. The temperature was then increased to 288°C. While maintaining the temperature at 288°C, the test fixture was cycled 25 times from 6.9 to 69 MPa, 25 times from 6.9 to 103 MPa, and 25 times from 6.9 to 138 MPa. After soaking at 288°C for 24 h, temperature was then reduced to room temperature and the fixture was repressurized to 138 MPa to verify leaktightness. It was concluded that Viton can serve satisfactorily for this seal for PTS conditions.

References

1. R. H. Bryan, *Quick-Look Report on Test of Intermediate Vessel V-8A — Tearing Behavior of Low Upper-Shelf Material*, ORNL/SST-4, Union Carbide Corp. Nuclear Div., Oak Ridge Natl. Lab., August 25, 1982.

2. P. P. Holz and R. H. Bryan, "Intermediate Test Vessel V-8A," in *Heavy-Section Steel Technology Program Quart. Prog. Rep. January–March 1981*, NUREG/CR-2141/V1 (ORNL/TM-7822), Union Carbide Corp. Nuclear Div., Oak Ridge Natl. Lab.

3. H. A. Domian, *Vessel V-8 Repair and Preparation of Lower Upper-Shelf Weldment*, ORNL/Sub/81-85813/1, Babcock and Wilcox Company, June 1982.

4. R. H. Bryan, "Preparation for Intermediate Vessel Test V-8A," in *Heavy-Section Steel Technology Program Quart. Prog. Rep. January–March 1982*, NUREG/CR-2751, Vol. 1 (ORNL/TM-8369/V1), Union Carbide Corp. Nuclear Div., Oak Ridge Natl. Lab.

5. R. H. Bryan and S. E. Bolt, "Ductile Fracture Vessel Test V-8A," in *Heavy-Section Steel Technology Program Quart. Prog. Rep. July–September 1982*, NUREG/CR-2751, Vol. 3 (ORNL/TM-8369/V3), Union Carbide Corp. Nuclear Div., Oak Ridge Natl. Lab.

6. R. H. Bryan, "ITV V-8A," in *Heavy-Section Steel Technology Program Quart. Prog. Rep. October–December 1981*, NUREG/CR-2141, Vol. 4 (ORNL/TM-8252), Union Carbide Corp. Nuclear Div., Oak Ridge Natl. Lab.

7. H. A. Domian and R. J. Futato, "J-Integral Test Results of HSST-ITV8A Low Upper Shelf Weld," submitted to Union Carbide Corporation Nuclear Division (1983).

8. R. H. Bryan and R. W. McCulloch, "Pressurized Thermal-Shock Studies," in *Heavy-Section Steel Technology Program Quart. Prog. Rep. October–December 1982*, NUREG/CR-2751, Vol. 4 (ORNL/TM-8369/V4), Union Carbide Corp. Nuclear Div., Oak Ridge Natl. Lab.

9. J. G. Merkle, "An Approximate Stress Intensity Factor Solution for a Deep Inside-Surface Longitudinal Crack in a Cylinder Under Thermal Loading," in *Heavy-Section Steel Technology Program Quart. Prog. Rep. October–December 1975*, ORNL/NUREG/TM-3, Union Carbide Corp. Nuclear Div., Oak Ridge Natl. Lab.

10. J. G. Merkle, "Approximate Stress Intensity Factor Calculations for Continuous Inside-Surface Circumferential Cracks in a Cylinder under Thermal Loading," in *Heavy-Section Steel Technology Program Quart. Prog. Rep. January–March 1976*, ORNL/NUREG/TM-28, Union Carbide Corp. Nuclear Div., Oak Ridge Natl. Lab.

11. J. G. Merkle, "Analysis of Crack Behavior Under Thermal Shock Loading," in *Heavy-Section Steel Technology Program Quart. Prog. Rep. July–September 1978*, ORNL/NUREG/TM-275, Union Carbide Corp. Nuclear Div., Oak Ridge Natl. Lab.

12. R. H. Bryan and J. W. Bryson, "Pressurized Thermal Shock Stress and Fracture Analysis," in *Heavy-Section Steel Technology Program Quart. Prog. Rep. July–September 1981*, NUREG/CR-2141, Vol. 3 (ORNL/TM-8145), Union Carbide Corp. Nuclear Div., Oak Ridge Natl. Lab.

13. K. J. Bathe, *ADINA — A Finite Element Program for Automatic Dynamic Incremental Nonlinear Analysis*, Report 82448-1, Massachusetts Institute of Technology, Cambridge, Mass., September 1975 (revised December 1978).

14. B. R. Bass and J. W. Bryson, *Applications of Energy Release Rate Techniques to Part-Through Cracks in Plates and Cylinders, Vol. 2, ORVIRT: A Finite Element Program for Energy Release Rate Calculations for 2-Dimensional and 3-Dimensional Crack Models*, NUREG/CR-2997, Vol. 2 (ORNL/TM-8527/V2), Union Carbide Corp. Nuclear Div., Oak Ridge Natl. Lab., February 1983.

15. F. J. Loss, *Dynamic Tear Test Investigations of the Fracture Toughness of Thick-Section Steel*, NRL-7056, U.S. Naval Research Laboratory, Washington, D.C., May 14, 1970.

16. H. T. Corten and R. H. Sailors, *Relationship Between Material Fracture Toughness Using Fracture Mechanics and Transition Temperature Tests*, T&AM Report 346, University of Illinois, Urbana, Ill., August 1, 1971.

17. R. D. Cheverton, "Thermal Shock Investigations," in *Heavy-Section Steel Technology Program Quart. Prog. Rep. October–December 1980*, NUREG-CR-1941 (ORNL/NUREG/TM-437), Union Carbide Corp. Nuclear Div., Oak Ridge Natl. Lab.

18. J. R. Dougan, *Relationships Between Charpy V-notch Impact Energy and Fracture Toughness*, NUREG/CR-2362 (ORNL/TM-7921), Union Carbide Corp. Nuclear Div., Oak Ridge Natl. Lab., 1982.

19. K. R. Thoms, "Pressurized Thermal-Shock Test Vessels," in *Heavy-Section Steel Technology Program Quart. Prog. Rep. October–December 1982*, NUREG/CR-2751, Vol. 3 (ORNL/TM-8369/V3), Union Carbide Corp. Nuclear Div., Oak Ridge Natl. Lab.

20. W. J. Stelzman and R. K. Nanstad, "Pressurized Thermal Shock Materials Characterization," in *Heavy-Section Steel Technology Program Quart. Prog. Rep. October–December 1982*, NUREG/CR-2751, Vol. 4 (ORNL/TM-8369/V4), Union Carbide Corp. Nuclear Div., Oak Ridge Natl. Lab.

21. American Society for Testing and Materials, *1980 Annual Book of ASTM Standards*, Part 10, E208-69, Philadelphia, 1980, pp. 409–28.

22. S. Onodera et al., *A Study of Pellini Test: Reproducibility and Welding Procedure*, R(MS)80-037, Japanese Steel Works, Limited (September 17, 1980).

23. H. Tsukada et al., *A Study on Drop-Weight Test Using A508 Cl. 2 Steel*, R(MS)81-60, Japanese Steel Works, Limited (December 1, 1981).

24. R. H. Bryan et al., "Proof Testing of Seals and Transducers," in *Heavy-Section Steel Technology Program Quart. Prog. Rep. April–June 1982*, NUREG/CR-2751, Vol. 2 (ORNL/TM-8369/V2), Union Carbide Corp. Nuclear Div., Oak Ridge Natl. Lab.

25. R. W. McCulloch and G. C. Robinson, "Pressurized Thermal-Shock Test Facility," in *Heavy-Section Steel Technology Program Quart. Prog. Rep. October–December 1981*, NUREG/CR-2751, Vol. 4 (ORNL/TM-8369/V4), Union Carbide Corp. Nuclear Div., Oak Ridge Natl. Lab.

6. STAINLESS STEEL CLADDING INVESTIGATIONS

W. R. Corwin R. K. Nanstad
G. M. Goodwin W. J. Stelzman

6.1 Clad Plate Experiments

Further testing of one-wire clad plate specimens has been deferred until data on the effects of irradiation have been obtained. The previously machined specimens will be held in inventory until such time as test definitions are clear.

A purchase specification was written and submitted to the Purchasing Department of Union Carbide Corporation—Nuclear Division for procurement of the machining, welding, and heat treatment necessary to provide clad plate specimens and material-characterization blocks of three-wire series-arc cladding overlay on a plate of A533 grade B steel (HSST 12). The specification calls for chemically and mechanically uniform cladding with a minimum Charpy V-notch impact energy of 54.2 J at a temperature at least 11°C lower than the drop-weight nil-ductility temperature of the base plate. This will allow the evaluation of the effects of relatively tough cladding, representative of commercially fabricated unirradiated material, on the initiation and arrest behavior of pressure vessel steel to complement the work already done with a moderately low toughness cladding.[1] In addition, the cladding is proposed for use in the irradiated stainless steel cladding task.

Discussions with the potential vendor have indicated that the requirements of the specification can be met. The schedules for contract placement and work performance are expected to lead to delivery in the fourth quarter of FY 1983.

6.2 Metallographic Cladding Examinations

The reactor pressure vessel (RPV) nozzle dropout received from Combustion Engineering was sectioned and examined metallographically. The weld overlay cladding on the dropout was applied, using the three-wire series-arc procedure. In this method, an arc is drawn between the two outside electrodes, typically of types 308 and 309 stainless steel welding wire, and the third wire of type 312 stainless steel is fed cold into the weld puddle. The dropout, consisting of a single layer of cladding applied onto A533 grade B base metal, had received ~2 h of postweld heat treatment (PWHT) at 621°C when it was received.

A macroscopic section of the cladding in the as-received condition, taken perpendicular to the welding direction (Fig. 6.1), shows the degree of overlap between successive passes. The fusion line [Fig. 6.2(*a*)] is already slightly decorated with carbide precipitates from the limited PWHT. The bulk of the cladding [Fig. 6.2(*b*)] exhibits a typical distribution of delta-ferrite in an austenite matrix.

To examine the effect of the longer PWHT typical of a finished RPV, a small piece of the dropout was given an additional PWHT of 38 h at 621°C

M&C PHOTO
Y190276

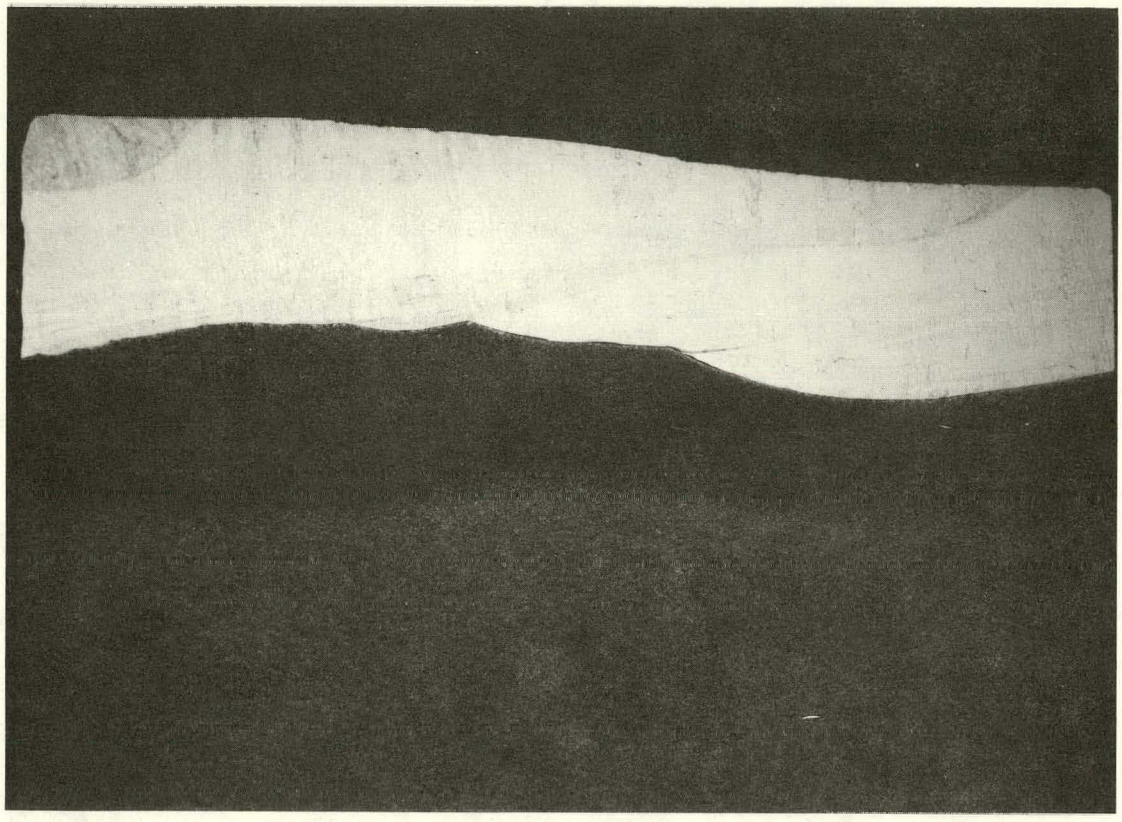

Fig. 6.1. Section through reactor pressure vessel nozzle dropout clad with three-wire series-arc weld overlay in as-received condition representing ~2 h of stress relief at 6^1°C.

for a total of 40 h. A macroscopic section through the 40-h heat-treated material (Fig. 6.3) shows little noticeable effect on the cladding, although tempering and decarburization of the base metal along the fusion line is evident. Closer examination [Fig. 6.4(*a*)] confirms that the austenite/delta-ferrite composition of the bulk of the cladding is virtually unchanged. However, the carbide precipitation at the fusion line and in the austenite grain boundaries near the fusion line is enhanced by the longer PWHT.

To investigate possible variations in the microstructure of weld overlay cladding, a small piece of 50-mm-wide strip cladding, which had been procured from a commercial nuclear vessel fabricator, was examined. The strip cladding of type 308 weld metal was deposited on A533 grade B base plate, and the weldment was given a 2-h PWHT at 621°C, similar to the heat treatment received by the three-wire series-arc cladding. By comparison with the series-arc cladding in a similar condition, the fusion line [Fig. 6.5(*a*)] is still clean after the limited heat treatment, showing only a martensite/austenite mixture in the relatively unmixed boundary layer of the cladding. The bulk of the cladding [Fig. 6.5(*b*)] is similar to the

ORNL–PHOTO 3417–83

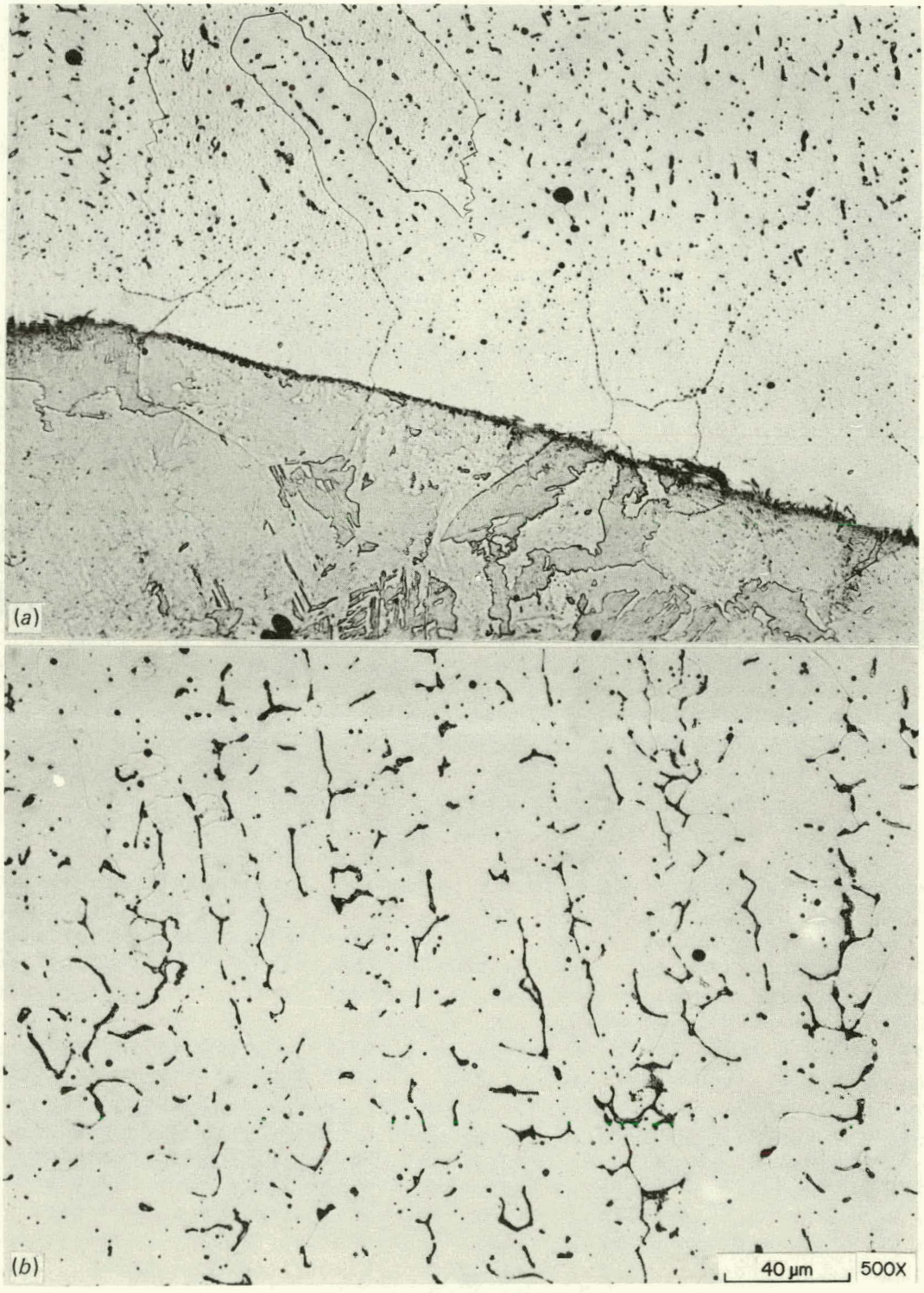

Fig. 6.2. Three-wire series-arc cladding after PWHT of 2 h at 621°C: (*a*) fusion line and (*b*) typical structure.

M&C PHOTO
Y190565

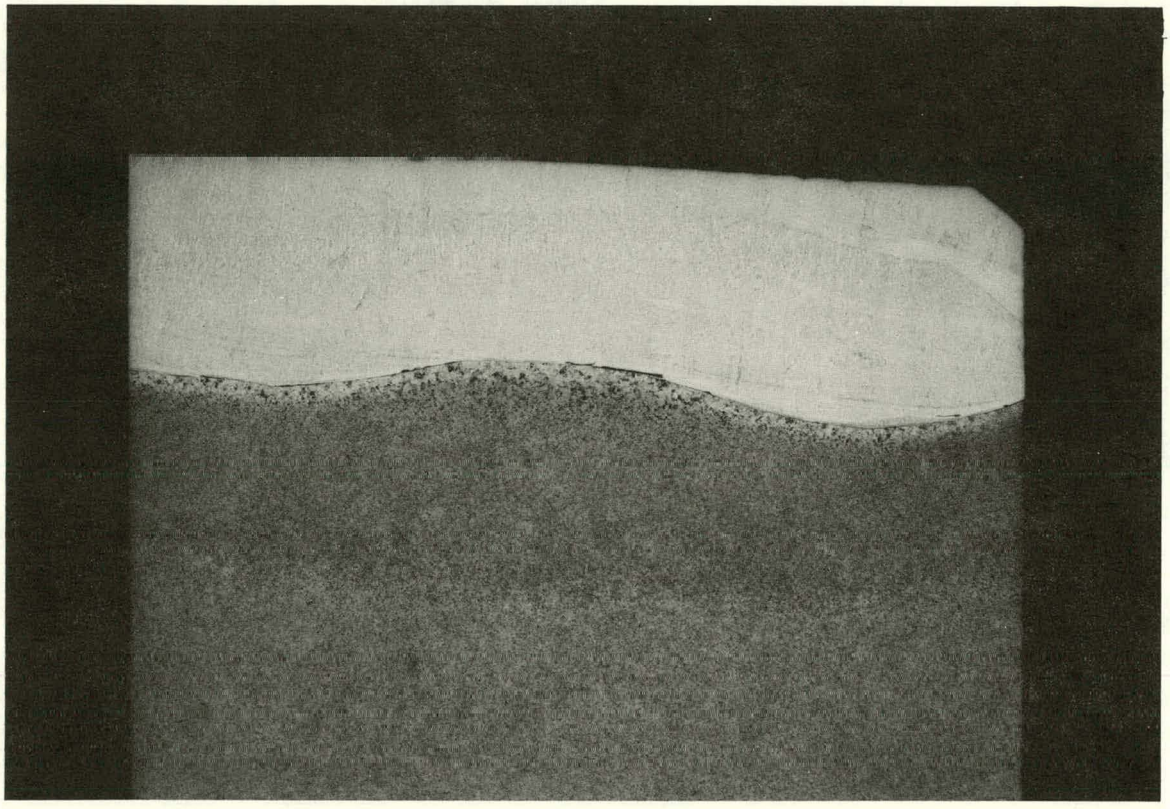

Fig. 6.3. Section through reactor pressure vessel nozzle dropout clad with three-wire series-arc weld overlay after 40-h PWHT at 621°C.

series-arc weldment, with slightly more delta-ferrite in an austenite matrix. A PWHT of 40 h total at 621°C produced a fusion line and nearby austenite grain boundaries highly decorated with carbide precipitates [Fig. 6.6(*a*)] and virtually no change in the bulk of the cladding [Fig. 6.6(*b*)], again very similar to the three-wire series-arc-deposited cladding.

The precipitation of carbides is illustrated well in the side-by-side comparison of the fusion line regions of both the three-wire series-arc and the strip-cladding weldments (Figs. 6.7 and 6.8, respectively) after 2 and 40 h of PWHT at 621°C.

The Oak Ridge National Laboratory (ORNL) single-wire cladding with a PWHT of 40 h at 621°C, which has been used for the clad plate tests[1] and is scheduled for irradiation experiments, was also examined metallographically. A macroscopic section taken perpendicular to the fracture surface and parallel to the welding direction of clad plate specimen CP-3 (Fig. 6.9) indicates a structure quite different from those of the single-layer strip or three-wire weldments. The single-wire weldment for the clad plates was deposited in two layers, using the oscillating submerged-arc technique. The welding wires used were types 309 and 308 stainless steel

ORNL–PHOTO 3418–83

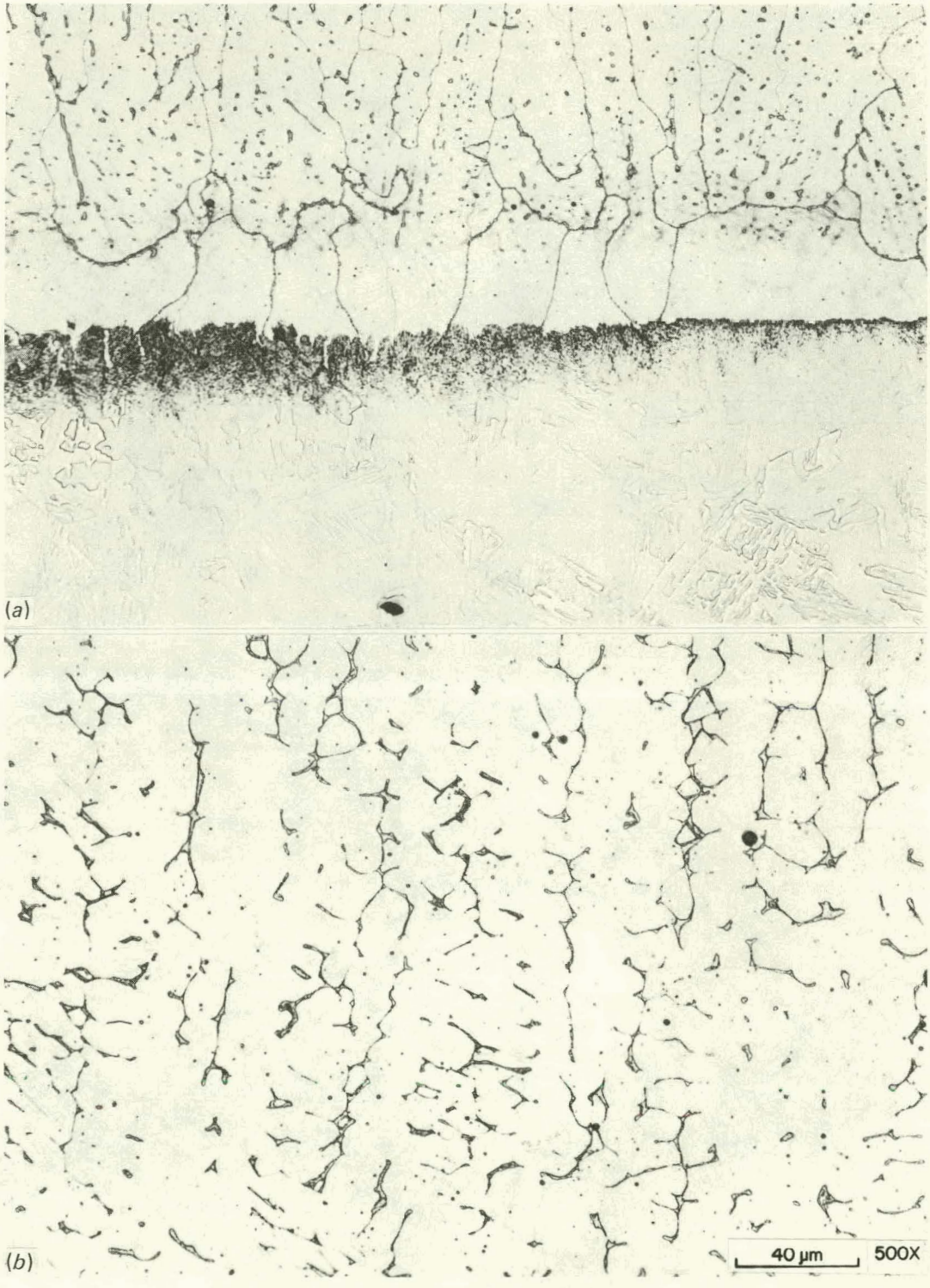

Fig. 6.4. Three-wire series-arc cladding after full PWHT of 40 h at 621°C: (*a*) fusion line and (*b*) typical structure.

ORNL–PHOTO 3419–83

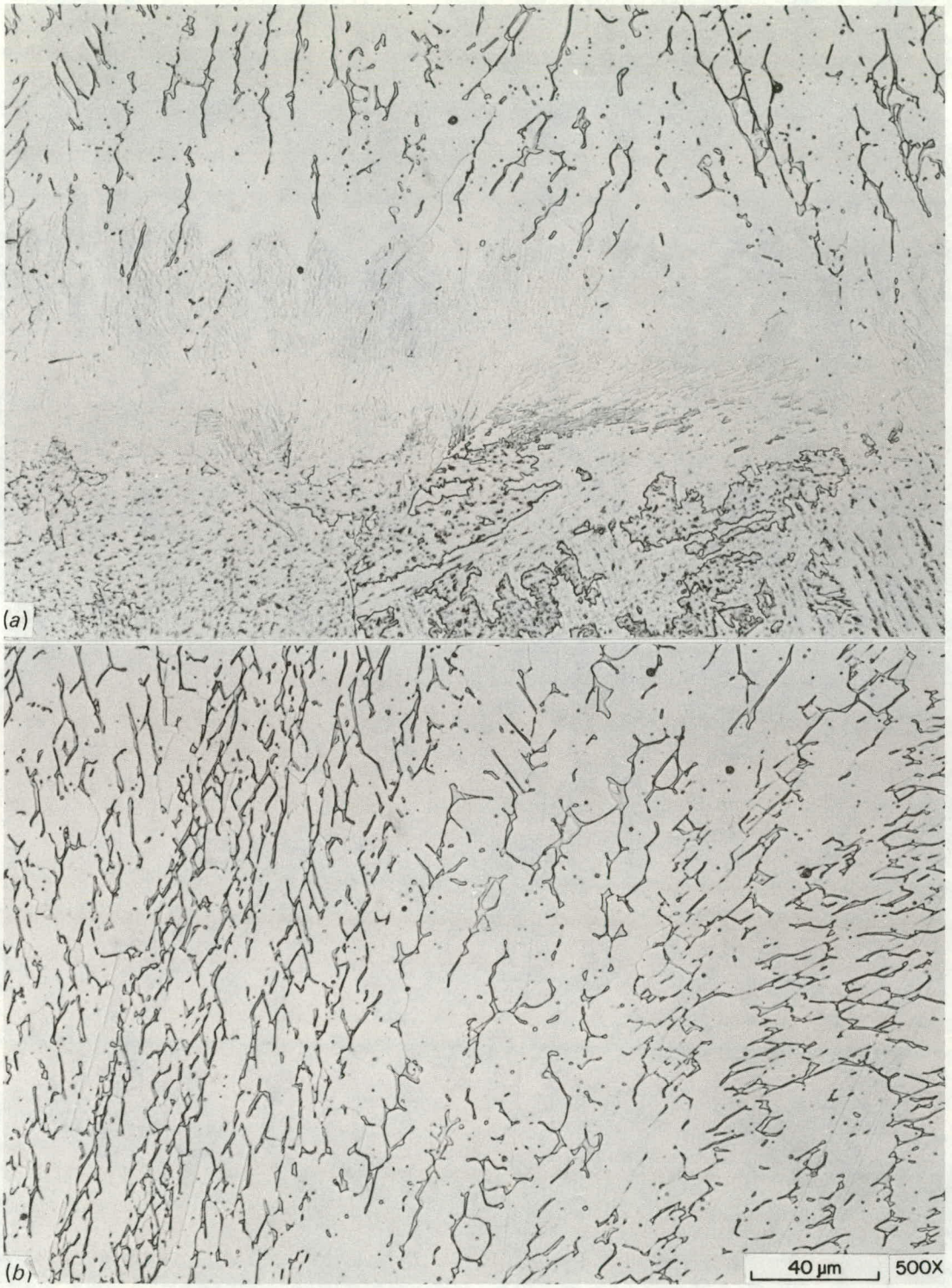

Fig. 6.5. Strip cladding after 2-h PWHT at 621°C: (*a*) fusion line and (*b*) typical structure.

ORNL–PHOTO 3420–83

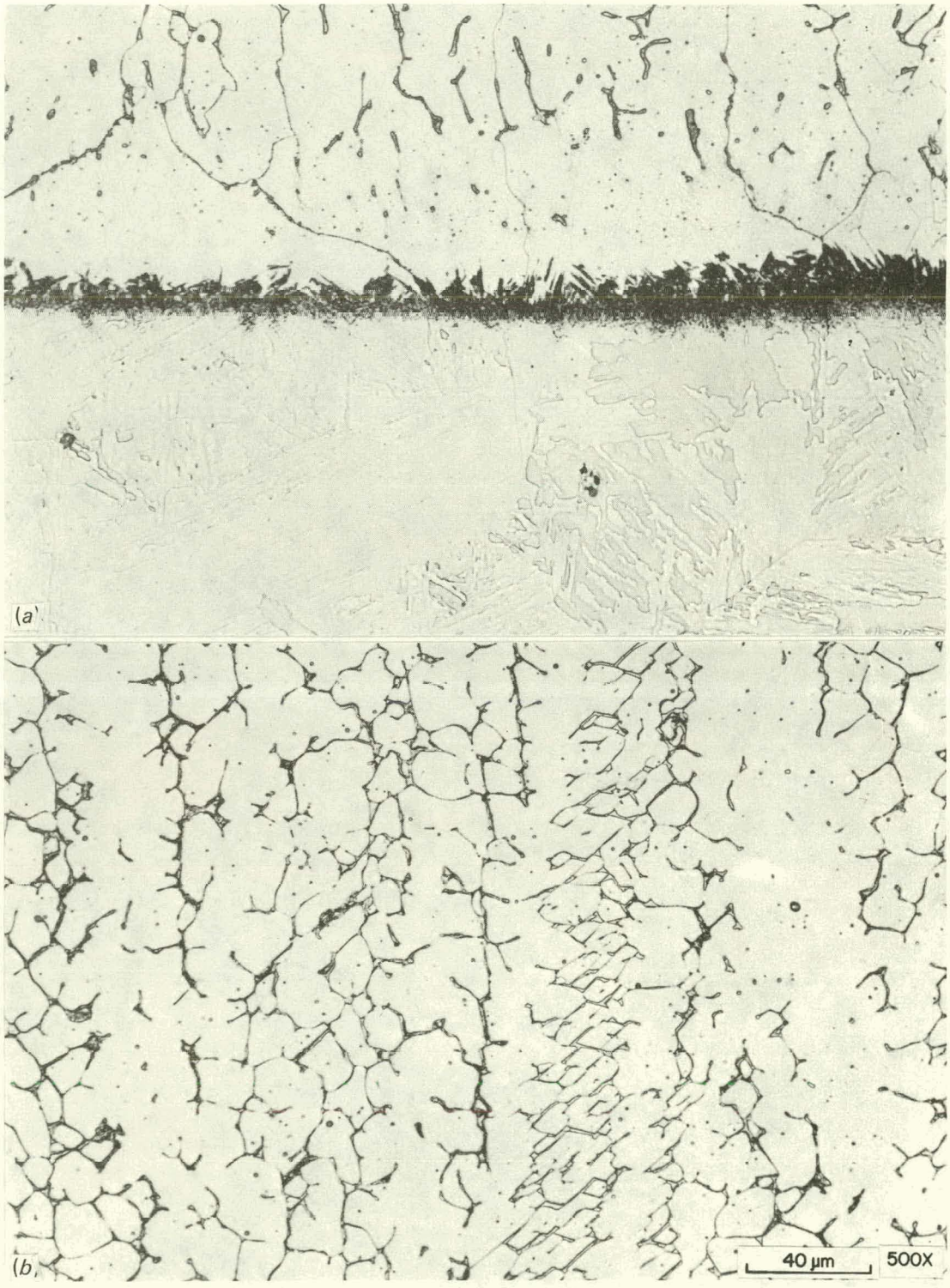

Fig. 6.6. Strip cladding after 40-h PWHT at 621°C: (*a*) fusion line and (*b*) typical structure.

ORNL–PHOTO 3421–83

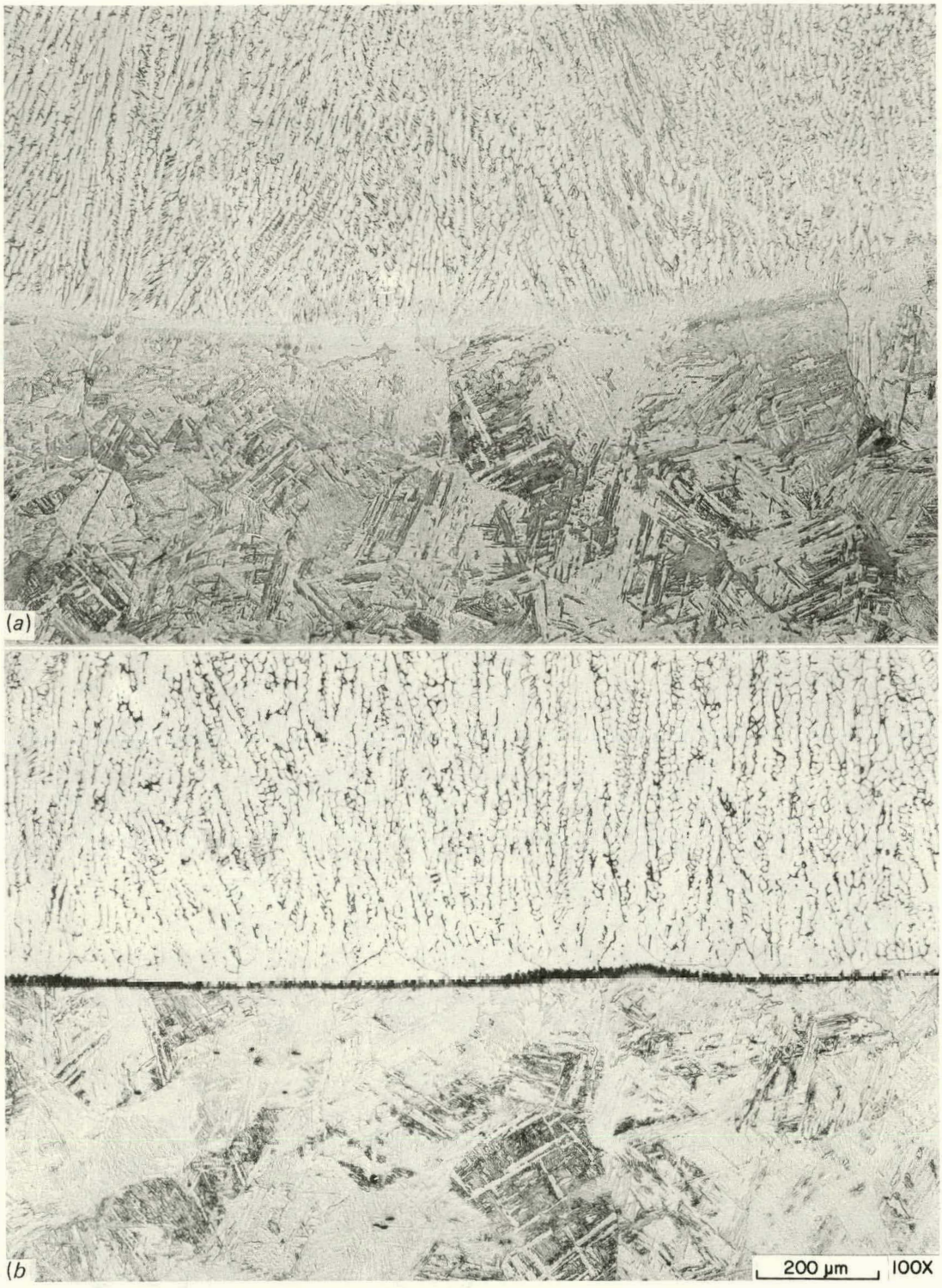

Fig. 6.7. Comparison of fusion line of strip cladding on A533 grade B steel with (*a*) 2-h and (*b*) 40-h PWHT at 621°C.

ORNL–PHOTO 3422–83

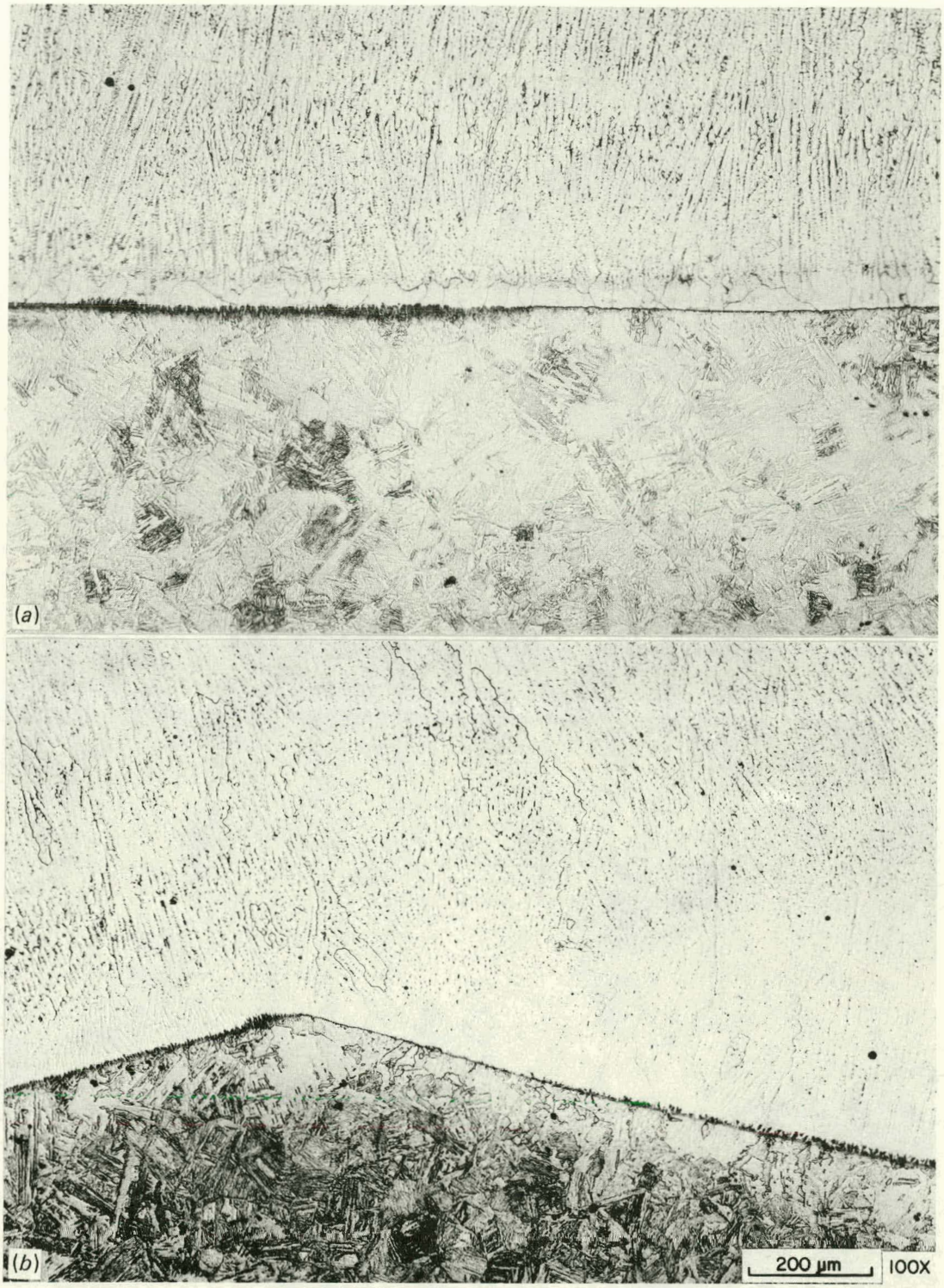

Fig. 6.8. Comparison of fusion line of three-wire series-arc cladding of A533 grade B base metal after (*a*) 2-h and (*b*) 40-h PWHT at 621°C.

for the first and second layers, respectively. The surface of the cladding was then machined to provide a flat surface on the test specimen. It can readily be seen from Fig. 6.9 that the resulting clad plate specimen is composed primarily of the base metal and the first weld overlay pass, with only a small amount of the second weld overlay pass remaining. In looking at the microstructures of the first and second passes (Fig. 6.10), it can be seen that the second pass is composed of delta-ferrite in an austenite matrix, very much like both the three-wire series-arc and strip cladding, but the first pass, with its three distinct regions, is noticeably different. The lightest regions appear to be austenitic, with the light-gray regions martensite, and the darkest regions upper bainite decorated with additional carbides precipitated during the PWHT. This microstructure was the result of excessive dilution of the first welding pass, which is estimated to be in the range of 50 to 55%. The metallurgical structure of weld cladding deposited on A302 grade B plate, with type 309 weld wire and base metal dilution of 38 to 61%, is predicted to be a mixture of austenite and martensite.[2] Dilution greater than 61% should produce all martensite. In the case of the clad plates and cladding material-characterization block, the combination of welding both before and

M&C PHOTO
Y190566

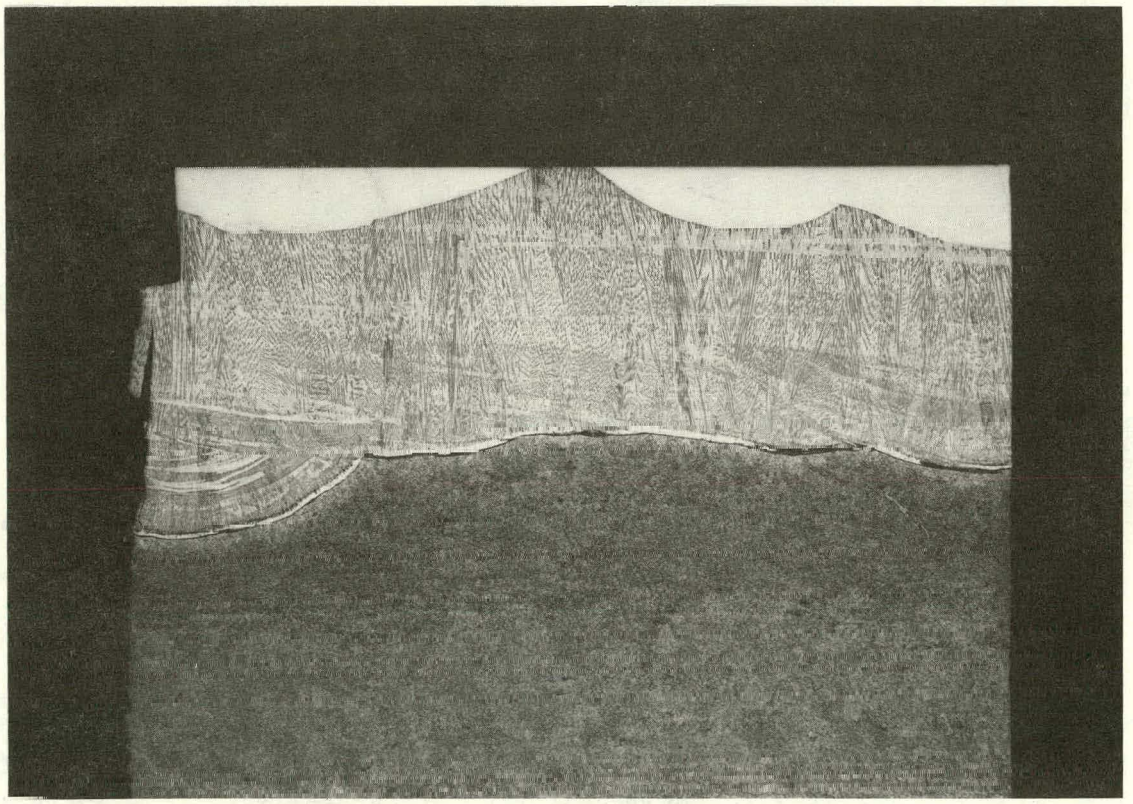

Fig. 6.9. Section perpendicular to fracture surface and parallel to welding direction of two-pass single-wire weld deposit on clad plate CP-3.

ORNL–PHOTO 3423–83

Fig. 6.10. Microstructures of types 309 and 308 stainless steel single-wire weld deposits typical of first and second passes used to clad beam test specimen CP-8. (*a*) Type 309, first pass; (*b*) type 308, second pass.

after heat treatment, PWHT, and microsegregation during soldification produced upper bainite as well. The effects of microsegregation during solidification are particularly evident near the fusion line (Fig. 6.11). Moving away from the low-dilution boundary layer, the beginning of martensite and bainite can be seen where the concentration of selected alloying elements in the weld puddle was increased by rejection from the solid phases of metal at the moving solidification boundary.

It would be expected that the different microstructures of the first and second layers comprising the weld overlay cladding of the clad plate specimens would exhibit different mechanical properties. Because the effects of neutron irradiation on this material will be examined within the irradiated stainless steel cladding portion of the Heavy-Section Steel Technology (HSST) Irradiation Program, the properties of this material in the unirradiated condition are being examined as well. Results of that work to date are discussed in Chap. 3 of this report. The clad plate tests were conducted at −40°C to accommodate the need for a frangible condition in the base metal. Although there is a sparsity of data for first-layer cladding and much scatter in the data set, the toughness of the first layer at −40°C appears to be somewhat lower than that of the second and third layers. At that temperature, however, all three cladding layers exhibit very low toughnesses relative to those in the upper-shelf region. Thus, the significance of the high-dilution first-layer cladding to the clad plate test results is considered to be small.

Although the investigation of high-dilution cladding was not the initial aim of the cladding studies, it may well be highly germane to the question of the effects of cladding on RPV integrity. High base metal dilution of cladding, caused by inadequate control of welding procedures, and the resulting microstructure has been documented[3,4] in commercial RPVs. Typically, the resulting material has poorer mechanical and/or corrosion properties in the unirradiated condition; no information is available on the irradiation damage of such material. The fact that such material is included in the clad plate and irradiated stainless steel cladding investigations may provide insight into the behavior of substandard weld overlay cladding representative of material actually in the field.

ORNL–PHOTO 3424–83

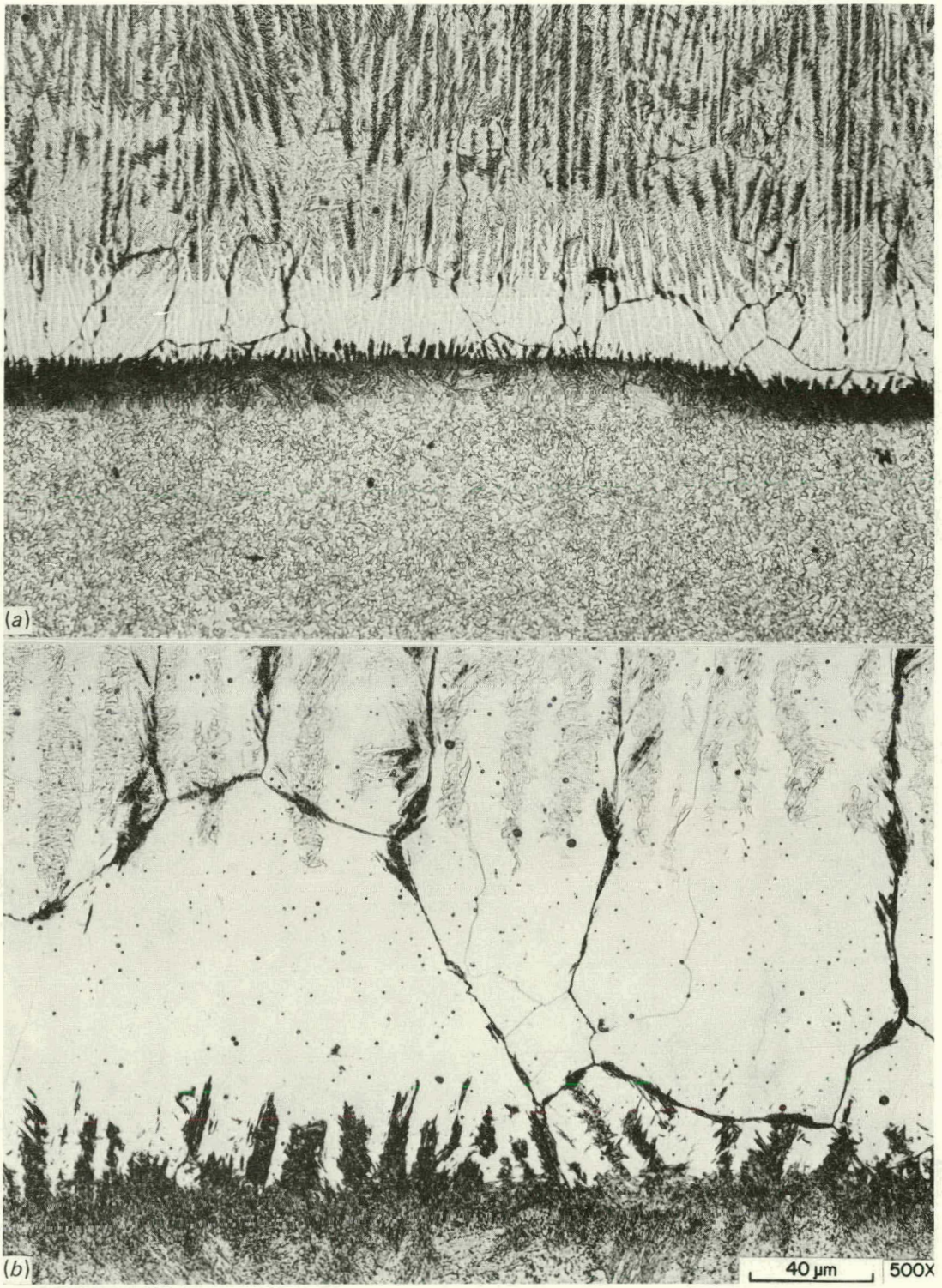

Fig. 6.11. Fusion line of two-pass single-wire type 309/308 stainless steel cladding deposition on A533 base plate (HSST 07). (*a*) 100x, (*b*) 500x.

References

1. R. K. Nanstad et al., "Stainless Steel Cladding Investigations," pp. 109–29 in *Heavy-Section Steel Technology Program Quart. Prog. Rep. April–June 1982*, NUREG/CR-2751, Vol. 2 (ORNL/TM-8369/V2), Union Carbide Corp. Nuclear Div., Oak Ridge Natl. Lab.

2. R. D. Wylie, J. McDonald, Jr., and A. L. Lowenberg, "Weld Deposited Cladding of Pressure Vessels," *British Weld. J.* 12, 378–93 (August 1965).

3. E. B. Norris, D. R. Ireland, and C. E. Lautzenheiser, *The Second Inspection of the Elk River Reactor Pressure Vessel After Operation*, SWRI 1228P9-13, Southwest Research Institute, San Antonio, Texas, July 21, 1967.

4. T. Kondo, H. Nakajima, and R. Nagasaki, "Metallographic Investigation on the Cladding Failure in the Pressure Vessel of a BWR," *Nucl. Eng. Design* 16, 205–22 (1971).

7. ENVIRONMENTALLY ASSISTED CRACK-GROWTH STUDIES*

W. H. Bamford† L. J. Ceschini†

7.1 Introduction

The objective of this task is to characterize the crack-growth rate in light-water-reactor materials exposed to primary coolant environments. The work now being conducted falls into four major areas: (1) corrosion-fatigue crack-growth tests in a simulated pressurized-water-reactor (PWR) environment, (2) static load K_{ISCC} tests in a simulated PWR environment, (3) fractographic examination of specimen fracture surfaces, and (4) characterization of the environment by measurement of its electro-chemical potential. The progress made in each of these areas is discussed in the following sections.

7.2 Fatigue Crack-Growth Test Results

Studies continued on characterizing the effect of material chemistry on the environmental acceleration of fatigue crack growth. This work is being carried out through the detailed study of four heats of reactor pressure vessel (RPV) steel plate. The chemistry chemical content of each of these specimens is given in Table 7.1, where it can be seen that the only important difference is the sulfur content. It has been demonstrated in earlier work[1] that the environmental acceleration of crack growth is proportional to the level of sulfur in the steel plate.

The four heats of steel plate are being studied through the matrix of tests shown in Table 7.2. During this report period, two additional tests were completed on the heat PN, which has an intermediate sulfur content. The tests were done under a sine loading at one cycle per minute with $R = 0.7$. Only two more tests are necessary to complete the matrix at this point, as can be seen from the table. The results of the two tests are shown in Figs. 7.1 and 7.2; as expected, a relatively high level of susceptibility to environmental enhancement is seen in the figures. It is interesting that the enhancement is essentially the same for both specimens, as seen in Fig. 7.3, since one specimen is from the TL orientation and the other, PN-8, is from the TS, or through-thickness, orientation.

This behavior is somewhat different from that observed in tests at this same heat with $R = 0.2$. Results of these tests were previously reported in the annual progress report for FY 1981 (Ref. 3) and are shown here in Fig. 7.4. The difference lies in the behavior of the TS-oriented specimens. The results obtained for specimens at $R = 0.2$ were much lower

---

*Work sponsored by HSST Program under Union Carbide Corporation-Nuclear Division (UCC-ND) Subcontract 11X-21598C between UCC-ND and Westinghouse Electric Corporation, Nuclear Technology Division.

†Westinghouse Electric Corporation, Power Systems, Nuclear Technology Division, Pittsburgh, PA 15230.

Table 7.1. Chemical content of four heats of RPV steel plate – matrix study of sulfur effects

Specimen	Elements										
	C	Mn	P	S	Si	Ni	Cr	Mo	Cu	V	Co
A533B Class 1											
Heat IN	0.21	1.26	0.012	0.026	0.25	0.47		0.47	0.19		
Heat TW	0.21	1.38	0.008	0.004	0.21	0.67		0.56	0.08		
Heat W7	0.23	1.40	0.005	0.004	0.25	0.70		0.57			
Heat PN	0.21	1.33	0.012	0.016	0.22	0.56		0.54	0.13		

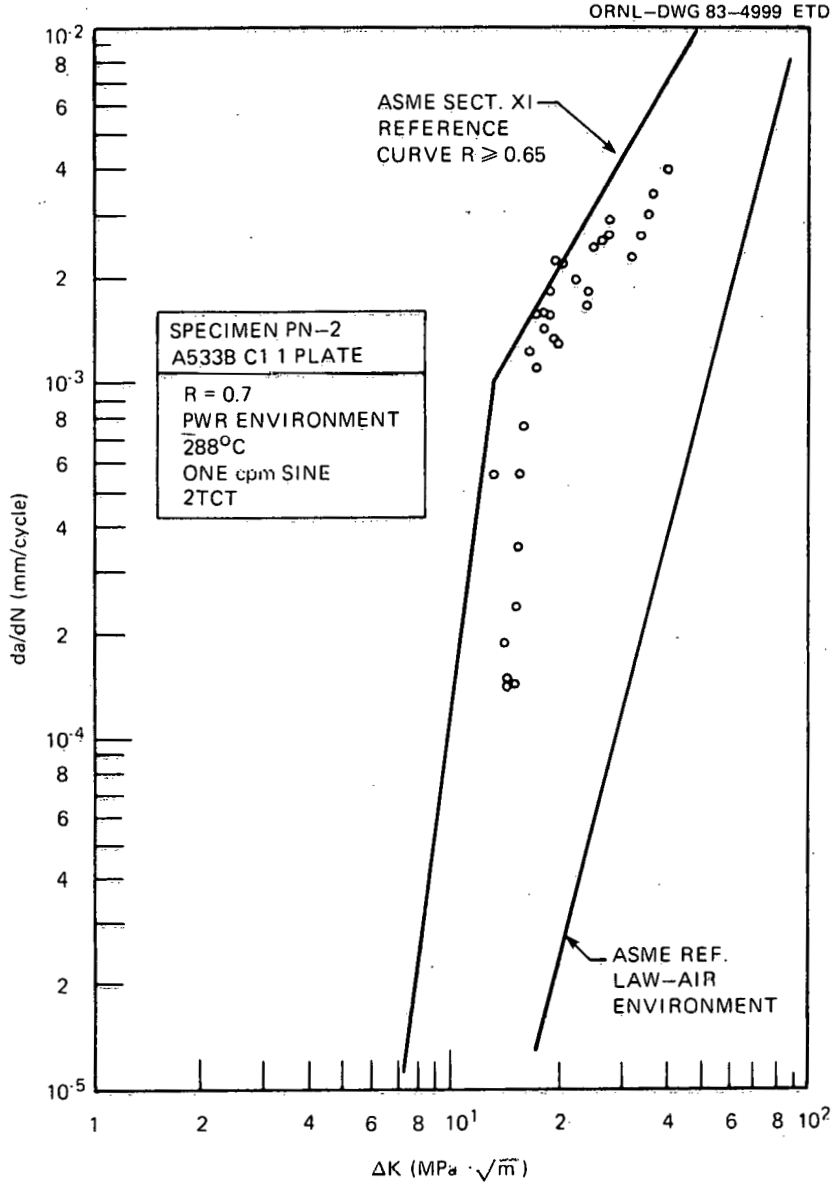

Fig. 7.1. Fatigue-crack-growth rate results to specimen PN-2, tested in PWR environment at R = 0.7.

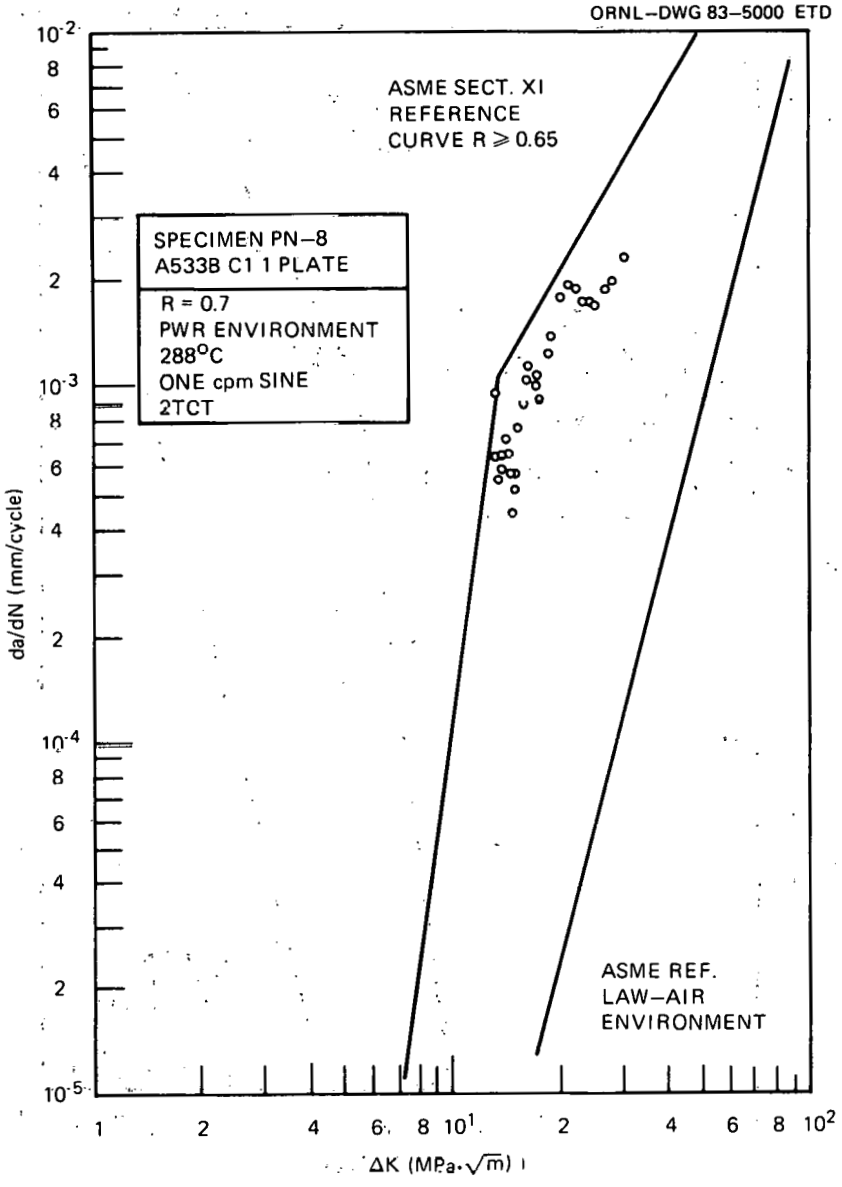

Fig. 7.2. Fatigue-crack-growth rate results for specimen PN-8, tested in PWR environment at R = 0.7.

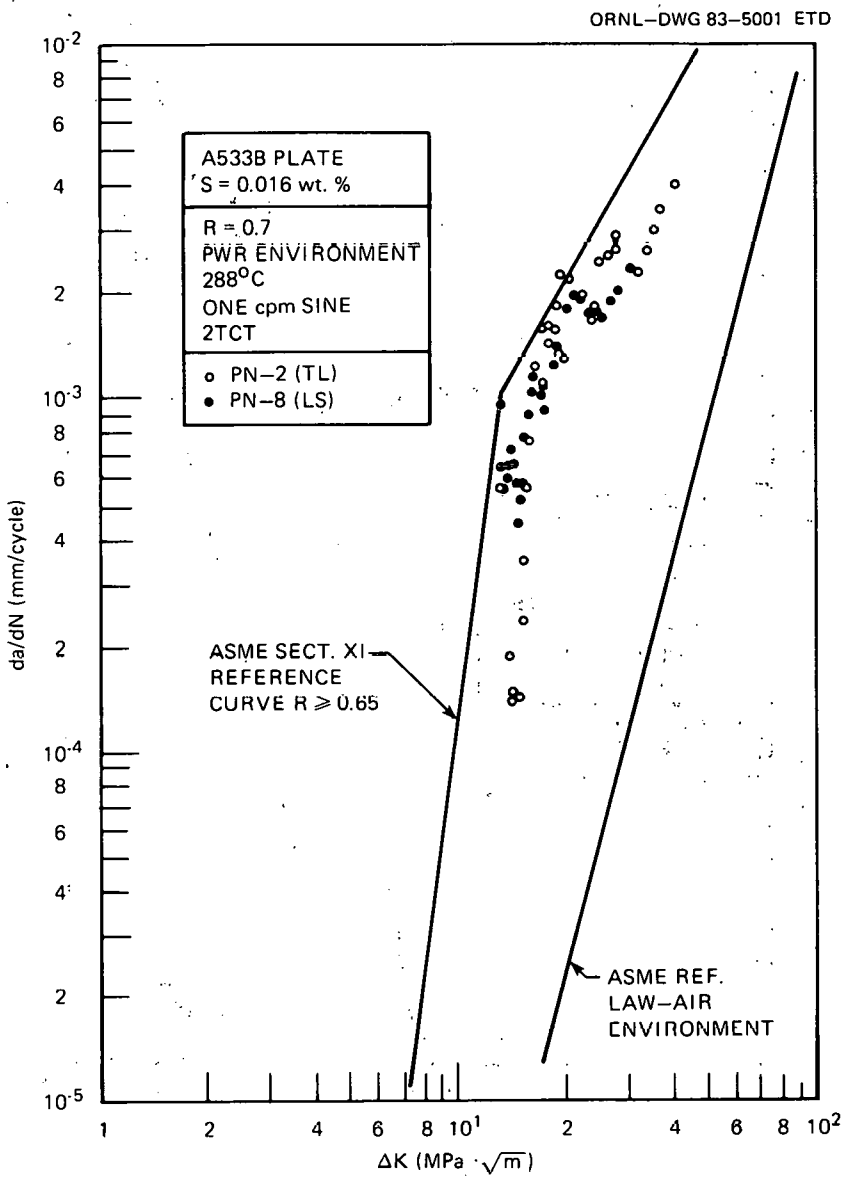

Fig. 7.3. Effect of specimen orientation on crack growth, medium sulfur plate PN, R = 0.7.

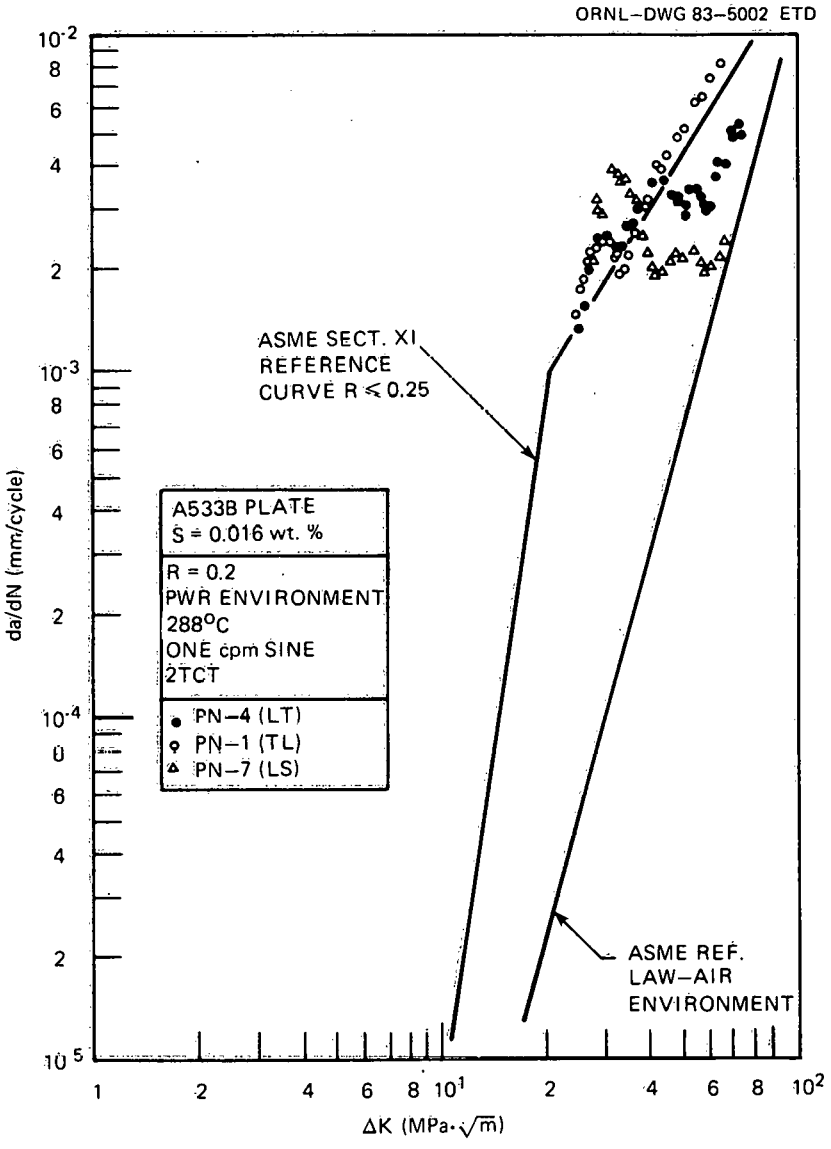

Fig. 7.4. Effect of specimen orientation on crack growth, medium sulfur plate, R = 0.2.[3]

Table 7.2. Tests completed in study of A533B class 1 plate[a]

Sulfur content of plate	Test conditions					
	R = 0.2			R = 0.7		
	Specimen orientation[b]			Specimen orientation[b]		
	TL	LT	TS	TL	LT	TS
S = 0.004	TW-1, W7-2C7	TW-4	TW-7	TW-2, W7-2C6	TW-5	TW-8
S = 0.016	PN-1	PN-4	PN-7	PN-2[c]		PN-8[c]
S = 0.026	IN-1	IN-4	IN-7	IN-2	IN-5	

[a]All tests were carried out in a simulated PWR environment at 288°C. All specimens were 2TCT, and the applied loadings were identical for all specimens at a given R ratio. Load form was a one-cycle-per-minute sine wave.

[b]Specimen orientations are described in Fig. 7.1 of Ref. 2.

[c]Completed this report period.

than the results obtained for the other two in-plane orientations, TL and LT, as shown in Fig. 7.4. It appears that at high R ratio specimens from the TS orientation are no different in behavior than those from the other orientations.

It is also worthy of note that the crack-growth behavior observed for this material at either high or low R ratio is bounded by the ASME Sect. XI reference crack-growth-rate curves for the water environment.[4]

During the next report period, the test matrix will be completed and the results summarized in the progress report for that period.

7.3 Crack-Growth Behavior in Static Tests

The behavior of cracks in the steels and welds of interest in a water environment has been under investigation, using bolt-loaded specimens, since 1974. The specimens are of the wedge-opening-loading (WOL) type, 2.54 cm thick, and loaded to a fixed displacement by a bolt of the same material. The specimens are positioned in the bottom of two of the operating corrosion-fatigue autoclaves.

Crack propagation under static load has been observed in several of the 19 specimens that have been tested thus far. Thirteen remain in testing, including specimens of A508 class 2, A533B class 1, a Linde 124 weld, and two heat-affected zones (HAZs). No further crack propagation was observed in this report period.

7.4 Examination of Specimen Fracture Surfaces

Examination of the fracture surfaces of the test specimens, using the scanning electron microscope (SEM), has long been a part of this program. Recent work has been carried out to compare the fracture surfaces of the statically loaded specimens with those tested in fatigue.

Earlier studies have shown that the fracture surface of the tested specimens is more a reflection of the material microstructure than either the imposed loading or the environment of the crack tip. Several different features of fracture surfaces have been found, including striation formaton, which is most common, and void coalescence, which is observed only on the weld materials. The welds show a combination of striation and void coalescence (Fig. 7.5).

ORNL–PHOTO 3425–83

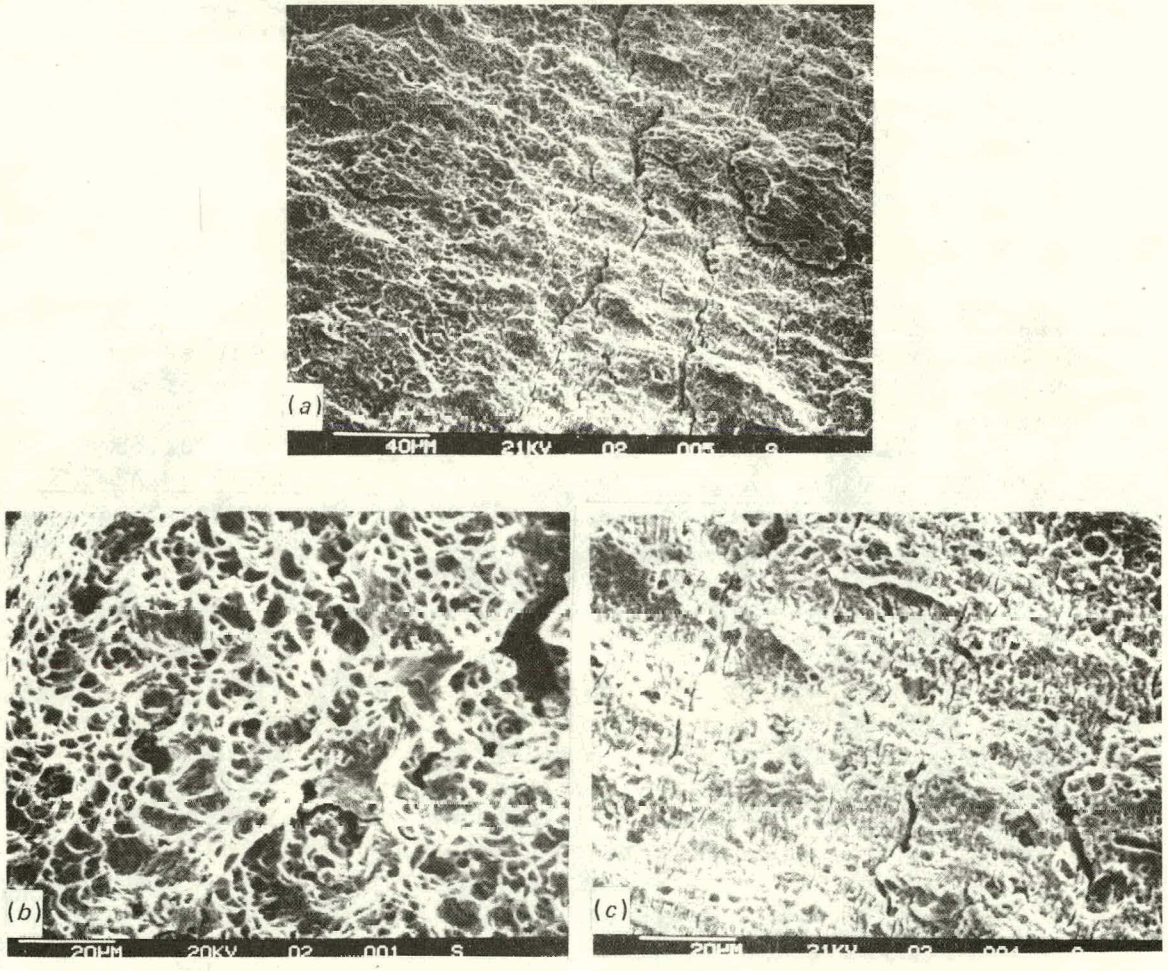

Fig. 7.5. Specimen C-2 WLD showing (*a*) transition from dimpled to striated growth, (*b*) high magnification of dimples, and (*c*) striated growth.

Another feature of fracture surfaces that is often observed in the base metal specimens is the occurrence of elongated regions parallel to the direction of crack growth, formed by the linking up of two cracks propagating at different elevations (Fig. 7.6). The density of such linked-up regions can be correlated to the roughness of fracture surface observed at low magnification. This can clearly be seen in the controlled series of specimens containing various sulfur levels, where the roughness of the fracture surface increased with sulfur content (Fig. 7.7). In the low-sulfur series (heat TW), the fracture surfaces were smooth and contained only striations, but in the high-sulfur series (heat IN), the surfaces contained a considerable number of elongated linked-up regions.

The features of the fracture surfaces of statically loaded specimens that have cracked are difficult to discern, because the oxidation that takes place over long time periods tends to erode them. It is interesting to note that the features that can be discerned are similar to those found in base metal specimens with accelerated crack growth – brittle-appearing linked-up regions. An example of these features on a statically loaded specimen is shown in Fig. 7.8.

7.5 Characterization of Water Environment Through Measurement of its Electrochemical Potential

Recent work[5,6] has demonstrated that significant differences in acceleration of crack-growth rate in water environments can occur. One explanation for these differences is the difference in the microstructure of the material, as reflected in the sulfur content or the number of manganese sulfide inclusions. This topic has already been discussed in this report. Another factor that appears to have an important impact is the enivronment itself.

A limited series of tests were performed on the same specimens in two different autoclave systems, the second operated under the supervision of P. M. Scott of the U.K. Atomic Energy Authority. The results of these comparative tests showed large differences in fatigue crack growth; they were reported in Ref. 1 and are shown here in Fig. 7.9. The major cause of the differences in crack-growth rate was postulated to be the difference in environment. Although the two autoclave systems had nominally the same water chemistry, the rate of water flow past the specimen was an order of magnitude higher in Scott's autoclave.

The best way to characterize the difference in water environments, as it might affect corrosion-fatigue processes, has been found to be the electrochemical potential. The International Cooperative Crack Growth Rate Committee (ICCGR) have discussed this subject at length, and several of the members have developed systems for measuring the free corrosion potential of an autoclave system.

A comparison of the various systems for measuring electrochemical potential has revealed that the two most reliable systems are the silver-silver chloride (Ag-AgCl) system developed by Andresen[7] and the hydrogen reference electrode. Both of these systems are being developed for installation on the Westinghouse Electric Corporation autoclaves.

ORNL–PHOTO 3426–83

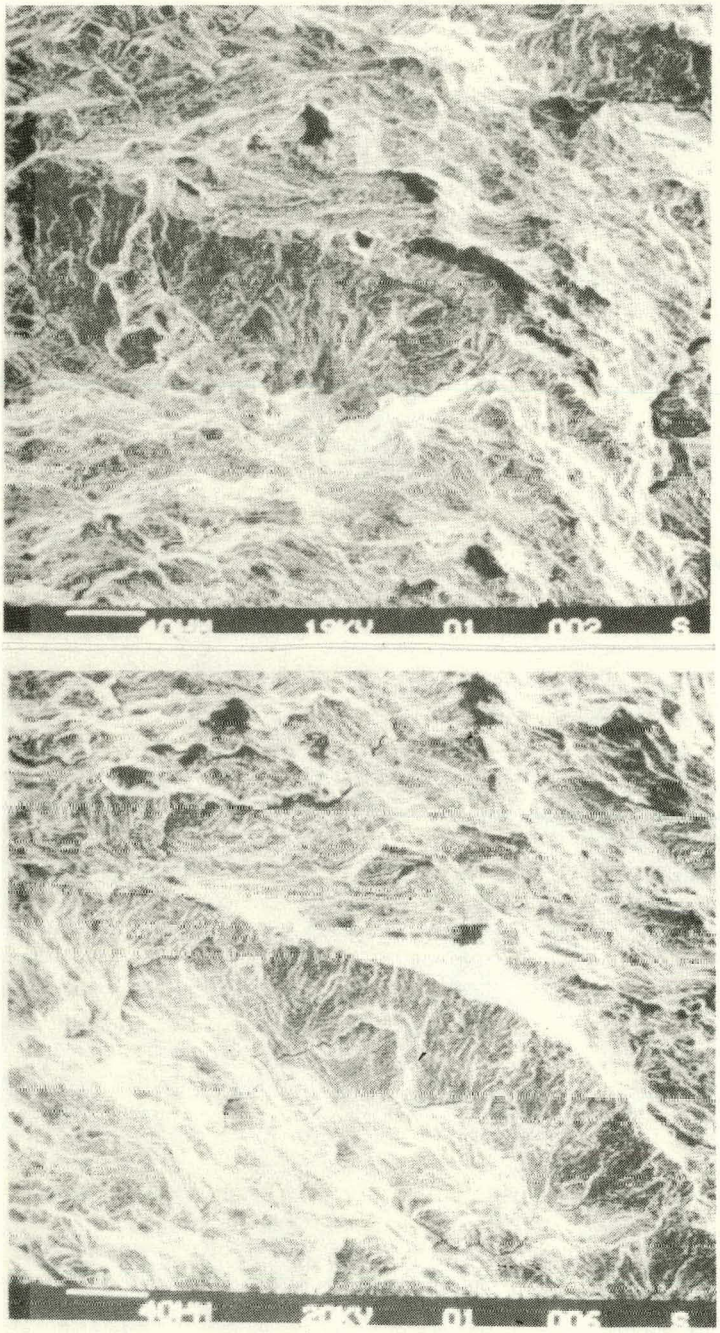

Fig. 7.6. Typical regions of fracture surface of specimen PN-4 containing areas elongated parallel to growth direction.

ORNL–PHOTO 3428–83

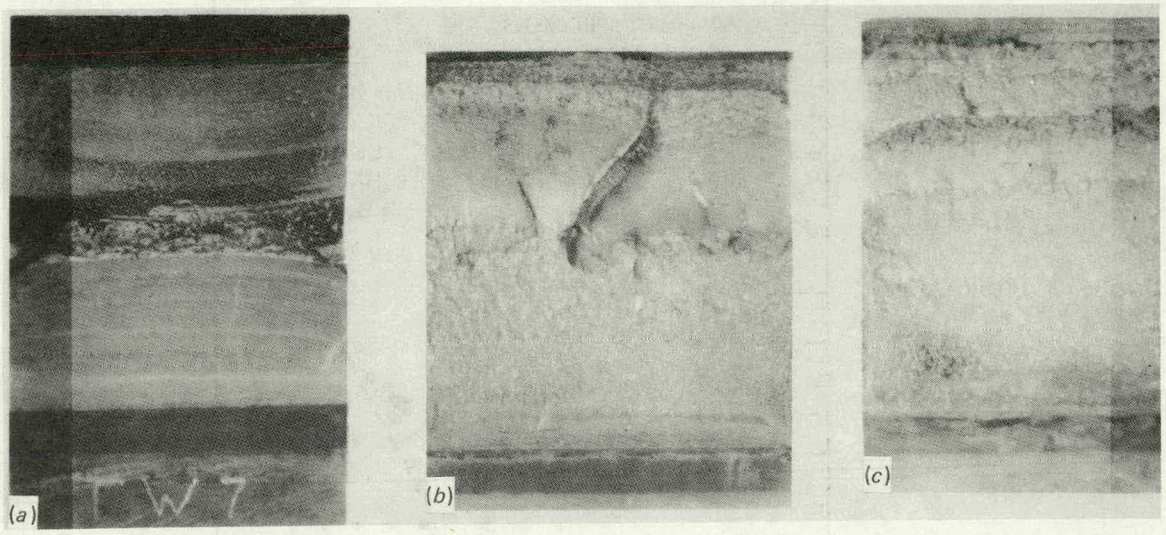

Fig. 7.7. Macrophotographs of specimens (*a*) TW-7, (*b*) PN-7, and (*c*) IN-7.

ORNL–PHOTO 1571–83

Fig. 7.8. Fracture surface of bolt-loaded specimen C-11 HAZ.

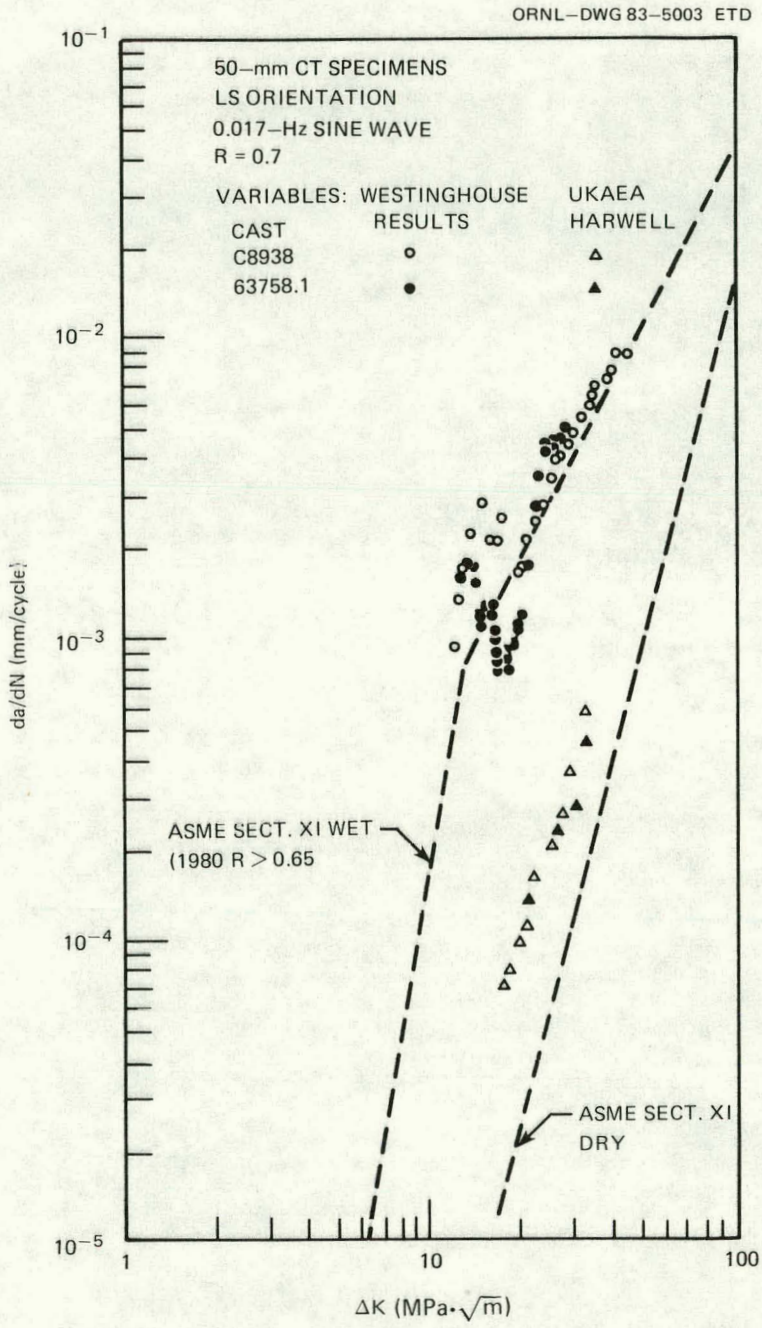

Fig. 7.9. Crack-growth rate data obtained on pressure vessel steels in water environment, using two different autoclave systems.

The Andresen Ag-AgCl electrode is mounted externally on the environmental chamber (see Fig. 7.10). A photo of a completed electrode is shown in Fig. 7.11. The device consists primarily of a 0.32-cm-diam silver rod in a solution of 0.1 *M* potassium chloride, which acts as a bridge. Porous zirconia is used as a separator between the liquid bridge and the environment. The reference electrode must be kept cool and pressurized, and

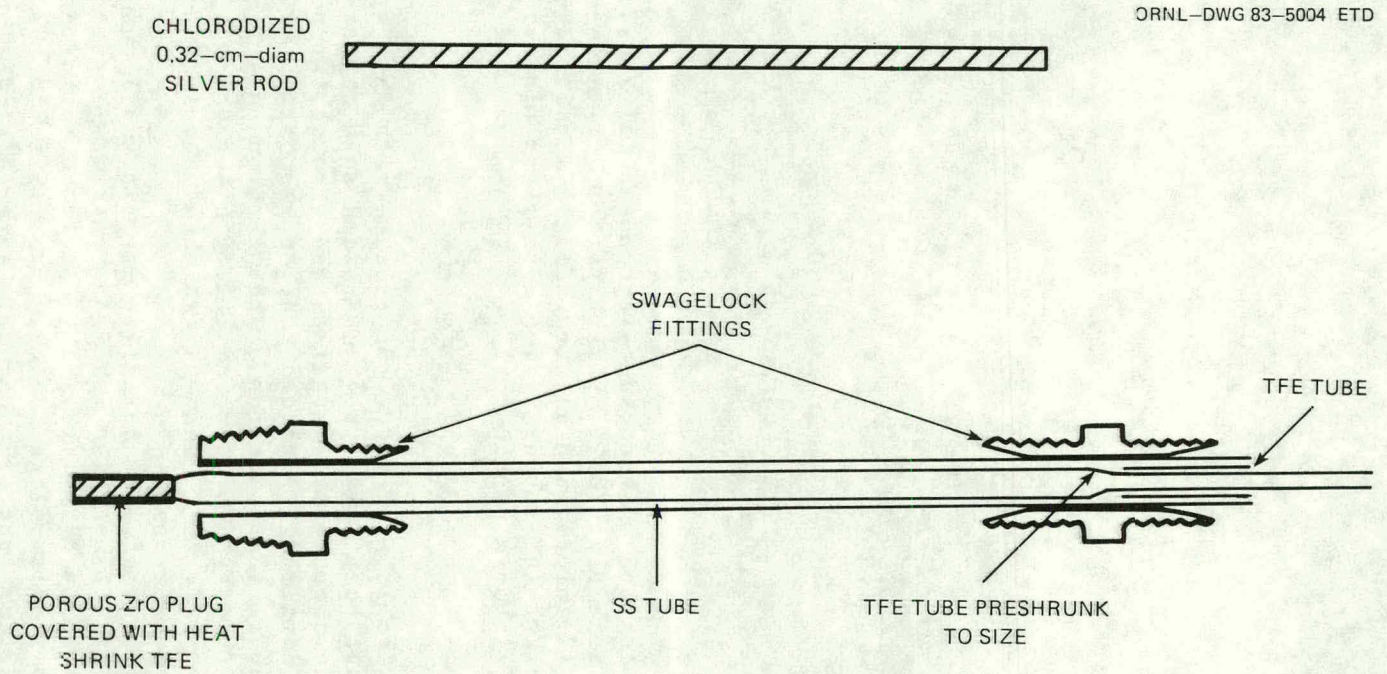

Fig. 7.10. Cross-sectional view of Andresen electrode parts.

ORNL–PHOTO 3429–83

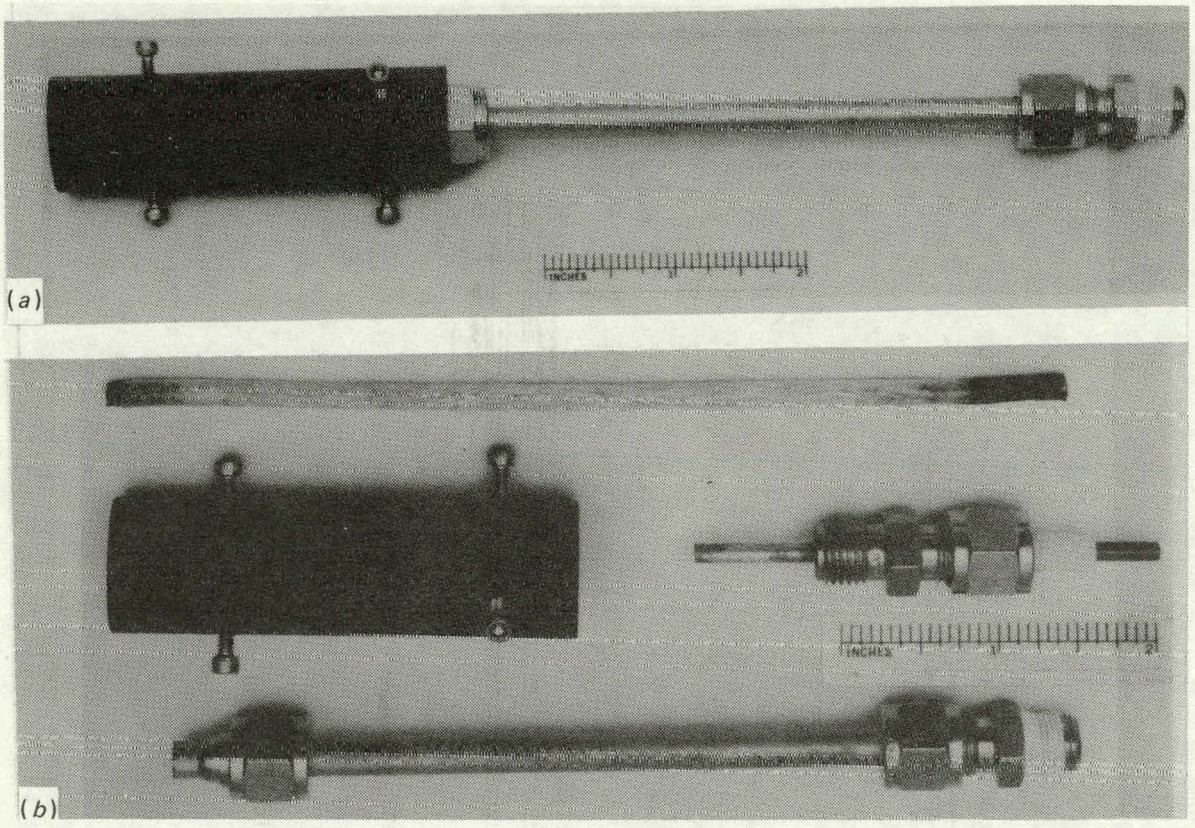

Fig. 7.11. Photograph of Andresen electrode. (*a*) Pressurized Ag/AgCl reference electrode assembly; (*b*) component parts: (1) external pressure tube with fittings; (2) cloridized silver rod; (3) micarta safcty holder for rod; (4) heat shrink TFE tubing filled with glass fibers; 0.1 N KCl solution and porous zirconia plug.

horizontal installation is preferred. Experience with this apparatus at other laboratories has been relatively good, with some reporting long service times before the electrolyte was dispersed through the porous plug and the operability impaired. A second problem associated with the failure of this electrode is contamination of the environment with chlorides. For this reason and to extend it service life, this electrode will first be installed in a separate small chamber, which may be isolated, at the exit of the environment chamber.

A hydrogen electrode will be installed in this small chamber as well as in the autoclave itself near the specimen. A cross-sectional sketch of this electrode is shown in Fig. 7.12. The electrode is formed from a closed-end tube of palladium-silver alloy, pressurized on the inside with pure hydrogen. The alloy tube is encased in a perforated sleeve, which allows water to be trapped between the tube and the sleeve, where it is saturated with hydrogen permeating through the wall of the tube. The electrode acts as a hydrogen reference electrode. The advantage of this

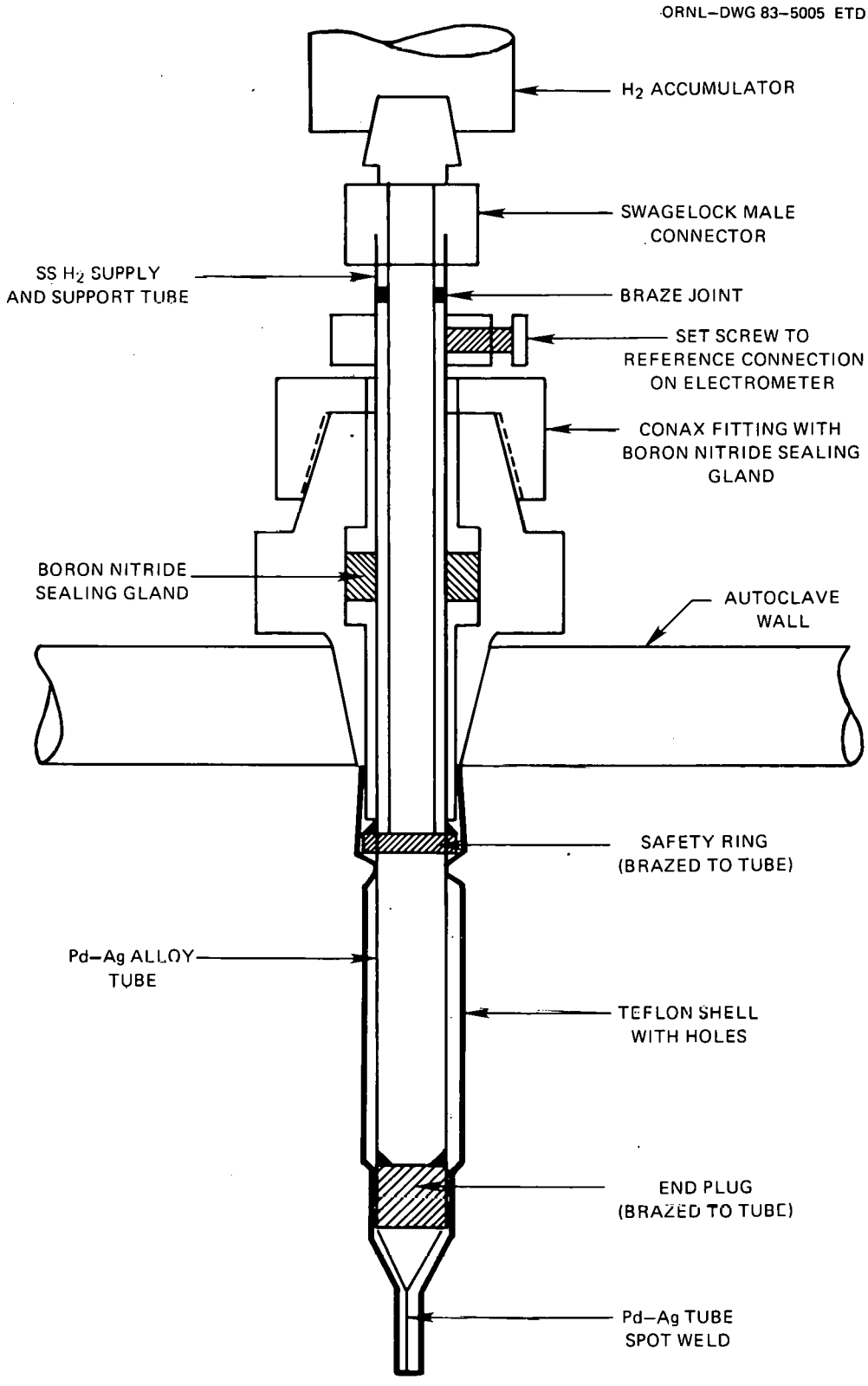

Fig. 7.12. Sketch of hydrogen reference electrode.

system is that its failure does not result in any contamination of the autoclave environment, since a hydrogen overpressure exists at all times.

Fabrication of both of these electrodes was begun during this report period, and installation is expected to be accomplished during the next period.

References

1. W. H. Bamford, "Environmental Cracking of Pressure Boundary Materials and the Importance of Metallurgical Considerations," in *Aspects of Fracture in Pressure Vessels and Piping*, ASME Publication PVP 58, American Society of Mechanical Engineers, New York, 1982.

2. W. H. Bamford, "Environmentally Assisted Crack Growth Studies," in *Heavy-Section Steel Technology Program Quart. Prog. Rep. September–December 1982*, NUREG/CR-2751, Vol. 4 (ORNL/TM-8369/V4), Union Carbide Corp. Nuclear Division, Oak Ridge Natl. Lab.

3. W. H. Bamford, D. M. Moon, and L. J. Ceschini, *Environmentally Assisted Crack Growth in Light Water Reactor Materials, Annual Technical Progress Report, Fiscal Year 1981*, Westinghouse Electric Corporation, Pittsburgh, Pa.

4. *ASME Boiler and Pressure Vessel Code*, Section XI, 1980 ed., Winter 1980 Addendum, American Society of Mechanical Engineers, New York, 1980.

5. W. H. Bamford, D. M. Moon, and L. J. Ceschini, "Studies of Statically and Dynamically Loaded Cracks in Simulated Pressurized Water Environment," in Proceedings of Corrosion 83, to be published in *Corrosion*.

6. P. M. Scott, "Chemistry Effects in Corrosion Fatigue" in Proceedings of the ASTM Conference on Corrosion Fatigue, St. Louis, Mo., October 1981, to be published by American Society for Testing and Materials in 1983.

7. P. L. Andresen, *Innovations in Experimental Techniques for Testing in High Temperature Aqueous Environments*, Report 81CRD088, General Electric Company, Schenectady, N.Y., May 1981.

CONVERSION FACTORS[a]

SI unit	English unit	Factor
mm	in.	0.0393701
cm	in.	0.393701
m	ft	3.28084
m/s	ft/s	3.28084
kN	lb_f	224.809
kPa	psi	0.145038
MPa	ksi	0.145038
$MPa \cdot \sqrt{m}$	$ksi \cdot \sqrt{in.}$	0.910048
J	ft·lb	0.737562
K	°F or °R	1.8
kJ/m^2	$in.-lb/in.^2$	5.71015
$W \cdot m^{-2} \cdot K^{-1}$	$Btu/h-ft^2-°F$	0.176110
kg	lb	2.20462
kg/m^3	$lb/in.^3$	3.61273×10^{-5}
mm/N	$in./lb_f$	0.175127

$T(°F) = 1.8\ T(°C) + 32$

[a]Multiply SI quantity by given factor to obtain English quantity.

NUREG/CR-3334
Volume 1
ORNL/TM-8787/V1
Dist. Category RF

Internal Distribution

1.	D. G. Ball	21.	J. G. Merkle
2.	B. R. Bass	22.	D. H. Morris
3.	R. G. Berggren	23.	R. K. Nanstad
4.	S. E. Bolt	24.	D. J. Naus
5-6.	R. H. Bryan	25-29.	C. E. Pugh
7.	J. W. Bryson	30.	G. C. Robinson
8.	R. D. Cheverton	31.	J. W. Roddy
9.	J. M. Corum	32.	G. M. Slaughter
10.	W. R. Corwin	33.	J. E. Smith
11.	J. R. Dougan	34.	W. J. Stelzman
12-13.	D. S. Griffith	35.	K. R. Thoms
14.	R. C. Gwaltney	36.	H. E. Trammell
15.	F. J. Homan	37-41.	G. D. Whitman
16.	S. K. Iskander	42.	ORNL Patent Office
17.	K. K. Klindt	43.	Central Research Library
18.	A. L. Lotts	44.	Document Reference Section
19.	S. S. Manson	45-46.	Laboratory Records Department
20.	R. W. McCulloch	47.	Laboratory Records (RC)

External Distribution

48. C. Z. Serpan, Division of Engineering Technology, Nuclear Regulatory Commission, Washington, DC 20555
49. M. Vagins, Division of Engineering Technology, Nuclear Regulatory Commission, Washington, DC 20555
50. Office of Assistant Manager for Energy Research and Development, DOE, ORO, Oak Ridge, TN 37830
51-52. Technical Information Center, DOE, Oak Ridge, TN 37830
53-327. Given distribution as shown in category RF (NTIS - 10)

NRC FORM 335 (11-81)

U.S. NUCLEAR REGULATORY COMMISSION

BIBLIOGRAPHIC DATA SHEET

1. REPORT NUMBER *(Assigned by DDC)*
NUREG/CR-3334, Vol. 1
ORNL/TM-8787/V1

4. TITLE AND SUBTITLE *(Add Volume No., if appropriate)*
Heavy-Section Steel Technology Program Quarterly Progress Report for January–March 1983

2. *(Leave blank)*

3. RECIPIENT'S ACCESSION NO.

7. AUTHOR(S)
C. E. Pugh

5. DATE REPORT COMPLETED
MONTH | YEAR

9. PERFORMING ORGANIZATION NAME AND MAILING ADDRESS *(Include Zip Code)*
Oak Ridge National Laboratory
P.O. Box X
Oak Ridge, TN 37830

DATE REPORT ISSUED
MONTH | YEAR

6. *(Leave blank)*

8. *(Leave blank)*

12. SPONSORING ORGANIZATION NAME AND MAILING ADDRESS *(Include Zip Code)*
Division of Engineering Technology
Office of Nuclear Regulatory Research
U.S. Nuclear Regulatory Commission
Washington, DC 20555

10. PROJECT/TASK/WORK UNIT NO.

11. FIN NO.
B0119

13. TYPE OF REPORT
Quarterly

PERIOD COVERED *(Inclusive dates)*
January through March 1983

15. SUPPLEMENTARY NOTES

14. *(Leave blank)*

16. ABSTRACT *(200 words or less)*

The Heavy-Section Steel Technology (HSST) Program is an engineering research activity conducted by the Oak Ridge National Laboratory for the Nuclear Regulatory Commission. The program comprises studies related to all areas of the technology of materials fabricated into thick-section primary-coolant containment systems of light-water-cooled nuclear power reactors. The investigation focuses on the behavior and structural integrity of steel pressure vessels containing cracklike flaws. Current work is organized into seven tasks: (1) program administration and procurement, (2) fracture-mechanics analyses and investigations, (3) investigations of irradiated materials, (4) thermal-shock investigations, (5) pressure vessel investigations, (6) stainless steel cladding investigations, and (7) environmentally assisted crack growth studies.

17. KEY WORDS AND DOCUMENT ANALYSIS

17a. DESCRIPTORS

Pressure vessels
Ferritic steels
Weldments
Irradiation
Cladding
Flaws
Thermal shock
Fracture mechanics
Toughness
Crack arrest
Crack growth

17b. IDENTIFIERS/OPEN-ENDED TERMS

AVAILABILITY STATEMENT
Unlimited

19. SECURITY CLASS *(This report)*
Unclassified

21. NO. OF PAGES

20. SECURITY CLASS *(This page)*
Unclassified

22. PRICE
$